

LIGHT SCATTERING STUDIES ON LECITHIN MICELLAR SOLUTIONS

by

Richard Addison Chamberlin, Jr.

B. S., University of California, Santa Barbara (1984)

SUBMITTED IN PARTIAL FULFILLMENT OF THE  
REQUIREMENTS FOR THE DEGREE OF  
DOCTOR OF PHILOSOPHY IN PHYSICS

at the

MASSACHUSETTS INSTITUTE OF TECHNOLOGY

May, 1991

(c) Massachusetts Institute of Technology, 1991

Signature of Author: \_\_\_\_\_

Department of Physics, May 1991

Certified by: \_\_\_\_\_

George B. Benedek, Thesis Supervisor

Accepted by: \_\_\_\_\_

George Koster, Chairman, Departmental Committee

MASSACHUSETTS INSTITUTE  
OF TECHNOLOGY

JUN 04 1991

LIBRARIES

# Light Scattering Studies on Lecithin Micellar Solutions

by

Richard Addison Chamberlin, Jr.

Submitted In Partial Fulfillment Of The Requirements For The Degree Of

Doctor Of Philosophy In Physics. May, 1991

## ....ABSTRACT....

Herein is described the design and construction of a general purpose light scattering instrument for the study of solution systems. Features of this instrument include high optical and thermal stability, and complete computer control. The instrument has multi-angle detection and can perform both static and dynamic light scattering experiments.

The described light scattering instrument was used to make detailed studies of several different types of lecithin micellar systems. The experimental findings presented here are compared with previous experimental observations and theoretical predictions.

Thesis supervisor: George B. Benedek

Title: Alfred H. Caspary Professor of Physics and Biological Physics

This work is dedicated to the memory of my grandmother

LYDIA RUTH KAHN LEVIN.

"May the Lord reward your deeds."

## ...CONTENTS...

1. Introduction	9
References for Chapter 1	18
2. Design and construction of an instrument suited for both static & dynamic light scattering	21
2.1 Review of Different Instrument Types	22
2.1.1 Instrument Type Employing Rotation Stage	22
2.1.2 Instrument With Stationary Optics	24
2.1.3 Low Angle Light Scattering Instrument	24
2.2 A Technical Description Of The Light Scattering	25
2.2.1 Introduction	25
2.2.2 The Optical Subsystem	26
2.2.3 Summary Of Essential Information About The Optical Setup	31
2.2.4 The Data Acquisition Subsystem	31
2.2.5 The Temperature Controller Subsystem	34
2.2.6 Mechanical Details	41
2.2.7 Optical Alignment Procedures	51
2.2.8 Instrument Assembly	56
2.2.9 Lens Design	61
References for Chapter 2	71
3. Light Scattered From Pure Fluids	75
3.1 Introduction	75
3.2 Optical extinction in an ideal gas of particles	76
3.3 Scattering from an ideal gas of particles: Rayleigh Scattering	79
3.4 Scattering from liquids	81
3.5 Instrument calibration procedures	83
3.6 Standard ways of reporting the Rayleigh ratio	87

3.7 The turbidity with depolarized light scattering	89
3.8 Light scattering intensity standards	89
3.9 The Rayleigh of water and its temperature dependence	91
3.10 The Rayleigh ratios and turbidities of several solvents used as scintillators	91
References for Chapter 3	98
4. Light Scattered From Model Macromolecular Systems	100
4.1 Introduction	100
4.2 The Rayleigh-Gans Approximation	101
4.3 The radius of gyration	106
4.4 The molecular weight	107
4.4.1 Particles suspended in space	107
4.4.2 Particles suspended in a solvent medium	108
4.4.3 Particle interactions and the apparent molecular weight	110
4.5 Dynamic light scattering	111
4.6 The results of measurements from model systems	114
4.6.1 Bovine serum albumin	115
4.6.2 Polystyrene latex spheres	117
4.6.3 Polystyrene dissolved in toluene	118
4.6.3.1 Sample preparation	118
4.6.3.2 Light scattering results	119
4.6.3.3 Discussion of Results	124
References for Chapter 4	130
5. Light Scattered From Short Chain Lecithin-Water Solutions	132
5.1 Introduction	132
5.2 Di-C <sub>7</sub> lecithin	138
5.2.1 Sample preparation	138
5.2.2 Light scattering measurements	140
5.2.3 Results and Discussion	143

5.3 Di-C <sub>8</sub> lecithin	148
5.3.1 Sample preparation	148
5.3.2 Light scattering measurements at 35 deg. C.	149
5.3.3 Light scattering measurements at 55 deg. C.	150
5.3.4 Results and discussion	154
5.4 Micelle shape	159
5.5 The effects of polydispersity on the deduction on the deduction of the micellar shape	173
5.6 Conclusion	184
References for Chapter 5	185
6. Light Scattering Studies Of Mixed Biological Lecithin and Detergent Micellar Systems	187
6.1 Introduction	187
6.1.1 A critical examination of the previous findings of Mazer et al.	190
6.1.2 Recent small angle neutron scattering work, and electron microscopy work in detergent, lecithin systems	192
6.1.3 Phase diagrams and dilution paths of the micellar systems studied in this work	193
6.2 Experimental Procedures	195
6.2.1 Apparatus	195
6.2.2 Static Light Scattering.	195
6.2.3 Dynamic Light Scattering.	203
6.2.4 Materials Preparation.	203
6.2.5 Sample dilution prior to light scattering	204
6.2.6 Measured values of dn/dc	204
6.3 Light scattering results	204
6.4 Discussion	207
6.5 Conclusion	209
References for Chapter 6	220
7. CONCLUSION	223

<b>References for Chapter 7</b>	<b>227</b>
<b>Autobiographical note</b>	<b>228</b>
<b>Acknowledgments</b>	<b>229</b>





## 1. Introduction

*At some point, even a worm turns.*

Paulette Eisenstadt, *on the dynamics of teacher, administrator interactions in the public school system.*

Understanding the physical-chemical properties of micellar solutions is significant to many fields of scientific and technological endeavor. A few areas of research where studies of micellar solutions are very important are: the physics of spontaneously self assembling molecular systems; lipid transport in biological systems; membrane, and vesicle formation; cholesterol precipitation in the gall bladder, and on arterial walls; enhanced petroleum recovery techniques; and novel drug delivery techniques. Many different experimental techniques have been used to study micellar solutions including nuclear magnetic resonance (NMR), electron microscopy, surface tension, small angle neutron scattering (SANS), and light scattering. The emphasis in this thesis will be the results obtained with light scattering on lecithin micellar systems.

The signature of light scattered from micellar solutions (or macromolecular solutions) is affected by the micelle size, micelle polydispersity, micelle shape, micelle interactions, micelle translational and rotational diffusion, and internal micelle dynamical modes. In normal macromolecular solutions, a common procedure is to study the solution in the limit of vanishing solute concentration, since in this limit, the macromolecules are far from one another and the light scattering signal is interpreted as simply due to average particle size, particle shape, particle polarizability (which is related to particle molecular weight), and particle self diffusion. In contrast, micellar systems usually must be studied at relatively high solute concentrations since the micelle size is itself a function of concentration. The interpretation of light scattering data at higher concentrations

is generally much more difficult because correlations in particle positions, and collective diffusive modes affect the intensity and the dynamical properties of the scattered light. Although collective diffusive properties, and inter-particle correlations are interesting in their own right, their convolution into the the light scattering data can make it hard to determine actual micelle size, shape, weight, and polydispersity as a function of concentration. This problem is significant since the verification of theories of micellar formation depends on accurately knowing the micelle size, shape, polydispersity, and weight as a function of concentration. In addition, even if micellar interactions are ignored, it may be possible to find more than one deconvolution of the experimental problem if insufficient data is obtained regarding the static and dynamic properties of the light scattered from the solution.

This thesis is divided into two parts. The first part is a detailed exposition of the general purpose light scattering instrumentation developed for this project. The second part of this thesis describes the results of light scattering measurements, made with the above instrument, on a variety of pure liquid, macromolecular, and lecithin surfactant systems.

The exposition of the first part describes the design and construction of an instrument suited for performing both static and dynamic light scattering measurements on macromolecular and colloidal solutions. Features of this instrument include high optical stability, and high sensitivity to scattered light intensity; an operational temperature range of 5° C to 55° C, with sub-millikelvin temperature stability; and, a computer data acquisition, and data reduction system implemented on a multiuser, multitasking computer.

The second part of this work begins with a description of the theory of Rayleigh scattering, and light scattering from pure fluids. Using this instrument we measured the absolute intensity of light scattered from pure water over the entire operational temperature range of the instrument and found that the Rayleigh ratio of the scattered intensity,  $R(0)$ , was nearly constant over most of the temperature range:  $R(0) = (2.54 \pm 0.06) \times 10^{-6}$ , at  $\lambda_0 = 488 \text{ nm}$ ,  $10^\circ \text{ C} < T < 55^\circ$ . We show that our findings are consistent with published findings at different incident light wavelengths,  $\lambda_0$ . We also present our findings for the turbidity (or, equivalently, total scattering cross section at  $\lambda_0 = 488 \text{ nm}$ ) for several scintillating fluids intended for possible use a solar neutrino detection experiment.

The theory of Rayleigh-Gans scattering from particles suspended in *vacuo* and in solution is presented. The problem of interparticle interaction effects on the scattered light intensity is introduced in terms of the virial expansion of the osmotic susceptibility. The theory of dynamic light scattering (also known in the literature as "quasi-elastic light scattering", "homodyne light scattering spectroscopy", and "photon correlation spectroscopy") is presented along with its connection to particle diffusion and particle hydrodynamic effective size. The results of trial measurements on three macromolecular model systems are presented. The model systems are: the protein, bovine serum albumin in aqueous buffer; commercially produced sub-micron size latex spheres in saline solution; and polystyrene polymer molecules suspended in toluene.

In the last parts of the thesis we present the results of detailed measurements of the osmotic susceptibility,  $(\frac{\partial \pi}{\partial c})_T$ , the static correlation range,  $\xi_s$ , and the hydrodynamic cor-

relation range,  $\xi_h$  for a variety of lecithin micellar aqueous solutions. The osmotic susceptibility was derived from the measurement of the scattered light intensity extrapolated to zero scattering angle. The static correlation range was derived from the angular dependence of the scattered light. The hydrodynamic correlation range was derived from the observation of fluctuations in the intensity of the scattered light extrapolated to zero scattering angle. Thus, the hydrodynamic correlation ranges we report here are in the long wavelength limit.

At low concentration where interparticle interactions are less significant, we have followed the practice of interpreting  $(\frac{\partial\pi}{\partial c})_T$ ,  $\xi_s$ , and  $\xi_h$  in terms of single particle properties. In this regime we can relate  $(\frac{\partial\pi}{\partial c})_T$  to the weight averaged molecular weight  $M_w$ ; we can relate  $\xi_s$  to the z-average of square of the radius of gyration,  $\langle R_g^2 \rangle_z$ ; and we can relate  $\xi_h$  to the z-average the reciprocal of the hydrodynamic radius,  $\langle 1/R_h \rangle_z$ . The relation of these averages to  $(\frac{\partial\pi}{\partial c})_T$ ,  $\xi_s$ , and  $\xi_h$  their definition, and their significance, will be elaborated on in Chapters 4, and 5.

The lecithin molecule has a zwitterionic head group and a double hydro-carbon tail. It has been shown previously [1, 2, 3, 4, 5] that variation of the length of the double hydro-carbon tail length has dramatic effects on the self-aggregative behavior of lecithin molecules. In this study, we present measurements of the concentration dependent growth of two types of short hydro-carbon tail lecithins in water: di-C<sub>7</sub> lecithin in H<sub>2</sub>O, and in D<sub>2</sub>O; and di-C<sub>8</sub> lecithin in H<sub>2</sub>O. In these three simple lecithin micellar systems, we used the intensity of the scattered light extrapolated to zero scattering angle to show that the low concentration dependence of the micelle aggregation number varied like the

square root of the amphiphile mole fraction. This observation is compatible with the predictions of the ladder model [6] for micellar growth, and with the earlier observations of Chen *et al.* [5] who used small angle neutrons scattering on di-C<sub>7</sub> lecithin micelles in D<sub>2</sub>O, and with the earlier observations of Tausk *et al.* who used static light scattering on Di-C<sub>7</sub> lecithin, and Di-C<sub>8</sub> lecithin micelles in H<sub>2</sub>O. In the di-C<sub>8</sub> lecithin system, we used the low concentration dependence of the micelle aggregation number to derive the ladder model growth potential  $\ln(K)$  on two isotherms: on the 35° C isotherm, we found  $T\ln(K) = 7200^\circ \text{ K}$ ; and on the 55° C isotherm, we found  $T\ln(K) = 7100^\circ \text{ K}$ , where  $T$  is the temperature in degrees kelvin. These values of  $\ln(K)$  are compatible with earlier measurements of Thurston [7] who used dynamic light scattering to find an effective hydrodynamic size of the micellar aggregates. Thurston found the concentration dependence of the micelle aggregation number by interpreting his hydrodynamic size data in the context of a hydrodynamic model for worm shaped particles. From his derived aggregation number, and a range of assumed worm stiffnesses from stiff rod to very flexible, Thurston found that  $6900^\circ \text{ K} < T\ln(K) < 7300^\circ \text{ K}$ .

Earlier Thurston *et al.* [8] proposed a new mean field theory to explain the phenomena of liquid-liquid phase separation observed in certain micellar systems such as C<sub>12</sub>E<sub>6</sub>, and di-C<sub>8</sub> lecithin. From their measurements of the position and the shape of the temperature, concentration coexistence curve for liquid-liquid phase separation in the di-C<sub>8</sub> lecithin system, Thurston *et al.* could derive the ladder model growth parameter  $\ln(K)$  in the context of their theory. Thus, they found that  $T\ln(k) = 8100^\circ \text{ K}$ . This value of  $T\ln(K)$  is different from the value we gave above which was obtained from static light

scattering, and from the earlier value of Thurston who used dynamic light scattering. The mean field theory of Thurston *et al.* can also predict the osmotic susceptibility. In this thesis, we measured the osmotic susceptibility on the 55° C isotherm and compared our measurements to the values predicted from the theory of Thurston *et al.* using parameters they derived from the location and shape of the coexistence curve. We found here that the theoretical curve for the osmotic susceptibility was an order of magnitude less than that observed using the scattered light intensity. These findings may indicate that the mean field theory of Thurston *et al.* may require some modification so that it can self consistently explain both the observed position of the coexistence curve, and the experimental measurements of the ladder growth parameter  $\ln(K)$  found from both static and dynamic light scattering.

The last part of this thesis is concerned with the issue of the shape of detergent, biological lecithin micellar aggregates. Biological lecithin is nearly insoluble in water by itself; however, in the presence of biological detergents, such as bile salts, or octylglucoside, biological lecithin becomes very soluble in the form of mixed detergent, lecithin micelles. In a widely accepted mixed detergent, lecithin model advanced by Mazer *et al.* [9], it was suggested that the mixed micelles resembled fragments of a lecithin bi-layer with a thickness corresponding to the length of two lecithin molecules; that is, the disk thickness would be about 5 nm. Mazer *et al.* used relative intensity light scattering at one scattering angle, and dynamic light scattering at one scattering angle, to deduce that the taurocholate, lecithin system could be described by a disk model. This bilayer disk model was generally accepted as a correct description of the phenomenology in a very large variety of mixed detergent, lecithin micellar systems.

The previously assumed generality of the bilayer disk mixed detergent, lecithin model has recently been challenged in a variety of physical experiments. Small angle neutron scattering was used by Hjelm *et al.* on the glycocholate, lecithin micellar system where evidence for rods of radius 2.7 nm was found, but no disks. Vinson *et al.* [10, 11] have used a cryo-transmission electron microscopy (cryo-TEM) technique to form images of octylglucoside, lecithin micelles, and sodium cholate, lecithin micelles. In the octylglucoside, lecithin system, the cryo-TEM images revealed worm like aggregates; in the sodium cholate, lecithin system, cryo-TEM images revealed rod like aggregates. In neither system, were disks observed.

In this thesis we will re-examine the problem of the shape of mixed detergent, lecithin micelles using static and dynamic light scattering. We will start by re-examining the published data of Mazer *et al.* [9], and show that their disk model interpretation of the light scattering is not unique; that is, we will show that a hydrodynamic model for worm like particles can also easily satisfy their data. Then, we will proceed to present the results of our detailed measurements on three mixed detergent, lecithin micellar systems: octylglucoside, lecithin; sodium cholate, lecithin; and sodium taurocholate, lecithin. In all three systems, we found that the dependence of  $M_{app}$  on  $R_h$  could not be fit by an oblate ellipsoid model, where we assumed an ellipsoid semi-minor axis of 2.5 nm. However, we did find that the data had some, but not complete correspondence to a rod model, with a rod radius of 2.5 nm.

For all of the micelle systems studied in this work, we also found that the magnitude of the experimentally measured ratio  $\frac{R_h}{M_{app}^{1/2}}$  was similar in magnitude and very weakly

concentration dependent over two decades of concentration range. The weak concentration dependence of the ratio  $\frac{R_h}{M_{app}^{1/2}}$  could suggest that the micellar aggregates were disks of constant thickness, but concentration dependent radii. However, as we will show from the magnitude of the ratio  $\frac{R_h}{M_{app}^{1/2}}$ , such disks could only be about 0.7 nm thick, and this value is inconsistent with the bilayer thickness assumed by the disk model of 5 nm. In a presentation of this work elsewhere [12], we stated in addition that the magnitude of  $\frac{R_h}{M_{app}^{1/2}}$  was consistent with a worm model in which the worm radius was 2.5 nm, and the worm persistence length as 26 nm. However, this simple interpretation requires that the worm contour length be large compared to the worm persistence length, which is not generally true for all the micellar systems presented here. Therefore, although we can use the magnitude of the ratio  $\frac{R_h}{M_{app}^{1/2}}$  to rule out the disk model, we should not try to use it as a sensitive measure of the persistence length in flexible rod like micelles. In addition to the above measurements, we also measured the ratio  $R_g/R_h$  as a function of concentration in all of the micellar systems. A disk model for the micellar aggregates would predict that  $R_g/R_h \approx 1.0$ . Instead, we found that  $R_g/R_h \geq 1.5$ , which is what would be predicted for systems of long rods, or worm-like flexible rods.

**A NOTE ON UNITS:** The metric system of units is used exclusively except in Chapter 2 which describes the light scattering instrument design. Since the instrument was intended to be fabricated in an American machine shop, actual dimensions on the shop drawings were given in inches. Accordingly, where machine dimensions are salient in the technical discussion of Chapter 2, dimensions will be expressed in inches. Dimen-



sion tolerance is indicated by the following conventions: (1) if the dimension is given in fractional units, then it was a nominal value only and was not held to tight tolerance; (2) if the dimension is expressed in decimal units, then the tolerance was plus or minus one half of the least significant digit, e.g. 3.001" means three and one thousandths inches plus or minus five ten thousandths inches.

## References for Chapter

- [1] R. J.M. Tausk, J. Karmiggelt, C. Oudshoorn, J. Th. G. Overbeek.  
Physical Chemical Studies Of Short-Chain Lecithin Homologues. I. Influence Of  
The Chain Length Of The Fatty Acid Ester And Of Electrolytes On The Critical  
Micelle Concentration.  
*Biophysical Chem.* 1:175-183, 1974.
- [2] R. J.M. Tausk, J. van Esch, J. Karmiggelt, G. Voordouw, J. Th. G. Overbeek.  
Physical Chemical Studies Of Short-Chain Lecithin Homologues. II. Micellar  
Weights of Dihexanoyl-and Diheptanoyllecithin.  
*Biophysical Chem.* 1:184-203, 1974.
- [3] R. J.M. Tausk, C. Oudshoorn, J. Th. G. Overbeek.  
Physical Chemical Studies Of Short-Chain Lecithin Homologues. III. Phase  
Separation and Light Scattering Studies on Aqueous Dioctanloyllecithin  
Solutions.  
*Biophysical Chem.* 2:53-63, 1974.
- [4] R. J.M. Tausk, J. Th. G. Overbeek.  
Physical Chemical Studies Of Short-Chain Lecithin Homologues. IV. A Simple  
Model For The Influence Of Salt And The Alkyl Chain Length On The Micellar  
Size.  
*Biophysical Chem.* 2:64, 1974.
- [5] Tsang-Lang Lin, Sow-Hsin Chen ,and Mary F. Roberts.  
Thermodynamic Analysis of the Structure and Growth of Asymmetric Linear  
Short-Chain Lecithin Micelles Based on Small-Angle Neutron Scattering  
Data.  
*Jornal of the American Chemical Soc.* 109():2321, 1987.
- [6] P.J. Missel, N.A. Mazer, G.B. Benedek, C.Y. Young.  
Thermodynamic Analysis of the Growth of Sodium Dodecyl Sulfate Micelles.  
*J. Phys. Chem.* 84():1044 - 1057, 1980.
- [7] G. M. Thurston.  
*Studies of Phase Separation in Micellar Solutions.*  
PhD thesis, Massachusetts Institute of Technology, 1986.
- [8] D. Blankschtein, G. M. Thurston, G. B. Benedek.  
Theory of Phase Separation in Micellar Solutions.  
*Phys. Rev. Lett.* 54(9):955-958, 1985.
- [9] N.A. Mazer, G.B. Benedek, M.C. Carey.  
Quasielastic Light-Scattering Studies of Aqueous Biliary Lipid Systems. Mixed  
Micelle Formation in Bile Salt-Lecithin Solutions.  
*Biochemistry* 19:601-615, 1980.
- [10] P. K. Vinson, Y. Talmon, and A. Walter.  
Micelle-Vesicle Transition of Phosphatidylcholine and Octyl Glucoside  
Elucidated by Cryo-Transmission Electron Microscopy.  
*Biophys. J.* 56:669-681, 1989.

- [11] P. K. Vinson, Y. Talmon, A. Walter.  
Cryo-TEM Reveals Structural Transitions of Egg PC and Sodium Cholate Mixtures.  
*Biophys. J.* , 1990.
- [12] R. A. Chamberlin, D. Cohen, G. M. Thurston, G. B. Benedek, M. C. Carey.  
Light Scattering Evidence for Worm-like Mixed Detergent Lecithin Micelles.  
Materials Research Society, in Boston, 27 Nov 1989.



## **2. Design and construction of an instrument suited for both static and dynamic light scattering**

*Knowledge earned is better than knowledge learned (if the price ain't too dear).*

*From a book on heavy air sailing.*

Light is scattered from materials that possess spatial and/or temporal fluctuations in density provided that the length scale over which the density fluctuations are correlated is comparable to the wavelength of the incident light. The intensity of the scattered light is proportional to the square of the amplitude of the density fluctuations [1]. The dependence of the scattered light intensity on scattering angle is related to the length scale over which density fluctuations are correlated [2]. The measurement of the time averaged light scattering intensity is known as static light scattering.

In fluid systems, the temporal variation of the fluid density results in temporal fluctuations in light scattering intensity at a given scattering angle [3, 4]. The measurement and characterization of these time dependent intensity fluctuations is known as dynamic light scattering.

The theory and practice of static and dynamic light scattering will be developed further in the following chapters.

This chapter is devoted to a technical description of an instrument suited for performing both static and dynamic light scattering on fluid systems as a function of temperature. This chapter is mainly an exposition of the design and construction this instrument.

The chapter will begin with a very brief review of light scattering instrument types.

## 2.1 Review of Different Instrument Types

This brief review is intended only to give the uninitiated reader some taste of the common instrument types and their relative merits. Those readers needing more detail should refer to the literature.

### 2.1.1 Instrument Type Employing Rotation Stage

Most light scattering instruments in use today have one feature in common: the detection optics are mounted on the end of an arm which is attached to a rotation stage. The axis of the rotation stage is centered on a stationary sample cell. The scattering angle  $\theta$  is varied by rotating the arm, and its associated optics, around the stationary sample.

Several different optical arrangements have been used for the detection in this kind of instrument [5]. In the schematic instrument shown in fig. 2-1, laser light scattered by the sample is focused by lens L1 onto the plane of aperture A2, i.e. an image of the scattering volume is focused onto A2. In this optical system, the clear aperture, and therefore the solid angle of accepted rays from a point source in the scattering volume, is determined by the aperture A1 which is close to the lens L1. The linear extent of the image of the scattered laser beam accepted into the optical system is determined by the size of aperture A2. Usually lens L2 is selected so as to focus the image of the aperture A1 on to the detector active area. The purpose of lens L2 is to diffuse the image of the scattered light reaching the face of the detector. The photo-active area of detectors such as photomultipliers or photodiodes generally have positionally dependent sensitivity. This means that a diffuse image will give a more uniform response if the image should move across the detector. In practice, the image of a scattering volume moves slightly

with respect to the detector surface when the scattering angle  $\theta$  is changed, since the optical system is never aligned perfectly. Therefore, a diffuse image gives a more uniform response as the scattering angle is changed.

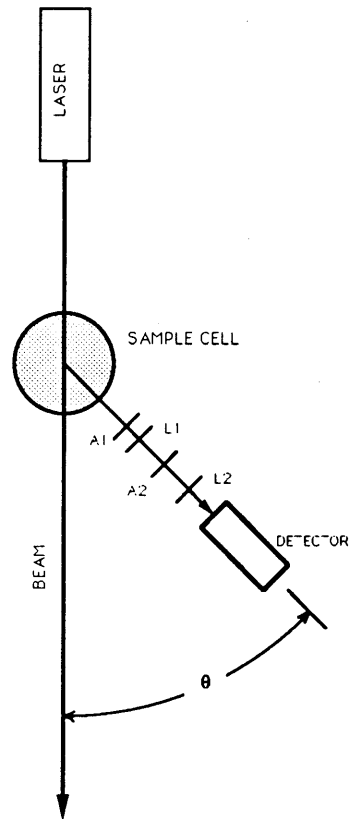


**Figure 2-1:** Schematic of a typical light scattering apparatus employing a rotation stage to vary scattering angle

L1 is the imaging lens. L2 is the diffusing lens. A1 is the clear aperture of the optical system: it determines the acceptance solid angle of the scattered rays. A2 is the aperture at the image plane: it determines the extent of the scattering volume accepted for detection.

The advantage of this type of setup is primarily its relative ease of construction. In

some of these setups, the sample is surrounded by an index matching bath such as toluene: a large diameter glass ring is used to contain the sample and index matching bath.

The problems with setups employing rotation stages seem to be related to maintaining precise and repeatable orientation of the detection optics with respect to the sample, and in reducing sources of stray light. (Stray light is created whenever a beam of light passes through, or is reflected from interfaces such as lenses, glass sample cells, metal tubes, etc. Light rays scattered from such interfaces enter the detection optics and reduce instrument sensitivity.)

### **2.1.2 Instrument With Stationary Optics**

Instrument performance with respect to the two problems listed above can be greatly enhanced by employing stationary detection optics, and immersing the sample cell in a very large diameter index of refraction matching bath. The large diameter bath helps move sources of stray light far away from the center of the scattering volume. The instrument constructed and used for this thesis, employ these desirable characteristics.

### **2.1.3 Low Angle Light Scattering Instrument**

A third type of instrument which is useful for absolute intensity measurements, and for size measurements of large dissolved particles is the low angle light scattering instrument of Kaye and Havlik [6]. (Here, "large particle", means particle size comparable to the wavelength of incident light.) (See sec. 4.3 for an explanation of how particle size can be obtained from the angular distribution of the scattered intensity.) In this type of instrument, scattered light is collected from a cone of scattered rays symmetrical around



the transmitted beam. Absolute intensity measurements are based on geometrical considerations that determine the scattering volume and collection solid angle.

Instruments of this type are not adapted for dynamic light scattering and they are not suitable for the size measurement of smaller particles. However, they do give excellent results for the absolute intensity of scattered light at small scattering angles providing the samples are prepared to be absolutely dust free.

## **2.2 A Technical Description Of The Light Scattering Instrument Used For This Thesis**

### **2.2.1 Introduction**

As mentioned above, the light scattering instrument used in this thesis employs stationary optics to enhance optical stability and repeatability of measurements. The instrument described here, is based mostly on the design principles given by Haller, Destor, and Cannell. [7]

Features of this instrument are: an ability to perform both static and dynamic light scattering experiments efficiently and rapidly; fixed multiple angle detection, using optical fibers to guide scattered light to one photomultiplier tube; complete computer control of data acquisition and data reduction; an operational temperature range of 5° C. to 55° C. with high thermal stability.

The rest of this chapter is devoted to a full technical description of this instrument. Details of the electronic, data acquisition, and optical subsystems are presented. Procedures for instrument construction, and optical alignment are explained and illustrated. The procedure for instrument light intensity calibration will be discussed in the next chapter.

### 2.2.2 The Optical Subsystem

The following description refers to the block diagram fig. 2-2. For simplicity, this figure only shows angle number 10; the other scattering angles are omitted. Laser light is generated by a water-cooled, vertically polarized argon-ion laser (Coherent Innova 90-5) operating on the 488 nm line. Laser beam direction is steered by mirrors M1, and M2. The beam is attenuated by rotation of the half wave plate P1 with respect to the Glan-Thompson prism GP1. GP1 is oriented such that the output beam electric field polarization is orthogonal to the plane in which the scattered light is to be detected. That is, the electric field vector of the polarized laser beam is orthogonal to the plane of the paper. In addition, the neutral density filter ND1 may be inserted into the beam path if additional attenuation is desired. The laser beam is focused by lens L19 to form a 100 micron beam waist diameter between L19 and L17. This beam waist is imaged by L17 into the center of the sample cell SC. The beam waist in the sample cell is set to be about 100 microns diameter. (See reference [8] for an explanation of the method of determining the propagation of a laser beam by ray matrices.) The sample cell is surrounded by a large diameter index matching, temperature controlled water bath TA. TA is also referred to as "the tank" later in this exposition. Lenses L1 through L18 are identical plano-convex type and also serve as windows through the water bath wall. Scattered light from the sample cell SC is imaged by lenses L2 through L16 onto slit planes (Oriel, model 77-279-2-501-1) SL2 through SL16. The long axis of the slits is orthogonal to the light scattering plane. Thus, the slit width (120 microns for all angles) determines the length of the scattering volume which is accepted into the ends of the optical fibers (F2 - F16)

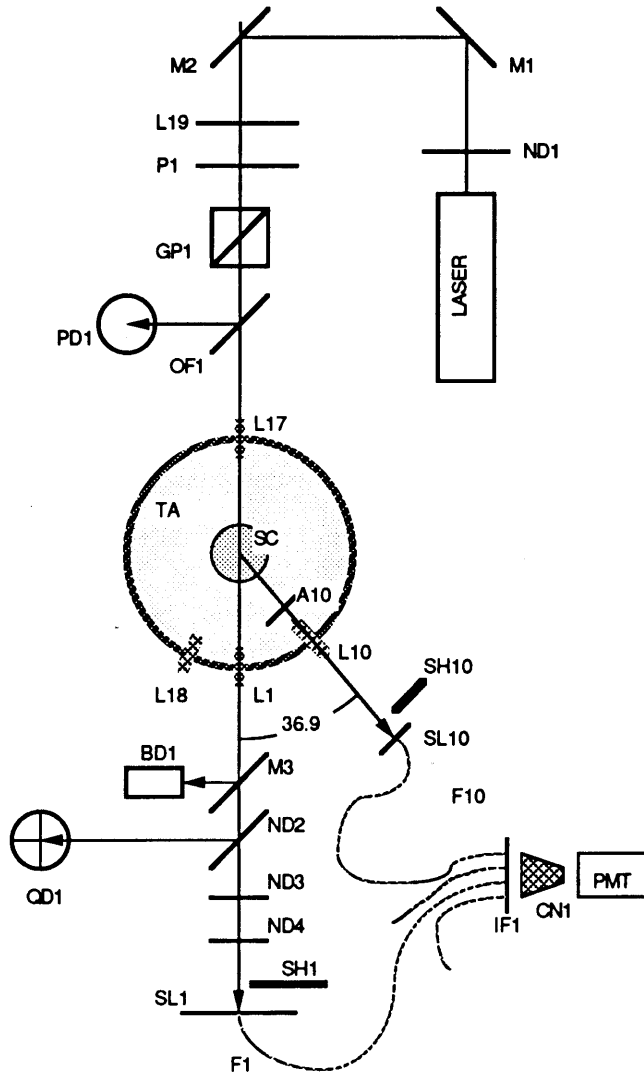


**Figure 2-2:** Block diagram of the optical setup in the light scattering instrument used in this thesis. Although there are 15 fixed scattering angles only one (angle #10) is shown.

(See text for explanation.)

behind each slit. In this way, the size of the scattering volume, and therefore the size of the coherence areas of the scattered light, is determined by the beam waist diameter and the slit width. (See reference [9] for an explanation of what a coherence area is.) The clear apertures of the optical system, and therefore the number of coherence areas accepted by the optics at each angle, is determined by the circular apertures A2 through A16 which are placed in the water bath in front of the lenses. Table 2-1 shows the values of the fixed scattering angles for this instrument, and some associated information.

**Table 2-1:** Values associated with instrument's fixed scattering angles

Spectro-photometer Angular Dependent Optical Quantities					
Angle Number	Scattering Angle $\theta$	Wave Vector, $ q $ ( $n = 1.333$ $\lambda_o = 488\text{nm}$ ) $\times 10^3 \text{cm}^{-1}$	Aperture Diameters (mm)	Solid Collection Angles (sterad.) ( $\times 10^5$ )	Approx. Number of Coherence Areas
1	0.00°	0			
2	2.50°	7.5	1.0	3.0	2.7
3	5.00°	15.0	1.0	3.0	2.7
4	8.50°	25.4	1.0	3.0	2.7
5	11.50°	34.4	1.0	3.0	2.7
6	14.50°	43.3	1.0	3.0	2.7
7	18.20°	54.3	1.5	6.8	6.1
8	23.00°	68.4	1.5	6.8	6.1
9	29.00°	85.9	1.5	6.8	6.1
10	36.90°	108.6	1.5	6.8	6.1
11	46.90°	136.6	1.5	6.8	6.1
12	60.20°	172.1	2.0	12.1	11.
13	78.20°	216.5	2.0	12.1	11.
14	90.00°	242.7	2.0	12.1	11.
15	105.20°	272.7	2.0	12.1	11.
16	162.60°	339.3	2.0	12.1	11.

The laser beam is transmitted through the sample in cell SC and focused onto the end of an optical fiber F1 by lens L1 after passing through a series of attenuators composed of: partially transmitting mirror M3; neutral density filters ND2, and ND3; and

optionally ND4. The combined optical attenuation of M3, ND2, and ND3 is set to about  $10^9$ . When a weak scatterer is to be studied, it may be necessary to increase the incident laser power to such a degree that the transmitted laser power begins to saturate the response of the PMT. In that event, ND4 is optionally inserted when a weak scatterer is to be studied so as to make the transmitted power detected more comparable to the scattered power.

The partially transmitting mirror M3 reflects most of the beam power into beam dump BD1. ND2 reflects part of the beam onto quadrant photodiode QD1 for monitoring the stability of laser beam pointing direction: QD1 detects the position of the geometrical center of the laser beam cross section. Monitoring the laser beam pointing direction also provides an indication of drift in the optical system alignment, and can be used for checking if the scattering cell SC is centered on the instrument mechanical axis. The mechanical axis referred to here is the axis of cylindrical symmetry of the the tank TA. If cell SC is rotated by hand, the beam passing through the cylindrical cell SC will be deflected if the cell is not concentric with the mechanical axis of the instrument. Fig. 2-3 shows a drawing of a typical sample cell in its base. The cell holder base is designed to fit into a receptacle in the instrument with dimensions 1/2" deep by 3.001" diameter. The laser beam height above the plane described by the bottom of the cell holder, is designed to be 1.00" when the cell is placed into the instrument tank TA.

Entrance of light onto the end of the optical fibers F1 - F16 is controlled by solenoid driven shutters SH1 - SH16. These shutters may be actuated manually, or under computer control. The solenoid drive electronics is arranged so that only one shutter may be

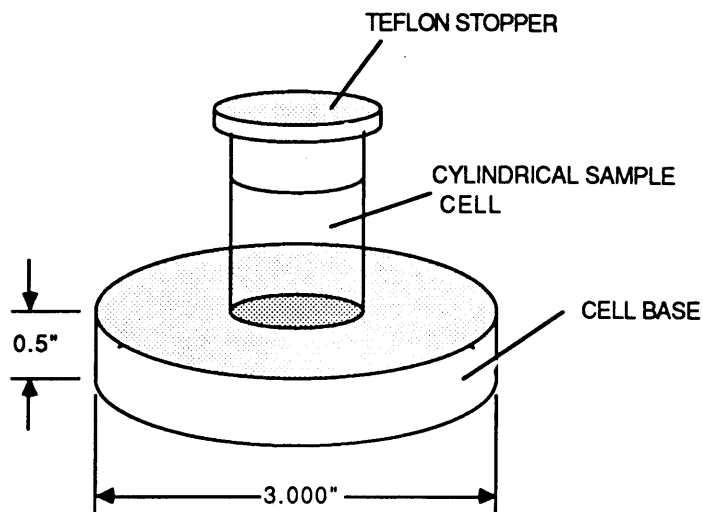


**Figure 2-3:** Example of a sample cell and the dimensions of its base.

opened at once. The optical fibers are 1mm in diameter and are specially treated so as to reduce breakage [10](Ensign Bickford, model HC-1006-T).

The optical fibers F1-F16 guide the transmitted and scattered light to a single photomultiplier tube (PMT). The bundle of optical fibers is coupled to the PMT through interference filter IF1 and conical light guide CN1. The interference filter IF1 (Corion, model P10-488-A,  $(488 \pm 5 \text{ nm})$ ) is used to block out stray room light which may enter the optical system, or to block out sample fluorescence. The conical light guide CN1 narrows the optical fiber bundle cross sectional area diameter (about 6 mm) down to match the PMT photocathode active area diameter (2.5 mm).

### 2.2.3 Summary Of Essential Information About The Optical Setup

The dimensions of the scattering volume are defined by the slit widths SL2 - SL16 (only SL10 was indicated in fig. 2-2), the beam waist, and the scattering angle  $\theta$ . Fig. 2-4 depicts the scattering geometry as seen from over the scattering plane. The shaded cylindrical object in fig. 2-4 represents the laser beam in the sample. The slit widths SL2 - SL16 are each 120 microns. The Beam waist is set by lens L19 to a 100 micron diameter in the sample volume. The length of the scattering volume,  $L$ , is given by inspection of fig. 2-4 as:

$$L = \frac{S_{app}}{\sin(\theta)} \quad (2-1)$$

where  $S_{app}$  is the image of the slit width, or the apparent slit width, in the scattering volume, and  $\theta$  is the scattering angle. The lenses L1 - L18 are selected to give about a one-to-one conjugate ratio in this optical system - that means that the image size is about the same as the object size. Therefore,  $S_{app}$  in eq. (2-1) is approximately the same as the slit width, i.e. 120 microns.

### 2.2.4 The Data Acquisition Subsystem

Block diagram, fig. 2-5 shows the physical arrangement of the electronic modules that compose the data acquisition subsystem. As described above, scattered light from each of the separate scattering angles is coupled, via optical fibers, to a single photomultiplier tube (PMT). (The PMT is an EMI, model 9863A, selected for low dark counts.) The PMT, which is used in an individual photon counting mode [11, p. 66], is coupled to a pulse amplifier-discriminator (PAD) (Langley-Ford, model PAD-1) that converts each photon induced current pulse into a TTL level [12, p. 16] voltage pulse with a 10 ns

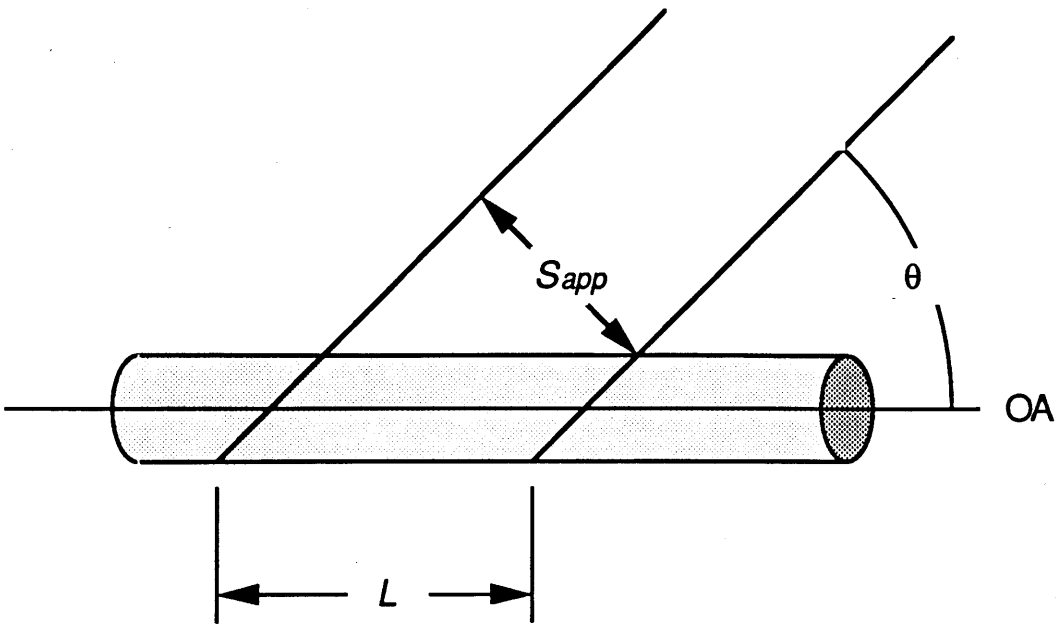


**Figure 2-4:** Schematic of scattering geometry as seen from over scattering plane.

$L$  is the length of the scattering volume,  $S_{app}$  is the apparent slit width image into the scattering volume, and  $\theta$  is the scattering angle. OA is the optical axis of the laser beam.

width. (TTL voltage levels are as follows: a low logic state implies  $0 < V < 0.8$  volts; and a high logic state implies  $2.3 < V < 5$  volts, where  $V$  is the signal voltage.) The TTL pulses from the PAD are fed via RG58 coaxial cable into two instruments: a correlator and a frequency counter. The correlator (Langley-Ford, model 1096) is matched to the PAD with a 50 ohm input impedance. The frequency counter (Hewlett-Packard, model 5316) which also shares the TTL signal from the PAD has a one megaohm input impedance.

The correlator, and the frequency counter are controlled by a computer (Digital Equipment, MicroVaxII) via an IEEE-488 general purpose interface bus (GPIB). Tech-



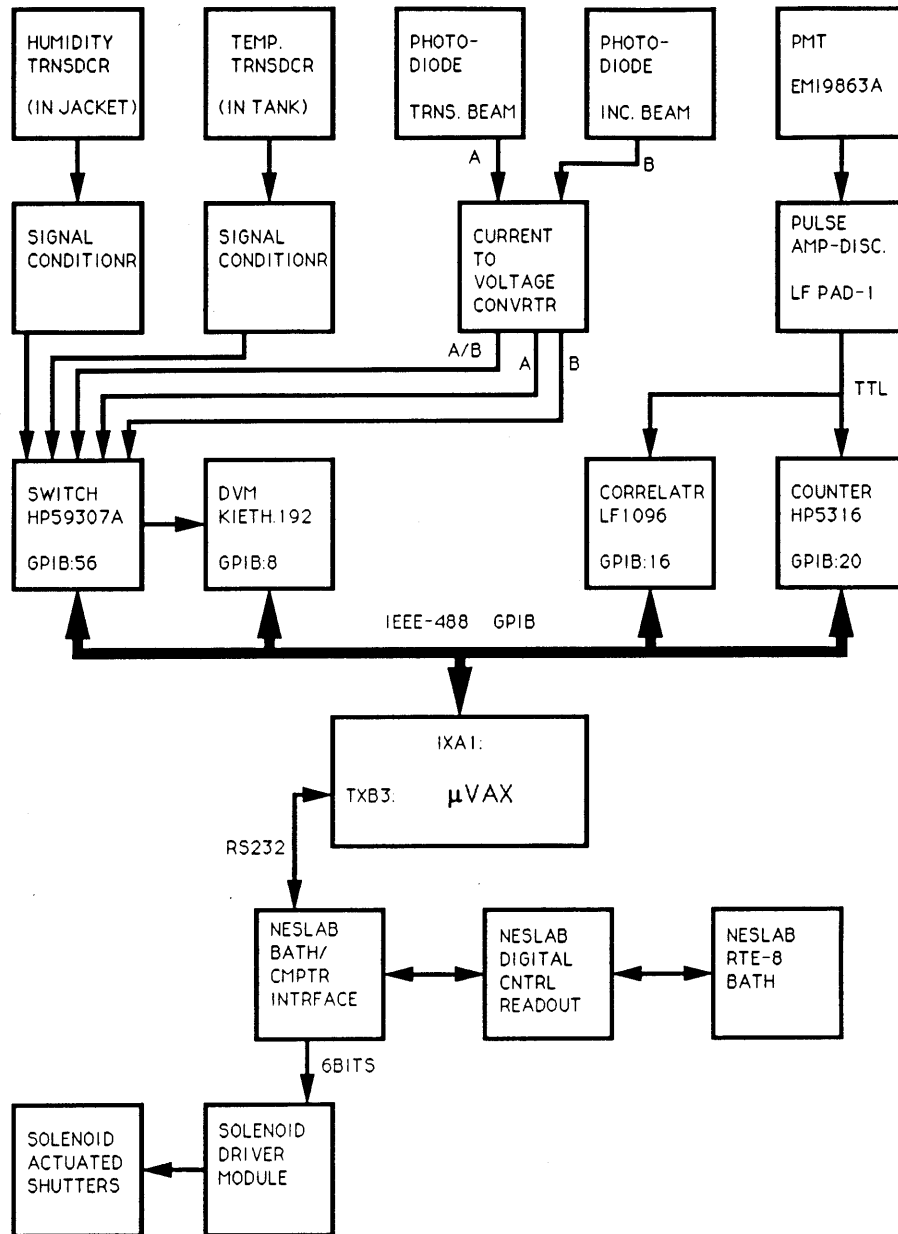


**Figure 2-5:** Block diagram of the data acquisition subsystem.

nical descriptions of use of the GPIB are available from many sources [13, 14, 15, 16]. The computer controls a temperature bath and the solenoid actuated shutters via a NESLAB BATH/COMPUTER INTERFACE which is linked to the computer via an RS232 serial data line. The NESLAB interface has a six bit output port which is used to control a prototype SOLENOID DRIVER MODULE. The solenoid driver module has 24 output lines, to control individual shutters. The solenoid actuated shutters at the light entrance end of each optical fiber can only be opened one at time, either under manual control, or under computer control.

The NESLAB interface also controls a temperature bath which is used to coarsely control the temperature of the instrument. The temperature control subsystem will explained in Sec. 2.2.5.

### **2.2.5 The Temperature Controller Subsystem**

The following discussion is in reference to fig. 2-6. In the center of the figure, the circular object labeled TA represents the tank, or water bath in which the light scattering cell is immersed. The tank, TA, is surrounded by a temperature controlled water jacket, JA, which protects TA from the ambient laboratory air convection and therefore makes possible the good thermal stability that this instrument can attain. In between TA and JA is an airspace, designated AS. When the instrument was to be operated at temperatures below the dew point of the ambient laboratory air, it was necessary to dehumidify the air in AS in order to prevent condensation on the lenses L1-L18 in the tank wall of TA (only lenses L1, L10, L17, and L18, are shown in fig. 2-2).

The temperature controller subsystem is itself divided into three subsystems: the in-



ner tank loop; the outer jacket loop; and the airspace desiccation loop. The primary device for controlling the system temperature in all of the three indicated subsystems, is the NESLAB (Neslab, model RTE-8) water bath shown in the lower right part of the figure. The NESLAB unit is a refrigerated water bath that can act as either a source, or a sink for heat over a rated temperature range of  $-30^{\circ}$  to  $+100^{\circ}$  C. The unit has a rated temperature stability of  $0.01^{\circ}$  C. When the unit is used with an auxiliary computer interface, controller (see NESLAB DIGITAL CNTRL READOUT, in fig. 2-5), it has a set temperature resolution of  $0.1^{\circ}$  C.

For many experiments, the coarse temperature control provided by the NESLAB is adequate.

When precise temperature control and high stability are needed for an experiment, the NESLAB is used to provide a slight heat sink for the inner tank loop circulation system. The inner tank loop is provided with an auxiliary temperature controller which can only add heat to the slightly cooled water coming from the NESLAB heat exchanger. The auxiliary controller was designed by Hans Haller [7]. When the temperature controller system is operated in this high precision mode, the NESLAB removes excess heat added by circulation pumps, temperature controller over-shoot, or the laboratory environment, and the auxiliary controller adds back precisely the right amount of heat to maintain the exact desired set temperature in the tank TA.

The following paragraphs describe the subcomponents indicated in fig. 2-6 in detail.

Inner tank water from TA is fed to a pump (March model AC-3C-MD) which maintains a flowrate through inner tank circulation system of about one gallon per minute.

Water from the pump is fed to a two way ball valve which can allow carbon (Millipore CDFC 012) and ion-exchange (Millipore CDMB 012) twelve inch filter cartridges to be placed into the circulation loop. The carbon filter cleans the water of organic impurities, and the ion-exchange filter clears the water of ionic impurities such as salts or stray metal molecules. These filters are essential for two reasons: the tank TA is constructed of aluminum and if stray metal molecules such as copper are allowed to circulate in the system, they will plate themselves onto the aluminum surfaces of TA and cause local sites for electrolysis; the water circulating in TA is itself used as a secondary light scattering intensity standard (see the next chapter) and for this reason it must be maintained with reagent grade purity. The two way valve is necessary, because these two filters must be removed from the circulation loop when the water temperature is set to exceed 30° C. since epoxies used to make these filters, and the ion exchange resin itself, start to break down above these temperatures. Circulation from the carbon and ion-exchange filters, or from the filter bypass loop (see figure), is recombined and forced through a 0.2  $\mu\text{m}$  particle ten inch cartridge filter (Millipore CVDI 01TP1). This filter is constructed without epoxy and can withstand water temperatures much higher than 30°C. The water is then fed to a flow meter (Dwyer, model RMC-142) and then to the NESLAB heat exchanger. The NESLAB heat exchanger was constructed of ten foot length of 3/8 inch stainless steel tubing bent into a helical coil of six inches in diameter. The water from the NESLAB is then fed past a heating element encased in a 4 inch by 10 inch stainless steel cylindrical tube. The processed water is then injected back into the tank TA. The final temperature of the processed water is monitored by a 100K $\Omega$  thermistor (Yellow Stone

Instruments, model 100/44011/1.0/1T/6.0/ST) just before it is injected back into the tank TA. The thermistor, designated  $R_t$  in the figure, forms one leg of a Wheatstone bridge. The bridge uses precision metal film  $100\text{K}\Omega$  resistors (Vishay, model S102K), and a precision decade box, designated  $R_s$ , to set the temperature. The bridge is powered with a 1.25 volt mercury dry cell battery; therefore, due to the low bridge voltage, ohmic heating of the thermistor  $R_t$  is minimized. Output of the bridge is fed to an instrumentation amplifier A1 (Intersil, model ICL 7695CJN), an integrator A2, and then to a power amplifier A3 (Apex Microtechnology, model PA12) which drives the heater element through which the tank water is circulated. The heater element is made from a tangled mess of a 75 foot length of 30 AWG gauge teflon coated wire and has a resistance of  $8\ \Omega$ . Except for the NESLAB heat exchanger, all tubing is made from 1/2 inch polyethylene tubing (Nalgene tubing) and covered with 1/2 inch wall thickness foam insulation (Rubatex, model FS 5579). All fittings and valves are made of teflon or stainless steel. The pump head is made of an inert, non-metallic material. At no point in the inner tank loop are any copper or brass fittings used. Religious avoidance of any source of stray copper ions is necessary to prevent electrolysis of the aluminum tank TA. At the time of the writing of this thesis, this instrument was in operation for four years and there are no signs of corrosion in the tank TA. The temperature of the inner tank may be monitored with an electronic thermometer (Analog Devices, model AD590) which is connected to a signal conditioner designated, TEMP. SIG. COND. in the figure. The output TEMP. SIG. COND. may be monitored by the MicroVax computer (see fig. 2-5).

Referring again to fig. 2-6, the jacket water line is fed through a heat exchanger

made from a glass chemistry set condenser, before it is returned to the NESLAB reservoir. The glass condenser heat exchanger is used maintain the temperature of the processed air being returned to the air space AS. Processed jacket water is fed directly from the NESLAB reservoir back into the jacket JA.

As mentioned above, when the instrument is operated below the ambient dew point of the laboratory air, the air in air space AS must be desiccated to prevent condensation on the lenses mounted in the tank wall of TA. The air space circulation system is as follows. An oil free diaphragm pump (Cole Parmer, model DOA-P104B-AA), draws air from the air space AS and forces it into two tandem  $\text{CaSO}_4$  desiccation filters (Drierite Co., Xenia, OH). The circulation for these two filters is controlled by a set of valves which may allow one filter to be removed and replaced while the other is still on line. This is necessary periodically because when the  $\text{CaSO}_4$  becomes saturated with water, it must be replenished with fresh material which has been dried out in an oven. The output of the desiccation filters is fed into a set of three two inch  $0.5 \mu\text{m}$  particle filters to remove  $\text{CaSO}_4$  dust (Millipore: prefilter membrane, model AD1504200;  $0.5 \mu\text{m}$  filter membrane, model FHLP 04700). The air is then forced into a particulate filter normally used for cleaning up gas from compressed gas cylinders (Balston model DFU grade BQ) and then into the glass condenser heat exchanger. The processed air is then fed through a final  $0.2 \mu\text{m}$  2 inch teflon filter (Millipore, model SLFG05010) just before it is injected back into the airspace AS. The relative humidity in the air space AS is monitored with an electronic humidity detector based on a capacitor with a humidity dependent dielectric constant (Thunder Scientific, model PC-2101). The capacitor is controlled by signal con-

ditioner designated HUM. SIG. COND. in the figure. The output of HUM. SIG. COND. is monitored with a digital multimeter which can be read from its front panel, or by the MicroVax (see fig. 2-5). The output of the signal conditioner can be used to estimate the actual dewpoint of the air in the air space AS to make sure that it is well below the instrument operating temperature.

The above temperature controller was calibrated as a system by comparison to a National Bureau of Standards (NBS) traceable mercury thermometer (Kessler, model #15-041 -1/51C in .1 div total immersion) over the range of 5° C. to 55 ° C. The calibration data was used as fit data for the empirical Steinhart-Hart three parameter non-linear thermistor response equation [17]. Operationally, the Steinhart-Hart equation was then used to calculate the bridge resistor  $R_s$  value for a given set point temperature. The deviation of the nominal set point temperature from the true temperature was caused by the approximate form of the Steinhart-Hart equation, and by limited resolution of the NBS traceable thermometer used for calibration ( $\pm 0.02^\circ$  C.). This total deviation was estimated to be less than  $\pm 0.06^\circ$  C. over the entire operational temperature range of the instrument, 5° C. to 55° C. The thermal stability of the instrument was measured at 20° C. with an external thermistor, Wheatstone bridge combination, and found to be better than  $\pm 0.0002^\circ$  over 24 hours.



## 2.2.6 Mechanical Details

The previous sections have given an overview of the instrument's optical setup, the data acquisition subsystem, and the temperature control subsystem. The purpose of this section is to discuss in detail the actual parts of the instrument. To aid the discussion, three mechanical drawings of the instrument have been included in this section. The first drawing, fig. 2-7 is an isometric cut-away view of the instrument. This view was made from the drawing in fig. 2-8, which is an orthogonal, cut-away view of instrument assembly. Both of these figures should be referred to in the following discussion. For simplicity, only one of the 16 shutters is shown in these figures. (15 shutters for the scattering angles, and one shutter for the transmitted beam.) The third mechanical drawing, fig. 2-9, is top view of the entire instrument layout on the NRC optical table.

In both figures, fig. 2-7 and fig. 2-8, the object labeled TA is "the tank" which was referred to in earlier sections. TA contains the temperature controlled water bath, and at its center is a cylindrical recess for accepting a light scattering cell such as the one depicted in fig. 2-3. For viewer reference, TA has a diameter of approximately 15 inches and is about 2 1/2 inches in height. Underneath and around TA is the airspace labeled AS. Surrounding AS is the water jacket labeled JA. JA has the shape of a cylindrical pill box. JA's top and bottom plates (fig. 2-8, parts JA1,JA2; and JA5,JA6) contain channels for the circulation of water from the NESLAB unit (see fig. 2-6). The cylindrical wall of JA, designated JA4 in fig. 2-8, is made from a solid piece of aluminum and has a wall thickness of 1/2 inch. The shutters SH, and associated optics, are mounted on the jig plate designated JP in both figures 2-7 and 2-8. JP is 45 inches square and one inch thick

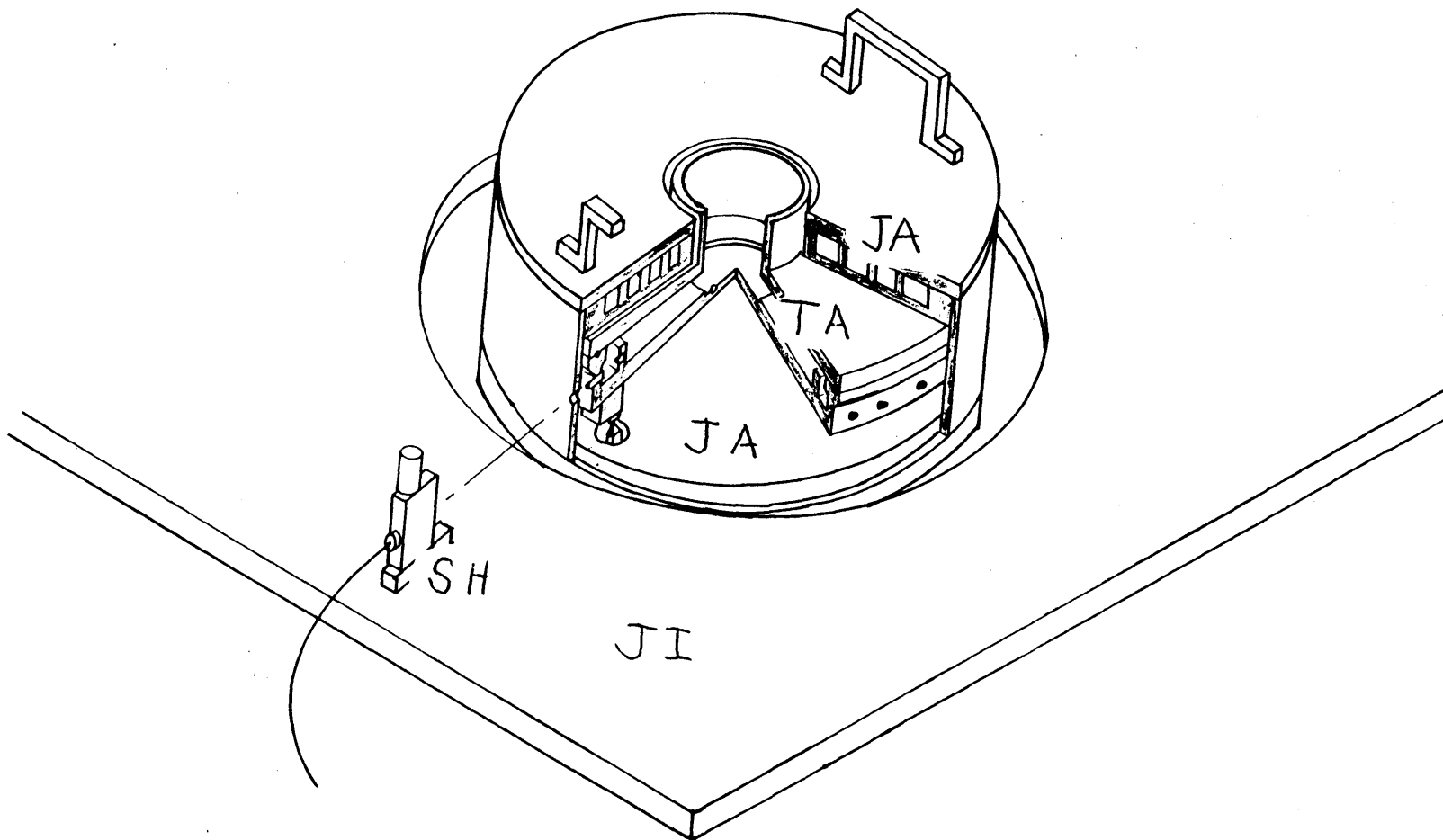


**Figure 2-7:** Isometric, cut-away view of light scattering instrument.  
TA is the tank assembly, JA is the jacket assembly, JI is the jig plate

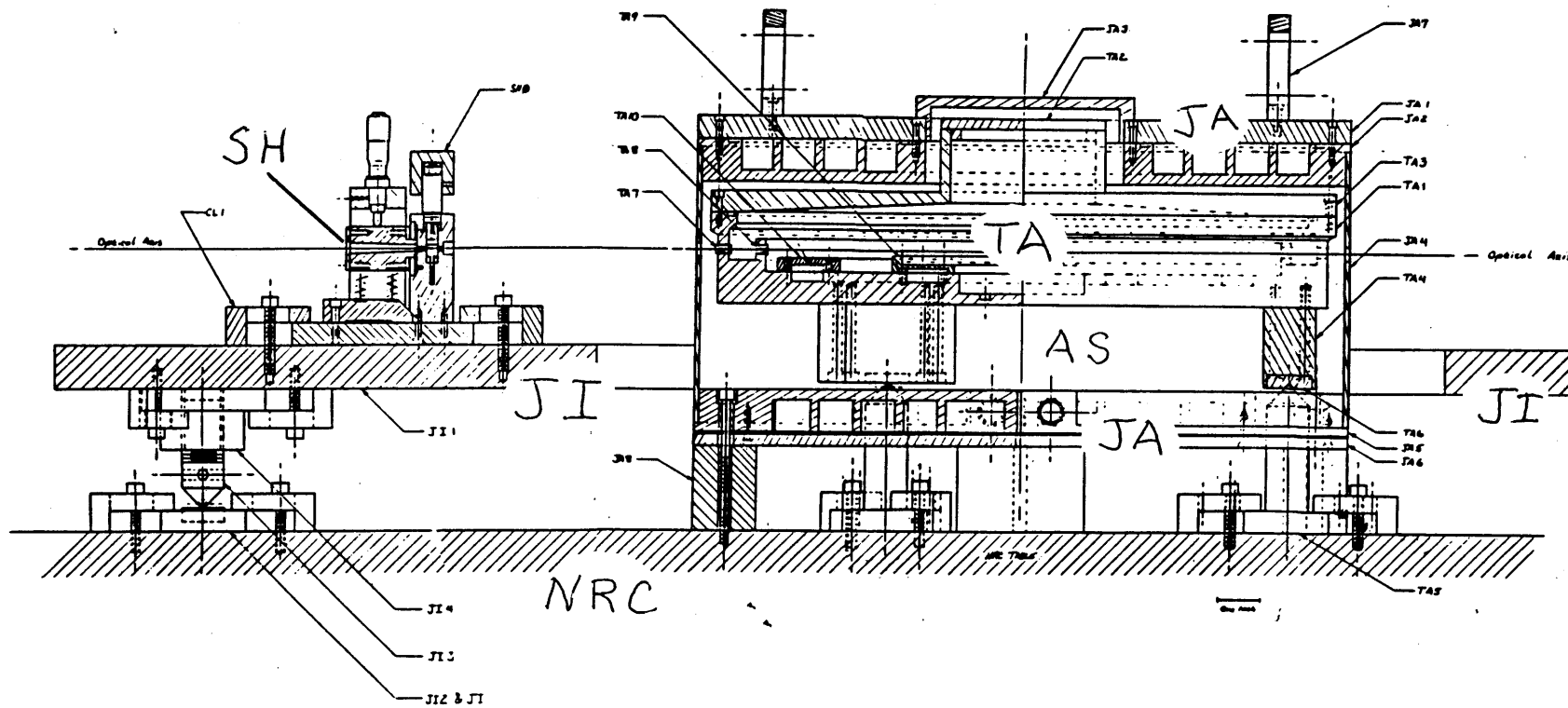
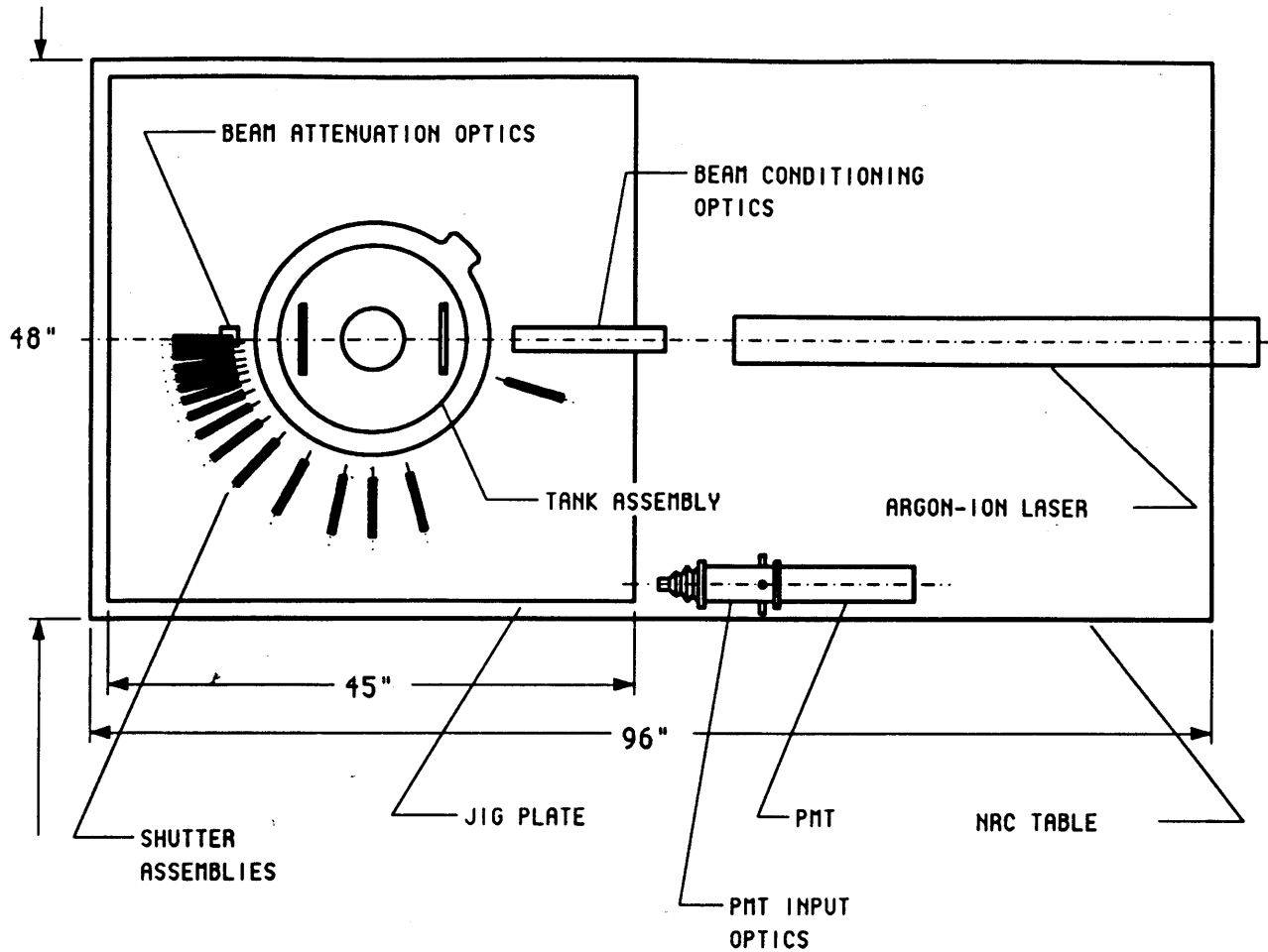


Figure 2-8: Orthogonal, cut-away side view of the light scattering instrument.  
 (See text for details)



**Figure 2-9:** Top view of entire instrument layout on NRC optical table.  
Optical fibers connecting shutters to PMT INPUT OPTICS are not shown.

aluminum. The central portion of JP is cut out to allow the tank and jacket assembly to rest directly upon the optical table (Newport Research Corp., model RS-48-8) designated NRC in fig. 2-8. The following paragraphs will discuss the details of the components indicated in fig. 2-8.

Referring to fig. 2-8, the water filled tank TA is composed of its main part TA1, and

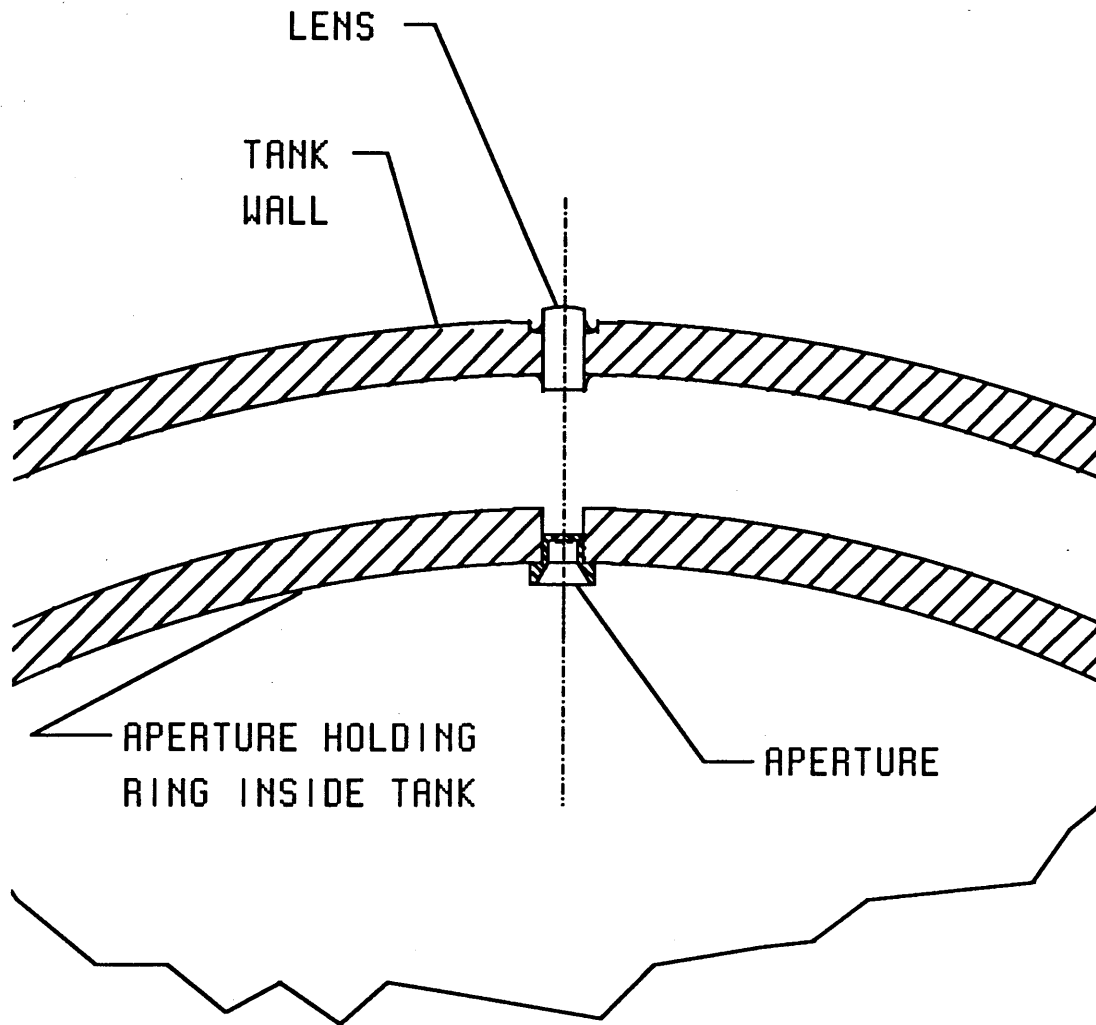


**Figure 2-10:** Partial, cut-away top view showing in detail how one of the apertures in the tank is positioned relative to the lens in the tank wall. (See text for details)

its lid TA3. TA1 is machined out of one piece of aluminum (type 6061, T4 hardened), and has a ring designed into it for accepting optical system apertures designated TA8 in fig. 2-8, and also designated A10 in the schematic diagram, fig. 2-2. Fig. 2-10 shows a top cut-away view of the tank wall and the aperture holding ring inside the tank. The purpose of this figure is to show the details of the aperture insert design and how the insert is mounted relative the lens.

Referring back to fig. 2-8, TA7 represents a lens in the tank wall of TA. TA7 is was glued into place using epoxy. The procedure for installing TA7 will be discussed in sec. 2.2.8. Lid TA3 is sealed to TA1 by a large O-ring mounted in the flange indicated on the top edge of TA1. TA3 has a vertical throat opening at its center which is 1 1/2 inches high to accommodate a possible overflowing of water in tank TA. The lid TA3 has itself a lid on top of its throat, designated TA2. Inside TA is an annular channel and channel cover, TA8, for the incoming temperature controlled water from the circulation system. The purpose of the this annular channel, and channel cover, is to evenly distribute the incoming circulation water around the circumference of the tank. The inlet holes in TA8 are angled at 45° with respect to the vertical, to direct water toward the recessed area between the apertures TA8 and the lenses TA7. This was done to prevent water from stagnating in the area of the tank TA. Water is removed from TA and returned to the circulation system by the annular channel and channel cover designated TA9. Channel cover TA9 has a knife edge on its top surface to help act as a baffle for reducing stray light [18,p. 128]. During their fabrication, the interior surfaces of TA1, TA2, and TA3 were blasted with a fine grit of aluminum oxide and black anodized. These surfaces were treated this way to help diffuse and absorb reflections of stray light beams.

TA is kinematically mounted [19,p. 41] to NRC in the following way. Three fiberglass blocks TA4 (fiberglass type G10) are screwed into the bottom of TA1 in equal spacing around it circumference. On the bottom of the three TA4 are hardened steel pads TA6 (Rockwell T51 hardened). One of the three pads TA6 is flat, one has a channel in it, one has a conical dimple it. Each of the three pads TA6 rests upon a ball bearing which

are held in their proper places by the three columns TA5. The TA5 are mounted directly to the NRC table. In this way, TA has a true kinematic mount with respect to NRC, and it is not overconstrained in the case of TA undergoing thermal expansion.

Under and around TA is the airspace AS. The space under TA and between TA5 is 1 3/4 inches high to allow for the necessary plumbing fixtures and detectors for the circulation and temperature control system (see fig. 2-6).

The water jacket JA assembly rests on four fiberglass blocks, JA8, placed around the bottom circumference of JA6. The four JA8 are mounted directly to NRC. The top section of JA has two handles mounted on it, JA7. The purpose of these handles is to make it possible to remove the top of the jacket assembly, JA1, JA2 for access to the top of the tank, TA. The jacket wall JA4 rests on top of JA5 and may be easily lifted away for accessing TA and the air space AS for occasional maintenance JA1, JA2 has an access hole for TA: the cover for the access hole is designated JA3.

The jig plate JI1 is also kinematically mounted to NRC. Three fixtures JI4 are mounted equi-distant close to the edges of JI1. The JI4 are threaded to accept threaded columns JI3 which have recesses in their conical bottoms for retaining ball bearings which interface to hardened steel pads JI2 which are attached to the NRC table. The threaded columns JI3 may be turned to adjust the height and level JI1. Not shown are large locking nuts which are counter-threaded on JI3 to exert pressure JI4 to prevent movement of JI3 relative to JI4 due to thread lash. (Thread lash results from the necessary clearances machined into the two threaded pieces.)

The "L" shaped objects designated CL1 in fig. 2-8 are just hold-down brackets for the above indicated objects JI2, SH, JI4, TA5.

The shutter assemblies (one shown) are designated SH. Fig. 2-11 shows one of the SH in Detail. S1 is a solenoid (Ledex, model 178763-035, with surge suppressors, model 126911-001) which is driven by the Solenoid Driver Module of fig. 2-5. When actuated S1 pushes down on shutter plug S2. The bottom of S2 pushes against a return spring S3 (Associated Spring, model ASC C057-006-0500). Plug S2 has a hole in its center which opens the optical path when the solenoid is actuated. Slit SL is mounted to back of shutter body S5. Slit SL is also designated SL10 in fig. 2-2. The optical fiber holder is held in a tapered hole bored through part S7 which is part of a vertical translations stage. S7 holds the end of the optical directly behind vertical slit SL. S6, a micrometer screw (Newport Research Corp, model SM05), pushes S7 against a pair of springs S8 (Associated Spring, model C0300-032-1000S). The vertical translation stage comprising of S6, S7, and S8, is mounted on a piece S9 which may be dismantled from base S10 for viewing the image of scattering volume behind slit plane SL during optical alignment. The alignment procedure will be discussed further in sec. 2.2.7. The base S10 is itself mounted to the jig plate JI of figures 2-7 and 2-8. S10 in fig. 2-11 is drawn differently from the same object in fig. 2-8 because of a design change made after 2-11 was drawn. The actual version of S10 used is correctly depicted in fig. 2-8.

The orthogonal cut-away view of fig. 2-12 depicts the light collection assembly which is designed for coupling the optical fiber bundle of fig. 2-2 to the PMT photo cathode. The collection assembly housing, PM4 and PM4B, is cylindrical in shape and designed to mate to a commercial PMT housing (Pacific Instruments, model 3262RF). The optical fiber bundle is held in place by assembly PM3, PM5. The fiber bundle is



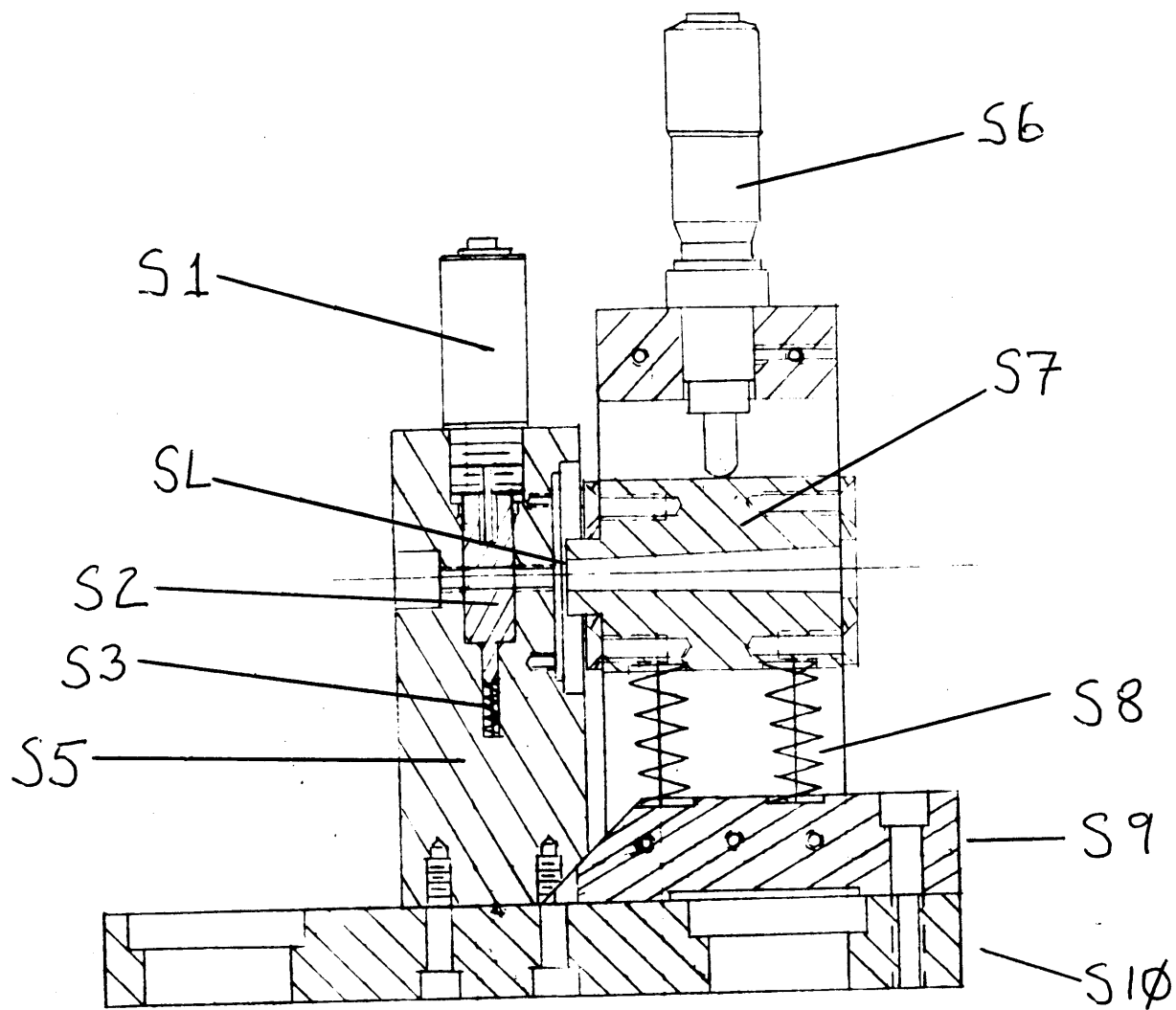


**Figure 2-11: Shutter assembly.**  
(See text for details)

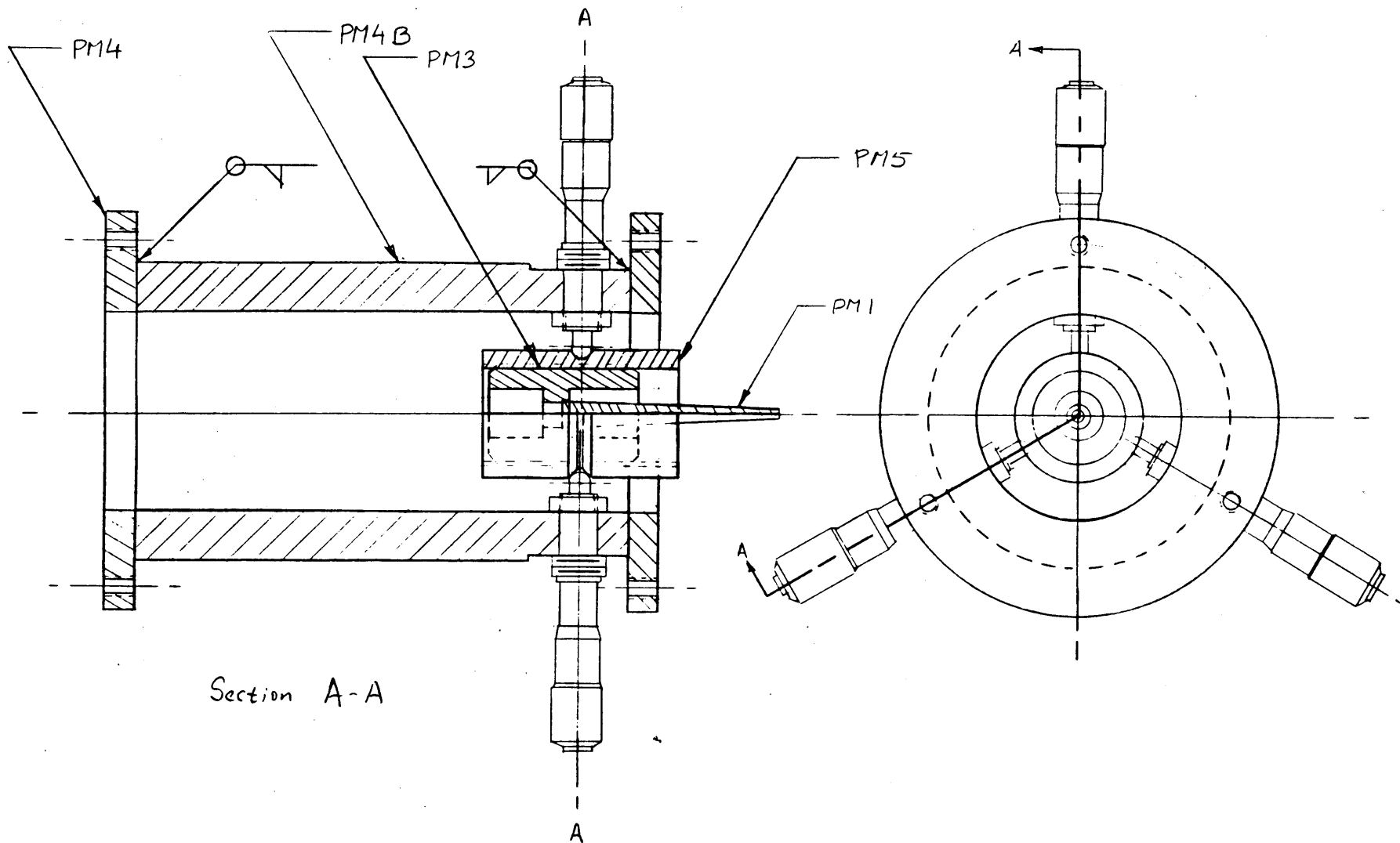


**Figure 2-12: PMT light collection assembly.**  
(See text for details)

attached to PM3 in the recess depicted in its left end. PM3 is threaded into PM5 so it can be translated along the longitudinal axis of the collection assembly housing. PM5 is held in place by three micrometer screws placed radially around a channel in its circumference. The conical light guide PM1, which narrows the diameter of the fiber optic bundle down to the PMT photo-active area, is made from clear plastic. The end of PM1 is mated to glass envelope of the PMT photocathode with a dab of optical coupling compound (Dow-Corning, model Q2-3067). The left flange of PM4 is mounted to a rubber boot (Minor Rubber Co., model ZFD-1028-0-19-25), which in combination with a strip of black felt fabric wrapped around the fiber-optic bundle, provides a light tight seal for the PMT.

### **2.2.7 Optical Alignment Procedures**

Referring again to fig. 2-2, the alignment of the optical system involves several steps. These steps are outlined as follows. The outlined alignment procedures will be elaborated on in subsequent discussion.

1. Steer the laser beam with mirrors M1 and M2 so that the laser beam is transmitted through the exact centers of lenses L17 and L1.
2. Adjust the position of the shutter assemblies so the image of the axis of rotational symmetry of tank TA is exactly centered on all of the focal planes of the shutter slits SL2 - SL16.
3. The purpose of this step is to center the end of the optical fiber held in shutter SH1 with the centroid of the transmitted laser beam. With the beam attenuation optics in place, view the spot of the transmitted laser beam from behind the slit SL1 and move the shutter SH1 until the beam is centered in the slit SL1. The slit SL1 is removed after shutter alignment.

4. Adjust the vertical position of the ends of the optical fibers F1-F16 using the shutter vertical translation stages on each shutter so that the number of photocounts from a scattering solution in the tank TA1 are maximized.

These steps are detailed below. (Note: during alignment steps one to three, the photomultiplier is de-energized. It is re-energized only for alignment step four.)

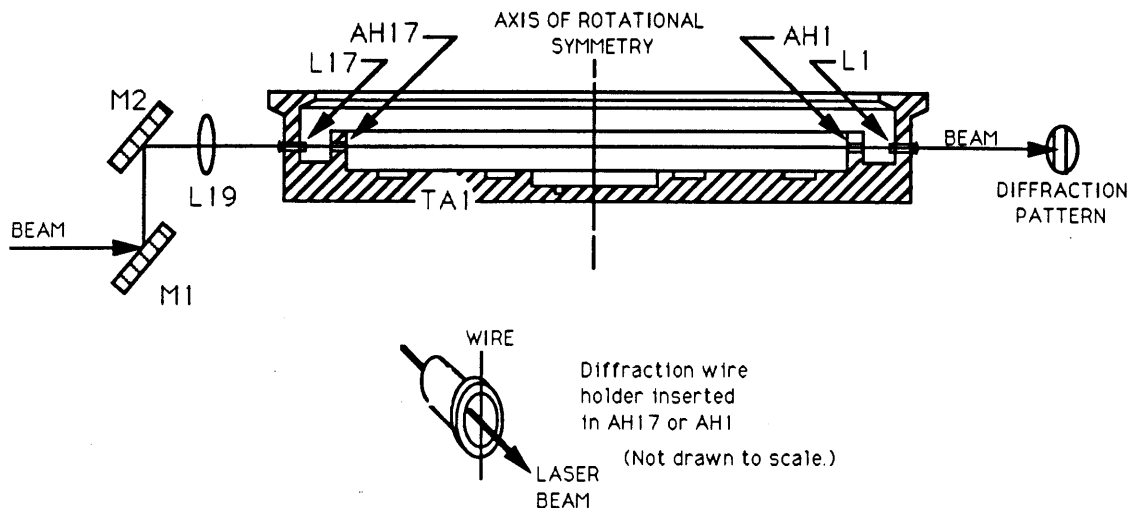


**Figure 2-13: Method of beam alignment.**  
(See text for details)

## 1. BEAM ALIGNMENT

The procedure for aligning the laser beam with the centers of L17 and L1 is as follows. Referring to fig. 2-13, mirrors M1 and M2 are used for steering the beam. All optical elements, such as L19, and the Glan-Thompson prism (not shown) are placed in their proper positions in the beam path. The tank TA1 must be filled with water above the levels of the lenses L1 - L18. Coarse laser beam alignment is accomplished by simply adjusting the mirrors M1, and M2, to make sure that laser beam can get through L17 and L1. During the coarse alignment, it may be necessary to adjust the positions of

other optical elements such as L19 to make sure that the laser beam goes through their centers. The tank TA1 is of kept course stationary, since it is fixed in its position on the optical table. The procedure for fine tuning the laser beam alignment is as follows.

1. A special target, made from a tube with a wire placed across its diameter, (see "Diffraction wire holder", in fig. 2-13) is placed in aperture holder AH17 in the tank TA1. If the wire on the target is rotated in AH17 to line up with the vertical direction, then a diffraction pattern of vertical stripes will be observed if the exit laser beam from L1 is projected onto a screen. M1 is adjusted until the diffraction pattern is symmetrical. (At this point, it can be checked if the wire on the target is truly on the tube's diameter by rotating the tube  $180^\circ$  in the aperture holder AH17 and seeing if the diffraction pattern is still symmetrical.)
2. The target is then removed from AH17 and placed in AH1 with the wire again oriented parallel to the vertical direction. Mirror M2 is then adjusted to make the projected diffraction pattern symmetrical.
3. The target is then replaced into AH17, and the entire procedure is repeated starting at step one until no further adjustments of M1 or M2 are required.
4. At this point, the laser beam should be exactly in the vertical plane that bisects the tank TA1 along its diameter through the centers of L17 and L1. The wire in the target is now rotated in AH17 so that it is now parallel to the horizontal direction. A diffraction pattern with horizontal stripes should now be observed in the laser beam transmitted through L1. The procedure for adjusted M1 and M2 given above is repeated until no further adjustment is necessary.
5. Steps one through four are repeated until no further adjustment of M1 and M2 are required.

## 2. SHUTTER ALIGNMENT

The next stage of the instrument alignment, is to make sure that the image of the axis of rotational symmetry of the tank TA1 is centered on the focal planes of the vertical slits SL2-SL16 of the shutter assemblies, SH. The shutter assemblies, with their optical fiber vertical translation subassemblies removed, are mounted to the jig plate, JI of fig. 2-8. The optical fiber vertical translation subassemblies are removed from the shutters by dismounting part S9 from part S10 of fig. 2-11. The image of the symmetry axis of TA1 in fig. 2-13 is designed to be in focus when the slit planes are placed 14 3/8" radially from it. The imaging system of this instrument has a large f-stop, and therefore a large depth of focus, so the radial distance to the shutter slit planes is not a critical dimension. (See Sec. 2.2.9 for more details about the optical design.) To accomplish the alignment, a target was prepared which seats in the cylindrical depression at the center of tank TA1. This target consists of 1/2" by 3.000" diameter base which holds a vertically aligned 0.010" drill bit at its center at the level of the laser beam height, 1.00". When this target is placed in position in the receiving recess at the center of tank TA1, and illuminated with a bright light, its image can be seen at the focal planes of slits SL2-SL16. It is probably wise not use the laser beam to illuminate the drill bit, since its illumination of the drill bit will not be uniform when viewed from all angles, and also laser light scattered from the drill bit may be too bright for safe viewing. The position of the shutter mounting base, S10 of fig. 2-11 is moved around on the jig plate by tapping it gently until the image of the drill bit is centered on the vertical slit mounted to the back of the shutter body, S5 of fig. 2-11. The image of the drill bit is viewed with a special 25X microscope mounted on the shutter base, S10 of fig. 2-11 instead of the optical fiber vertical trans-

lation assembly. The image of the drill bit is viewed through the back side of the vertical slit with this microscope. When the image of the drill bit is centered in the vertical slit, then the two clamps, CL1 of fig. 2-8, on each end of the shutter base are tightened down to fix the position of the shutter. The position of drill bit image is then re-checked to ascertain that it didn't move relative the shutter during the clamp tightening.

### 3. TRANSMITTED BEAM SHUTTER ALIGNMENT

The shutter assembly for the transmitted laser beam must be positioned with the beam attenuation optics (M3, ND2, ND3, and ND4, of fig. 2-2) in place. The beam attenuation optics makes it impossible to see the image of the target used in the previous alignment step. Therefore, to accomplish the alignment, the spot of the transmitted laser beam is used. With attenuation optics in place, the laser beam spot intensity should be dim enough for direct viewing with the unprotected eye, but this should be checked first by projecting the attenuated spot onto a screen and verifying that it has a weak intensity.

For the purposes of this alignment, the slit SL1 of fig. 2-2 is mounted to back of the shutter body, S5 of fig. 2-11. The shutter base should be gently tapped until the transmitted laser beam spot is symmetrical with respect to the center of vertical slit SL1. After the shutter base is clamped to the jig plate the proper position of the shutter should be re-checked. At this point the slit SL1 should be removed without disturbing the position of the shutter body.

### 4. OPTICAL FIBER POSITIONING

At this stage of the alignment process, the laser beam is aligned with the tank TA1, and the focal planes of the vertical slits in the shutters are centered on the image of the axis of rotational symmetry in the tank TA1.

To align the optical fibers, remount the optical fiber vertical translation stages onto the shutter mounting bases, S10 of fig. 2-11, and plug the tapered optical fiber holders back into the vertical translation stages. The power to the photomultiplier, which should have been cut off during all of the above manipulations, can now be restored. When restoring power to the PMT, carefully monitor the number of dark counts, because an excessive amount might indicate a mistake such as leaving the end of one optical fiber uncovered, or unattached to its shutter. Remove the drill bit target and replace it with a scattering cell containing a dust free fluid such as toluene. Open a shutter and use the vertical optical fiber translation stage of the shutter to move the fiber until the photocounts received by the PMT are maximized. The ends of the optical fibers are not perfectly polished and the received signal may sometimes be further increased by gently rotating the optical fiber in its holder in the vertical translation stage. Naturally, care must be taken not to rotate the fiber too much as the torsional strain on the optical fiber can cause it break. If this rotation is attempted, then the vertical position of the fiber should be re-checked. Vertically align the optical fibers in all shutters.

### **2.2.8 Instrument Assembly**

The purpose of this subsection is not give the entire procedure for assembly of the instrument described above. Rather, its purpose is to illuminate a few of the subtleties involved in its construction.

#### **1. INSTALLATION OF THE TANK LENSES**

Lenses L1-L18 of fig. 2-2 were glued into position using an epoxy designed for mating glass to metal surfaces (Armstrong A-271 epoxy). The procedure for glueing the lenses is given below.



1. The tank, TA1 of fig. 2-8 was supported on a stand constructed so that it was fixed in position with its cylindrical side resting on a horizontal surface. The tank was rotated in its supporting stand until the lens hole to be glued was positioned at the top.
2. A specially prepared nylon spacer plug, fig. 2-14, was inserted into the aperture receiving hole in the aperture holding ring. The plug was held in place because it was designed to have an interference fit with the receiving hole. The lens was then carefully inserted from outside the tank so that it would rest on top of the plug. In this way, the nylon plug guaranteed the correct insertion distance of the lens into the tank wall.
3. The epoxy, which had a relatively low viscosity in its uncured state, was drawn into a pipette and deposited in the groove around the lens in the tank wall, fig. 2-15. The groove was machined into the tank wall around the lens for the purpose of receiving the epoxy. The capillary action of the epoxy drew it into the narrow clearance space between the lens and the tank wall. The surface tension of the epoxy caused it to form a nice fillet around the cylindrical surface where the lens separates from the inside of the tank wall, see fig. 2-14.

The tank was left undisturbed overnight to allow the epoxy sufficient time to set.

## 2. MOUNTING THE TANK TO THE OPTICAL TABLE

The tank was mounted to an optical table having a top surface with dimensions 48 by 96 inches square. The tank was mounted, centered on one half of the table, fig. 2-9. The axis described by a line through the centers of lenses L17 and L1 was aligned with long axis of the optical table.

The tank, TA1 fig. 2-16, was checked for being level with respect to the plane described by the surface of the optical table as follows. A machinist's indicator mounted

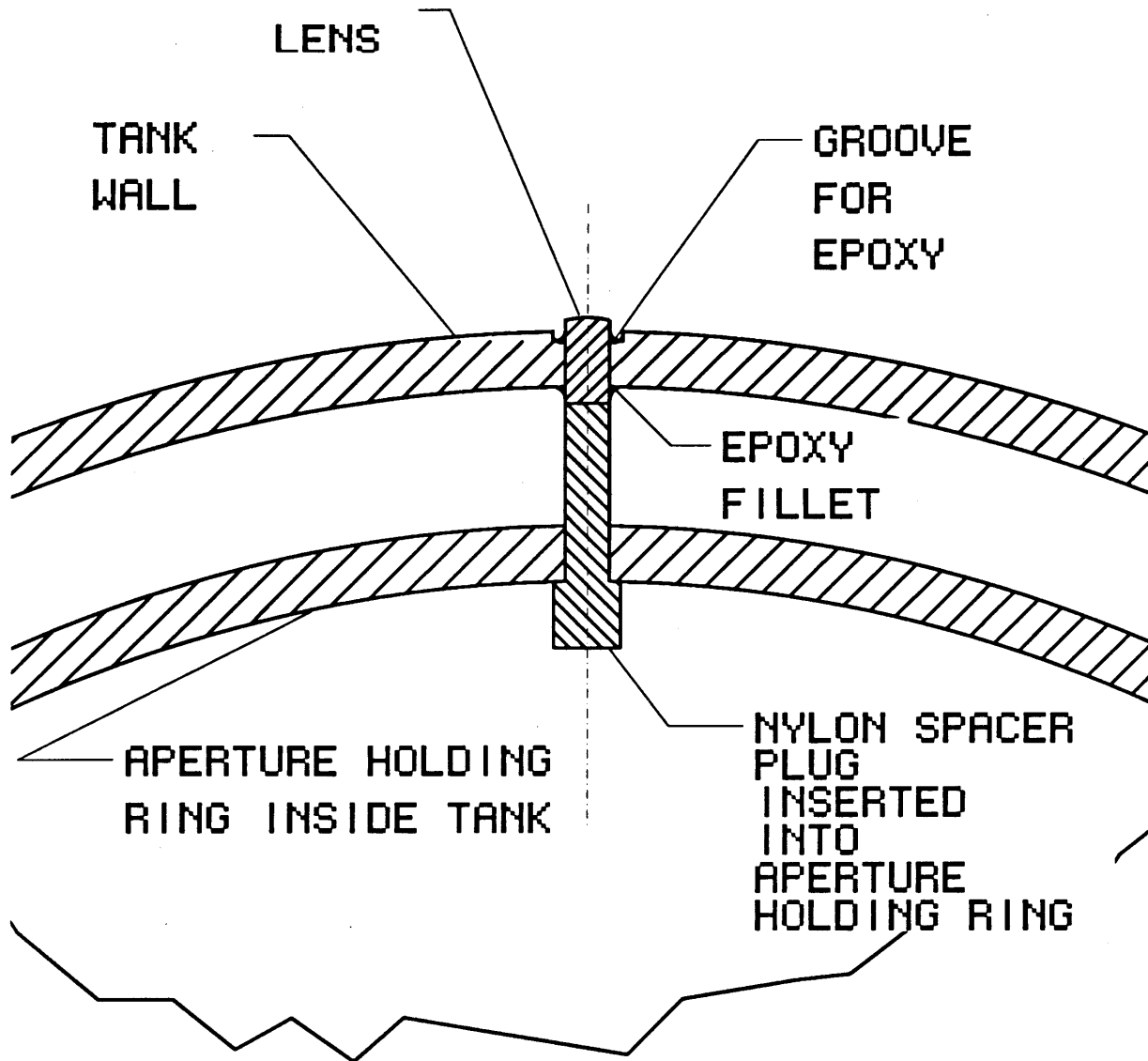


**Figure 2-14:** The positioning of a lens for gluing into the tank wall.  
(See text for details.)

a base resting on the surface of the optical table, was used to check the height of the rim of the tank TA1 at all points around its circumference. If the height tank rim above the table surface varied by more than  $\pm 0.003$ " around its average value, then the tank was dismantled, and the three fiberglass supporting blocks (only two are shown in fig. 2-16) were removed for machining. The procedure was repeated until the tank was level.

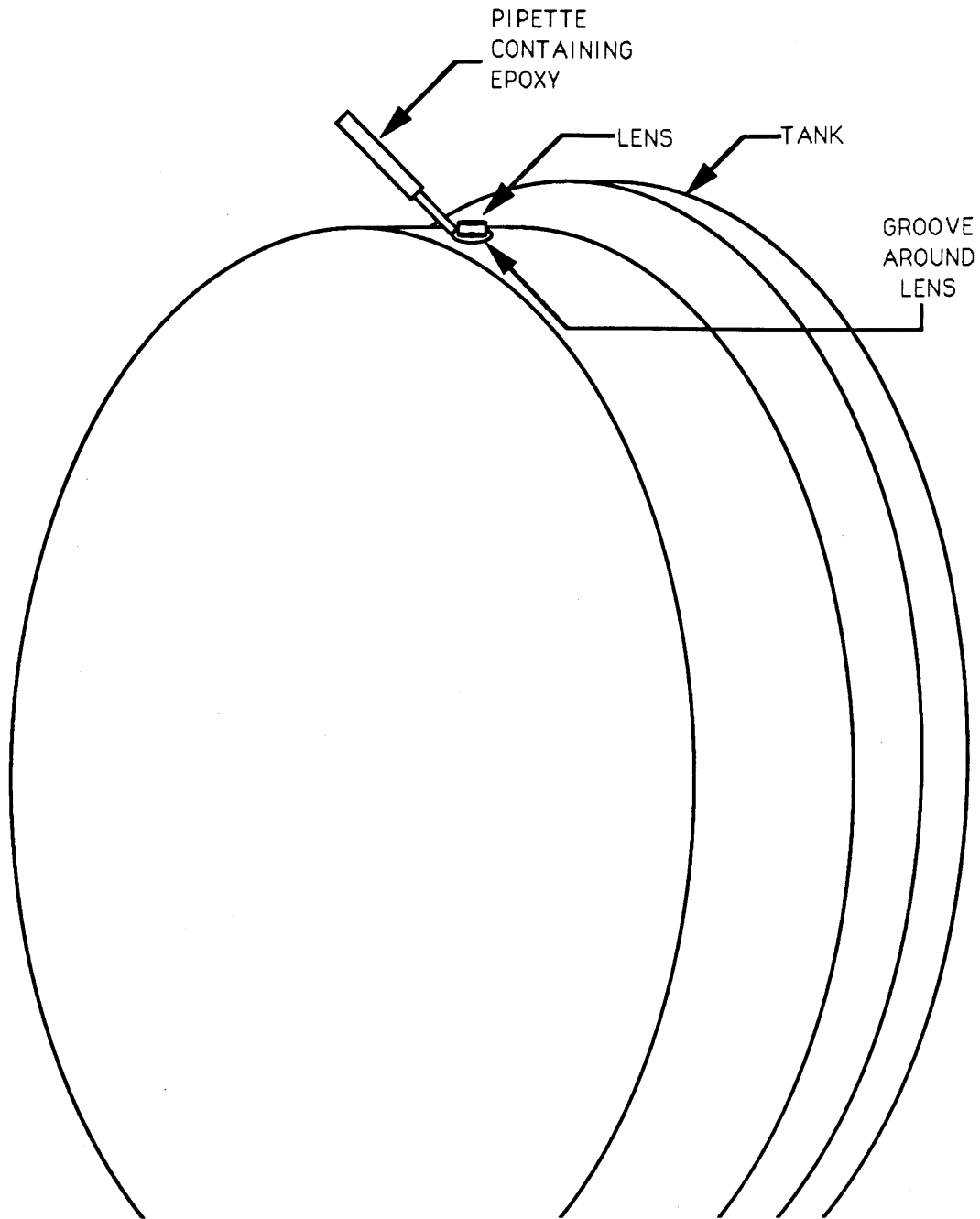


**Figure 2-15:** Installation of the tank lenses.  
(See text for details.)

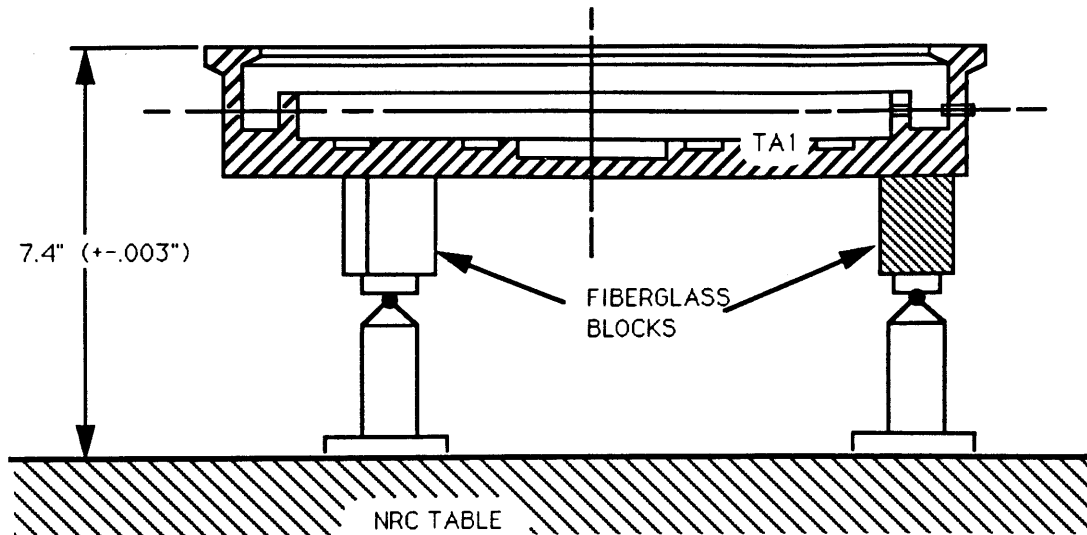


**Figure 2-16: Installation of the tank, TA1.**  
(See text for details.)

### 3. MOUNTING OF THE JIG PLATE

The jig plate which is 45 by 45 inches square, was mounted so that its center would be coincident with the axis of the tank TA1, and that it would be square with the end of the optical table on which it was mounted, fig. 2-9.

The plane described by the surface of the jig plate JI was checked for being level with respect to the rim of the tank, TA1 fig. 2-17, by using a machinist's indicator gauge to check the vertical deviation of the distance between the top of the rim of TA1 and the surface of the jig plate adjacent to TA1. If the deviation was found to be more than  $\pm 0.001$ " from its average value, then the three jig plate kinematic mounting posts, JI3 of fig. 2-8 (only one of three posts is shown in the figure), were turned to adjust the height of the jig plate until it was level with respect to the tank. At this point, nuts threaded onto

the three posts, JI3 (not shown in fig. 2-8), were counter tightened against the surface of JI4 fig. 2-8, to prevent movement of the jig plate due to thread lash. The level of the jig plate with respect to the tank was then rechecked.

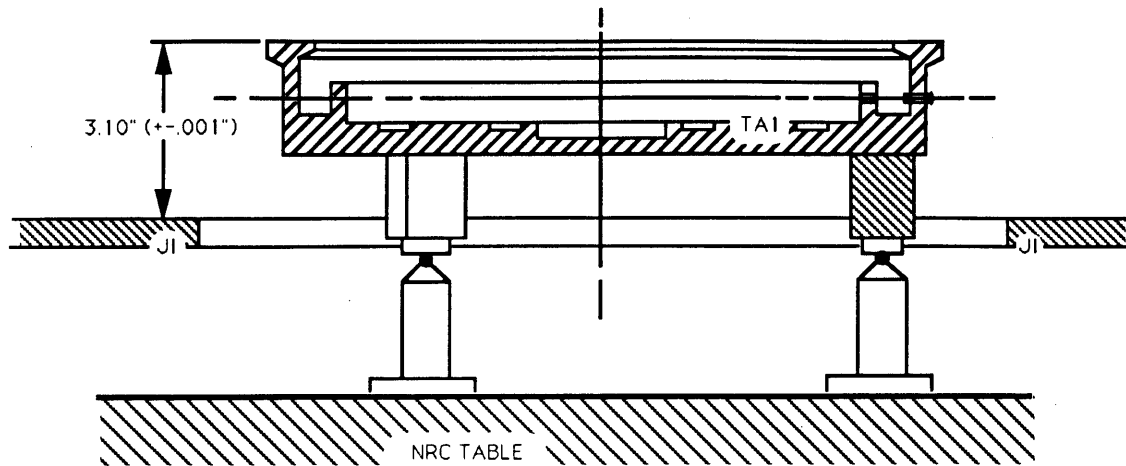
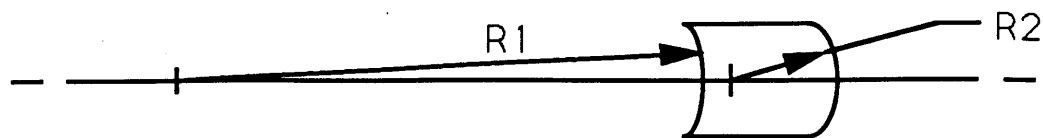


**Figure 2-17:** Installation of the jig plate.  
(See text for details.)

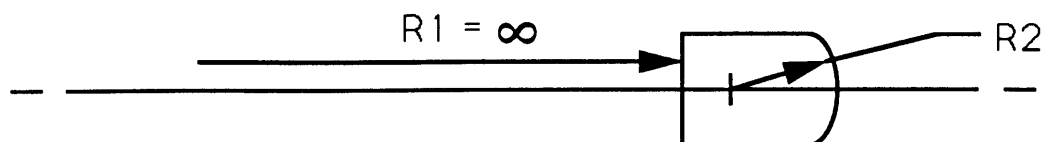
### 2.2.9 Lens Design

The optical system used for this instrument is similar to, but not exactly identical to, the optical system of the instrument from which its design is derived [7]. The principal differences are two fold:

1. The predecessor instrument used meniscus lenses in its tank wall. A meniscus lens has two spherically curved optical surfaces, one concave, and one convex (see fig. 2-18). The radius of curvature of the concave surface, R1 of the figure, was designed to equal the distance from the center of tank to the tank wall. This selection of R1 was made so that the solvent type for the tank bath could be changed (with the concomitant change in index of refraction), without changing the focusing power of the lenses.



MENISCUS LENS



PLANO-CONVEX LENS

**Figure 2-18:** The cross sectional shapes of two types of spherical lenses.

For the instrument subsequently constructed for for this thesis work, it was decided to use only water as a solvent for the tank bath. Accordingly, plano-convex type lenses were chosen for use in the tank wall since their manufacture was substantially cheaper.

2. In the predecessor instrument, the apertures that defined the acceptance solid angle of the scattered light, were located external to the tank, on the air side of the tank wall. The apertures were mounted in a separate aperture holding ring. This ring was attached to the tank during the instrument assembly.

In the subsequent instrument, substantial changes were made to the tank design with the objective of simplifying the tank's manufacture, and of simplifying the procedures for instrument assembly, and disassembly. One of the changes that affected the configuration of the optical system, was the

design decision to locate the apertures inside the tank wall where they would be immersed in the tank bath solvent. This decision was made for three reasons: (1) the aperture holding ring could be machined as in integral part of the tank: therefore, fabrication involved fewer steps, and no subsequent alignment of the ring would be required; (2) the placement of the apertures in front of the lenses would help shield the lens surfaces from sources of stray light; and (3) so that lens centration errors caused during lens fabrication and lens installation would have no effect on instrument light scattering angles (this point will be expanded on subsequently).

The two design differences mentioned above required the tank wall lenses would be redesigned.

### **Criteria for lens design**

The general criteria used for the above lens design are listed below.

1. The distance of the image of the scattering volume from the tank wall should be compatible with the dimensions of an optical table. Also, the image should be as large as possible, consistent with the tank dimension (radius = 7"), and the previous stated condition. A large image size is desirable since it minimizes the effects of microscopic defects on the detection optics at the image plane. That is to say, if the image is large compared to defects like bits of dust on the slit or scratches on the optical fiber end, then the effects of these defects on the detected light intensity will be reduced. The method of determining the value of R2 actually used in the above specifications will be explained below.
2. The lenses should have a large center thickness,  $T_c$  fig. 2-19, for aiding mechanical engagement to the receiving hole in the tank wall.
3. The lenses should have small diameter so that many of them can be near to one another in the tank wall.

4. The lenses diameter must not be too small for the aperture size used, or the laser beam diameter at the entrance and exit lenses, L1 and L17 of fig. 2-2.
5. The lens centration must be good enough so that the position of the image is not too far from its ideal position. This condition on the position of the image also dictates that the mechanical tolerance of the lens diameter to the receiving hole in the tank wall be held to close tolerance.
6. To help prevent stray light from being scattered into the receiving optics, the lenses should be substantially free from scratches, and be made from a material with high resistance to scratching.

### **Lens Design Specifications**

The tank wall lenses, L1-L18, actually used were manufactured to the following specifications by J. L. Wood Optical Systems of Santa Anna, CA.

#### **Lens Specifications:**

<b>Type</b>	<b>= plano-convex (spherical)</b>
<b>R1</b>	<b>= <math>\infty</math></b>
<b>R2</b>	<b>= 1.4212 inches</b>
<b>Tolerance</b>	<b>= 3 F @<math>\lambda_0</math></b>
<b>Figure tolerance</b>	<b>= 1/2 F @<math>\lambda_0</math></b>
<b>Centration</b>	<b>&lt; 3'</b>
<b>Clear aperture</b>	<b>= 0.140 inches</b>
<b>Diameter</b>	<b>= 0.2005<math>\pm</math>.0005 inches</b>
<b>Center thickness, Tc</b>	<b>= 0.375 inches</b>
<b>Surface quality</b>	<b>= 20-10</b>
<b>Material</b>	<b>= Suprasil I</b>



The meaning of the terms used in the above specifications are as follows.

1. R1 and R2 are the radii of curvature of the two lens surfaces.
2. The tolerance is a measure of how well the manufactured lens corresponds to the test plate surface. The unit of measurement is the number of Newton's rings observed when the test plate-lens surfaces are observed with a sodium lamp ( $\lambda_0 = 589.3$  nm). In this case, the specification is for a fit tolerance of 3 Newton's ring or less. The "F" in the specification is shorthand for the word "fringe".
3. The figure tolerance is a measure of the non-sphericity permitted in the lens with respect to the test plate. In this case one half of one of Newton's rings or less is permitted.
4. Centration is a measure of how well the lens mechanical axis corresponds to the lens optical axis. In this case, the units are given in arc seconds.
5. Clear aperture is the diameter of the lens which is free enough from chips and other defects to be used as an optical surface.
6. Diameter is the actual mechanical diameter of the whole lens.
7. Center thickness is the distance from the center of the first optical surface to the second.
8. Surface quality is a measure of how free the lens is from defects. The first two numbers give the width of a scratch in the surface in units of microns. The second two numbers give the diameter of a dig, pit, chip, or void, in units of one hundredths of a millimeter. In the specification used here, a scratch 20 microns wide would be allowed, and a dig of 0.10 millimeters would be allowed.
9. The material specified here is Suprasil I which is brand name for synthetic

fused quartz. Suprasil I is annealed to remove optical birefringence and is suitable for ultra-violet light transmission. This material is also harder, and therefore more resistant to scratching than regular optical glass. The index of refraction of Suprasil I is 1.457 @ $\lambda_0 = 633$  nm, and 1.465 @ $\lambda_0 = 488$  nm.

10. In addition to the above specifications, the lenses L1 and L17 for the incident, and transmitted laser beam respectively, were anti-reflection "V" coated for  $\lambda_0 = 488$  nm on their exterior, curved surfaces. The plano surfaces which interface to the tank water were not coated.

Further discussion on the meaning of the specifications used here can be found in any book on optical engineering such as Smith's *Modern Optical Engineering* [18], or the *Melles Griot Optics Guide* [20].

### Determination of lens power

The dimensions of the optical table, 48 by 96 inches, the tank diameter, 14 inches, and the need for some space behind the shutters for the optical fibers to bend, suggested that the largest practical lens to image distance,  $s_3$  in fig. 2-19, would be about 7 inches.

The approximate magnification  $M$  of the optical system is given by

$$M \approx s_3 / (s_1 + s_2) \quad (2-2)$$

where  $s_1 + s_2$  is the distance from the center of the scattering volume to the lens. Since  $(s_1 + s_2) = s_3 = 7''$ , then  $M \approx 1$ . To determine the radius of curvature of the lens we use the paraxial lens formulas [20, p.1-10]

$$k = \frac{n_{lens} - n_{air}}{R_2} \quad (2-3)$$

and

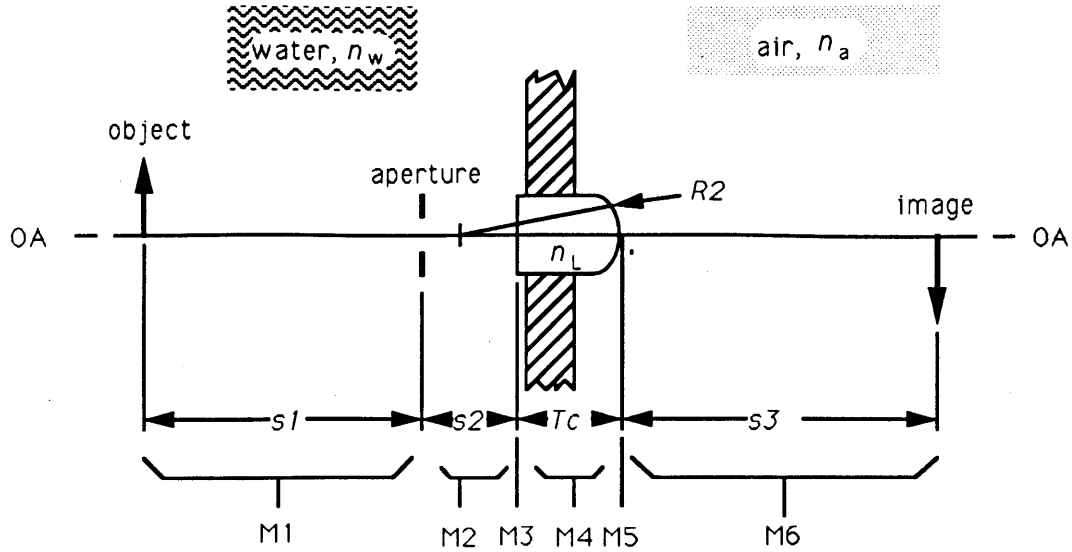
$$k = \frac{n_{air}}{s3} + \frac{n_{water}}{(s1+s3)} \quad (2-4)$$

where  $R2$  is the radius of curvature of the lens' non plano surface, and  $n_{air}$  and  $n_{water}$  are the index of refraction of air and water respectively. Eq. (2-3) is given in a simplified form for use with a plano-convex lens. With ( $s1 + s2 = s3 = 7''$ ), eq. (2-4) gives  $R2 = 1.395$  inches. The  $R2$  actually chosen was 1.4212 inches. This  $R2$  was chosen to save money, since the manufacturer of the lenses (J.L. Wood, Santa Anna, CA), had a test plate already fabricated with this radius.

### Paraxial Raytracing

A useful guide to the method of paraxial raytracing is Yariv's *Optical Electronics* [8]. The method and its application to the current optical system will be briefly described here.

Paraxial raytracing uses geometrical optics, combined with the assumption that angles of incidence and refraction,  $\theta_i$  and  $\theta_r$ , are small enough so that  $\theta_i$  and  $\theta_r$  may be substituted for  $\sin(\theta_i)$  and  $\sin(\theta_r)$ . The formal procedure is simplified by using matrices to represent the effects of optical elements on the height,  $r$ , and angle,  $r'$ , of a ray with respect the optical axis. The optical axis is the axis of symmetry of the optical system. The height and angle of a ray are represented by a column vector. Fig. 2-19 indicates shows the method. In this figure, the optical axis is given by line OA. A ray starting at the position of the object is transformed to an new height,  $r$ , at the position of the aperture, by matrix M1. The matrix product  $M2 * M1$  transforms a ray starting at the object to an new  $r$  at the position of  $s1 + s2$ . The matrix M3 represents the effect of Snell's law



$$\begin{pmatrix} r \\ r' \end{pmatrix}_{OUT} = \begin{pmatrix} m1 & m2 \\ m3 & m4 \end{pmatrix} \begin{pmatrix} r \\ r' \end{pmatrix}_{IN}$$

$$M1 = \begin{pmatrix} 1 & s1 \\ 0 & 1 \end{pmatrix} \quad M2 = \begin{pmatrix} 1 & s2 \\ 0 & 1 \end{pmatrix}$$

$$M3 = \begin{pmatrix} 1 & 0 \\ 0 & n_w/n_L \end{pmatrix} \quad M4 = \begin{pmatrix} 1 & Tc \\ 0 & 1 \end{pmatrix}$$

$$M5 = \begin{pmatrix} 1 & 0 \\ (n_L - n_a)/(n_a * R2) & n_L/n_a \end{pmatrix} \quad M6 = \begin{pmatrix} 1 & s3 \\ 0 & 1 \end{pmatrix}$$

$$\begin{pmatrix} r \\ r' \end{pmatrix}_{IMAGE} = M6 * M5 * M4 * M3 * M2 * M1 \begin{pmatrix} r \\ r' \end{pmatrix}_{OBJECT}$$

**Figure 2-19:** Illustration of the method of paraxial raytracing using matrices.

on  $r'$  at the water, lens interface on a paraxial ray. Matrix M5 represents the effect of the lens, air curved interface on  $r'$  for a paraxial ray. The final height  $r$ , and angle  $r'$  of ray ending up at the position of the image is given by the matrix product  $M6 * M5 * M4 * M3 * M2 * M1$  acting on the starting height and angle at the position of the object.

Paraxial raytracing was used to verify the image position, depth of focus, and that the lenses had adequate clear aperture.

### **Lens Centration**

Lens centration error is the angular deviation of lens optical axis from the lens mechanical axis. Lens centration error causes an unintended deviation of a ray direction when it is refracted by a lens. In the instrument described here lens centration error is results from finite fabrication error, and imperfect alignment during installation into the tank walls. If the lens apertures were placed external to the tank, on the image side of the lenses, the lens centration error would cause some error in the actual scattering angle detected with respect to its nominal value. However, in this instrument the apertures are placed on the object side of the lenses, so lens centration error has no effect on the scattering angle detected provided that shutters are aligned with the procedures outlined previously in Sec. 2.2.7.

Fig. 2-20 shows how lens centration error can lead to errors in scattering angle and displacement of the image. Referring to the figure, ray AB which starts from the object and ends up being blocked at the aperture stop, is initially coincident with the optical axis OA, but is redirected as a result of the lens centration error. Ray AC which ends up at the image, just barely makes it through the lens and aperture stop. Inspection of the figure

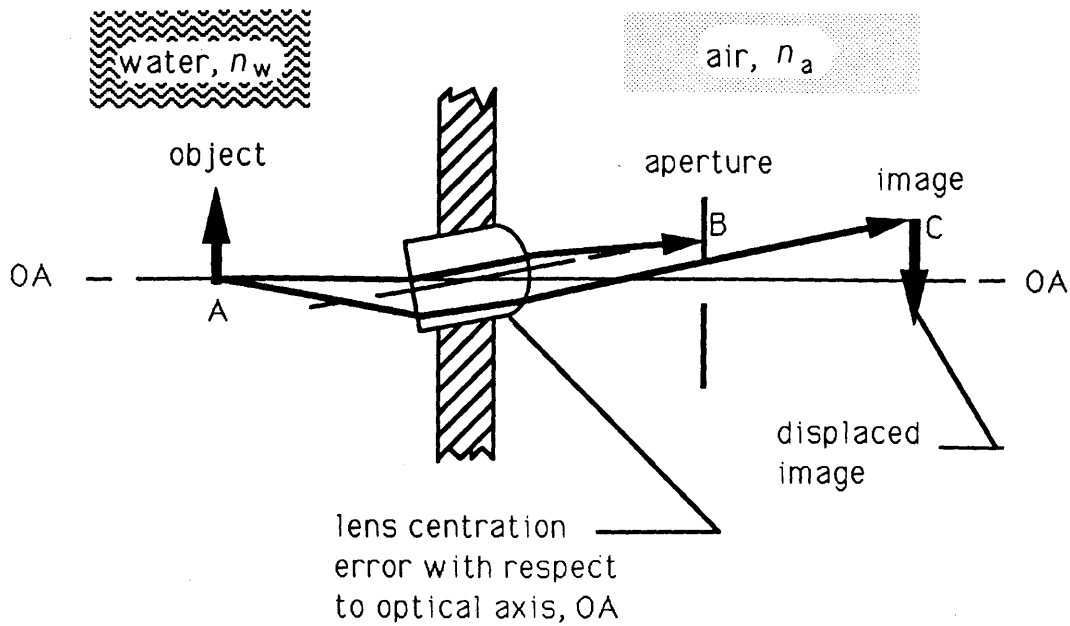


**Figure 2-20:** The effect of lens centration error on effective scattering angle, and image position.

shows that rays received at the image are scattered from the object in a direction which is biased away from the optical axis. If the optical axis was meant to coincide with a particular scattering angle, then this bias would cause an error in the scattering angle from its intended value. Such an error can be avoided by placing the aperture stop on the object side of the lens. If the aperture stop must be on the image side of the lens, then it should be placed as close to the lens as possible.

## References for Chapter

- [1] A. Einstein.  
*Ann. Physik* 33():1275, 1910.  
 English Trans. in *Colloid Chemistry* (J. Alexander, ed.), Vol 1, p. 323-339. Reinhold, New York, 1926.
- [2] L. Ornstein, F. Zernike.  
*Proc. Acad. Sci. Amsterdam* 17:793, 1914.
- [3] G. Benedek, and T. Greytak.  
 Brillouin Scattering in Liquids.  
*Proc. IEEE* 53(10):1623-1629, 1965.
- [4] G. B. Benedek.  
 Optical Mixing Spectroscopy, with Applications to Problems in Physics,  
 Chemistry, Biology and Engineering.  
*Polarization, Matter, and Radiation*.  
 Presses Universitaire de France, 1969, pages 49 - 84.
- [5] H.R. Haller.  
 A photon detection system for dynamic light scattering.  
*J. Phys. E: Sci. Instrum.* 14:1137-1138, 1981.  
 See also references, contained therein.
- [6] W. Kaye and A. J. Havlik.  
 Low Angle Light Scattering - Absolute Calibration.  
*Applied Optics* 12(3):541 - 550, 1973.
- [7] H. R. Haller, C. Destor, and D. S. Cannell.  
 Photometer for quasielastic and classical light scattering.  
*Rev. Sci. Instrum.* 54:973-983, 1983.
- [8] A. Yariv.  
*Optical Electronics*.  
 Holt, Rinehart, and Winston, 1985.
- [9] S. B. Dubin.  
*Quasielastic Light Scattering From Macromolecules*.  
 PhD thesis, Massachusetts Institute of Technology, 1970.
- [10] W.B. Beck and M.H. Hodge.  
 Hard Clad Silica: A New Family of Optical Fibers.  
*Laser Focus* :90 - 96, December, 1984.
- [11] R. W. Engstrom.  
*RCA Photomultiplier Handbook: Theory, Design, Application*.  
 RCA PMT-62, Radio Corporation of America, 1980.  
 This handbook may be obtained from: Burle Industries, New Products Division,  
 Lancaster, PA 17604 1-(800)-233-0155.

- [12] P. Horowitz, and W. Hill.  
*The Art of Electronics.*  
Cambridge University Press, 1980.
- [13] .  
*IEEE-488-1978 Standard.*  
...
- [14] .  
*Application Bulletin, IEEE-488-1978.*  
AB-36, John Fluke Manufacturing Co., Inc., .
- [15] .  
*Technical Bulletin, Troubleshooting Information, IEEE-488-1978.*  
C0076, John Fluke Manufacturing Co., Inc., .
- [16] .  
*IEX-VMS-DIRVER: User's and Installation Guide.*  
, Digital Equipment Corp., 1985.
- [17] J. S. Steinhart, and S. R. Hart.  
.  
*Deep-Sea Res.* 15:497, 1968.
- [18] W. J. Smith.  
*Modern Optical Engineering: The Design of Optical Systems.*  
McGraw-Hill Book Co., 1966.
- [19] J. H. Moore, C. C. Davis, and M. A. Coplan.  
*Building Scientific Apparatus: A Practical Guide to Design and Construction.*  
Addison-Wesley Publishing Co., 1983.
- [20] Melles Griot.  
*Optics Guide 4.*  
Technical Report, Melles Griot, 1988.  
This handbook may be obtained from: Melles Griot, 1770 Kettering Street, Irvine  
CA 92714, (714) 261-5660.







### 3. Light Scattered From Pure Fluids

*The sun, an hour above the horizon, is poised like a bloody egg upon a crest of thunderheads; the light has turned copper: in the eye portentous, in the nose, sulphurous, smelling of lightning.*

*From William Faulkner's As I Lay Dying.*

#### 3.1 Introduction

The light scattering instrument described in the previous chapter was used for measuring light intensity scattered from pure liquids, as well as macromolecular systems which will be described in later chapters. This chapter will begin with a description of some of the measurement conventions which pertain to static light scattering. The theory of light scattered from an ideal gas of non-interacting particles (Rayleigh scattering) will be introduced because it is the foundation of all that follows. The motivation and the results of the thermodynamic theory of light scattered from the liquid state will then be described briefly.

The second half of the chapter will explain the method of calibrating the light scattering instrument response with respect to a known standard reference solvent. At this point, the topic of depolarized scattering from anisotropic scatterers will be introduced since it is needed for correcting experimental results so that they can be compared with the literature. Presentation of the experimental results for the intensity of light scattered from pure water as function of temperature, as well as results from several other solvents will conclude the chapter.

### 3.2 Optical extinction in an ideal gas of particles

The transmission of a light beam through a medium containing suspended particles will be attenuated by particle absorption and scattering. Absorption and scattering are two distinct physical processes. Absorption removes energy from the incident light beam by excitation of particle internal modes. By means of particle collisions, energy contained in the excited internal modes can be transformed into a higher average kinetic energy per particle, and therefore a higher temperature.

In contrast to absorption, the optical scattering process leaves the internal energy state of the scattering particle unchanged, and the scattered radiation is, to first order, not shifted in frequency. The scattering process may be thought of as individual photons colliding with the particles in the medium and therefore having their momentum vectors changed in direction, and perhaps very slightly in magnitude.

The combined effects of absorption and scattering by the particle medium are called extinction. The transmitted intensity  $I(L)$  of a monochromatic light beam of intensity  $I_0$  incident upon a medium of thickness  $L$  is given by

$$I(L) = I_0 \exp(-L\tau_{ext}). \quad (3-1)$$

where

$$\tau_{ext} = \tau_{scatt} + \tau_{abs}. \quad (3-2)$$

$\tau_{scatt}$  is known as the turbidity.  $\tau_{abs}$  is the part of  $\tau_{ext}$  resulting from absorption.

The basis of Eq. (3-1) can be understood from examination of Fig. 3-1, which shows a beam of incident, intensity  $I$  upon a slab of volume element of thickness  $\Delta L$  containing particles. The decrease in transmitted intensity,  $\Delta I$ , due to absorption and scattering of particles in the slab, must be proportional to the width of the slab volume,  $\Delta L$ , and to the intensity incident on the slab,  $I$ . Therefore,

$$\Delta I = A I \Delta L \quad (3-3)$$

from which follows Eq. (3-1) in the that limit  $\Delta L \rightarrow 0$  with  $A \equiv -\tau_{\text{ext}}$ . The coefficient  $\tau_{\text{ext}}$  is proportional to the number density of particles,  $\rho_N$ , and the extinction cross section per particle  $C_{\text{ext}}$ , that is to say

$$\tau_{\text{ext}} = \rho_N C_{\text{ext}} \quad (3-4)$$

with  $C_{\text{ext}}$  being a sum of the absorption cross section  $C_{\text{abs}}$ , and the scattering cross section  $C_{\text{scat}}$ . The total scattered power per particle  $w$  is given by

$$w = I C_{\text{scat}} \equiv (I/\rho_N) \int R(\theta'', \phi) d\Omega \quad (3-5)$$

where  $R(\theta'', \phi)$  is the Rayleigh ratio and  $\Omega$  is the solid angle.  $R(\theta'', \phi)$  is defined as [1, p. 38]

$$R(\theta'', \phi) = (I(\theta'', \phi, D)/I)(D^2/V) \quad (3-6)$$

where  $I(\theta'', \phi, D)$  is the intensity scattered into a detector at angular position  $(\theta'', \phi)$  at a distance  $D$  from scattering volume  $V$ . Fig. 3-2 shows the scattering geometry to which the coordinates  $(\theta'', \phi)$  are referred. Therefore, using Eq. (3-5) we can link the microscopic quantity  $C_{\text{scat}}$  to the macroscopic standard measurement of scattering power  $R(\theta'', \phi)$ , that is

$$C_{\text{scat}} = \int R(\theta'', \phi) / \rho_N d\Omega. \quad (3-7)$$

It also follows from Eq. (3-4) and Eq. (3-7) that

$$\tau_{\text{scat}} = \int R(\theta'', \phi) d\Omega. \quad (3-8)$$

Eq. (3-8) is a general relation, not specific to an ideal gas: this equation will be used again later in the chapter. From the preceding discussion, we can also identify the relation

$$i(\theta'', \phi, D) = (R(\theta'', \phi) / \rho_N) (I/D^2) \quad (3-9)$$

where  $i(\theta'', \phi, D)$  is the intensity of light scattered from a single particle. Henceforth,  $\tau_{\text{scat}}$  will be referred to as simply  $\tau$ .

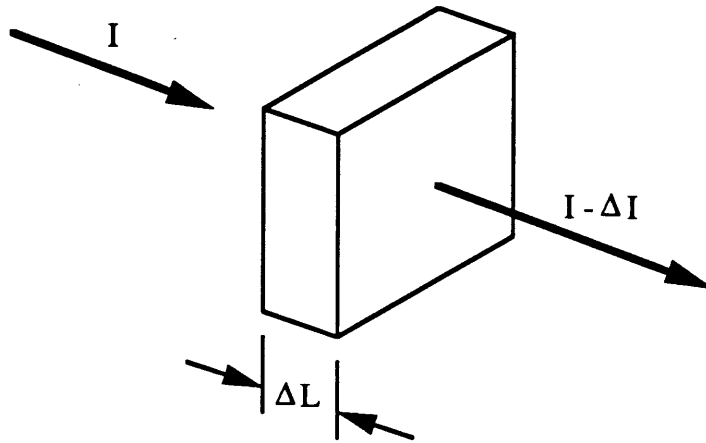


**Figure 3-1:** Light beam incident on slab of volume containing particles.

$\Delta L$  is the thickness of the slab;  $I$  is the intensity of the light beam incident from the left; and  $\Delta I$  is the change in the beam intensity.

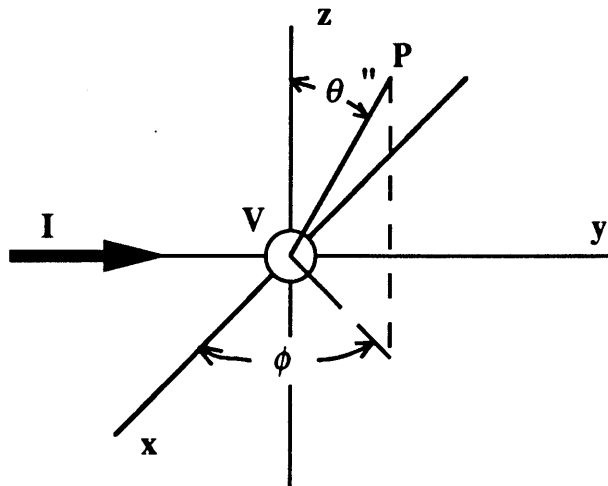


**Figure 3-2:** The scattering geometry.

The scattering volume,  $V$ , is located at the origin; the detector is located at point  $P$ , which is at distance  $D$  from the origin; the incident light beam of intensity  $I$  is on the left half of the  $y$  axis; the transmitted light beam is on the right half of the  $y$  axis.

### 3.3 Scattering from an ideal gas of particles: Rayleigh scattering

So far, we have discussed only some of the formalism relating measurement of scattered power to light beam attenuation. Now we will examine the physics causing the scattering in first place. We will focus on the scattered intensity due to one particle  $i(\theta'', \phi, D)$  so as to simplify our picture. Imagine a particle of characteristic dimension  $a$  where  $a \ll \lambda_0$  where  $\lambda_0$  is the wavelength of the incident light. This scattering problem was solved by Lord Rayleigh at the end of the last century; therefore, light scattered from very small particles at positions uncorrelated in space, (such as molecules in an ideal gas) is known as Rayleigh scattering. In the limit  $a \ll \lambda_0$ , an individual particle can be thought of as an oscillating electric dipole with an induced dipole moment  $p(t)$  being caused by the time varying incident electric field, i.e.  $p(t) = \alpha E(t)$ , where  $\alpha$  is the (molecular) polarizability, and  $E(t) = E_0 \exp(i\omega t)$  is the time varying incident electric field with amplitude  $E_0$  and angular frequency  $\omega$ . It can be shown that [2, p. 603]

$$i(\theta'', \phi, D)_p = \frac{c_{light} p_0^2 \omega^4}{32 \pi^2 \epsilon_0 D^2} \sin(\theta'')^2 \quad (3-10)$$

where the subscript  $p$  on  $i(\theta'', \phi, D)_p$  denotes the fact that the incident light is polarized,  $c_{light}$  is the speed of light,  $p_0$  is the amplitude of the induced oscillating dipole moment,  $\epsilon_0$  is the electric field permeativity in *vacuum*, and the incident electric field is polarized along the  $\theta = 0$  direction.  $\omega = 2\pi/\lambda_0$  where  $\lambda_0$  is the wavelength of the incident light *in vacuum*. Naturally, we may also express Eq. (3-10) in terms of the the molecular polarizability and incident intensity  $I_0$ , since  $p_0^2 = \alpha^2 E_0^2$  and  $I_0 = 1/2 c_{light} \epsilon_0 E_0^2$  (in MKS units), giving

$$i(\theta'', \phi, D)_p = \frac{\omega^4 I_0}{16 \pi^2 \epsilon_0^2 D^2} \alpha^2 \sin(\theta'')^2. \quad (3-11)$$

For rarefied gases and simple liquids, the *Clausius-Mossotti* equation [2, p. 115] may be used to express  $\alpha$  in terms of the bulk index of refraction of the dispersed material,  $n$ ; that is,

$$\alpha = \frac{3 \epsilon_o}{\rho_N} \frac{n^2 - 1}{n^2 + 2}. \quad (3-12)$$

Also,  $\rho_N$  is related to the molecular weight of the particles  $M$  and their mass density in the media  $\rho$  by

$$\rho_N = \rho (N_A / M) \quad (3-13)$$

where  $N_A$  is Avogadro's number. In the regime where  $n \sim 1$  then, Eq. (3-12) can be written as

$$\alpha = \frac{\epsilon_o}{\rho_N} (n^2 - 1) = \frac{\epsilon_o}{\rho_N} 2(n - 1). \quad (3-14)$$

Eq. (3-10) takes a different form if the incident light is unpolarized. Specifically, the  $\sin(\theta)^2$  term is altered. Consider the situation depicted in Fig. 3-3 where the electric field vector  $\mathbf{E}$  has a random direction in the  $x$ - $z$  plane at the origin where the polarizable molecule is located. In this figure,  $\mathbf{E}$  propagates along the direction of the  $y$  axis and subtends angle  $\xi(t)$  with respect to the  $z$  axis at the instant in time  $t$ . If we observe the intensity at angular position  $(\theta'', \phi = 90^\circ, D)$  (in the  $y$ - $z$  plane), then the scattered intensity at instant in time  $t$  is

$$i(\theta'', \phi, D, t')_u = \frac{c_{light} p_o^2 \omega^4}{32 \pi^2 \epsilon_o D^2} \sin(\eta(t))^2 \quad (3-15)$$

where  $\eta(t)$  is the angle between the time dependent direction of the induced dipole and the direction from the origin to our observation point at  $(\theta'', 90^\circ, D)$ ,  $t'$  is the retarded time at the observation point:  $t' = t + D/c$ . At the time instant  $t$ , we have from analytical geometry,



$$\cos(\eta(t)) = \cos(\theta'') \cos(\xi(t)) \quad (3-16)$$

so Eq. (3-15) can be written

$$i(\theta'', \phi, D, t')_u = \frac{c_{light} p_o^2 \omega^4}{32 \pi^2 \epsilon_o D^2} [1 - \cos(\theta'')^2 \cos(\xi(t))^2]. \quad (3-17)$$

Since the angle of  $\mathbf{E}$  with respect to the  $z$  axis,  $\xi(t)$ , is random in time, we have

$$\langle \cos(\xi(t)) \rangle_{time} = 0$$

and therefore

$$\langle 1 - \cos(\theta'')^2 \cos(\xi(t))^2 \rangle_{time} = 1 - \cos(\theta'')^2 (1/2) \langle 1 + \cos(2\xi(t)) \rangle_{time} = 1 - (1/2) \cos(\theta'')^2 \quad (3-18)$$

If we take  $\theta'$  to be angle between the point of observation and the  $y$  axis (i.e.,  $\theta' = 90^\circ - \theta''$ ), then Eq. (3-18) can be written

$$\langle 1 - \cos(\theta'')^2 \cos(\xi(t))^2 \rangle_{time} = 1 - (1/2) \sin^2(\theta') = (1/2)(1 + \cos(\theta')^2) \quad (3-19)$$

So for unpolarized incident light the (time averaged) scattered intensity,  $i(\theta')_u$ , is given by

$$i(\theta')_u = \frac{c_{light} p_o^2 \omega^4}{32 \pi^2 \epsilon_o D^2} [(1/2)(1 + \cos(\theta')^2)]. \quad (3-20)$$

Because  $\mathbf{E}$  is unpolarized,  $i(\theta')_u$  is symmetric with respect to rotation around the  $y$  axis.

### 3.4 Scattering from liquids

The picture we used above is of a medium containing scattering particles, small compared to the incident light wavelength, and having completely random positions with respect to one another. The case of the liquid state is more complicated because the constituent molecules of the liquid are closely packed and do not have random positions with respect to each other: in the jargon of physics, we say that liquids have strong short range interactions (that lead to short range ordering). The characteristics of the spatial

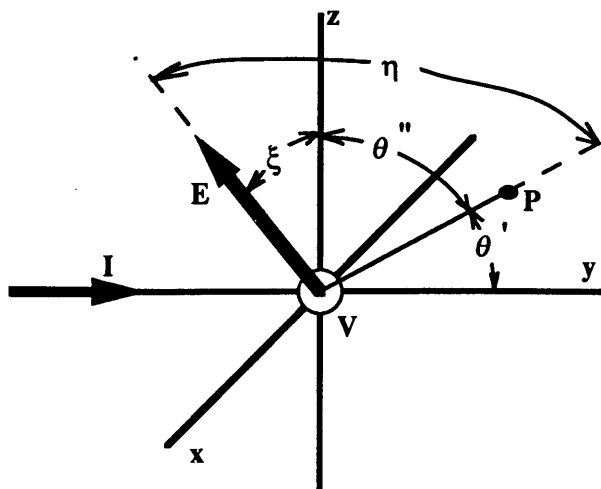


**Figure 3-3:** Instantaneous direction of electric field vector.

$\xi$  is the time dependent angle between the incident electric field vector,  $\mathbf{E}$  located at the scattering volume, and the  $z$  axis. The direction of the incident light beam  $\mathbf{I}$  is along the  $y$  axis: therefore,  $\mathbf{E}$  is in the  $z$ - $x$  plane.  $\eta$  is the angle between  $\mathbf{E}$  and the point of observation  $\mathbf{P}$  which is the  $y$ - $z$  plane.

ordering can be quantified in a function called the static structure factor. (Reference [3] contains a very good discussion of the topic of structure in fluids.)

Because of the strong short range ordering in fluids, the intensity of light scattered from them is much less than expected solely from the Rayleigh theory described previously [1, Chap. 9]. To paraphrase Kerker, Smoluchowski who was interested in explaining critical phenomena, proposed a model for the liquid state in which the liquid was viewed as a continuous media having adjacent domains of differing density, with each domain treated as a single Rayleigh scatterer. The domains of differing density are created by entropy and pressure fluctuations in the medium. Light scattered from entropy fluctuations at constant pressure is called Landau-Placzek scattering, and light scattered from pressure fluctuations at constant entropy (acoustic waves) is called Brillouin scattering [4, and references therein]. The wavelength of Placzek scattering is unshifted

with respect to the incident light, but the frequency of Brillouin scattering is shifted away from the center frequency by the frequency of the Fourier resolved acoustic waves in the medium traveling away from and toward the detector: the spectrum of Brillouin scattering therefore is a doublet centered on the Placzek line [5]. Fig. 3-4 shows the spectrum of light scattered from pure water. In the case of water Fig. 3-4 the amplitude of the center Placzek line is exceeded by the thermally driven Brillouin Scattering in the wings of the spectrum. The instrument used for the measurements in this thesis is not capable of resolving a spectrum like the one shown in fig. 3-4, rather it measures the total scattered intensity from the liquid sample.

The model using density fluctuations can be used to predict the total intensity, and turbidity (using Eq. (3-8)) of light scattering from a fluid in terms of thermodynamic properties of the liquid. The results of the theory give [1,p. 496]

$$\tau = \frac{32\pi^3 kT\beta_T}{3\lambda_o^4 a_p^2} n^2 \left(\frac{\partial n}{\partial T}\right)^2_P \quad (3-21)$$

where  $\beta_T$  is the isothermal compressibility, and  $a_p$  is given by

$$a_p = \frac{1}{V} \left(\frac{\partial V}{\partial T}\right)_P. \quad (3-22)$$

### 3.5 Instrument calibration procedures

The instrument described in Chapter 2 was routinely calibrated by comparing its response to scattering from a reference solvent with a known Rayleigh ratio. (The Rayleigh ratio was defined in Eq. (3-6).) This calibration was accomplished as follows. Usually about 50 individual intensity, measurements,  $I(\theta, P, C)$  were made at each scattering angle,  $\theta$ , with the HP5316 frequency counter in Fig. 2-5 gated at about 0.5 seconds. Fig. 3-5 shows the scattering geometry. The variables  $P$ , and  $C$ , in  $I(\theta, P, C)$  are

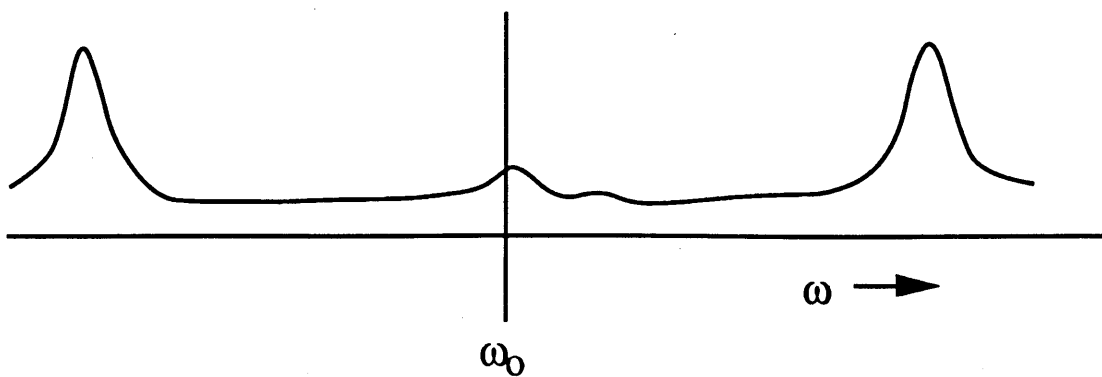


**Figure 3-4:** The spectrum of light scattered from pure water measured with a Fabry-Perot interferometer.

The spectrum of light scattered from pure water measured with a Fabry-Perot interferometer (data reproduced from reference [5]). The center peak at  $\omega_0$  is the Placzek line, and the two peaks centered on Placzek line are the Brillouin doublet.

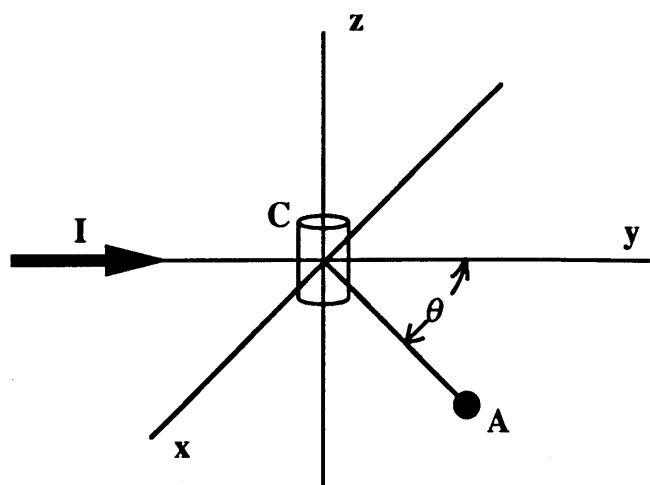


**Figure 3-5:** The scattering geometry.

Scattered light originating in the sample cell  $C$  is collected at the aperture  $A$  which is at angle  $\theta$  from the transmitted beam  $I_t$ . The incident light beam  $I$  is linearly polarized along the direction of the  $z$  axis. The center of  $A$  is in the  $x$ - $y$  plane.

the pass number and cycle number, and their meaning is defined below. In one cycle, each scattering angle was measured once, in sequence, starting with the transmitted beam  $I_t(P,C)$ . To make one cycle, a shutter was opened by the computer and photo counts were accumulated until the frequency counter gated the measurement, then shutter was closed and the next shutter opened, repeating the measurement process until the last angle was measured. A pass usually consisted of a group of 10 cycles, and usually 5 passes were measured, making 50 measurements at each angle. To summarize, a cycle is defined as one sequential measurement of the light intensity scattered at each scattering angle. A pass, is defined as group of cycles.  $I(\theta,P,C)$  is the value of the measured intensity for scattering angle  $\theta$ , of cycle number  $C$ , of pass number  $P$ .

The data were reduced by first normalizing the intensity at each angle,  $I(\theta,P,C)$ , with the measured transmitted laser intensity  $I_t(P,C)$ : that is,  $P(\theta,P,C) \equiv$

$I(\theta, P, C)/I_t(P, C)$ . Measuring each angle sequentially, and then dividing each cycle measurement by the transmitted beam, removed instrument response dependence on photomultiplier and laser power drift. Dividing the scattered intensity by the transmitted intensity also removed the effect of sample turbidity from  $P(\theta, P, C)$  since the scattered and transmitted light followed optical paths of identical lengths through the scattering cell if cylindrical sample cells were used, as was usually the case.

Dust discrimination was accomplished by forming the average and standard deviation for each group of pass measurements for each scattering angle. Each measurement in the pass was then compared to the average value and rejected if it exceeded the average value plus 5 standard deviations. The pass average values for each scattering angle were then recomputed minus the rejected measurements. The entire pass for an angle was rejected if more than two measurements per pass were rejected.

The final stage of the data reduction was to average the dust discriminated pass values for each angle. If the above measurements were made from a reference solvent, then the Rayleigh ratio  $R_{samp}(\theta)$  of an unknown sample could be obtained from

$$R_{samp}(\theta) = \frac{\langle P_{samp}(\theta) \rangle}{\langle P_{ref}(\theta) \rangle} (n_{samp} / n_{ref})^2 R_{ref} \quad (3-23)$$

where  $\langle P_{samp}(\theta) \rangle$  is the average of the pass values for the sample,  $\langle P_{ref}(\theta) \rangle$  is the average of the pass values for the reference solvent,  $n_{samp}$  is the index of refraction for the sample,  $n_{ref}$  is the index of refraction for the reference solvent, and  $R_{ref}$  is the Rayleigh ratio of the reference solvent, which was assumed to be independent of  $\theta$ . Angular dependent instrument response is removed by taking the ratio  $\frac{\langle P_{samp}(\theta) \rangle}{\langle P_{ref}(\theta) \rangle}$  in Eq. (3-23).

A factor  $n_{samp} / n_{ref}$  in Eq. (3-23) corrects for the change in the length of the scattering

volume with change of index of refraction when a cylindrical scattering cell is used. An additional factor of  $n_{\text{samp}}/n_{\text{ref}}$  in Eq. (3-23) corrects for the change in acceptance solid angle for each scattering source point in the scattering volume, also when a cylindrical scattering cell is used. The necessity of the two  $n_{\text{samp}}/n_{\text{ref}}$  correction factors can be shown using paraxial raytracing (or see reference [6]).

### 3.6 Standard ways of reporting the Rayleigh ratio

Laboratory methods of static light scattering predate the advent of the laser by many years. Earlier researchers utilizing static light methods used monochromatic, incoherent, unpolarized light sources, such as one emission line from a mercury or sodium lamp. In those earlier days, it was common practice to report the Rayleigh ratio of a solvent scattered at  $90^\circ$  to the direction of the incident beam from the unpolarized light source, denoted  $R(\theta=90^\circ)_u$ .

Today, it is typical for a researcher using static light scattering methods to employ a polarized laser light source, and to measure the intensity of scattered light in the scattering plane normal to the polarization vector of the incident electric field as shown in Fig. 3-5. In this scattering plane, the Rayleigh ratio  $R_p$  of light scattered from sources much smaller than the light wavelength is uniform for all scattering angles and different from  $R(\theta)_u$  except in the limit  $\theta \rightarrow 0^\circ$ , and in the limit  $\theta \rightarrow 180^\circ$ . That is to say,

$$R_p = \lim_{\theta \rightarrow 0} R(\theta)_u = \lim_{\theta \rightarrow 180} R(\theta)_u. \quad (3-24)$$

To compare literature values of  $R(\theta=90^\circ)_u$  to  $R_p$  we need an explicit expression for  $\lim_{\theta \rightarrow 0} R(\theta)_u$  which can be expressed in terms of  $R(\theta=90^\circ)_u$ . An ideal scattering source would not depolarize the scattered light. The convention is to write the observed

Rayleigh ratio,  $R(\theta)_u$ , as the product of an ideal part which does not depolarize scattered light,  $R(\theta)_{ideal}_u$ , and a correction factor for the depolarization,  $C(\theta)_u$ . That is,

$$R(\theta)_u = R(\theta)_{ideal}_u C(\theta)_u \quad (3-25)$$

where  $C(\theta)_u$  is known as the Cabbanes factor for an unpolarized light source and is given as [1, p. 584]

$$C(\theta)_u = \frac{1 + \rho + (1 - \rho)\cos(\theta)^2}{(1 - (7/6)\rho)(1 + \cos(\theta)^2)} \quad (3-26)$$

where  $\rho$  is the depolarization ratio of light scattered from the sample using an unpolarized light source and measured at  $90^\circ$ . Also, Eq. (3-20) implies

$$R(\theta)_{ideal}_u = R(90^\circ)_{ideal}_u (1 + \cos(\theta)^2). \quad (3-27)$$

Combining Eqs. (3-25), and (3-27) gives

$$R(\theta)_u = [R(90^\circ)_{ideal}_u (1 + \cos(\theta)^2)] C(\theta)_u. \quad (3-28)$$

Inserting Eq. (3-26) into Eq. (3-28) gives.

$$R(\theta)_u = [R(90^\circ)_{ideal}_u] \frac{1 + \rho + (1 - \rho)\cos(\theta)^2}{(1 - (7/6)\rho)} \quad (3-29)$$

which could be written as

$$R(\theta)_u = [R(90^\circ)_u] \frac{1 + \rho + (1 - \rho)\cos(\theta)^2}{(1 + \rho)} \quad (3-30)$$

by using Eqs. (3-25) and (3-26). Using Eqs. (3-30) it follows that

$$R_p = \lim_{\theta \rightarrow 0} R(\theta)_u = R(90^\circ)_u \frac{2}{1 + \rho} \quad (3-31)$$

where  $R(90^\circ)_u$  is the observed value of the Rayleigh ratio at  $\theta = 90^\circ$  (i.e., *not* the ideal value).



### 3.7 The turbidity with depolarized light scattering

In the ideal case of no depolarized light scattering, the turbidity  $\tau_{ideal}$  is found from inserting Eq. (3-27) into Eq. (3-8) giving

$$\tau_{ideal} = \int R(90^\circ)_u^{ideal} (1 + \cos(\theta)^2) d\Omega = (16\pi/3) R(90^\circ)_u^{ideal} \quad (3-32)$$

In the case of depolarized light scattering, we can find the turbidity by inserting Eq. (3-30) into Eq. (3-8), giving

$$\tau = \int [R(90^\circ)_u] \frac{1 + \rho + (1 - \rho)\cos(\theta)^2}{(1 + \rho)} d\Omega = R(90^\circ)_u \frac{16\pi}{3} \frac{1 + \rho/2}{1 + \rho}. \quad (3-33)$$

Using Eqs. (3-31) in (3-33) we can then write

$$\tau = \frac{8\pi}{3} (1 + \rho/2) R_p \quad (3-34)$$

Also, we can use [1 p. 585]

$$\rho = \frac{2\rho_v}{1 + \rho_v} \quad (3-35)$$

where  $\rho_v$  is the depolarization ratio measured at  $\theta = 90^\circ$  using a vertically polarized light source (such as a laser source with an incident electric field vector polarized normal to the scattering plane).

### 3.8 Light scattering intensity standards

The static light scattering standards used for most experiments in this thesis were spectrophotometric grade toluene<sup>1</sup> and benzene which were used without further purification, filtering, or centrifugation. The scattering cell used for the standards was a 32 mm diameter cylindrical glass scattering cell pre-rinsed with spectrophotometric grade toluene to remove dust and other residues. Light scattered from the standard solvents

---

<sup>1</sup>Aldrich Chemical Co, Milwaukee, WI

was checked to be dust free by visual inspection in the light scattering apparatus with a 20X microscope mounted at a  $\theta = 17.5^\circ$  scattering angle. The Rayleigh ratios,  $R$ , of the toluene and benzene standards were taken from the data of Bender *et al.* [7] and were  $39.6 \times 10^{-6} \text{ cm}^{-1}$  and  $35.4 \times 10^{-6} \text{ cm}^{-1}$  respectively at  $25^\circ \text{ C}$ . and  $\lambda_0 = 488 \text{ nm}$ . The temperature dependence of the benzene Rayleigh ratio was taken from data measured by Ehl [8] at  $\lambda_0 = 546 \text{ nm}$ . Ehl [8] also compared the intensity of light scattered from toluene at  $20^\circ \text{ C}$  to the intensity scattered at other temperatures, and from his data, plus knowledge of the temperature dependence of the index of refraction for toluene, we can use a correction equation like Eq. (3-23) to determine toluene's Rayleigh ratio temperature dependence at  $\lambda_0 = 488 \text{ nm}$ . The temperature dependence of the index of refraction at  $\lambda_0 = 488 \text{ nm}$  for benzene was interpolated from the data provided by Waxler [9]. The results of the interpolation are shown in Table 3-1 along with the temperature dependence of the index of refraction for toluene. Reference [10] gives the index of refraction of toluene at  $\lambda_0 = 486.1 \text{ nm}$  for two temperatures: at  $T = 20^\circ \text{ C}$ ,  $n = 1.50781$ ; at  $T = 80^\circ \text{ C}$ ,  $n = 1.47539$ . The other values of  $n$  for toluene given in Table 3-1 were inferred by linear extrapolation, and interpolation based on the two literature values.

Table 3-2 gives the temperature dependence of the Rayleigh ratio of toluene at  $\lambda_0 = 488$  which was determined from

$$\frac{R(488, T)}{R(488, 20^\circ \text{C.})} = \frac{I(546, T)}{I(546, 20^\circ \text{C.})} \left( \frac{n(T)}{n(20^\circ \text{C.})} \right)^2 \quad (3-36)$$

where  $R(488, T)$  is the Rayleigh ratio at  $\lambda_0 = 488 \text{ nm}$  and temperature  $T$ ,  $\frac{I(546, T)}{I(546, 20^\circ \text{C.})}$  is the ratio light scattered at temperature  $T$ , to light scattered at  $20^\circ \text{ C}$ . at  $\lambda_0 = 546 \text{ nm}$  from the data of Ehl [8]. The value of  $\frac{n(T)}{n(20^\circ \text{C.})}$  was taken from Table 3-1. Eq. (3-36) is an ap-

proximation because it assumes that the ratios  $\frac{I(546,T)}{I(546,20^{\circ}\text{C})}$ , and  $\frac{n(T)}{n(20^{\circ}\text{C})}$  are not wavelength dependent.

### 3.9 The Rayleigh of water and its temperature dependence

Using benzene and toluene as primary standards we calibrated the light scattered from the tank water which circulates in the instrument. This calibration was done so that the tank water could be used as a secondary standard for instrument calibration. The results of the tank water calibration are give in Table 3-3. Remarkably, the Rayleigh ratio of water at  $\lambda_0=488\text{nm}$  is nearly independent of temperature from  $T=10^{\circ}\text{C}$ . to  $T=55^{\circ}\text{C}$ .:  $R(0) = (2.52 \pm 0.04) \times 10^{-6} \text{ cm}^{-1}$ . This observation of near temperature independence is consistent with the earlier of observations of Cohen, *et. al.* [11] at  $\lambda_0 = 546\text{nm}$  and  $\lambda_0 = 436\text{nm}$ . Using literature values of  $R(0)$  for water [11, 12], we also observed that the wavelength dependence of  $R(0)$  was near to  $\lambda_0^{-4}$  dependence expected from Eq (3-21) (ignoring dispersion in the  $n$ , and in  $\frac{\partial n}{\partial T}$ ) Fig. 3-6 shows a plot of the wavelength dependence of the Rayleigh ratio of water from the data presented here and elsewhere.

### 3.10 The Rayleigh ratios and turbidities of several solvents used as scintillators

A dilemma in the field of solar astrophysics, is the experimental observation that the flux of 14.06 MeV neutrinos produced in our sun is only about one third of that expected on the basis of the standard solar model [13]. To help resolve this discrepancy, Raghavan *et al.* [14] have proposed a new type of solar neutrino experiment (BOREX), which in principle can detect a larger variety of solar neutrinos than is possible with current ex-

**Table 3-1:** The refractive index,  $n$ , of benzene and toluene vs. temperature at  $\lambda_0 = 488$  nm, and  $\lambda_0 = 486.1$  nm.

$n$  for benzene was interpolated from values given in reference [9].  $n$  for toluene was interpolated from values given in reference [10].

Temp. (deg. C)	$n$ benzene (@488nm)	$n$ toluene (@486.1nm)
5	1.5234	1.516
10	1.5201	1.513
15	1.5167	1.511
20	1.5133	1.50781
24.8	1.5101	
25	1.5099	1.505
30	1.5065	1.502
34.5	1.5035	
35	1.5031	1.500
40	1.4998	1.497
45	1.4964	1.494
50	1.4930	1.492
54.34	1.4901	
55		1.489
70		1.481
80		1.47539

**Table 3-2: Toluene Rayleigh ratios,  $R(488,T)$  vs. temperature  $T$ .**

$I(546,T)/I(546,20)$  is absolute intensity of light scattered at temperature  $T$  divided by the intensity scattered at  $T = 20$  deg. C at 90 deg. scattering angle with  $\lambda_0 = 546\text{nm}$  taken from Ref. [8].  $R(488,T)/R(488,20)$  is the Rayleigh ratio of the toluene at temperature  $T$  over the Rayleigh ratio of the toluene at  $T = 20$  deg. C.  $R(488,T)/R(488,20)$  was calculated by extrapolating  $I(T)/I(20)$  to the needed temperatures and then using Eq. (3-36) compensate for the change in scattering volume and solid acceptance angle with change in temperature dependent index of refraction. Indexes of refraction were taken from Table 3-1.  $R(488,T)$  was determined from  $R(488,25)$  which is reported in Reference [7].]

$T$ (deg. C)	$I(T)/I(20)$ 546nm	$R(T)/R(20)$ 488 nm	$R(488, T)$ ( $\times 10^{-6} \text{ cm}^{-1}$ )
5		0.977	38.4
10		0.985	38.7
15		0.922	39.0
20	1.000	1.000	39.3
25		1.008	39.6
30	1.025	1.015	39.9
35		1.024	40.2
40		1.031	40.5
45		1.039	40.8
50	1.079	1.049	41.2
55		1.055	41.5
70	1.129	1.077	42.3
80	1.158	1.094	43.0

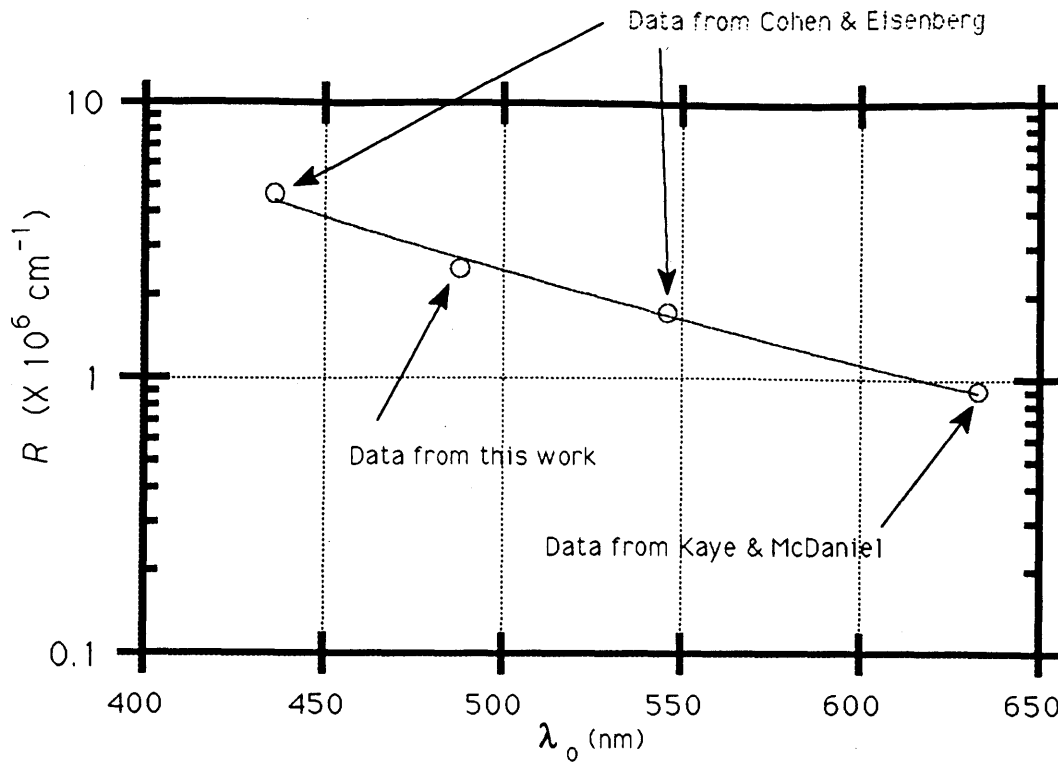


**Figure 3-6:** The wavelength dependence of the Rayleigh ratio for water.

The vertical axis is the rayleigh ratio of water at zero scattering angle,  $R(0)$ . The horizontal axis is the vacuum wavelength of the incident light.

From the curve through the four experimental points, we found that  $R(0) \sim \lambda_0^{-4.26}$ . Data are taken from references [11] and [12], and the present work. The measurements were made at 25° C.

**Table 3-3:** The Rayleigh ratio of water vs. temperature at  $\lambda_0 = 488\text{nm}$ .

R(T) is the temperature dependent Rayleigh ratio of the tank water in the light scattering apparatus which was obtained from comparing its scattering power to toluene and benzene, and then using equation (3-23) to correct for the effects of differing indices of refraction between water and the standard solvents. R(T) is the average value of R( $\theta$ ,T): i.e., R(T) is the average of all scattering angles.]

T (deg. C)	R(T) ( $\times 10^{-6}$ $\text{cm}^{-1}$ )	Standards compared to	# of measurements
5	2.62+- .04	toluene	1
10	2.52+- .05	toluene	1
15	2.50+- .03	toluene	1
20	2.51+- .03	toluene	5
25	2.49+- .06	benzene & toluene	4
30	2.49+- .06	benzene & toluene	6
35	2.52+- .03	benzene & toluene	2
55	2.52+- .02	toluene	1

periments. This experiment is designed to use approximately 500 m<sup>3</sup> of boron loaded scintillator as a target for solar neutrinos. Because of the large volume of scintillator fluid to be used in this experiment, it became necessary to know if the turbidity of the scintillator fluid was low enough to preclude multiple scattering of photons created by neutrino reactions with the scintillator.

In this section, we will present the turbidity found from light scattering, for several scintillators intended for possible use in the BOREX experiment. The scintillators studied were provided by Raghavan *et al.* and used without further purification or filtering.

The scintillator fluids studied were trimethylborate (TMB), and psuedocumean (PS).

A small amount of the photon wavelength shifter PMP was added to one of the samples. TMB and PS are very hydroscopic, so they were handled in a nitrogen environment at all times. The material was packaged in 5 ml ampules (Kimble 12012-LAB), temporarily sealed with teflon tape, and then flame sealed. All glassware was rinsed with isopropyl alcohol, and then acetone, and then blown dry with nitrogen. Some of the material was set aside for index of refraction measurements with an Abbe refractometer (Bausch and Lomb, model Abbe-3L). All measurements were made at 20° C.

Table 3-4 presents the results of measurements on the scintillators. The column labeled  $n_D$  is the index of refraction of the scintillators on the sodium D line, 589.3 nm. The column labeled  $R(0)$  is the Rayleigh ratio of the scintillators at zero scattering angle measured with the procedures outlined in Sec. 3.5. The column labeled  $\rho_v$  is the depolarization ratio of the scintillators measured at 90° scattering angle with a vertically polarized light source at 633 nm. The column labeled  $\tau$  is the scintillator turbidity at  $\lambda_0 = 488$  nm which was obtained as follows: the experimentally obtained values of  $R(0)$ , and  $\rho_v$  were used in Eqs. (3-34) and (3-35) with  $R(0) \equiv R_p$  from Eq. (3-24).

As a result of the turbidity measurements presented in Table 3-4, it was found that the level of multiple scattering in the TMB, and PS solvents was low enough to make them practical for use in BOREX experiment.



Table 3-4:

The index of refractions (measured on a Bausch & Lomb Abbe 3L refractometer), measured rayleigh ratios, depolarization ratios  $\rho_v$ , and calculated turbidities from using Eq. (3-35) in Eq. (3-34).

Solvent type	$n_D$	R(0) ( $\times 10^{-6} \text{ cm}^{-1}$ )	$\rho_v$	$\tau$ ( $\times 10^{-6} \text{ cm}^{-1}$ )
TMB	1.3584	10.2	.088	92
PS	1.5064	46.1	.38	492
TMB+PS (20% TMB)	1.3894	29.2	.10	267
TMB+PS+PMP (2% PMP)	1.3898	26.3	.072	234
Toluene standard			.32	417

### References for Chapter 3

- [1] M. Kerker.  
*The Scattering of Light And Other Electromagnetic Radiation.*  
Academic Press, 1969.
- [2] Lorrain, and Corson.  
*Electromagnetic Fields and Waves.*  
W.H. Freeman & Co., San Francisco, 1970.
- [3] D.L. Goodstein.  
*States of Matter.*  
Prentice-Hall, Inc., 1975.
- [4] A. T. Young.  
Rayleigh Scattering.  
*Applied Optics* 20(4):533 - 535, 1981.
- [5] G. Benedek, and T. Greytak.  
Brillouin Scattering in Liquids.  
*Proc. IEEE* 53(10):1623-1629, 1965.
- [6] D. J. Coumou.  
Apparatus For The Measurement Of Light Scattering In Liquids: Measurement  
Of The Rayleigh Factor Of Benzene And Some Other Pure Liquids.  
*J. Colloid Science* 15:408-417, 1960.
- [7] Bender, T.M., Lewis, R.J. and Pecora, R.  
Absolute Rayleigh ratios of four solvents at 488 nm.  
*Macromolecules* 19:244-245, 1986.
- [8] J. Ehl, C. Loucheux, C. Reiss, and H. Benoit.  
Mesure de l' increment d' indice de refraction de differentes solutions de hauts  
polymeres, et du rapport de Rayleigh de quelques liquides, en fonction de la  
temperature.  
*Makro. Chem.* 75:35, 1964.
- [9] R. M. Waxler, C. E. Weir, H. W. Shamp Jr.  
Effect of Pressure and Temperature Upon the Optical Dispersion of Benzene,  
Carbon Tetrachloride and Water.  
*J. Res. Natl. Bur. Stand., Sect A* 68A(5):489, 1964.
- [10] Ed. R. Bechman.  
Optische Konstanten.  
*Landolt-Boernstein, 6th Edition, Volume II, Part 8.*  
Springer Verlag, 1962, pages 5-633.
- [11] G. Cohen, and H. Eisenberg.  
Light Scattering of Water, Deuterium Oxide, and Other Pure Liquids.  
*J. Chem. Physics* 43(11):3881-3892, 1965.
- [12] W. Kaye and J. B. McDaniel.  
Low Angle Light Scattering - Rayleigh Factors and Depolarization Ratios.  
*Applied Optics* 13(8):1934 - 1937, 1974.

- [13] H. Zirin.  
*Astrophysics of the Sun.*  
Cambridge University Press, New York, NY, 1988.
- [14] T. Kovacs, J. Mitchell, P. Raghavan, R. S. Raghavan S. J. Freedman, J. Kay,  
C. E. Lane, R. I. Steinberg C. Cattadori, A. Donati, S. Pakvasa, M. Deustch,  
P. Rothschild, C. Arpesella, G. Bellini, S. Bonetti, M. Campanella, P. Inzani,  
I. Manno, E. Meroni, G. Ranucci, F. Ragusa, G. Cecchet, A. de Bari,  
M. Gallorini, A. Perotti.  
BOREX: Solar Neutrino Experiment Via Weak Neutral And Charged Currents In  
Boron-11.  
*Solar Physics* **128**:61-65, 1990.

## 4. Light Scattered From Model Macromolecular Systems

*We can say about electronic aids to navigation, then, that although they may be valuable, they are subject to various weakness and misinterpretations and so are at best supplementary to clock and compass, not substitutes for them. To be useful, they must be practiced in clear weather and their possible aberrations and limitations must be studied. The skipper who would rather sail his boat than gaze at an electronic display on a pleasant afternoon might prefer to stay with clock and compass, and with log, lead, and lookout.*

*From R. F. Duncans Sailing In The Fog*

### 4.1 Introduction

The previous chapter introduced Rayleigh scattering which applies when the scattering sources (or aggregate of sources) are much smaller than the wavelength of the scattered light. This chapter will introduce the Rayleigh-Gans approximation which applies to larger scattering sources. It will be then shown how the absolute intensity and angular dependence of the scattered light intensity may be used to deduce the molecular weight and characteristic size of the scattering sources in the absence of interactions.

The subject of interactions will be addressed in a very superficial way by invoking a virial expansion of the apparent molecular weight obtained from light scattering. The relationship between the theory of dynamic light scattering, particle diffusion, and particle characteristic sizes will be described.

Elements of the theories presented in this chapter will be illustrated with light scattering measurements made on three model systems: the protein, bovine serum albumin in saline buffer; polystyrene spheres suspended in water; and linear polystyrene molecules suspended in toluene.

## 4.2 The Rayleigh-Gans Approximation

In our discussion in Chapter 3, we assumed that the scattering sources may be viewed as induced dipoles, with spatial positions independent from one another. When the characteristic size,  $a$ , of the scattering particles is no longer small enough to satisfy the limiting condition  $a \ll \lambda_0$  then the dipole approximation is no longer valid: the equation for Rayleigh scattering Eq. (3-10) begins to fail to account for the observed scattered intensities at scattering angles different from zero due to intra-particle interference. To calculate the scattering from a large particle, we may subdivide the particle into small enough regions so that dipole scattering formalism is valid, and then consider the interference of each of the electric fields scattered from each of the small regions onto the active area of the detector. To see how this intra-particle interference comes about, con-

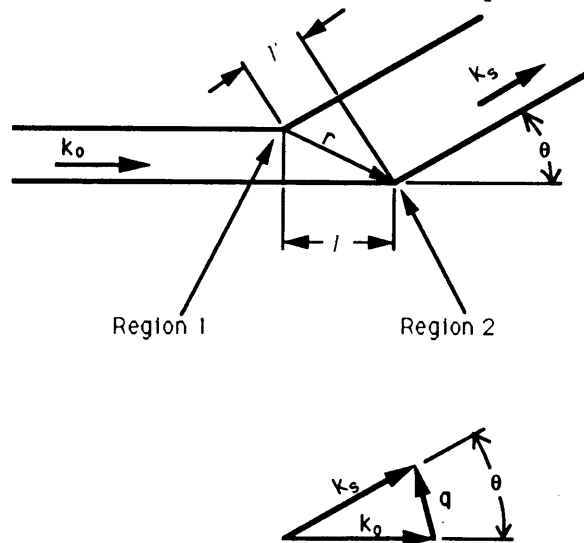


**Figure 4-1:** Intra-particle interference of scattered light.

Incident wave enters picture from left and scatters from region 1 first. The scattered waves from region 1 and region 2 mix together at the detector which is at an angle  $\theta$  away from the propagation direction of the wavefront.

Consider Fig. 4-1 which shows scattering from two different regions from within the same particle. A wave front in the incident plane wave, first strikes region 1 which scatters

some of the incident photons in all directions; and then, a short time later, the wave front arrives at region 2 and scatters more photons out of the incident beam. Photons scattered from region 1 and region 2 will have some destructive interference at the detector photo-active surface (far distant, at scattering angle  $\theta$ ) because the path optical path lengths the photons travel differ by the distance  $l' - l$ , see Fig. 4-1. If we place the origin of our coordinate system at region 1, then the phase shift of the photons scattered from region 2 with respect to region 1 is given by

$$\text{phaseshift} = (2\pi/\lambda_o) (l' - l) = \mathbf{r} \cdot \mathbf{k}_s - \mathbf{r} \cdot \mathbf{k}_o \quad (4-1)$$

where  $\mathbf{k}_o$  is the incident wave vector,  $\mathbf{k}_s$  is the scattered wave vector, and  $\mathbf{r}$  is the spatial vector directed from region 1 to region 2. Accordingly we define the wave vector  $\mathbf{q}(\theta)$

$$\mathbf{q}(\theta) = \mathbf{k}_s - \mathbf{k}_o \quad (4-2)$$

with

$$|\mathbf{q}(\theta)| = (4\pi n/\lambda_o) \sin(\theta/2) \quad (4-3)$$

where  $\theta$  is the angle between direction of light propagation (the y axis in Fig. 4-2) and the point of observation at **P**. So, we can write Eq. (4-1) as

$$\text{phaseshift} = \mathbf{q} \cdot \mathbf{r}. \quad (4-4)$$

Returning to the situation where the incident electric field is polarized in the same direction as the z axis, we can then use Eq. (4-4) to write the scattered electric field  $\Delta E_l$  at the detector originating from effective dipole in the volume element  $\Delta v$  of region  $l$  as [1, p. 602]

$$\Delta E_l(\mathbf{q}(\theta), \theta'') = -\frac{p_o \omega^2}{4\pi \epsilon_o D} \exp(j\omega t - j\mathbf{q} \cdot \mathbf{r}_l - j|q|D) W \sin(\theta'') \Delta v \quad (4-5)$$

where, in this case  $p_o = \alpha_v E_o$  and  $\alpha_v$  is the polarizability per unit particle volume:  $\alpha_v = \alpha/v$  where  $\alpha$  would be the polarizability of a whole single particle, and  $v$  is the volume of the particle.  $D$  is the distance from the origin to the detector, and  $\mathbf{r}_l$  is the vector directed from the origin to region  $l$  in the particle.

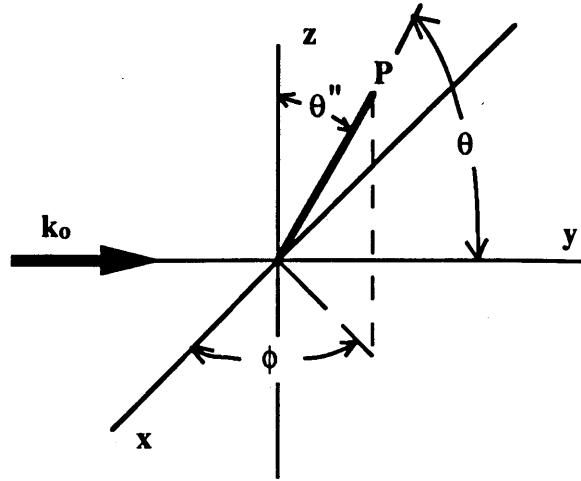


Figure 4-2: Scattering geometry.

The angle  $\theta$  is subtended between the direction of propagation of the incident electric field, and the direction from the origin to the point of observation at  $P$  at distance  $D$ .  $\theta''$  is the angle between the direction of the incident field polarization (parallel to the  $z$  axis) and  $P$ .  $\mathbf{k}_0$  is the incident field wave vector.

For scattering from a particle divided into  $N$  elements, the total electric field at the detector is then given by  $\sum_{l=1}^N \Delta E_l$ . The scattered intensity  $i(\mathbf{q}, \theta'')_p$  at the detector is then [1, p. 465]

$$i(\mathbf{q}, \theta'')_p = c_{light} \epsilon_o \langle (\sum E_l) (\sum E_n)^* \rangle_{time} \quad (4-6)$$

$$= c_{light} \epsilon_o \left[ \frac{P_o \omega^2}{4\pi \epsilon_o D} \right]^2 \sin^2(\theta'')^2 \Delta v^2 \frac{1}{t_c} \int_0^{t_c} \cos(\omega t)^2 dt \left[ \sum_l \exp(j\mathbf{r}_l \cdot \mathbf{q}) \sum_n \exp(j\mathbf{r}_n \cdot \mathbf{q}) \right]$$

where  $t_c$  is the time for one cycle of the incident wave. It follows that

$$i(\mathbf{q}, \theta'')_p = 1/2 c_{light} \epsilon_o \left[ \frac{P_o \omega^2}{4\pi \epsilon_o D} \right]^2 \sin^2(\theta'')^2 \Delta v^2 \left[ N + \sum_n \sum_{l \neq n} \exp(j\mathbf{q} \cdot (\mathbf{r}_l - \mathbf{r}_n)) \right]. \quad (4-7)$$

The number of terms in Eqs. (4-6) and (4-7) is  $N^2$  where  $N$  is the number of volume elements in the particle. Therefore, in the limit that  $\mathbf{q} = 0$ , i.e. zero scattering angle Eq.

(4-7) gives an intensity proportional to the particle volume squared, since  $\Delta v * N = v$ .

The product of summations in the given in brackets of Eq. (4-6) can be written as the product of integrals in the limit that  $\Delta v \rightarrow 0, N \rightarrow \infty$ , i.e.

$$i(\mathbf{q}(\theta), \theta)_p = I_o A \sin(\theta)^2 \int d^3r' \int d^3r \exp(j\mathbf{q} \cdot (\mathbf{r} - \mathbf{r}')) \quad (4-8)$$

which can also be written as

$$i(\mathbf{q}(\theta), \theta)_p = I_o A \sin(\theta)^2 \left[ \int d^3r \exp(j\mathbf{q} \cdot \mathbf{r}) \right]^2 \quad (4-9)$$

where  $A$  is identified as

$$A = \left[ \frac{\alpha_v \omega^2}{4\pi\epsilon_o D} \right]^2 \quad (4-10)$$

and we used the relations,  $I_o = 1/2 c_{light} \epsilon_o E_o^2$ , and  $p_o = \alpha_v E_o$ . If the incident light is unpolarized, then the time averaged scattered intensity from one particle  $i(\theta)_u$  is given by

$$i(\mathbf{q}(\theta))_u = I_o A (1/2)(1 + \cos(\theta)^2) \left[ \int d^3r \exp(j\mathbf{q} \cdot \mathbf{r}) \right]^2 \quad (4-11)$$

from the argument that led to Eq. (3-20).

Eqs. (4-9) and (4-11) are the Rayleigh-Gans approximation for polarized and unpolarized incident light, respectively. These equations are accurate providing the phase shifting factor  $\mathbf{q} \cdot \mathbf{r}$  is small. One reason why we can see that Eq. (4-9) is an approximation is that we have implicitly assumed that each volume element is illuminated *only* by the same incident plane wave which must be false since the other elements emit scattered waves; *i. e.* we have neglected effects of refraction, reflection, and diffraction on the wave incident on each particle, and we also assumed that the detector was far away from the particle. Mie solved the scattering problem exactly for spheres of arbitrary size and refractive index but his solution will not be discussed here. Eqs. (4-9) and (4-11) are adequate for dealing with small particles with moderate polarizabilities. The excellent book by Van de Hulst [2, Chap. 7] contains a more rigorous derivation of the Rayleigh-Gans approximation and its range of validity.

Using Eq. (3-7) and the discussion following it, we can calculate the total scattering cross section  $C_{scat}$  using  $i(\mathbf{q})_u$ :



$$C_{scat} = \int \frac{i(\mathbf{q})_u}{I_o} D^2 d\Omega. \quad (4-12)$$

In the case of Eq. (4-12), the total scattered power is determined by integrating over all scattering angles:  $\mathbf{q}$  is implicitly considered to be a function of the angular coordinates  $\theta$ , and  $\phi$  in Fig. 4-2. However, the scattering pattern is symmetrical around the  $y$  axis because the incident light is unpolarized; therefore, Eq. (4-12) reduces to a one dimensional integral on the variable, angle  $\theta$  which was defined in Fig. 4-2.

If we assume that the particles are spherical with radius  $a$ , then it is fairly easy to calculate  $i(\mathbf{q}(\theta))_u$  from Eq. (4-11). With the origin sited at the center of the spherical particle, and using  $\mathbf{q} \cdot \mathbf{r} = qr \cos(\psi)$ , where  $\psi$  is the angle between  $\mathbf{q}$  and  $\mathbf{r}$  within the particle we can write Eq. (4-11) as

$$\begin{aligned} i(\mathbf{q}(\theta))_u &= I_o A (1/2)(1 + \cos(\theta)^2) \left[ 2\pi \int_0^a dr \int_0^\pi d\psi r^2 \sin(\psi) \exp(jqrcos(\psi)) \right]^2 \\ i(\mathbf{q}(\theta))_u &= I_o A (1/2)(1 + \cos(\theta)^2) \left[ \frac{4\pi}{q^3} (\sin(qa) - qa\cos(qa)) \right]^2 \end{aligned} \quad (4-13)$$

Likewise, in the case of polarized incident light, Eq. (4-9) gives

$$i(\mathbf{q}(\theta), \theta)_p = I_o A \sin(\theta)^2 \left[ \frac{4\pi}{q^3} (\sin(qa) - qa\cos(qa)) \right]^2. \quad (4-14)$$

So, if we assumed a spherical particle shape, and unpolarized incident light to cause symmetry in the scattering pattern around the  $y$ -axis, we could insert the result of Eq. (4-13) into Eq. (4-12) and obtain a tractable, but somewhat tedious to solve, integral for  $C(a, \lambda_o)_{scat}$ , where  $C(a, \lambda_o)_{scat}$  is the total scattering cross section for a spherical particle of radius  $a$  for incident light wavelength  $\lambda_o$ .

The scattering formula derived above show that the  $C_{scat}$  is proportional to  $1/\lambda_o^4$  for a particle of characteristic dimension  $a$  where  $a \ll \lambda_o$ . If  $a \sim \lambda_o$ , the solution of Eq.

(4-12) (not solved here) shows [2, p. 91] that  $C_{\text{scat}}$  is proportional to  $1/\lambda_0^2$ . That is, in both cases shorter wavelengths suffer more attenuation due to scattering than longer wavelengths so the transmitted light is "reddened" with respect to the incident light. It is for this reason that the sun low on the horizon of our aerosol filled atmosphere appears orange, or red, and inspires prose like the example at the start of Chapter 3.

### 4.3 The radius of gyration

In the limit  $qa \ll 1$ , and with  $\theta'' = \pi/2$  (as in Fig. 3-5), Eq. (4-14) can be expanded as a Taylor series to give

$$i(q)_p = i(0)_p \left[ 1 - \frac{(qa)^2}{5} \right] \quad (4-15)$$

where  $I(0)_p$  is the scattered intensity in the limit that  $q \rightarrow 0$ , with  $q \equiv |q|$ . For an object of uniform density, the radius of gyration,  $R_g$ , is defined from

$$R_g^2 = \frac{\int r^2 d^3r}{\int d^3r}. \quad (4-16)$$

If Eq. (4-16) is solved for a sphere of radius  $a$ , then

$$R_g^2 = \frac{3}{5}a^2. \quad (4-17)$$

Eq. (4-17) inserted into Eq. (4-15) gives

$$i(q)_p = i(0)_p \left[ 1 - \frac{(q R_g)^2}{3} \right]. \quad (4-18)$$

Although Eq. (4-18) was shown to be true for a spherical particle of radius  $a$ , it is actually true for arbitrarily shaped particles subject to the limiting condition  $q R_g \ll 1$ . Thus, experimental measurement of the initial slope of  $i(q)_p$  versus  $q^2$ , provides direct information about the characteristic size of the particle,  $R_g$ , in the absence of particle interactions.

## 4.4 The molecular weight

### 4.4.1 Particles suspended in space

In the limit of  $q(\theta) \rightarrow 0$ , (forward scattering) Eqs. (4-9), (4-11), and (3-11) all give

$$i(0) = I_o \left[ \frac{\alpha \omega^2}{4\pi \epsilon_o D} \right]^2. \quad (4-19)$$

Following the approach suggested in Tanford [3, p. 278] we can use Eq. (3-14) and expand the index of refraction as a function of particle concentration,  $c$  (in total particle weight per total system volume), that is

$$n = 1 + \frac{dn}{dc} c \quad (4-20)$$

which will be valid when  $n \sim 1$ . The quantity  $\frac{dn}{dc}$  is known as "the refractive index increment", and is determined by experiment. Using Eq. (4-20) in (3-14) gives

$$\alpha = 2 \frac{\epsilon_o}{\rho_N} \frac{dn}{dc} c \quad (4-21)$$

which can be inserted into Eq. (4-19) to give

$$i(0) = I_o \frac{4\pi^2 c M}{\lambda_o^4 D^2 N_a \rho_N} \left[ \frac{dn}{dc} \right]^2 \quad (4-22)$$

where  $M$  is the molecular weight, and we used  $\rho_N = c \frac{N_a}{M}$ . If we use Eq. (3-9), we can write

$$\frac{Kc}{R(0)} = \frac{1}{M} \quad (4-23)$$

where  $R(0) \equiv \lim_{q \rightarrow 0} R(q)$ ,  $I(0) \equiv \lim_{q \rightarrow 0} I(q)$ , and

$$K = \frac{4\pi^2}{\lambda_o^4 N_a} \left[ \frac{dn}{dc} \right]^2 \quad (4-24)$$

If the scattering angle  $\theta$  is different from zero, Eq. (4-23) is modified to

$$\frac{Kc}{R(\theta)} = \frac{1}{M P(\theta)} \quad (4-25)$$

where  $P(\theta)$  is the form factor which describes the angular dependence of the scattered light and is normalized such that  $\lim_{\theta \rightarrow 0} P(\theta) = 1$ . For example Eq. (4-18) gives

$$P(\theta) = \frac{i(q)_p}{i(0)_p} = \left[1 - \frac{(q R_g)^2}{3}\right]. \quad (4-26)$$

which can be inverted to give

$$\frac{1}{P(\theta)} = \left[1 + \frac{R_g^2}{3} q^2\right]. \quad (4-27)$$

#### 4.4.2 Particles suspended in a solvent medium

The intensity of light scattered from particles suspended in solvent medium will depend upon the excess polarizability,  $\alpha_{\text{excess}}$ , of a particle compared to the solvent it displaces; that is,

$$\alpha_{\text{excess}} = \alpha_2 - v_2(\alpha_1 \rho_{N1}^0) \quad (4-28)$$

where  $\alpha_2$  is the polarizability of a single particle,  $\alpha_1$  is the polarizability of a single solvent molecule,  $v_2$  is the volume of a single particle, and  $\rho_{N1}^0$  is the number density of solvent molecules in the limit  $c \rightarrow 0$ . The term  $v_2(\alpha_1 \rho_{N1}^0)$  is the total polarizability of the solvent displaced by the particle. Eq. (4-28) tells us that if the particle and the solvent had the same polarizability per unit volume, then we would not see any extra intensity in the scattered light above the level of scattered intensity from the pure solvent: that is, the particles would be "invisible" to light scattering.

Our chore is to express  $\alpha_{\text{excess}}$  in terms of  $\frac{dn}{dc}$ , and the index of refraction of the pure solvent,  $n_0$ . The first step is to express Eq. (3-12) in a form suitable for a two component system, suspended particles, and solvent. We can use the elementary book by Lorrain and Corson [1, p. 105, p. 115] to help us find a modified form of the Clausius - Mossotti equation,

$$\frac{n^2-1}{n^2+2} = \frac{\rho_{N1}\alpha_1 + \rho_{N2}\alpha_2}{3\epsilon_o} \quad (4-29)$$

where  $n$  is the index of refraction of the suspension (particles + solvent)  $\rho_{N1}$  is the number density of solvent molecules, and  $\rho_{N2}$  is the number density of suspended particles.

From Eq. (4-29) we can write

$$\frac{\rho_{N2}\alpha_2}{3\epsilon_o} = \frac{n^2-n_o^2}{n_o^2+2} \quad (4-30)$$

which is valid providing  $n \sim n_o$ , and  $1 \gg v_2\rho_{N2}$ . (The conditions  $n \sim n_o$ , and  $1 \gg v_2\rho_{N2}$  are equivalent to saying that the suspension is dilute.) We can express  $n$  as function of concentration  $c$  in the dilute limit giving

$$n = n_o + \frac{dn}{dc}c. \quad (4-31)$$

Inserting Eq. (4-31) into Eq. (4-30) gives

$$\alpha_2 = 2 \frac{n_o\epsilon_o}{\rho_{N2}} \frac{dn}{dc}c \quad (4-32)$$

if  $n_o \sim 1$ . If the particle polarizability per unit volume is much more than the solvent's it replaces, then Eq. (4-28) becomes  $\alpha_{\text{excess}} = \alpha_2$ . Using Eq. (4-32) in Eq. (4-19) gives the same result as Eq. (4-23), except that  $R(0)$  is the Rayleigh ratio in excess of what is observed using pure solvent (i.e., the light intensity in excess of the solvent background), and

$$K = \frac{4\pi^2 n_o^2}{\lambda_o^4 N_a} \left[ \frac{dn}{dc} \right]^2 \quad (4-33)$$

which is the same as Eq. (4-24), except for the extra  $n_o^2$  factor.

The above "derivation" is a bit unsatisfactory since Eq. (4-29) is an approximation and we had to assume  $n_o \sim 1$ . However, a more sophisticated approach [4, 3] treats the

polarizability,  $\alpha$ , as a statistically fluctuating quantity and gives the same result, but without the limitation  $n_o \sim 1$ .

#### 4.4.3 Particle interactions and the apparent molecular weight

Eq. (4-23) is only true in the limit  $c \rightarrow 0$ . At non-zero particle concentrations Eq.

(4-23) takes the form [4]

$$\frac{1}{M_{app}} = \frac{1}{M} + 2Bc + 3Cc^2 + \dots = \frac{1}{R_{gas}T} \left( \frac{\partial \pi}{\partial c} \right)_T \quad (4-34)$$

where  $\frac{Kc}{R(0)} \equiv \frac{1}{M_{app}}$ ,  $\pi$  is the osmotic pressure,  $\left( \frac{\partial \pi}{\partial c} \right)_T$  is the osmotic susceptibility,  $R_{gas}$  is the molar gas constant,  $T$  is the temperature in degrees Kelvin, and  $B$ ,  $C$ , etc., are known by the mysterious name of virial coefficients; their job is to account for particle interactions which become more significant as the solution becomes more concentrated. ( $M_{app}$  will be referred to as the apparent molecular weight.) In general, the coefficients  $B$ , etc, are unknown *a priori* and must be determined by measuring  $M_{app}$ , or  $\pi$ , as a function of concentration. If  $M$  is also unknown, then it can be determined by extrapolating  $R(0)$  to zero  $c$ . Such an extrapolation works fine for many systems of interest, such as protein water solutions, or polystyrene toluene solutions: in such solutions the molecular weight of the suspended substance is not itself a function of concentration. If the suspension is polydisperse (meaning more than one particle size is present), then  $M$  in Eqs. (4-34) and (4-23) turns out to be a weight averaged molecular weight,  $M_w$  [3, p. 290].

The fluctuation theory approach which led to Eq. (4-34), can also be used to present an interpretation of  $P(\theta)$  [5, 6, p. 104]:

$$\frac{1}{P(\theta)} = [1 + \xi_s^2 q^2]. \quad (4-35)$$

where  $\xi_s$  is a measure of the length scale over which concentration fluctuations are corre-

lated.  $\xi_s$  is known as the static correlation range. Then, in the limit of infinite dilution (no inter-particle interactions), we can make the identification from Eq. (4-27) that,

$$\xi_s^2 = \frac{R_g^2}{3}. \quad (4-36)$$

## 4.5 Dynamic light scattering

Many excellent reviews of dynamic light scattering exist [7, 8, 9, 10, 11]. This section will present the salient results from the theory. The intensity of scattered light into angle  $\theta$  fluctuates as the scattering sources diffuse through the scattering volume, because the optical path lengths from each of the sources to the detector active surface varies with time. Modern instrumentation allows direct measurement of the time autocorrelation function  $g^2(q, \tau)$  of the intensity scattered into angle  $\theta$ .  $g^2(q, \tau)$  is defined by

$$g^2(q(\theta), \tau) = \lim_{N \rightarrow \infty} \frac{1}{N} \sum_{i=1}^N I(q, t_i) I(q, t_i + \tau) \quad (4-37)$$

where  $I(q, t_i)$  represents a discrete sample of the scattered intensity at time  $t_i$ . In a monodisperse, non-interacting system of particles

$$g^2(q(\theta), \tau) = A + B \exp(-2\Gamma\tau) \quad (4-38)$$

where

$$\Gamma = q^2 D_s, \quad (4-39)$$

$D_s$  is the self diffusion coefficient, and  $A$  and  $B$  are fitting coefficients determined by instrument response and signal to noise ratio.  $A$  is usually referred to as the "baseline" of the correlation function. If the sample is polydisperse then [11, p.49 and references therein]

$$g^2(q(\theta), \tau) = A + [B \sum_i \exp(-D_i q^2 \tau) P(\theta)_i \rho_i M_i^2]^2 \quad (4-40)$$

where the interesting quantity is  $\rho_i$  which is the number density of particles with dif-

fusion coefficient  $D_i$ , form factor  $P(\theta)_i$ , and molecular weight  $M_i$ . The product under the summation in Eq. (4-40),  $P(\theta)_i \rho_i M_i^2$ , is there to apply the appropriate intensity weighting implied by Eq. (4-25). Many schemes [12, 13, 14] have been devised for inverting Eq. (4-40) to determine  $\rho_i$ , but the most simple one is the cumulants method [15] which assumes that distribution is monomodal.

To see what Eq. (4-40) means we can rearrange it a little bit, and expand the exponential term in the summation as a function of  $\tau$  giving

$$g^1(\tau) \equiv \sqrt{g^2(q(\theta), \tau) - A} = B \sum_i [1 - \Gamma_i \tau + \Gamma_i^2 \frac{\tau^2}{2!} - \dots] P(\theta)_i \rho_i M_i^2 \quad (4-41)$$

where we used  $\Gamma_i = D_i q^2$ . From Eq. (4-41) we can see that if we take  $\tau = 0$ , then we can identify the coefficient  $B$  as

$$B = \frac{\sqrt{g^2(q^2(\theta), 0) - A}}{\sum_i P(\theta)_i \rho_i M_i^2} \quad (4-42)$$

In other words, Eq. (4-41) gives

$$g^1(\tau) = \sqrt{g^2(q(\theta), 0) - A} [1 - \langle D \rangle q^2 \tau + \langle D^2 \rangle q^4 \frac{\tau^2}{2!} - \dots] \quad (4-43)$$

where the brackets,  $\langle \rangle$ , symbolize the averaging operations implied in Eq. (4-41). That is,

$$\langle D \rangle = \frac{\sum_i D_i P(\theta)_i \rho_i M_i^2}{\sum_i P(\theta)_i \rho_i M_i^2} \quad (4-44)$$

From Eq. (4-43) we can see explicitly that  $\langle D \rangle q^2$  is proportional to the initial slope of the decaying function  $g^1(\tau)$ . Furthermore, if we extrapolate  $\langle D \rangle$  to the limit  $\theta \rightarrow 0$ , then  $P(\theta) \equiv 1$ , and  $\langle D \rangle$  becomes a  $z$  averaged quantity where a  $z$  averaged function,  $\langle F \rangle_z$ , is formally defined as



$$\langle F \rangle_z = \frac{\sum_i F_i \rho_i M_i^2}{\sum_i \rho_i M_i^2} \quad (4-45)$$

If the diffusion coefficient extracted from Eq. (4-38) was from a system of monodisperse, non-interacting spheres, then we could use the the Stokes-Einstein equation to relate the radius of one of the spheres,  $r_{\text{sphere}}$ , to the diffusion coefficient,  $D$ :

$$r_{\text{sphere}} = \frac{k_B T}{6\pi\eta D} \quad (4-46)$$

where  $k_B$  is Boltzman's constant,  $T$  is temperature in degrees Kelvin, and  $\eta$  is the viscosity of the solvent medium.

If the monodisperse system was of arbitrarily shaped particles then it is customary to define a quantity called the hydrodynamic radius,  $R_h$ , which is the same value as the radius of a sphere having the same observed diffusion coefficient. If the system was made from polydisperse, arbitrarily shaped particles, then it is common practice to use  $\langle D \rangle$  extracted from Eq. (4-43) to define a characteristic particle size  $R_h$  for the whole system by inserting  $\langle D \rangle$  into Eq. (4-46). That is,

$$R_h \equiv \frac{k_B T}{6\pi\eta \langle D \rangle}. \quad (4-47)$$

To examine just what kind of average  $R_h$  is, in this case, let us consider the limit  $\theta \rightarrow 0$ , so that  $\langle D \rangle \rightarrow \langle D \rangle_z$ . For a single particle size,  $r_i$ , we have from inverting Eq. (4-46)

$$D_i = \frac{k_B T}{6\pi\eta r_i} \quad (4-48)$$

where  $r_i$  is the hydrodynamic radius of a particle having diffusion coefficient  $D_i$ . Therefore, the z-average of  $D_i$  is (see Eq. (4-45))

$$\langle D_i \rangle_z = \left\langle \frac{k_B T}{6\pi\eta r_i} \right\rangle_z = \frac{k_B T}{6\pi\eta} \left\langle \frac{1}{r_i} \right\rangle_z \quad (4-49)$$

Comparing Eq. (4-49) to Eq. (4-47), we can make the identification

$$R_h \equiv \left\langle \frac{1}{r} \right\rangle_z \quad (4-50)$$

where we dropped the  $i$  subscript from the  $r$  in the implicit summation.

The above discussion of course assumed that inter-particle interactions could be neglected. In the most general situation, where particle interactions may be present, we adopt the previous convention of reference [16] and write,

$$\xi_h \equiv \frac{k_B T}{6\pi\eta D_o} \quad (4-51)$$

a where  $\xi_h$  is length scale over which hydrodynamic fluctuations are correlated, and  $D_o$  is the longwavelength diffusion coefficient; i.e.,  $D_o \equiv \lim_{q \rightarrow 0} \frac{\Gamma(q)}{q^2}$ . According to this definition,  $R_h = \xi_h$  in the limit of no inter-particle interactions.

## 4.6 The results of measurements from model systems

In this section, light scattering results from three model systems will be presented. The first result will be the determination by light scattering of the molecular weight of Bovine Serum Albumin (BSA) in aqueous solution. The second result will be a comparison of the radius of gyration and the hydrodynamic radius of latex spheres suspended in aqueous solution. The third result will be a brief study of the concentration dependence of the osmotic susceptibility, the static correlation range, and the hydrodynamic correlation range for a system of linear polystyrene suspended in toluene.

The measurements presented in this section are not intended to be definitive

measurements: rather, they are intended to show that we can use the light scattering instrumentation described in Chapter 2, and the theory described in the previous sections to find the location of certain landmarks in the fog. That is, we are verifying our instrumentation, and theoretical knowledge on known systems, just as the quotation at the beginning of this chapter suggests that the small boat navigator do with his electronic aids.

#### 4.6.1 Bovine serum albumin

Bovine serum albumin (Miles scientific, Pentex monomer standard, nominal molecular weight = 66,300 gm/mole) was dissolved in phosphate-buffered saline (0.15 M NaCl, 0.01 M  $\text{KH}_2\text{PO}_4/\text{K}_2\text{HPO}_4$ , 0.02% [wt/vol] sodium azide, pH 7.2) and prepared as noted previously [17]. The BSA solution was diluted to 5.3 mg/ml as determined by optical absorption at 280 nm with  $A_{280}^{0.1\%, 1\text{cm}} = 0.60$  ml-cm/mg, and  $\frac{dn}{dc} = 0.19$  ml/gm as determined previously [17].

The solution was sealed in a 32mm diameter cylindrical light scattering cell (NSG Precision Cells, Farmingdale, NY) and connected to special closed loop filtration system. The filtration system was made of two hypodermic needles, a length of silicone tubing, a peristaltic pump, and a hypodermic filter (Millex GV 0.22 $\mu\text{m}$ , Millipore, Bedford, MA). Solution was drawn into the filtration loop, and returned to the solution through the two hypodermic needles inserted through holes in the cover of the sealed light scattering cell. The solution was filtered continuously until it was observed to be free of dust by observation of light scattered from a helium neon laser beam at a small scattering angle with a  $\sim$  X10 microscope. This filtration took about 30 minutes. At the end of the light scattering experiment the protein concentration was rechecked by optical absorbance and found to be 4.3 mg/ml.

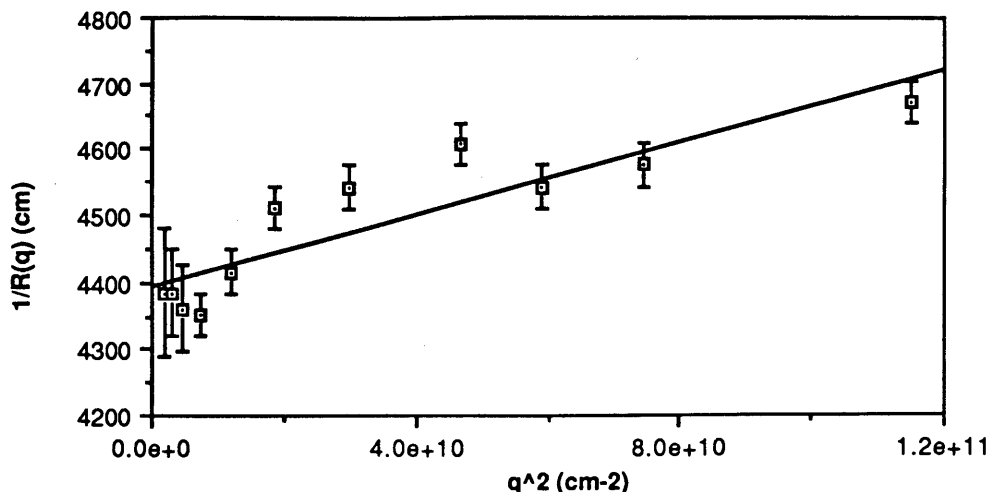


**Figure 4-3:** The reciprocal of the Rayleigh ratio vs.  $q^2$  for BSA.

The line through the data points was used in Eq. (4-27) to determine an apparent  $R_g$ . However, the magnitude of the apparent  $R_g$  may be due to particle interactions.

The intensity of light scattered from the solution was measured in accordance with procedures outlined in Sec. 3.5 and the results as a function of scattering angle are presented in Fig. 4-3. The data in Fig. 4-3 is displayed as  $\frac{1}{R(q)}$  versus  $q^2$ . The zero intercept of  $\frac{1}{R(q)}$  was used in Eqs. (4-23) and (4-33) to determine  $M_{app}$  which was found to be 70,700 gm/mole, 6% higher than the expected value of 66,300. The diffusion coefficient of the protein was measured with dynamic light scattering at several scattering angles and found to correspond to an  $R_h$  of 3.9 nm. Fig. 4-3 shows a slight anisotropy in the intensity of the scattered light. According to Eq. (4-27) this anisotropy would correspond to an  $R_g$  of  $(12 \pm 2)$  nm: however, since the protein is expected to be a prolate ellipsoid of axial ratio 3.4 [18],  $R_g$  would be expected to be near to  $R_h$  according to the appropriate equations from reference [19]. Therefore, the anisotropy observed in the intensity in Fig. 4-3 may be due to molecular interactions: however, measurements were not made at several solution concentrations to check out this possibility.

The apparent molecular weight of 70,700 gm/mole is fairly close to the expected value considering that our use of Eqs. (4-23) and (4-33) did not account for molecular interactions, and that the concentration,  $c$ , and refractive index increment,  $\frac{dn}{dc}$ , were determined to only two significant digits.

#### 4.6.2 Polystyrene latex spheres

Sulfated polystyrene latex spheres (nominal diameter = 30 nm, Cat no. 2-17-56, IDC, Portland, OR) were diluted to  $\sim 0.004\%$  by weight in an aqueous solution of 0.003 M NaCl. The solution was sealed in a 32 mm diameter cylindrical light scattering cell and filtered until it was observed to be free of dust in accordance with the procedure outlined above. Slightly saline solution was used to screen out interparticle interactions.

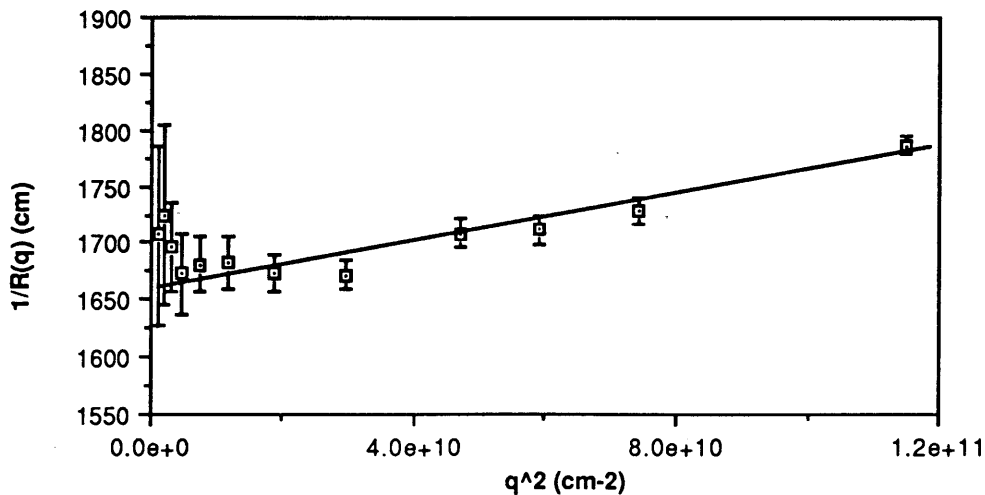


**Figure 4-4:** The reciprocal of the Rayleigh ratio vs.  $q^2$  for latex spheres. The line through the data points was used in Eq. (4-27) to determine  $R_g$ .

The diffusion coefficient was measured at several scattering angles by dynamic light scattering and found to correspond to  $R_h = 19.5$  nm. Fig. 4-4 shows results of static light scattering: fitting to Eq. (4-27) gave  $R_g = (14 \pm 2)$  nm. According to Eq. (4-17), this value of  $R_g$  would correspond to a particle diameter of  $R_{sphere} = (18 \pm 2)$  nm which agrees with the value expected from  $R_h$  to within experimental accuracy. Also, these measurements do indicate that the nominal diameter of 30 nm for this particular batch of latex spheres is incorrect.

### 4.6.3 Polystyrene dissolved in toluene

This section will be divided into three parts. The first part will discuss sample preparation procedures for the polystyrene-toluene solutions. The second part will present the results of static and dynamic light scattering measurements. The third part will compare the results presented here to earlier published findings.

#### 4.6.3.1 Sample preparation

Broad molecular weight polystyrene pellets (Type 706, National Bureau of Standards, Washington, D. C.; nominal molecular weight:  $M_w = 257,800$ ;  $M_z:M_w:M_n = 2.9:2.1:1$ ) were dissolved in toluene (Spectroscopic grade, Aldrich, Milwaukee, WI) to make up a stock solution of 0.0468 gm/ml. To make sure of homogeneity, the solution was stirred aggressively with a teflon coated stirring bar, and checked visually to be free of index of refraction gradients. A sample of the stock solution was taken and sealed under flame in a 2 ml ampul (Kimble 12012-L, diameter = 12 mm). The air space in the ampul was purged with dry, filtered Nitrogen, and temporarily sealed with teflon tape before flame sealing to prevent the Toluene vapor from flashing. By dilution of the

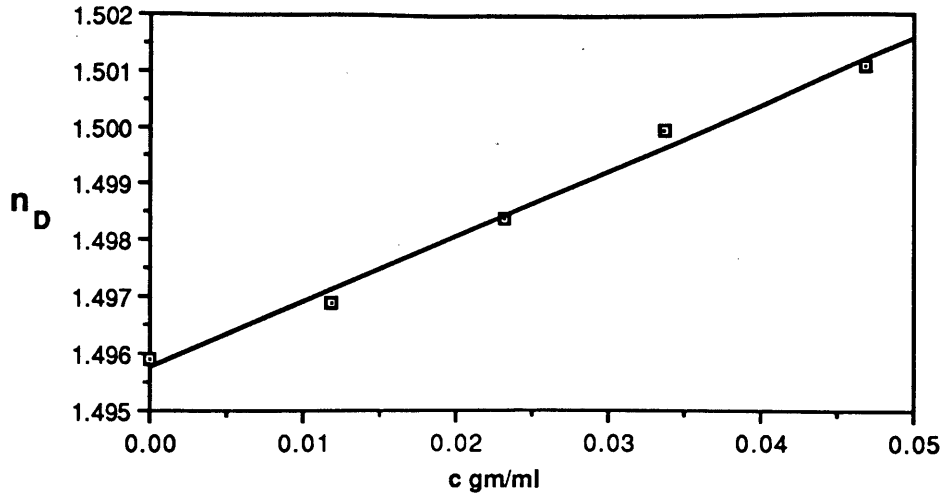
remaining stock solution, a total of seven samples were prepared, and packaged in 2 ml ampuls by the above procedure. The most dilute sample was 0.00183 gm/ml. During the above packaging process, some of solution was put aside and sealed for index of refraction measurements to be performed later. All quantities were measured by weight, and the density of toluene was used to determine solvent volume. Before light scattering experiments, dust was eliminated from the samples by centrifugation for 15 to 30 minutes at  $\sim 100 X g$ , where  $g$  is the acceleration of gravity. (Special centrifuge rotor inserts were fabricated to accommodate the flat bottomed ampuls which were used as light scattering cells.)

Fig. 4-5 shows the result of index of refraction measurements at several concentrations. The horizontal axis is the concentration of the polystyrene solution. These measurements were performed on an Abbe type refractometer (Bausch and Lomb, model Abbe-3L). The refractive index increment was determined from best fit of a straight line to this data:  $\frac{dn}{dc} = 0.117 \text{ ml/gm}$ .

#### 4.6.3.2 Light scattering results

Fig. 4-6 show the results of a static light scattering measurement on the most dilute sample, at 0.00183 gm/ml. According to this data, and using Eq. (4-35),  $\xi_s = (9.3 \pm 2)$  nm.  $R(0)$  was determined from the zero intercept of the straight line drawn through the points in Fig. 4-6. After subtracting the background intensity due to solvent scattering,  $R(0)$  was used in Eq. (4-23) to obtain the apparent molecular weight:  $M_{app} = 138,000 \pm 3,000$ .

Dynamic light scattering data was collected at twelve scattering angles. Fig. 4-7



**Figure 4-5:** The index of refraction of dissolved polystyrene versus concentration.

The vertical axis, label  $n_D$  represents the index of refraction of the sample with respect to the sodium D line, 589.3 nm. The horizontal axis represents the weight of dissolved polystyrene with respect to total sample volume.

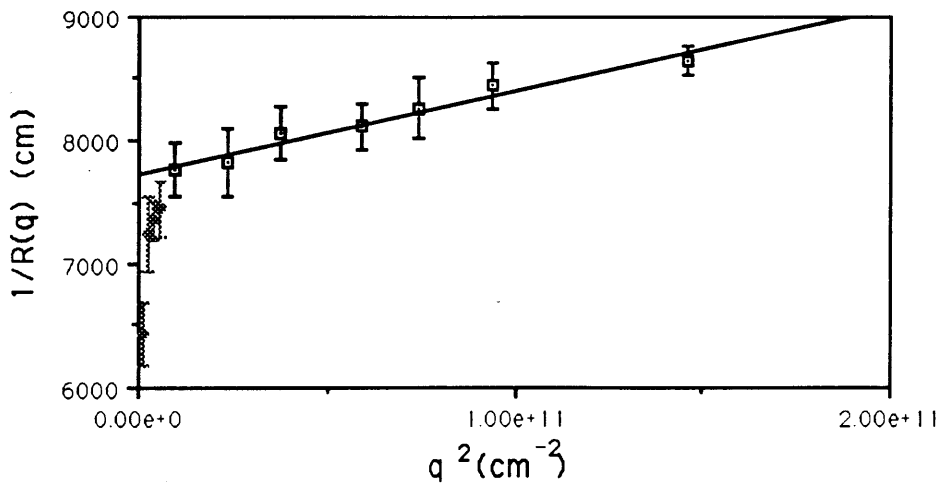


**Figure 4-6:** The inverse Rayleigh ratio vs.  $q^2$  of dissolved polystyrene.

The concentration of the polystyrene is  $c = 0.00183$  gm/ml, the most dilute sample studied. The straight line through the points represents a best fit. The four points shown as hatched over at the lowest concentrations were not used in the fit, since it was suspected that stray light from the 12 mm scattering cell contributed to excess intensity at the smallest scattering angles.

show the time auto-correlation function,  $g^2(\tau)$ , of the scattered intensity collected at one



scattering angle,  $\theta = 23^\circ$ . This somewhat noisy data was fit by the cumulants expansion method [15] to find the rate of the initial decay,  $\Gamma(q)$ . A one order cumulants expansion, equivalent to the single exponential form

$$g^2(\tau) = A + B \exp(-2\Gamma(q) \tau), \quad (4-52)$$

was found to give a good fit to the data in Fig. 4-7. In fact, Eq. (4-52) gave an adequate fit to dynamic light scattering data from all angles, except for the smallest angle at  $11.5^\circ$  which required a third order cumulants expansion to find  $\Gamma(q)$ . Intensity auto-correlation functions from other, higher concentration samples were found to usually have a good fit to a second order cumulants expansion.

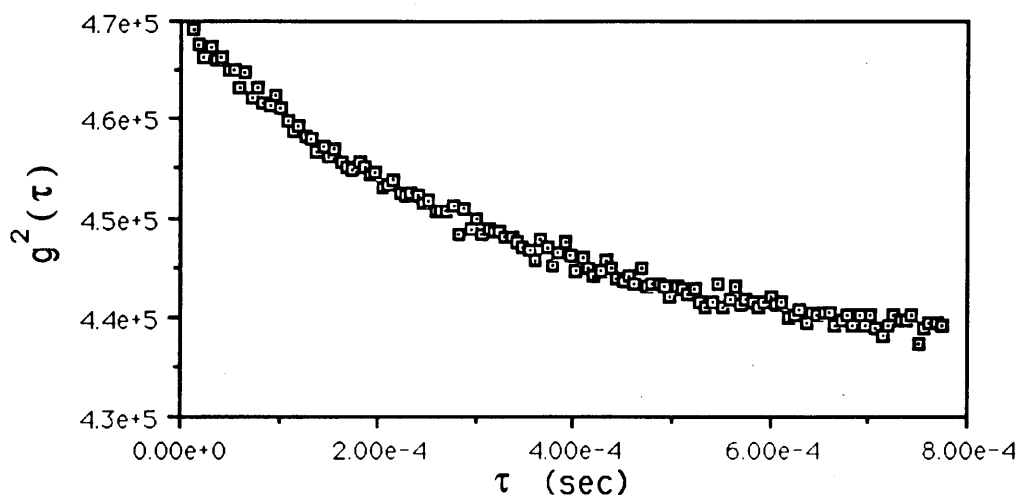


**Figure 4-7:** The time auto-correlation function of the intensity of light scattered from a polystyrene-toluene sample.

The concentration of the polystyrene is  $c = 0.00183$  gm/ml, the most dilute sample studied.  $g^2(\tau)$  is expressed in terms of correlator channel counts. The delay time  $\tau$  is expressed in seconds. The baseline of this correlation function was about  $4.35 \times 10^5$ .

Fig. 4-8 shows the angular dependent behavior of the function  $\frac{\Gamma}{q^2}$  vs.  $q$ . The quotient  $\frac{\Gamma}{q^2}$  is sometimes called the effective diffusion coefficient,  $D(q)_{eff}$ . If the dynamic light

scattering data was dominated by particle self diffusion, then  $D(q)_{eff}$  would be an average self diffusion coefficient weighted according to Eq. (4-44). To determine the hydrodynamic correlation range,  $\xi_h$ , we will use the zero intercept of the best fit straight line from Fig. 4-8, in Eq. (4-51).  $D_o$  from Fig. 4-8 was  $(2.33 \pm 0.07) \times 10^{-7}$  cm<sup>2</sup>/s, which gave a hydrodynamic correlation length of  $\xi_h = (14.2 \pm 0.5)$  nm. No significant angular dependence of  $D(q)_{eff}$  was found for any of the higher concentration samples.

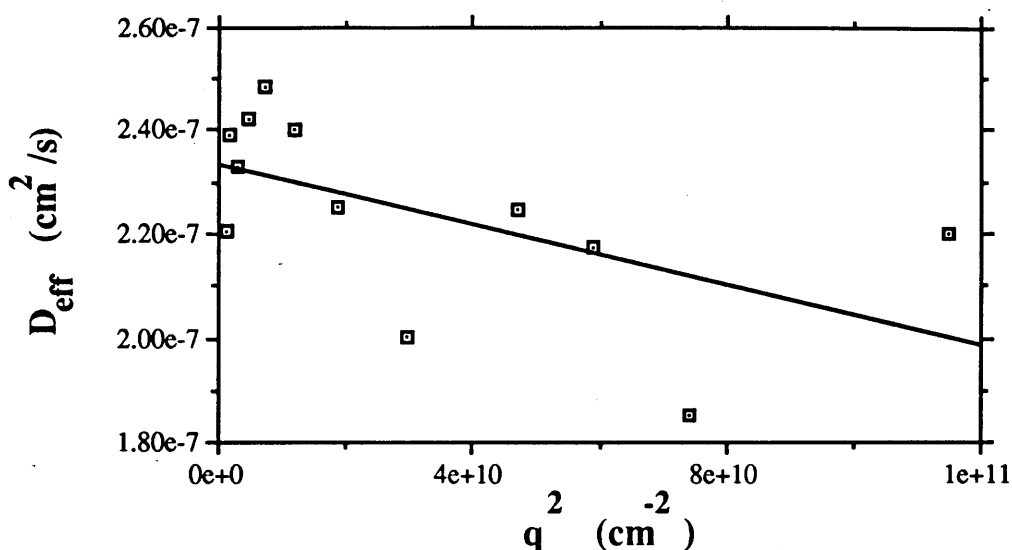
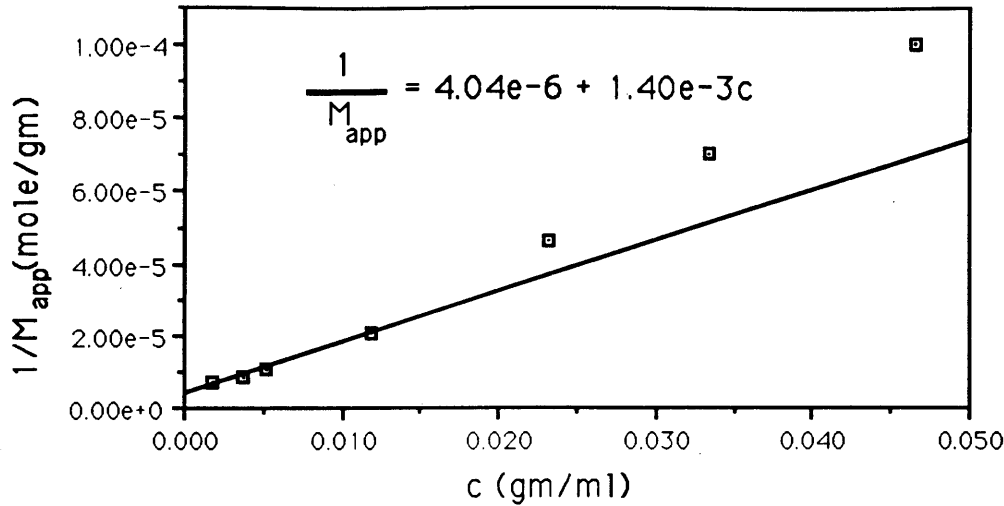


Figure 4-8: The effective diffusion coefficient,  $\frac{\Gamma}{q^2}$ , vs.  $q^2$  for a polystyrene-toluene sample.

The concentration of the polystyrene is  $c = 0.00183$  gm/ml, the most dilute sample studied. This data was fit to a straight line, and the zero intercept was used to determine the long wave length diffusion coefficient.

Identical light scattering experiments were performed on the other higher concentration samples in the dilution series. Fig. 4-9 shows the apparent molecular weight of all seven samples versus concentration. The four lowest concentration points in the figure were fit to a straight line to determine the weight averaged molecular weight,  $M_w$ , and the second virial coefficient by comparison with Eq. (4-34). According to the data in Fig.

4-9,  $M_w = 248,000 \pm 40,000$  gm/mole. This value of  $M_w$  is remarkably close the nominal value of 257,800 gm/mole when we consider the sparsity of data points at low concentration in Fig. 4-9



**Figure 4-9:** The apparent molecular weight,  $1/M_{app}$ , versus concentration for a polystyrene-toluene system.

A straight line is fit to the four lowest concentration points. If we identify the zero intercept and slope of the line with Eq. (4-34), then we find that data gives a weight average molecular weight of  $M_w = 248,000 \pm 40,000$  gm/mole, and a second virial coefficient of and  $B = (0.70 \pm 0.05) \times 10^{-3}$  mole-cm<sup>3</sup>/gm<sup>2</sup>.

Fig. 4-10 shows the static and dynamic correlation lengths for each of the samples plotted versus concentration. The static correlation lengths,  $\xi_s$  of the two highest concentrations are not shown because their values are too small to be detected by the instrument. If the lowest concentration values  $\xi_s$  can be assumed to represent single particle properties, and we use the fact that  $R_g = \sqrt{3} \xi_s$  (see Eq. (4-36)), then it follows from the data in Fig. 4-10 that  $R_g \sim 16$  nm.

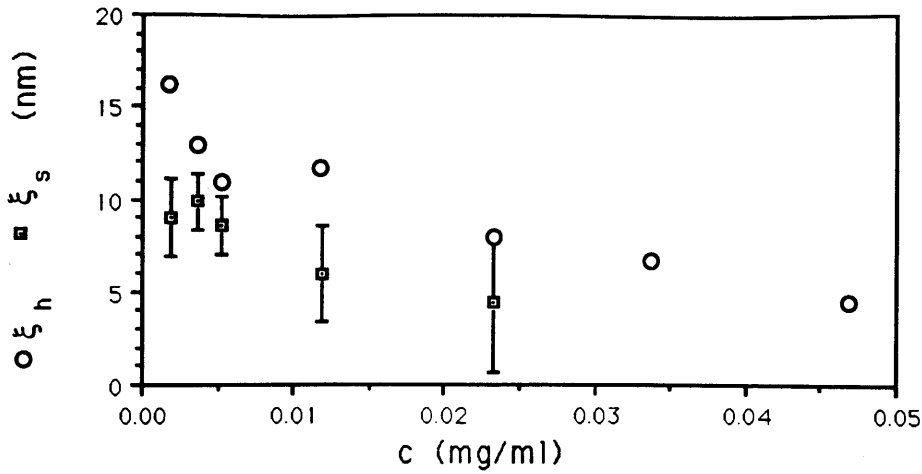


**Figure 4-10:** The static correlation length,  $\xi_s$ , and the dynamic correlation length,  $\xi_h$ , versus concentration for the polystyrene-toluene sample.

#### 4.6.3.3 Discussion of Results

One could visualize a single linear polystyrene polymer chain in solution as the trajectory of a random walk in 3-space. The distance along the trajectory is called the contour length, and we will refer to the trajectory itself as a random coil. When the solution is in the dilute end of its concentration range, the polymer random coils can translate freely, and only occasionally encounter each other. Flory [20, Chap. 12, 21, p. 77] showed that in the dilute regime that the polymer random coils could be modeled as hard spheres of radius  $r_f$ . As the concentration is increased, eventually the coils start to overlap, and interpenetrate. The concentration,  $c^*$ , near which this overlap behavior might be expected to occur is

$$c^* \approx \frac{M_w}{N_a (2r_f)^3} \quad (4-53)$$

where  $N_a$  is Avogadro's number.  $c^*$  would be the concentration of spheres of radius,  $r_f$ ,

close packed into a simple cubic lattice. Although we have no value for the Flory effective hard sphere radius,  $r_f$ , we might be able to estimate it from the magnitude of the second virial coefficient  $B$  if we assume that excluded volume interactions are the primary mode of particle interaction at low concentrations. In that case  $B$  is given by [3, p. 195] as

$$B = \frac{N_a u}{2 M^2} \quad (4-54)$$

where  $u$  is the excluded volume. For a spherical particle of radius  $r_f$  [3, p. 196],

$$u = (32/3)\pi r_f^3, \quad (4-55)$$

or eight times the volume of a hard sphere of radius  $r_f$ . If we obtain the magnitude of  $B$  from Fig. 4-9, and use a nominal molecular weight for the polymer as 250,000 gm/mole, then it follows that  $u = 0.15 \times 10^{-15} \text{ cm}^3$  from Eq. (4-54). If we use this result for  $u$  in Eq. (4-55) then we obtain the result  $r_f = 17 \text{ nm}$  which is very similar to the value of 16 nm we obtained for  $R_g$  in the previous section by using the angular dependence of the scattered light intensity. We can now estimate the overlap concentration from Eq. (4-53) as  $c^* \sim 0.012 \text{ gm/ml}$ .

Supporting the above estimate of the magnitude of  $c^*$  we note that qualitative examination of the data in Fig. 4-9 does show a distinct change in the way  $\frac{1}{M_{app}}$  varies with concentration between  $c = 0.010 \text{ gm/ml}$  and  $c = 0.020 \text{ gm/ml}$ . This change in behavior may indicate a cross over from dilute to semi-dilute behavior.

If the system does cross over to semi-dilute behavior above 0.010 to 0.020 gm/ml, then according to previous theoretical predictions, and experimental observations [22], we can expect that

$$\left(\frac{\partial\pi}{\partial c}\right)_T \sim c^{5/4} \quad (4-56)$$

where we are using the  $\sim$  sign to mean the thing on the left side of Eq. (4-56) varies like the thing on the right side. This expected behavior motivated the drawing of Fig. 4-11 which is the same data as presented in Fig. 4-9, except that it is drawn on a log-log plot and the vertical axis is re-labeled in terms of  $\left(\frac{\partial\pi}{\partial c}\right)_T$  (using the identity  $\frac{1}{R_{\text{gas}}T} \left(\frac{\partial\pi}{\partial c}\right)_T = 1/M_{\text{app}}$ , see Eq. (4-34)). Indeed,  $\left(\frac{\partial\pi}{\partial c}\right)_T$  for the four higher concentration points in Fig. 4-11 (which only span half a decade) do seem to obey a power law similar to Eq. (4-56).

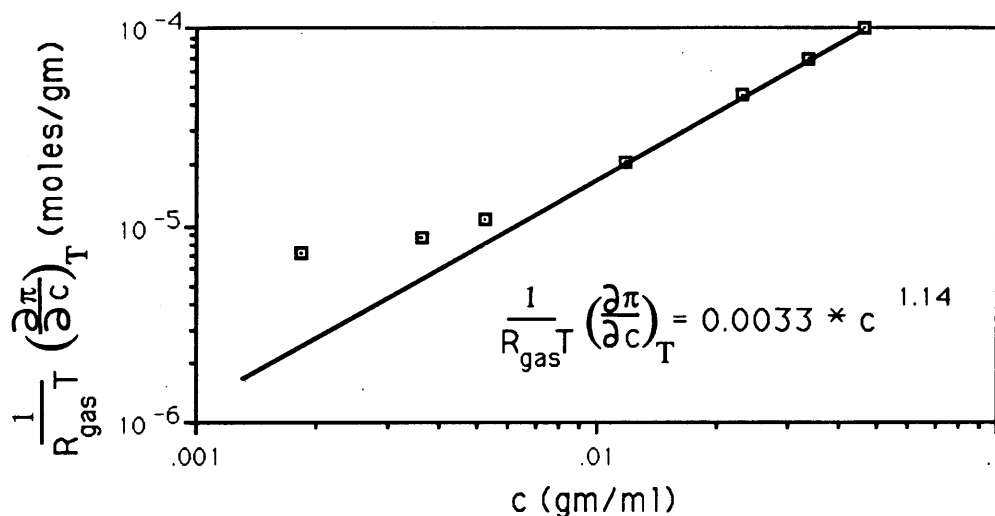


**Figure 4-11:** The osmotic susceptibility versus concentration for the polystyrene-toluene sample.

We see from this plot the higher concentration points, seem to obey a concentration dependent power law with an exponent similar what has been predicted and observed previously in polymer systems in the semi-dilute regime [22].

It was earlier reported by Wiltzius, *et al.*, reference [16], that the ratio  $\frac{\xi_h}{\xi_s}$  had a theoretically unexpected concentration dependence. The limited results presented here support the earlier finding. In Fig. 4-12 the data from Fig. 4-10 is plotted as  $\frac{\xi_h}{\xi_s}$  versus

concentration on top of data for a similar molecular weight sample from the earlier report [16, Fig. 2].

A related finding of Wiltzius, *et al*, pertained the concentration dependence of the hydrodynamic correlation length  $\xi_h$  in the semi-dilute regime. Whereas theoretical considerations led to the prediction that  $\xi_h \sim c^{-0.77}$ , they found [16, Fig. 1] experimentally that,

$$\xi_h \sim c^{-0.67} \tag{4-57}$$

Again, the limited data presented here, supports the previous finding, see Fig. 4-13.

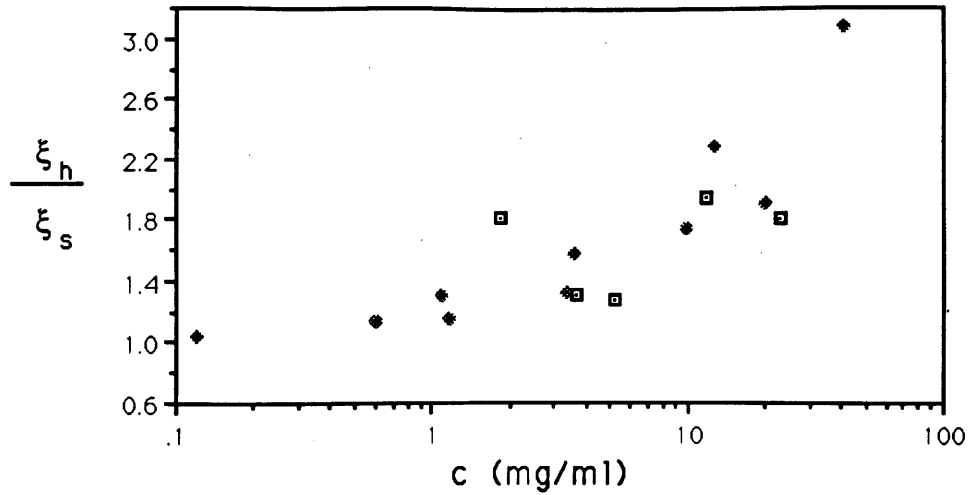


**Figure 4-12:** The ratio of  $\xi_h$  to  $\xi_s$  versus concentration for the polystyrene-toluene sample.

Data from Fig. 4-10 was used to form the ratio  $\frac{\xi_h}{\xi_s}$  and plotted (square data points) versus concentration. For comparison with earlier findings in a similar system, data from reference [16] is also plotted as hatched data points. The data displayed in Fig. 4-10 from reference [16] was taken for polystyrene,  $M_w = 300,000$ , in the good solvent toluene, and also in the marginal solvent methyl ethyl ketone.



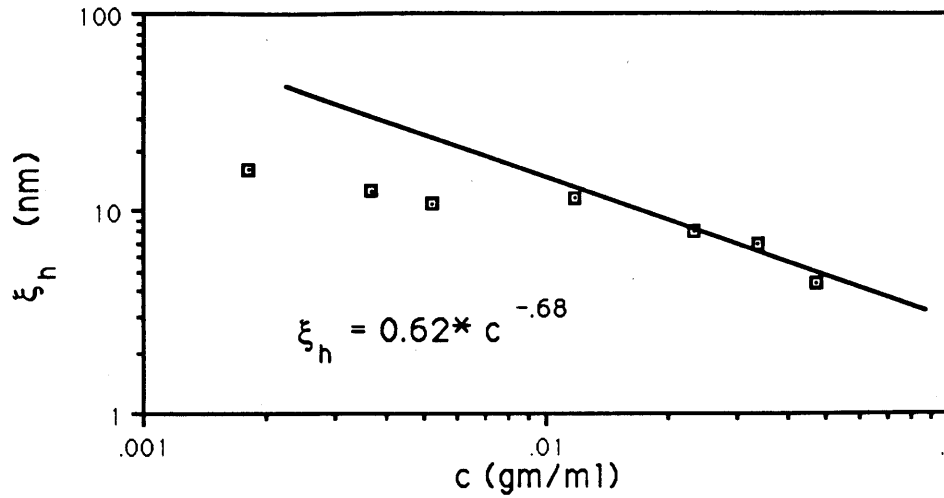


**Figure 4-13:** The concentration dependent scaling behavior of the dynamic correlation length in the putative semi-dilute regime for the polystyrene-toluene system.

This limited data for  $\xi_h$  supports the earlier findings of Wiltzius, *et al.* (reference [16]), that  $\xi_h \sim c^{-0.67}$  in the semi-dilute concentration range.

## References for Chapter 4

- [1] Lorrain, and Corson.  
*Electromagnetic Fields and Waves.*  
W.H. Freeman & Co., San Francisco, 1970.
- [2] H. C. van de Hulst.  
*Light Scattering by Small Particles.*  
Dover Publications, Inc., New York, 1981.
- [3] C. Tanford.  
*The Physical Chemistry of Macromolecules.*  
John Wiley and Sons, Inc., 1961.
- [4] P. Debye.  
*J. Phys. and Colloid Chem.* **51**:18, 1947.
- [5] L. Ornstein, F. Zernike.  
*Proc. Acad. Sci. Amsterdam* **17**:793, 1914.
- [6] H. E. Stanley.  
*Introduction to Phase Transitions and Critical Phenomena.*  
Oxford, New York, 1971.
- [7] S. B. Dubin, J. H. Lunacek, G. B. Benedek, G.B.  
Observation of the Spectrum of Light Scattered by Solutions of Biological Macromolecules.  
*Proc. Nat. Acad. Sci.* **57**(5):1164-1171, 1967.
- [8] G. B. Benedek.  
Optical Mixing Spectroscopy, with Applications to Problems in Physics, Chemistry, Biology and Engineering.  
*Polarization, Matter, and Radiation.*  
Presses Universitaire de France, 1969, pages 49 - 84.
- [9] N. A. Clark, J. H. Lunacek, and G. B. Benedek.  
A Study of Brownian Motion Using Laser Light Scattering.  
*Am. J. of Phys.* **38**(5):575-585, 1970.
- [10] H. Z. Cummins and E. R. Pike, eds.  
*Photon Correlation Spectroscopy and Velocimetry.*  
Plenum, New York, 1976.
- [11] R. Pecora.  
*Applications of Photon Correlation Spectroscopy.*  
Plenum Press, 1985.
- [12] N. Ostrowsky, D. Sornette, P. Parker, and E.R. Pike.  
Exponential Sampling Method for Light Scattering Polydispersity Analysis.  
*Optica Acta* **28**:1059, 1981.

- [13] S.W. Provencher.  
CONTIN: A General Purpose Constrained Regularization Program For Inverting Noisy Linear Algebraic and Integral Equations.  
*Computer Physics Communications* 27:229 - 242, 1982.
- [14] A. K. Livesey, P. Licinio, and M. Delaye.  
Maximum entropy analysis of quasielastic light scattering from colloidal dispersions.  
*J. Chem. Phys.* 84(9):5102-5107, 1985.
- [15] D. E. Koppel.  
Analysis of Macromolecular Polydispersity in Intensity Correlation Spectroscopy: The Method of Cumulants.  
*The Journal of Chemical Physics* 57(11):4814 - 4820, 1972.
- [16] P. Wiltzius, H. R. Haller, D. S. Cannell, and D. W. Schaefer.  
Dynamics of Long-Wavelength Concentration Fluctuations in Solutions of Linear Polymers.  
*Phys. Rev. Let.* 53(8):834 - 837, 1984.
- [17] Murpy R.M., Slayter, H., Schurtenberger, P., Chamberlin, R.A., Colton, C.K., Yarmush, M.L.  
Size and Structure of Antigen-Antibody Complexes.  
*Biophys. J.* 54():45-56, 1988.
- [18] D. G. Neal, D. Purich, and D. S. Cannell.  
Osmotic susceptibility and diffusion coefficient of charged bovine serum albumin.  
*Med. Phys.* (), 1984.
- [19] C. Y. Young, P. J. Missel, N. A. Mazer, G. B. Benedek, M. C. Carey.  
Deduction of Micellar Shape from Angular Dissymmetry Measurements of Light Scattered from Aqueous Sodium Dodecyl Sulfate Solutions at High Sodium Chloride Concentrations.  
*J. Phys. Chem.* 82:1375-1378, 1978.
- [20] P. Flory.  
*Principles of Polymer Chemistry.*  
Cornell University Press, Ithaca, NY, 1971.
- [21] P. de Gennes.  
*Scaling Concepts in Polymer Physics.*  
Cornell University Press, Ithaca, NY, 1979.
- [22] M. Daoud, J. P. Cotton, B. Farnoux, G. Jannink, G. Sarma, H. Benoit, R. Duplessix, C. Picot.  
*Macromolecules* 8():804, 1975.

## 5. Light Scattered From Short Chain Lecithin-Water Solutions

*Scum always rises to the top.*

-Chris Chamberlin, *from a germane observation about interfacial phenomena.*

### 5.1 Introduction

This chapter will use all the tools of light scattering explained in the previous chapters to study the lecithin-water micellar system. The types of lecithins being studied here are short hydrocarbon tail lecithins, having double hydrocarbon tails of lengths 7, and 8 carbons long. Fig 5-1 shows the chemical structure of di-C8 lecithin: the head group of the molecule is zwitterionic. The di-C<sub>7</sub> lecithin studied here has exactly the same chemical structure, except for the length of its double hydrocarbon tail.

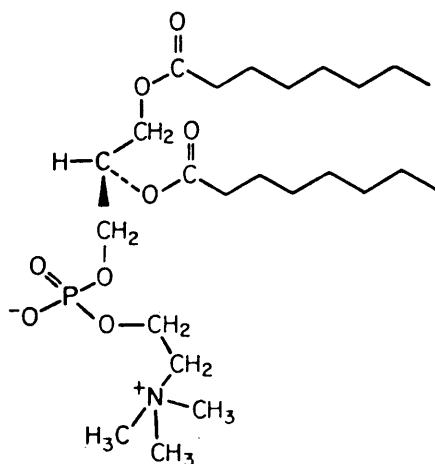


**Figure 5-1:** The di-C<sub>8</sub> lecithin molecule

This diagram of the chemical structure of the di-C<sub>8</sub> lecithin molecule was reproduced from the thesis of G. Thurston [1].

The lecithin molecule is known as an amphiphilic molecule. Amphiphilic molecules are schizophrenic: one part of them loves water and hates oil; the other part of them loves oil and hates water. In the case of the lecithin molecule, the zwitterionic head group is hydrophilic (water loving), and the hydrocarbon tails are hydrophobic (water hating). This type of molecule is used to make soaps and detergents because it likes to locate itself between polar and non-polar fluids and therefore reduces surface tension. For example, a detergent would preferentially locate at a water, oil interface therefore making oily substances more soluble in water. In biological systems, lecithins are used by nature for fat solubilization and lipid transport, and for making biological structures, such as the cell membrane.

Biological lecithins, the subject of the next chapter, are of a long hydrocarbon tail variety (16 - 22 carbons long), and are nearly insoluble in water by themselves. In contrast, the short chain synthetic lecithins studied in this chapter, are extremely soluble in water. As the concentration of lecithins is increased, they self aggregate to form structures called micelles. This self-aggregation is driven by the tendency of the hydro-carbon parts of the molecules to cluster together to minimize their exposure to the water environment. Several theories have been devised to predict the size of the aggregates formed from amphiphilic molecules in solution [2, 3, 4].

The short chain lecithins were extensively studied by Tausk, *et al.* [5, 6, 7, 2] who used static light scattering and surface tension measurements. The work in this chapter follows a long the lines laid down by Tausk *et al.* and adds to the picture results obtained from dynamic light scattering.

From experiments by Tausk *et al.* [5], the phenomenology of lecithin micellar aggregation is as follows. Di-C<sub>6</sub> lecithins have a critical micelle concentration (CMC) of 6.5 mg/ml in 10<sup>-2</sup> mole/l phosphate aqueous buffer, pH = 6.9. This value for the CMC was determined using surface tension measurements. The micelles formed do not grow much larger as the lecithin concentration is increased. The CMC is the approximate concentration at which the energetic advantage of the amphiphiles associating with each other starts to outweigh the entropic advantage of mixing in the solution.

Di-C<sub>7</sub> lecithins, with their slightly longer, water hating, hydro-carbon tails, show more of a tendency to self aggregate so they have a lower CMC than the Di-C<sub>6</sub> lecithin molecules. These micelles continue to grow in size as the lecithin concentration is increased. The model for the micelle growth is as follows: at the CMC spherical, or perhaps, prolate ellipsoidal, micelles are formed. As more material is added to the solution, additional amphiphilic molecules find it energetically advantageous to make the micelles elongated since there is less curvature in the elongated part of the micelles than in the endcap regions: that is, when amphiphile concentration is increased, it requires less energy to make the existing micelles longer compared to creating new micelles. The CMC of the di-C<sub>7</sub> lecithin micellar solution was found to be [5] 0.8 mg/ml under the same conditions as cited above for the di-C<sub>6</sub> lecithin micellar solution. Chen *et al.* [8] have reported small angle neutron scattering data supporting a model for rod-like one dimensional growth in di-C<sub>7</sub> lecithin micellar systems.

Di-C<sub>8</sub> lecithin micelles grow linearly like Di-C<sub>7</sub> lecithin micelles, but inter-micellar interactions also lead to a liquid-liquid phase separation with an upper consolute point [7]

at about 45° C. Fig. 5-2, which is from data in reference [1], shows the location of the coexistence curve in the temperature, concentration plane. The CMC of di-C<sub>8</sub> lecithins was found to be [5] 0.12 mg/ml under the same conditions as cited above. Tausk *et al.* [7] found that their static light scattering data was consistent with a micellar morphology in which the micelles formed "a very extended structure, probably wormlike with an increasing flexibility with increasing size. Perhaps we should not think of unbranched rods but visualize the micelles more as an extended network."

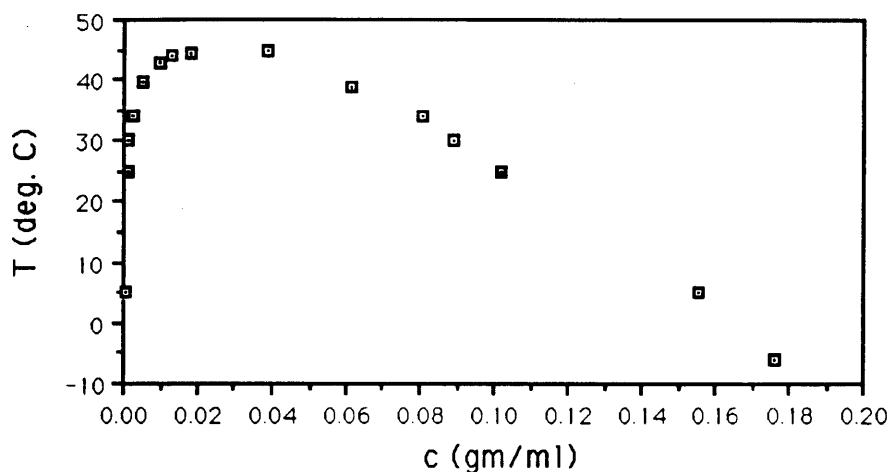


**Figure 5-2:** The coexistence curve for liquid-liquid phase separation in di-C<sub>8</sub> lecithin.

The data depicted here is from reference [1], Fig. III-4. The locus of data points describing the coexistence curve were derived from cloud point determinations and from comparison of the relative volumes of the phase separated material. The region above the coexistence curve is a one phase region: a solution prepared with a temperature and concentration that places it above the curve will be one isotropic phase. A solution prepared with a temperature and concentration below the curve will separate into two coexisting phases with different lecithin concentrations.

In this chapter, static and dynamic light scattering experiments on di-C<sub>7</sub> lecithin, and di-C<sub>8</sub> lecithin (diheptanoyl-, and dicapryloyl phosphatidylcholine; molecular weights: 482 gm/mole, and 510 gm/mole) dissolved in pure water (and also pure D<sub>2</sub>O in

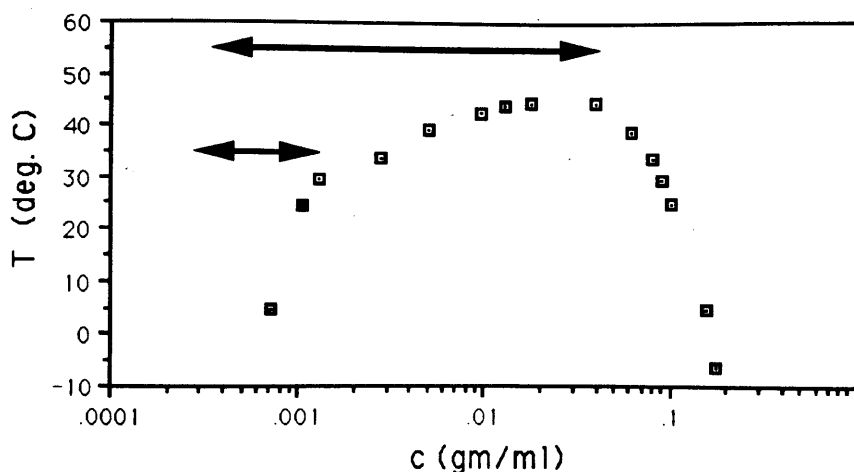


**Figure 5-3:** The data of Fig. 5-2 plotted on semi-log graph to show more detail at low concentration.

The two horizontal, double ended arrows in the single phase region of the phase diagram show the position and the extent of the two isotherms that were studied in detail by static and dynamic light scattering as described below.

the case of di-C<sub>7</sub> lecithin) will be used to deduce micellar morphology, and micellar size concentration dependence. The experimental evidence from both static and dynamic light scattering results will be found to support a "stiff-rod" model for the micelle shape in pure water. Results from the experiments will be analyzed in the context of the "ladder model" [3] for one dimensional micellar growth, and comparisons will be made to results from small angle neutron scattering where applicable. Results of the measurement of the osmotic susceptibility in di-C<sub>8</sub> lecithin solutions will compared to explicit predictions made by Thurston *et al.* [1, 9, 10, 11] for micellar systems exhibiting phase separation behavior

The results presented in this chapter for di-C<sub>8</sub> lecithin will also include light scattering data showing the divergence of the osmotic susceptibility and the correlation range as the upper consolute point is approached by decreasing temperature along an isochore.



**...A note on the representation of quantities measured in light scattering...**

In this chapter we will use the following expressions interchangeably:  $\frac{1}{M_{app}}$ , and  $\frac{1}{R_{gas}T} \left(\frac{\partial\pi}{\partial c}\right)_T$ ;  $R_g$ , and  $\sqrt{3} \xi_s$ ; and  $R_h$ , and  $\xi_h$ . As explained in the previous chapter,  $M_{app}$  is the apparent molecular weight as determined from the scattered intensity, and  $\left(\frac{\partial\pi}{\partial c}\right)_T$  is the osmotic susceptibility;  $R_g$  is an ensemble average of individual particle radii of gyration, and  $\xi_s$  is the static correlation range of concentration fluctuations; and  $R_h$  is an ensemble average of individual particle hydrodynamic radii, and  $\xi_h$  is the hydrodynamic correlation range.

In the limit of no interparticle interactions (such as in a very dilute solution), then  $M_{app} = M_w$  where  $M_w$  is the weight averaged molecular weight. In the more general case where interactions are present, then referring to  $1/M_{app}$  is just a shorthand way of referring to the osmotic susceptibility, see Eq. (4-34). Likewise, even though some of the following figures refer to  $\xi_s$  in terms of  $R_g$ , it should be understood that  $R_g$ , standing by itself, probably only has meaning in terms of single particle properties in the most dilute concentration ranges of data presented from the following experiments. Similar limitations can be expected to apply to our representation of  $R_h$ .

When more than one size of particle is present in the solution, then  $R_g$ , and  $R_h$  are actually ensemble averages. That is, when we report an experimentally measured  $R_g$ , what is actually being reported is the average  $\langle R_g^2 \rangle_z^{1/2}$ , where the "z" subscript on the bracket signifies a z-average, see Eq. (4-45). When we report an experimental value for  $R_h$ , what is actually being reported is  $\langle 1/R_h \rangle_z^{-1}$ . The implications of these ensemble averages for our conclusions regarding particle shape will be considered in Sec. 5.5.

## 5.2 Di-C<sub>7</sub> lecithin

### 5.2.1 Sample preparation

Di-C<sub>7</sub> lecithin, dissolved in chloroform, was obtained from Avanti Polar Lipids (L- $\alpha$ -diheptanoyl phosphatidylcholine; cat # 850306; Lot #'s C70-11, C7-10; Avanti Polar Lipids, Birmingham, AL). The chloroform was dried out from the lecithin - chloroform mixture under a stream of dry, filtered nitrogen, and then the resulting thin film of lecithin was placed in a vacuum for at least 24 hours for further drying. The dried lecithin was re-suspended in pure H<sub>2</sub>O (Milli Q water system, Millipore Corp, Bedford, MA), or in pure D<sub>2</sub>O (Cambridge Isotope Laboratories, Woburn, MA). Stock solution of the lecithin was diluted to known concentrations and packaged in 2 ml ampuls (Kimble 12012-L, diameter = 12 nm). Before flame sealing, the ampuls were purged with nitrogen and temporarily sealed with teflon tape. Both the H<sub>2</sub>O and the D<sub>2</sub>O solvents were boiled for 10 minutes in a vacuum at room temperature to remove dissolved gasses before their use. All materials were handled in a nitrogen environment to prevent oxygen contamination. The dried lecithin films were at no time in their preparation exposed to oxygen.

A trial light scattering run on pure D<sub>2</sub>O, packaged as described above, showed it to be contaminated with large colloidal sized particles having sizes on the order of several microns. The scattered light intensity at 90° was ten times that expected from pure water. Fortunately, it was found that centrifugation of the D<sub>2</sub>O sample at ~200 X *g*, where *g* is the acceleration of gravity, for 20 minutes was sufficient to make the D<sub>2</sub>O sample free from scattering particles. After the centrifugation, the intensity of light scattered from the

D<sub>2</sub>O sample was comparable to the scattered intensity from pure H<sub>2</sub>O. The particulate contamination of the D<sub>2</sub>O apparently originated during its manufacture, since visual examination of a beam of laser light through the glass bottle in which the material was packaged, also showed large particle scattering, and generally, a very high level of scattered light. All lecithin-water samples were centrifuged at ~200 X g for 20 to 30 minutes prior to light scattering. All glassware was acid washed, and then rinsed thoroughly with pure H<sub>2</sub>O (Milli Q water system) before drying. Light scattering measurements were made at T = 20.2° C. for all samples.

Fig. 5-4 show the results of index of refraction measurements on the lecithin - D<sub>2</sub>O samples. According to these measurements,  $\frac{dn}{dc} = 0.126$  ml/gm which is comparable to the value of  $\frac{dn}{dc} = 0.125$  ml/gm that Tausk *et al.* [6, Table 2] found for di-C<sub>7</sub> lecithin in aqueous buffer (10<sup>-2</sup> M phosphate buffer, pH = 6.9).

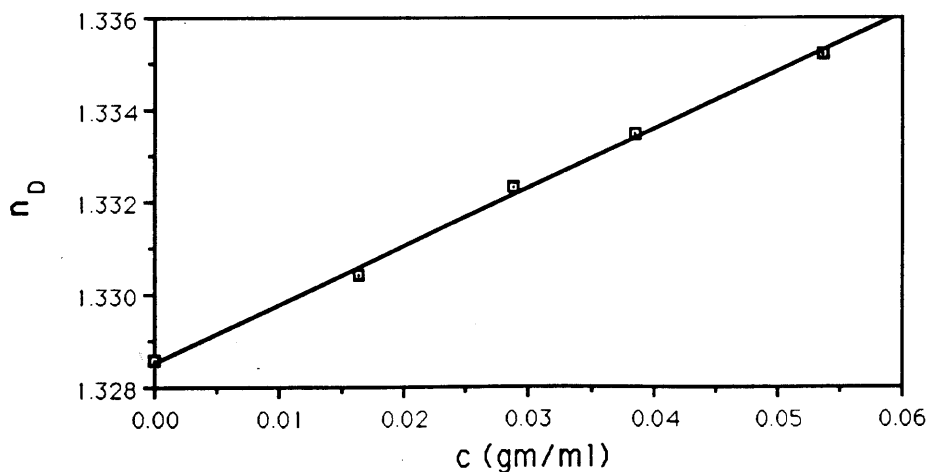


**Figure 5-4:** The index of refraction of di-C<sub>7</sub> lecithin dissolved in D<sub>2</sub>O versus lecithin concentration.

The vertical axis, label  $n_D$  represents the index of refraction of the sample with respect to the sodium D line, 589.3 nm. The horizontal axis represents the weight of lecithin with respect to total sample volume. The temperature of the samples was 20° C.

### 5.2.2 Light scattering measurements

The Rayleigh ratios of all the lecithin - H<sub>2</sub>O, and lecithin - D<sub>2</sub>O samples were measured, and the apparent molecular weights found by application of Eqs. (4-23), and (4-33). Recall the Eqs. (4-23), and (4-33) tell us that  $M_{app}$  is proportional to the Rayleigh ratio extrapolated to zero scattering angle. The results of these measurements are shown in Figs. 5-5 and 5-6. In Fig. 5-5 the more detailed data from the earlier study of Tausk *et al.* [6] is also shown for comparison. Although, they used a buffered solvent, their results are not greatly different than the findings of this study which used a pure water solvent. In comparing Fig. 5-5, and Fig. 5-6 we see that micelles in the D<sub>2</sub>O are larger than those in H<sub>2</sub>O. At the same temperature, D<sub>2</sub>O has stronger hydrogen bonding than H<sub>2</sub>O. By self-aggregating to form larger micelles in D<sub>2</sub>O, perhaps D<sub>7</sub> lecithin micelles break fewer of the hydrogen bonds.

The micellar aggregates in these samples were too small to cause any detectable angular dependence in the scattered light so no radius of gyration is reported.

Figs. 5-7 and 5-8 show the results of dynamic light scattering on these samples. Like in the previous figures, it can be seen that the same concentration, the micelles are larger in the D<sub>2</sub>O solvent. The data in these figures was reduced in accordance with the procedures described in Sec. 4.6.3 to find  $\xi_h$ . Here, in the way the data is displayed, we make the implicit assumption that  $\xi_h = R_h$ .

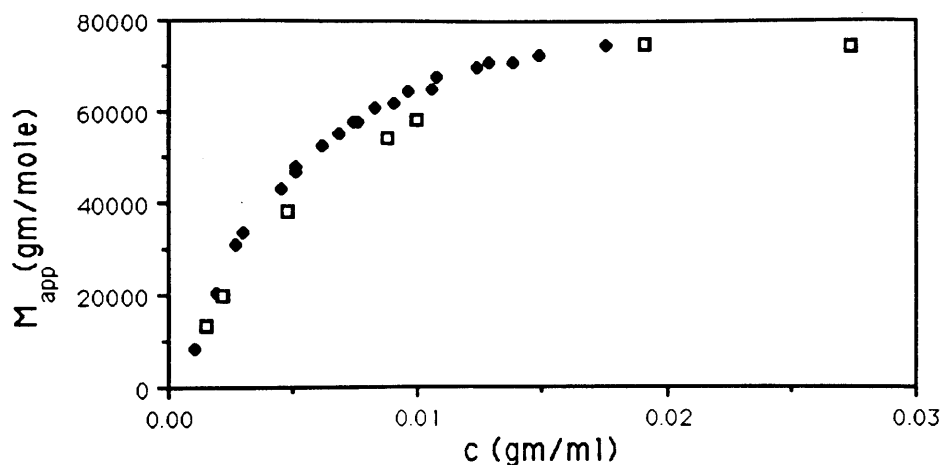


**Figure 5-5:** The apparent molecular weight of Di-C<sub>7</sub> lecithin micelles with respect to total lecithin concentration. The solvent is H<sub>2</sub>O.

Data of Tausk *et al.* from reference [6, Fig. 10] is shown as black diamonds. Tausk *et al.* used aqueous buffer as the solvent ( $10^{-2}$  M phosphate buffer, pH 6.9), and his measurements were made at room temperature,  $\sim 22^{\circ}$  C. The open squares are the results of light scattering in this current study. Unbuffered, pure H<sub>2</sub>O was used as the solvent at a temperature of  $20.1^{\circ}$  C.

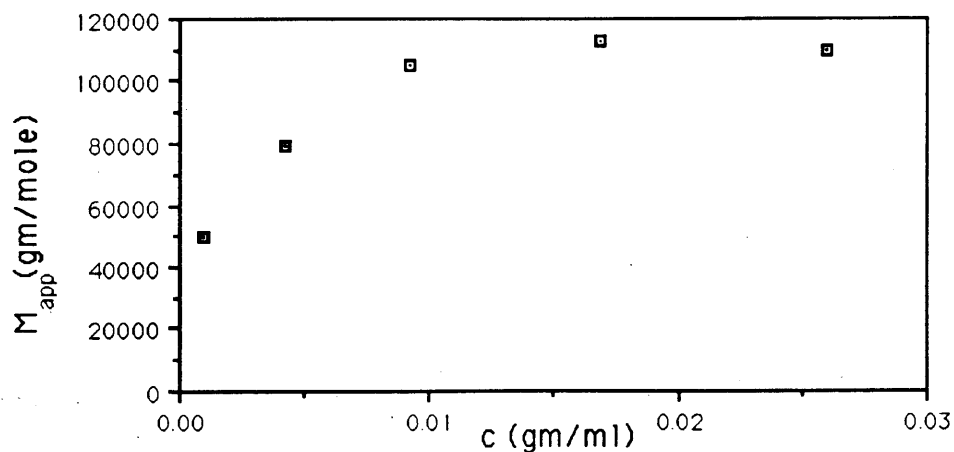


**Figure 5-6:** The apparent molecular weight of di-C<sub>7</sub> lecithin micelles with respect to total lecithin concentration. The solvent is pure D<sub>2</sub>O.

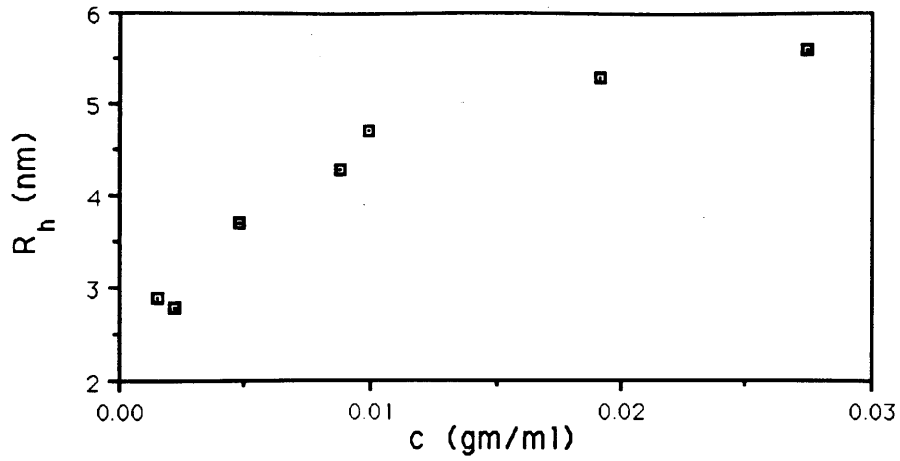


**Figure 5-7:** The hydrodynamic radius,  $R_h$ , with respect to concentration of di-C<sub>7</sub> lecithin micelles in pure H<sub>2</sub>O.

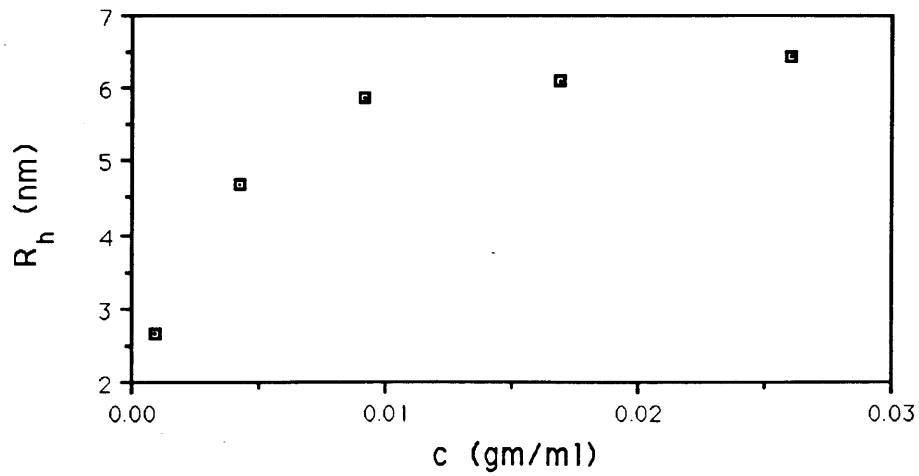


**Figure 5-8:** The hydrodynamic radius,  $R_h$ , with respect to concentration of di-C<sub>7</sub> lecithin micelles in pure D<sub>2</sub>O.

### 5.2.3 Results and Discussion

In systems that undergo self assembly such as micellar systems, it is expected that the molecular weight is itself a function of concentration. For example, the "ladder model" for one dimensional, rod-like micellar growth [3] predicts

$$M_w \approx m (b_o + 2\sqrt{K(X - X_B)}) \quad (5-1)$$

where  $m$  is the molecular weight of a single amphiphile,  $b_o$  is the number of amphiphiles in a minimum micelle,  $K$  is determined by the energy advantage of an amphiphile being placed in the less curved cylindrical region as compared to the micelle's end cap region,  $X$  is the total mole fraction of amphiphile monomers in solution, and  $X_B$  is determined by the energy advantage of an amphiphile being placed cylindrical region the micelle as opposed to being a monomer in the solvent. If the micelles immediately grow into rods at concentrations above the CMC, then  $X_B \approx X_{CMC}$ , see reference [3, Appendix 1].

We can attempt to analyze the data presented in Figs. 5-6 and 5-5 using Eq. (5-1). The results of that attempt are presented in Figs. 5-9, 5-10, and 5-11. In Eq. (5-1), we used  $X_b \equiv X_{CMC}$ , with  $X_{CMC} = 3 \times 10^{-5}$  corresponding to values given in reference [6] for H<sub>2</sub>O, and in reference [8] for D<sub>2</sub>O, for the CMC's in H<sub>2</sub>O and D<sub>2</sub>O. According to the fits of the ladder model, Eq. (5-1), to the data presented in Figs. 5-9 and 5-10, the logarithm of the growth potential parameter  $\ln(K)$  is: in the di-C<sub>7</sub> lecithin - D<sub>2</sub>O solutions,  $\ln(K) = 16.8$ ; and in di-C<sub>7</sub> lecithin - H<sub>2</sub>O solutions,  $\ln(K) = 16.3$ . Chen *et al.* [8] measured  $\ln(K)$  as 16.5 in di-C<sub>7</sub> lecithin - D<sub>2</sub>O solutions using small angle neutron scattering. One slightly troubling problem with the curve fit in Fig. 5-10 is that it gives a  $b_o = -7$ : that is, the fit gives a negative value for the minimum micelle number. If we use a higher value for  $X_b$ , say  $X_b = 5.5 \times 10^{-5}$  which is near the lowest measured concentration, then we get  $b_o = 18$  and  $\ln(K) = 15.9$ , see Fig. 5-11.

The above deduction of the ladder model parameter  $\ln(K)$  from the data Figs. 5-5 and 5-6 basically assumed that the solution had ideal behavior, meaning that  $B$  and the higher order virial coefficients in Eq. (4-34) were identically zero. In any case, the higher concentration points in Figs. 5-9, and 5-10 were not well fit by Eq. (5-1), so if the ladder model is the correct model for micellar growth, then the higher order virial coefficients are not zero. If the virial coefficients are not zero (or small), then the assumption that  $M_{app} \approx M_w$  may not be a good one but that could be hard to determine with certainty *a priori*. Since the molecular weights of the micelles change with concentration, we can not measure the virial coefficients directly as we did in the case of the polymer - toluene system of Sec. 4.6.3.

Naturally, applying an interpretation to the data such as the one embodied in Eq. (5-1) assumes that  $M_{app}$  primarily represents single particle properties. If the interparticle interactions were primarily of a short range nature, this assumption would be equivalent to saying that our samples are far below the particle overlap threshold concentration  $c^*$  of Eq. (4-53). To make an estimate of  $c^*$  we can use the data of the preceding figures, and set  $R_h = r_f$  and  $M_{app} = M_w$ . The quantity  $r_f$  is the effective hard core radius of the micelle: that is, we make an assumption that the micelles could be treated as hard spheres for the purpose of computing  $c^*$ . According to such an estimate,  $c^*$  is greater than 0.1 gm/ml at all experimental concentrations, except for the highest concentration data point at 0.027 gm/ml where  $c^*$  is 0.09 mg/ml. Naturally, Eq. (4-53) may substantially over estimate the magnitude of  $c^*$  since the micellar particles could hypothetically grow as rigid rods. However, if the rigid rod like micelles were overlapping we could



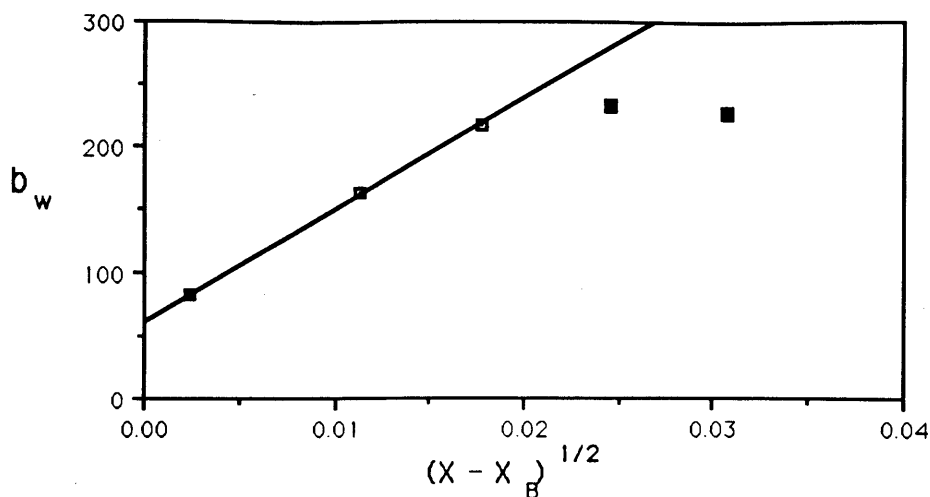


**Figure 5-9:** A fit of the data in Fig. 5-6 to the ladder model for micellar growth.

The solvent is  $D_2O$ .  $b_w$  is the weight average aggregation number which is assumed to be  $M_{app}/m$  where  $M_{app}$  is taken from the data of Fig. 5-6, and  $m$  is the molecular weight of a single amphipile. The concentration of lecithin  $X$  is in mole fraction units, and is plotted as  $(X - X_B)^{1/2}$  for comparison with Eq. (5-1).  $X_B$  is assumed to be the same as  $X_{CMC}$ , the concentration of the CMC. Only the three lowest concentration points were used to fit the data, as the two higher concentration points do not fit the ladder model, perhaps because of intermicellar interactions. According to this fit (of only three points), the ladder model parameters are  $\ln(K) = 16.8$ , and  $b_o = 62$ .

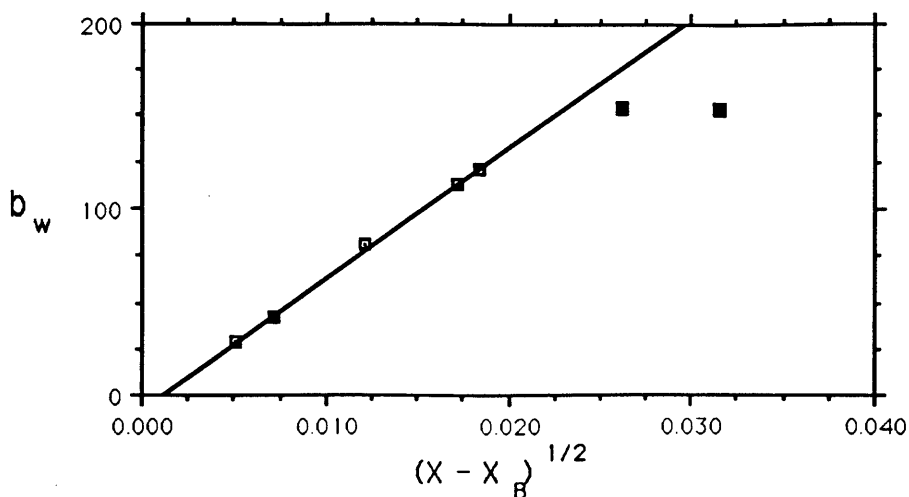


**Figure 5-10:** A fit of the data in Fig. 5-5 to the ladder model for micellar growth.

The solvent is  $\text{H}_2\text{O}$ . As in the previous figure, the two highest concentration points were not used in the fit to the ladder model. According to this fit,  $\ln(K) = 16.3$ , and  $b_o = -7$ . In this fit,  $X_b$  may be too low since it was assumed to be the same as the CMC for this system which was not measured here, but taken from the data of Tausk *et al.* [6].

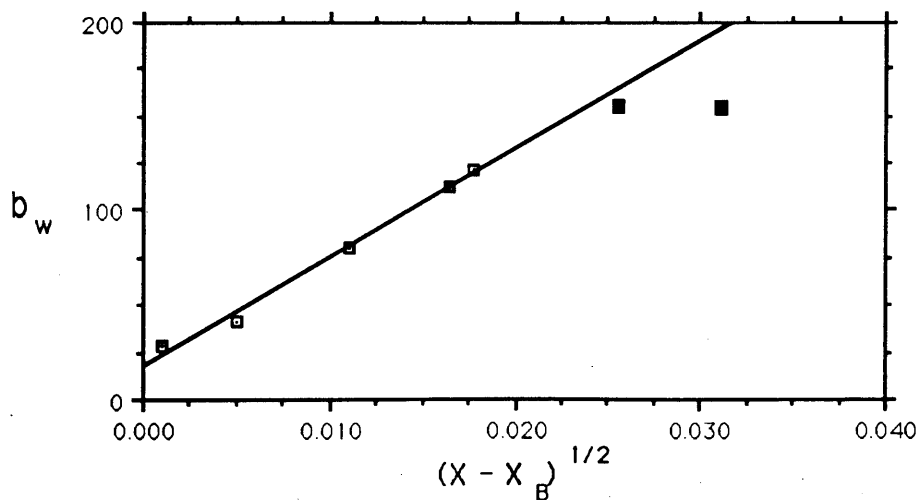


**Figure 5-11:** A fit of the data in Fig. 5-5 to the ladder model for micellar growth with a larger assumed value for  $X_b$  than in Fig. 5-10.

In this figure, which is based on the same data as Fig. 5-10, we assume a value for  $X_b$  which is similar to the lowest concentration measured. According to the new fit to Eq. (5-1),  $\ln(K) = 15.9$ , and  $b_o = 18$ .

expect  $M_{app}$  and  $R_h$  to start decreasing with increasing concentration in analogy to what happens in semi-dilute polymer systems, see Sec. 4.6.3. Since both  $M_{app}$  and  $R_h$  continue to increase with increasing concentration, the micelles are probably still in a dilute regime. However, it is worthy to note that the growth in  $M_{app}$  and  $R_h$  of Figs. 5-6, 5-5, 5-8, and 5-7 does essentially level off at 0.015 gm/ml.

A very interesting feature of this data is the way the ratio  $\frac{R_h}{M_{app}^{1/2}}$  scales with concentration. Fig. 5-12 shows that this ratio has at most a very weak concentration dependence, except for the lowest concentration points. Even though  $R_h$  changes by a factor of two over this range, the ratio  $\frac{R_h}{M_{app}^{1/2}}$  changes by only ~20% (except for the lowest concentration points). This observation is similar to the earlier observation made by Tausk *et al.* in di-C<sub>8</sub> lecithin solutions [7, Fig. 6] that the ratio  $[\langle r_g^2 \rangle_z / M_w]^{1/2}$  was essentially concentration independent.

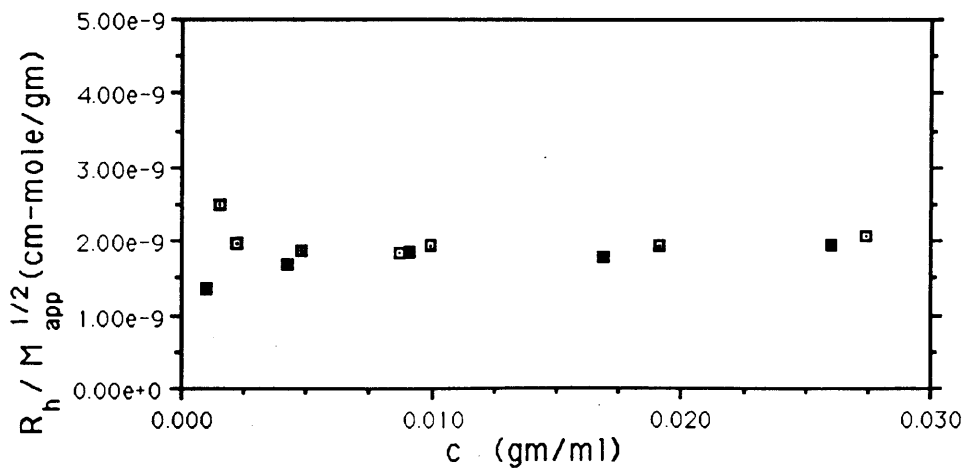


**Figure 5-12:** The ratio  $R_h/M_{app}^{1/2}$  versus concentration for di-C<sub>7</sub> lecithin in H<sub>2</sub>O and D<sub>2</sub>O.

The open squares are from di-C<sub>7</sub> lecithin dissolved in a pure water solvent. The closed squares are data from di-C<sub>7</sub> lecithin dissolved in D<sub>2</sub>O.

## 5.3 Di-C<sub>8</sub> lecithin

### 5.3.1 Sample preparation

Di-C<sub>8</sub> lecithin, dissolved in chloroform, was obtained from Avanti Polar Lipids (L- $\alpha$ -Dicapryloyl phosphatidylcholine; cat # 850315; Lot #'s C80-19, & C80-26). The chloroform was dried off and the lecithin mixed with H<sub>2</sub>O and packed 2 ml ampuls as described in Sec. 5.2.1 for the di-C<sub>7</sub> lecithin water solutions.

Fig. 5-13 presents the results of measuring the index of refraction of di-C<sub>8</sub> lecithin - H<sub>2</sub>O solutions with respect to lecithin concentration. The resulting index of refraction increment from this data is  $\frac{dn}{dc} = 0.126$  ml/gm at 55° C, and  $\lambda_0 = 598.3$  nm. This value of  $\frac{dn}{dc}$  is comparable to the value measured previously by Tausk *et al.* [7, Fig. 3]: they found  $\frac{dn}{dc} = 0.124$  ml/gm at 55° C., and  $\lambda_0 = 578$  nm, in 10<sup>-2</sup> phosphate buffer, pH = 6.9.

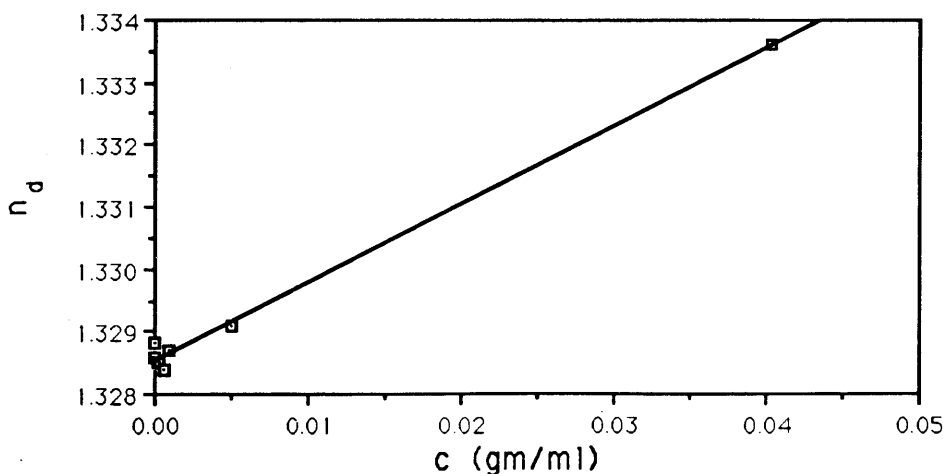
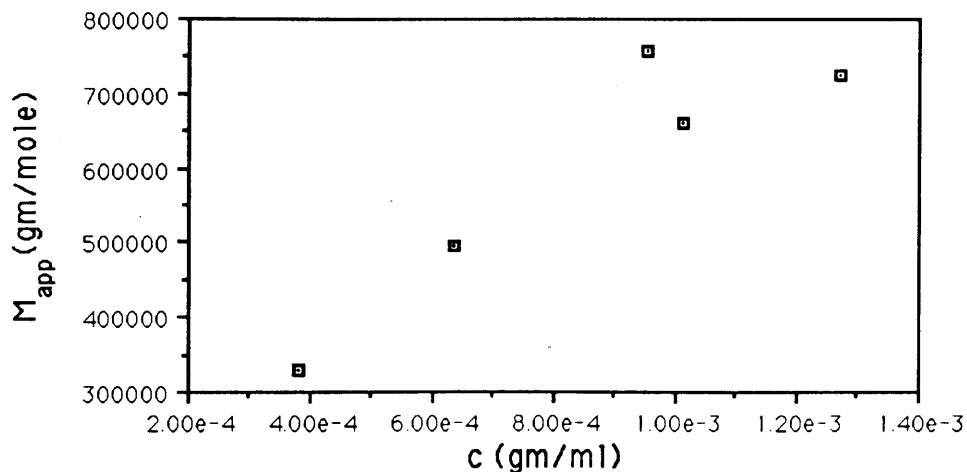


**Figure 5-13:** The index of refraction of di-C<sub>8</sub> lecithin dissolved in pure H<sub>2</sub>O versus lecithin concentration.

The vertical axis, label  $n_D$  represents the index of refraction of the sample with respect to the sodium D line, 589.3 nm. The horizontal axis represents the weight of lecithin with respect to total sample volume.

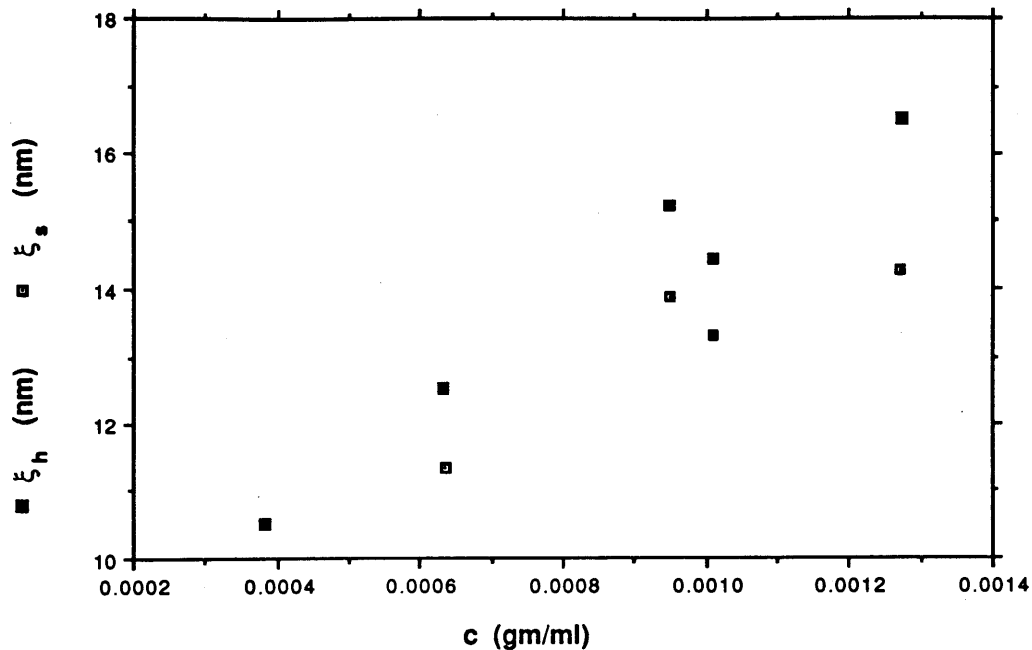
### 5.3.2 Light scattering measurements at 35 deg. C.

Fig. 5-14 presents the concentration dependence of the apparent molecular weight,  $M_{app}$  versus concentration, on the 35° C isotherm. The data in Fig. 5-14 was derived from the scattered light intensity extrapolated to zero scattering angle in accordance with the procedures outlined previously in Sec. 4.6. In the figure,  $M_{app}$  shows a steady increase, which may be indicative of aggregative phenomena. The data ends at  $c \approx 0.0013$  gm/ml because of the proximity of the coexistence curve for liquid-liquid phase separation. Also shown, in Fig. 5-15, is static correlation range,  $\xi_s$ , and the hydrodynamic correlation range,  $\xi_h$ , on the 35° C isotherm. This data was reduced from the light scattering data in accordance with procedures outlined in Sec. 4.6.



**Figure 5-14:** The apparent molecular weight of Di-C<sub>8</sub> lecithin micelles with respect to total lecithin concentration. The solvent is pure H<sub>2</sub>O.

These measurements were made along the 35° C. isotherm in the low concentration, one phase region: see the coexistence curve in Fig. 5-3.



**Figure 5-15:** The static correlation length,  $\xi_s$ , and the dynamic correlation length,  $\xi_h$ , in the di-C<sub>8</sub> lecithin - water solution along the 35° C. isotherm.

### 5.3.3 Light scattering measurements at 55 deg. C.

The concentration dependence of the apparent molecular weight on the 55° C isotherm is presented in Figs. 5-16, and 5-17. The apparent molecular weight peaks at  $c \sim 0.020$  gm/ml which is near the peak of the temperature - concentration coexistence curve in Fig. 5-2. Fig. 5-17 shows the same data as Fig. 5-16 except that it is displayed on a log-log plot to elucidate data points at low concentration. Fig. 5-18 shows the concentration dependence of  $\xi_s$ , and  $\xi_h$ . The same data is also displayed in Fig. 5-19 on a log-log plot to elucidate the data in the low concentration regime.

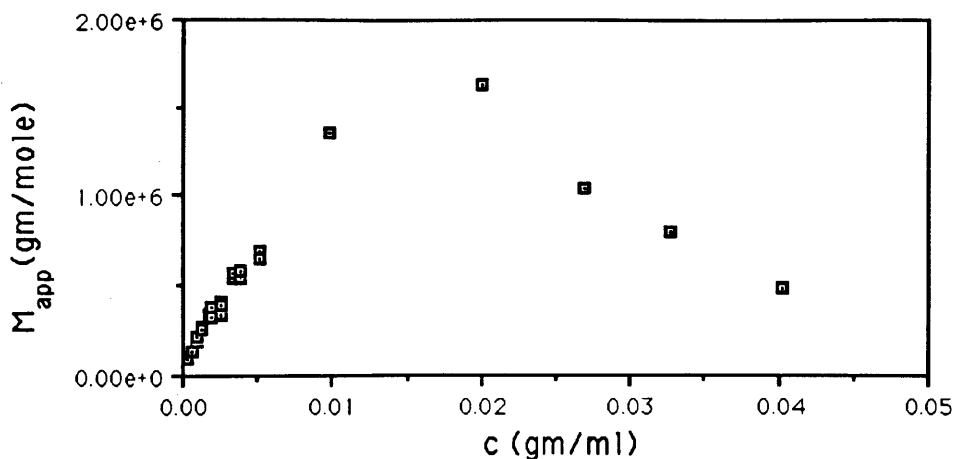


**Figure 5-16:** The apparent molecular weight of Di-C<sub>8</sub> lecithin micelles with respect to total lecithin concentration. The solvent is pure H<sub>2</sub>O.

These measurements were made along the 55° C. isotherm, in the one phase region, 10° C. above the upper consolute point, see Fig. 5-3.

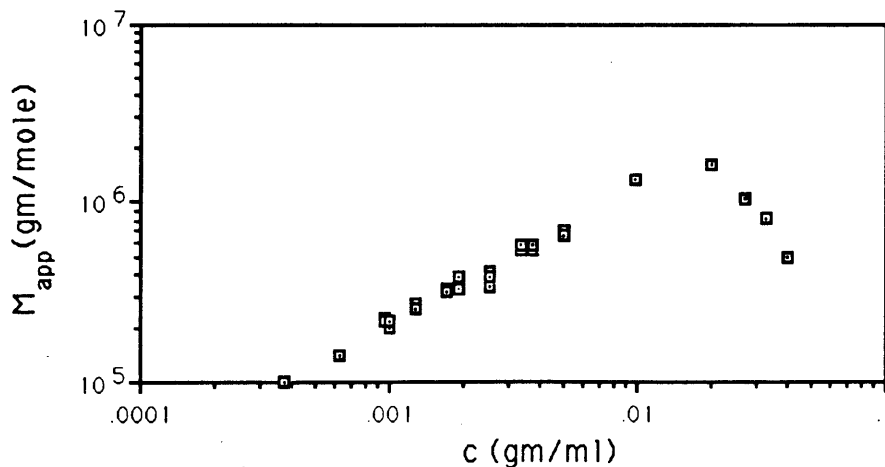


**Figure 5-17:** The data of Fig. 5-16 is replotted on a log-log graph to elucidate experimental data points at low concentration.

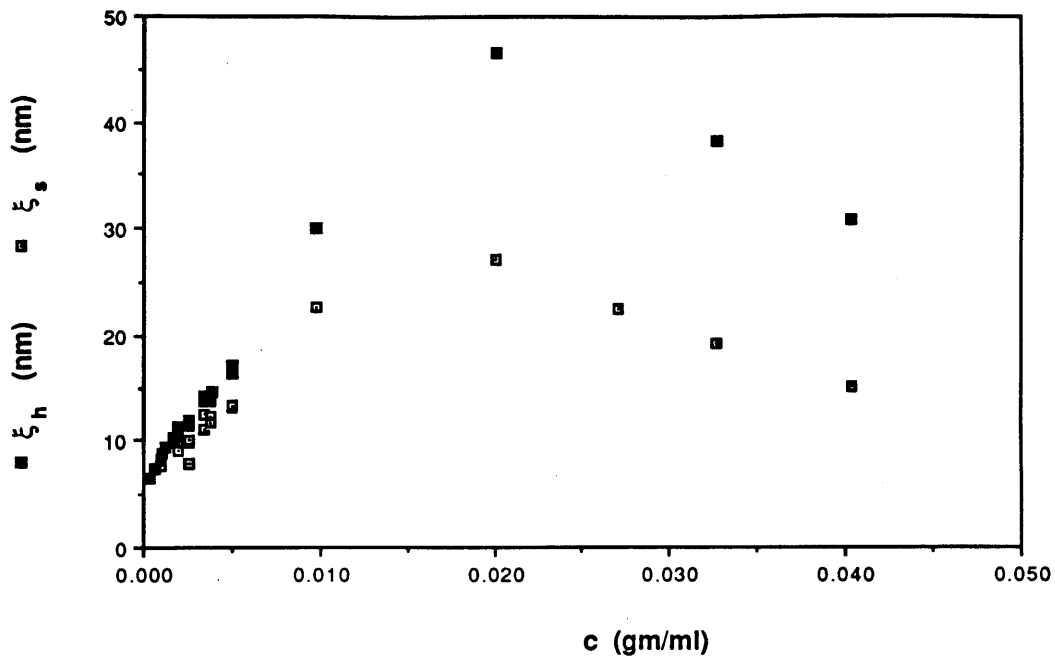


**Figure 5-18:** The static correlation range,  $\xi_s$ , and the dynamic correlation range,  $\xi_h$  of Di-C<sub>8</sub> lecithin micelles with respect to total lecithin concentration. The solvent is pure H<sub>2</sub>O.

These measurements were made along the 55° C. isotherm, in the one phase region, 10° C. above the upper consolute point, see Fig. 5-3.



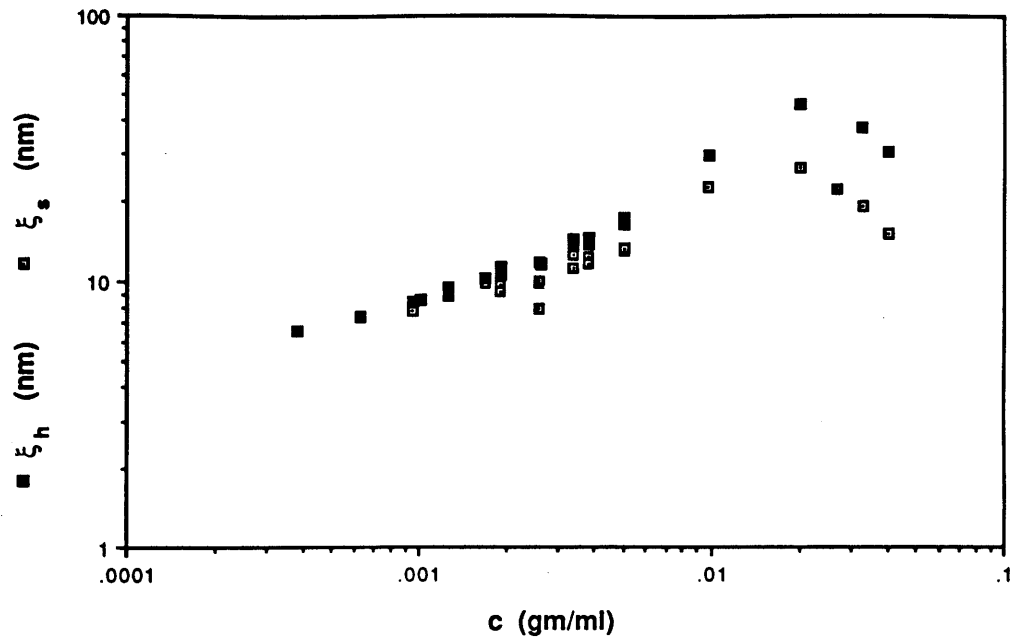


**Figure 5-19:** The data of Fig. 5-18 is replotted on a log-log graph to elucidate experimental data points at low concentration.

### 5.3.4 Results and discussion

If we assume that the weight averaged micelle aggregation number  $b_w$  is equal to  $M_{app}/m$ , where  $m$  is the molecular weight of a di-C<sub>8</sub> lecithin monomer, then we can attempt to fit the apparent molecular weight data of Fig. 5-16 to the ladder model for micellar concentration dependent growth, Eq. (5-1). The results of such a fit are displayed in Fig. 5-20. To aid in fitting to Eq. (5-1), the ordinate axis is expressed as  $(X - X_B)^{1/2}$ , where  $X$  is the mole fraction of di-C<sub>8</sub> lecithin in the solution. We used  $X_B \approx X_{CMC}$  where  $X_{CMC}$  was taken from the surface tension measurements of Tausk *et al.* [5] as 0.00012 gm/ml. As in Fig. 5-10, the fit of the concentration dependence of the aggregation number to Eq. (5-1) is unsatisfactory because of the the negative minimum micelle number produced from the fit. This "problem" can be fixed by using a larger value of  $X_B$  which would produce a small change in the derived value of the growth parameter  $\ln(K)$ : for example, see Fig. 5-11.

According to the ladder model fit to the data in Fig. 5-20,  $\ln(K) = 21.6$ . Only the low concentration points, represented as open squares in the figure, were fit to the ladder model. The higher concentration points, presented as closed diamonds, clearly deviate from the ladder model prediction for the concentration dependence of the micelle aggregation number, perhaps because of the effects of concentration fluctuations on  $M_{app}$  due to proximity of the coexistence curve for liquid-liquid phase separation, see Fig. 5-3. A previous worker, G. Thurston, attempted to measure the ladder growth parameter  $\ln(K)$  in a slightly different way [1]. Thurston used dynamic light scattering to measure  $R_h$  in the di-C<sub>8</sub> lecithin-water solutions as function of concentration and temperature. In order

to deduce the micelle aggregation number from his data for  $R_h$ , Thurston assumed that the micelles formed "worm-like" aggregates with a local segment diameter of 4 nm. According to his estimates of the "worm" stiffness, Thurston found a range of possible values for the ladder model growth parameter:  $21.3 < \ln(K) < 22.3$  at 55° C. Thurston's range of estimates for  $\ln(K)$  were based on choosing a range of values for the persistence length,  $\xi_p$ : he used the range  $15 \text{ nm} < \xi_p < \infty$ . The persistence length, a measure of the "worm" stiffness, is formally defined in Eq. (5-6) and the accompanying discussion. So we see that Thurston's method of using dynamic light scattering measurements interpreted in terms "worm-like" micellar shape produced a very similar estimate of  $\ln(K)$  when compared to the more direct method of this study, which obtained the micellar aggregation number by measuring the scattered light intensity.

Thurston, Blankshtein, Fisch, and Benedek [9] produced a theoretical form of the Gibbs free energy for micellar solutions which undergo liquid-liquid phase separation. Based on their form of the Gibbs free energy, and the shape of and position of the coexistence curve, the theory of Thurston *et al.* can predict the ladder model growth parameter  $\ln(K)$ , and the magnitude of a phenomenological intermicellar attractive interaction parameter  $C$ . From their Gibbs free energy, Thurston *et al.* also predicted the osmotic susceptibility: they gave,

$$\frac{v_w}{K_B T} \left( \frac{\partial \Pi}{\partial X} \right)_T = X/(X-1) + 1/(2\sqrt{KX}) - \frac{\gamma}{K_B T} CX/[1 + (\gamma-1)X]^3 \quad (5-2)$$

where  $v_w$  is the volume of a water molecule, and  $\gamma$  is the ratio of the volume of an amphiphile molecule to the volume of a water molecule. Thurston *et al.* used Eq. (5-2), and the parameters  $\ln(K)$ , and  $C$  deduced from the shape and position of the coexistence curve in

the  $C_{12}E_6$  micellar system to correctly predict the osmotic susceptibility along the critical isochore in the same system. The  $C_{12}E_6$  is a non-ionic amphiphile, and when mixed with water, the solution, under the right temperature and concentration conditions, exhibits a liquid-liquid phase separation with a lower consolute point.

In this study, we will see if Eq. (5-2) can successfully predict the osmotic susceptibility along the  $55^\circ\text{C}$  isotherm in the di- $C_8$  lecithin-water micellar system. In his thesis, Thurston measured the position of the coexistence curve for liquid-liquid phase separation for the di- $C_8$  lecithin micellar system. His data is reproduced in Figs. 5-2, and 5-3. Using his model for the Gibbs free energy, and this experimentally measured coexistence curve, Thurston predicted that  $\ln(K) = 24.4$ , and  $\frac{\alpha C}{k_B} = 365^\circ\text{K}$ , when his data is extrapolated to the  $55^\circ\text{C}$  isotherm. The solid line in Fig. 5-21 shows the theoretical prediction of the osmotic susceptibility versus mole fraction on  $55^\circ\text{C}$  isotherm, using Eq. (5-2). The open circles in the figure are the experimentally measured values of the osmotic susceptibility on the  $55^\circ\text{C}$  isotherm, derived from data already presented in Fig. 5-16. As we can see from the figure, the theoretical curve underestimates the osmotic susceptibility, and it places the critical isochore (presumably at the minimum point in the curve) at too high a concentration.

In the context of the theory of Thurston *et al.*, another way to measure the parameters  $\ln(K)$ , and  $\frac{\alpha C}{k_B}$  would be to fit Eq. (5-2) to the osmotic susceptibility data of Fig. 5-21. In Fig. 5-22 we used Eq. (5-2) to generate two theoretical curves which have better agreement with the experimental data: we used the trial sets of parameters  $\ln(K) = 21.6$ , and  $\frac{\alpha C}{k_B} = 200^\circ\text{C}$ ; and  $\ln(K) = 21.6$ , and  $\frac{\alpha C}{k_B} = 365^\circ\text{C}$ . (Note that  $\ln(K) = 21.6$

corresponds to  $T \ln(K) = 7080^\circ \text{K}$ , where  $T$  is the temperature in Kelvin. Here  $T = 328^\circ \text{K}$  on the  $55^\circ \text{C}$  isotherm. Unfortunately, the use of the symbol  $K$  for Kelvin, and the use of the symbol  $K$  for the micelle growth potential, as in  $\ln(K)$ , is slightly ambiguous.) We then used these two trial sets of parameters to generate two theoretical coexistence curves using the theory of Thurston *et al.* presented in reference [10]. These two theoretical coexistence curves are presented in Fig. 5-23 along with the experimental data of Thurston, which was already presented in Fig. 5-2. As we can see from the figures, making Eq. (5-2) fit the osmotic susceptibility data, has the effect of substantially depressing the theoretically expected position of the coexistence curve.

Recall that we also have a limited set of  $M_{app}$  versus concentration data from the  $35^\circ \text{C}$  isotherm. If we fit this data to the ladder model Eq. (5-1) we obtain  $\ln(K) = 23.3$ . At  $35^\circ \text{C}$  Thurston used his theoretical explanation of the position of the coexistence curve presented in references [1], [10] to predict that  $\ln(K) = 26.6$ . Again, as on the  $55^\circ \text{C}$  isotherm, the theory of Thurston *et al.* substantially over estimates the magnitude of the ladder model parameter  $\ln(K)$ .

This discrepancy between the predictions of the theory of Thurston *et al.* and experimental observations, does suggest that the theory may need modification in order to extend its range of validity to the di-C<sub>8</sub> lecithin-water system.

Tausk *et al.* [7] previously made the interesting observation that the experimentally derived ratio  $\frac{R_s}{M_{app}^{1/2}}$  had a very weak concentration, and temperature dependence in the di-C-(8) lecithin - aqueous buffer system ( $10^{-2} \text{M}$  phosphate buffer,  $\text{pH} = 6.9$ ,  $0.2 \text{M LiI}$ ). The data of Tausk *et al.* for the concentration dependence of  $\frac{R_s}{M_{app}^{1/2}}$  on the  $25^\circ \text{C}$  isotherm

is given by the open squares in Figs. 5-24, and 5-25. Also presented in these figures are the analogous data from this study from the 55° C (open circles), and 35° C (closed circles) isotherms. The similar magnitude and weak concentration dependence of  $\frac{R_s}{M_{app}^{1/2}}$  over the wide range of temperature, and solution conditions presented in Figs. 5-24 and 5-25 is quite interesting because it may have important implications for the micelle morphology. The micelle shape will be discussed in Sec. 5.4.

In addition, in Figs. 5-26 and 5-27, we also present the concentration dependence of the ratio  $\frac{R_h}{M_{app}^{1/2}}$  for the di-C<sub>8</sub> lecithin system on the 55° C isotherm (open circles), and for the 35° C isotherm (closed circles). For comparison, we also included the data presented earlier for the di-C<sub>7</sub> lecithin-H<sub>2</sub>O system (open squares), and the di-C<sub>7</sub> lecithin-D<sub>2</sub>O system (closed diamonds).

An interesting difference between the concentration dependence of  $\frac{R_s}{M_{app}^{1/2}}$  and  $\frac{R_h}{M_{app}^{1/2}}$  on the 55° C isotherm is that fact that  $\frac{R_h}{M_{app}^{1/2}}$  eventually starts diverging from a constant value for  $c > 0.005$  gm/ml while  $\frac{R_s}{M_{app}^{1/2}}$  increases by about only 30% between  $c = 0.005$  gm/ml, and  $c = 0.020$  gm/ml. Between  $c = 0.020$  gm/ml and  $c = 0.040$  gm/ml  $\frac{R_s}{M_{app}^{1/2}}$  basically does not change at all despite the substantial decrease in  $M_{app}$ , and  $\xi_s$  on this concentration range, see Figs. 5-16, 5-17, 5-18, and 5-19.

If we permit ourselves some speculation at this juncture, perhaps the ratio  $\frac{R_s}{M_{app}^{1/2}}$  is nearly concentration independent despite the proximity of the coexistence curve because the critical divergences in the osmotic compressibility (that is, the reciprocal of the osmotic susceptibility), and in the static correlation range nearly cancel out of the ratio.

That is to say, if the critical divergences cancel out in the ratio  $\frac{R_g}{M_{app}^{1/2}}$ , then the magnitude of this ratio is representative of what we would see far away from the coexistence curve. To explicitly see how this cancellation could come about, let us consider the mean field theory predictions for the critical divergences  $\frac{\partial c}{\partial \pi}$ , and  $\xi_s$ . Mean field theory would predict near the critical isochore that

$$\left(\frac{\partial c}{\partial \pi}\right)_T = A t^{-1} \quad (5-3)$$

and

$$\xi_s = B t^{-1/2} \quad (5-4)$$

where  $A$  is a prefactor which is related to the magnitude of  $\frac{\partial c}{\partial \pi}$  far away from the coexistence curve,  $B$  has similar meaning for  $\xi_s$ , and  $t$  is the reduced temperature, defined as

$$t = (T - T_c)/T_c \quad (5-5)$$

where  $T_c$  is the critical temperature. If we use  $1/M_{app} = \frac{1}{R_{gas}T} \frac{\partial \pi}{\partial c}$ , and  $R_g = \sqrt{3}\xi_s$ , then it follows from Eqs. (5-3) and (5-4) that the effects of the critical divergences cancel out of the ratio  $\frac{R_g}{M_{app}^{1/2}}$ .

## 5.4 Micelle shape

Establishing the shape of the micelles is a key determination: in order to apply a thermodynamic analysis to the observed concentration dependent micellar growth, it is first necessary to determine if the growth is one dimensional, or two dimensional. An example of one dimensional micellar growth would be the rod-like micelle. As more amphiphilic material is added, the rod-like micelle grows in one dimension only, along its longitudinal axis. An example of two dimensional micellar growth would be the disk-

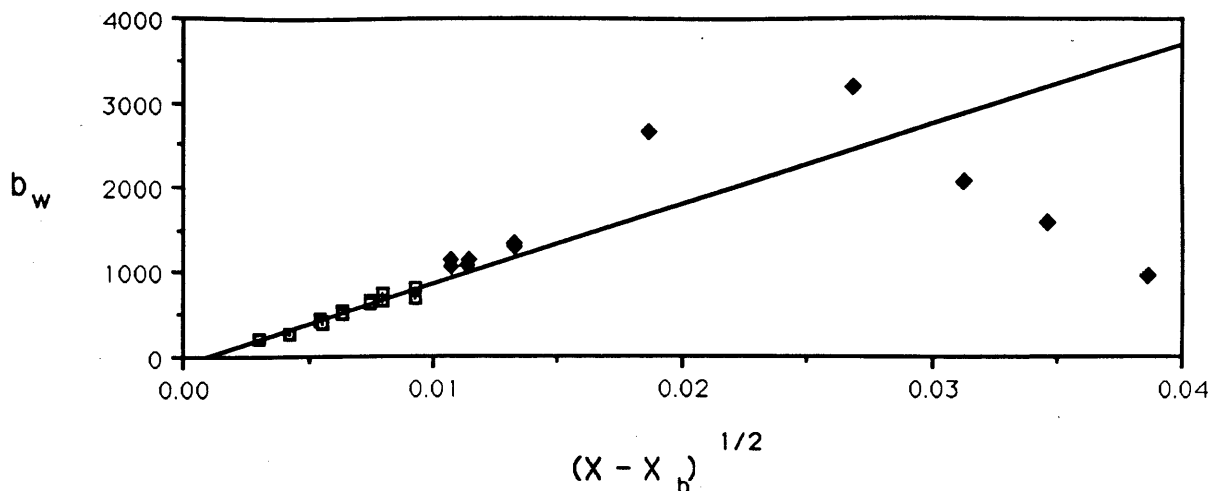


**Figure 5-20:** A fit of the ladder model to the micelle aggregation number in a di-C<sub>8</sub> lecithin-H<sub>2</sub>O system on the 55° isotherm.

The data presented in this graph is derived from the concentration dependence of  $M_{app}$  on the 55° C isotherm which was presented in Fig. 5-16. The aggregation number,  $b_w$ , was assumed to be equal to the quotient  $\frac{M_{app}}{m}$  where  $m$  is the molecular weight of a di-C<sub>8</sub> lecithin molecule. The horizontal axis was plotted as  $(X - X_b)^{1/2}$ , where  $X$  is the mole fraction of lecithin molecules, to aid in fitting to the ladder model for micellar growth, Eq. (5-1).  $X_b$  assumed to be the same as  $X_{CMC}$ , which was determined by Tausk *et al.* as 0.00012 gm/ml by surface tension measurements [5]. Only the low concentration points, presented as open squares, were fit to Eq. (5-1). The higher concentration points, which are presented as closed diamonds, and are also on the 55° C isotherm, are not included in the fit. According to this fit, the ladder model parameters are:  $\ln(K) = 21.6$ ; and  $b_o = -90$ . Again, as in Fig. 5-10 the minimum micelle number  $b_o$  is a negative number. Increasing our value of  $X_b$  would "fix" this problem, and lead to a slightly smaller value of  $\ln(K)$ . Our present finding for  $\ln(K)$  is in good agreement with the earlier findings of Thurston [1, p. 171] who used dynamic light scattering, and an assumed "worm-like" particle shape to estimate the micelle aggregation number. Thurston found,  $21.3 < \ln(K) < 22.3$  at 55° C.



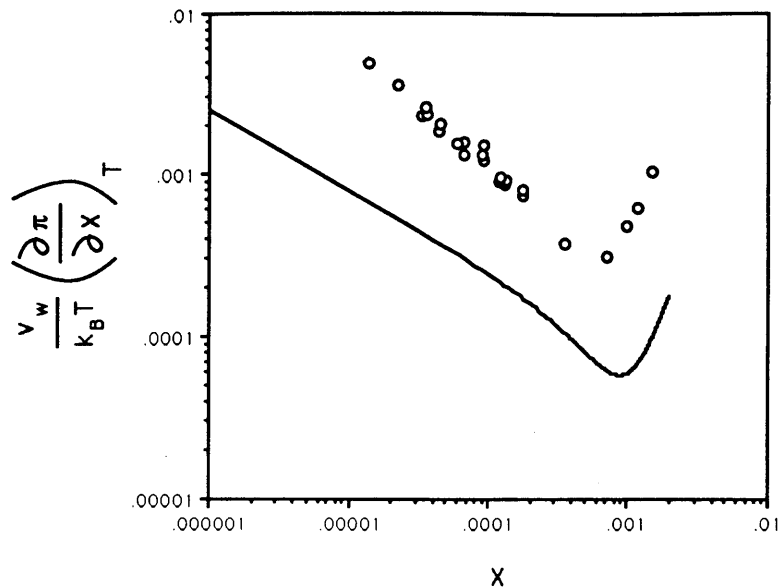


**Figure 5-21:** The osmotic susceptibility versus mole fraction on the 55°C isotherm.

The osmotic susceptibility versus mole fraction data presented in this figure (open circles) are derived from the concentration dependence of  $M_{app}$  on the 55° C isotherm. The solid line is from the theoretical prediction of Thurston *et al.*, Eq. (5-2), using experimental parameters from reference [1], p. 173, and p. 147. These parameters were predicted on the basis of the experimentally determined position of the upper consolute point, and also by the position and shape of the temperature-concentration coexistence curve for liquid-liquid phase separation. Their values extrapolated to the 55° C isotherm are:  $\ln(K = 24.4)$ ; and  $\gamma C/k_B = 365^\circ \text{ K}$ . (Note that the parameters taken from reference [1] showed very weak temperature dependence, so it is unlikely significant error was made by our extrapolation to 55° C.)

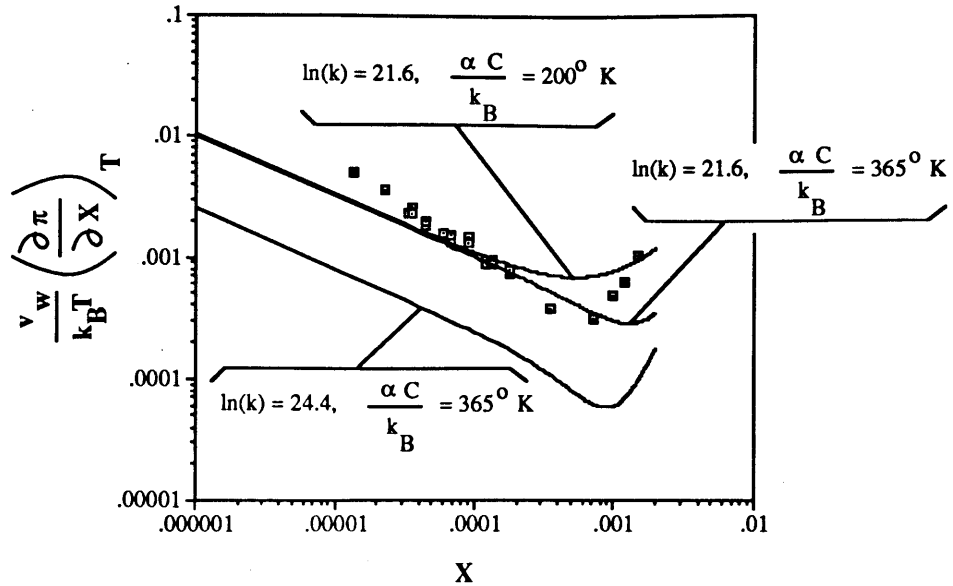


**Figure 5-22:** The osmotic susceptibility on the 55° C isotherm.

In this figure, we attempt to use Eq. (5-2) to fit the experimental data of Fig. 5-21 by letting  $\ln(K)$ , and  $\frac{\alpha C}{k_B}$  in Eq. (5-2) be adjustable parameters. The lower curve in the figure is the same as the one already shown in Fig. 5-21.

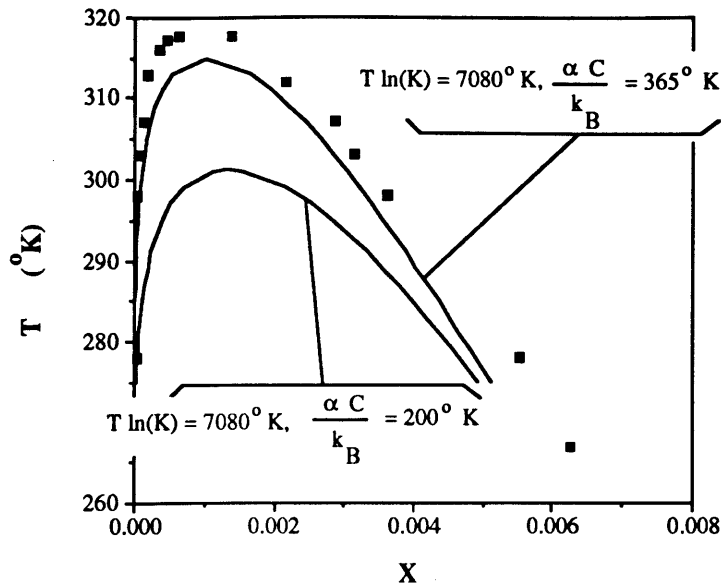


**Figure 5-23:** Predictions of the position of the coexistence curve.

We used the two sets of parameters for  $\ln(K)$ , and  $\frac{\alpha C}{k_B}$  taken from the fit of Eq. (5-2) to the data in Fig. 5-22 to generate two predictions for the position of the coexistence curve. The theoretical curves were generated from the theory presented in reference [10].

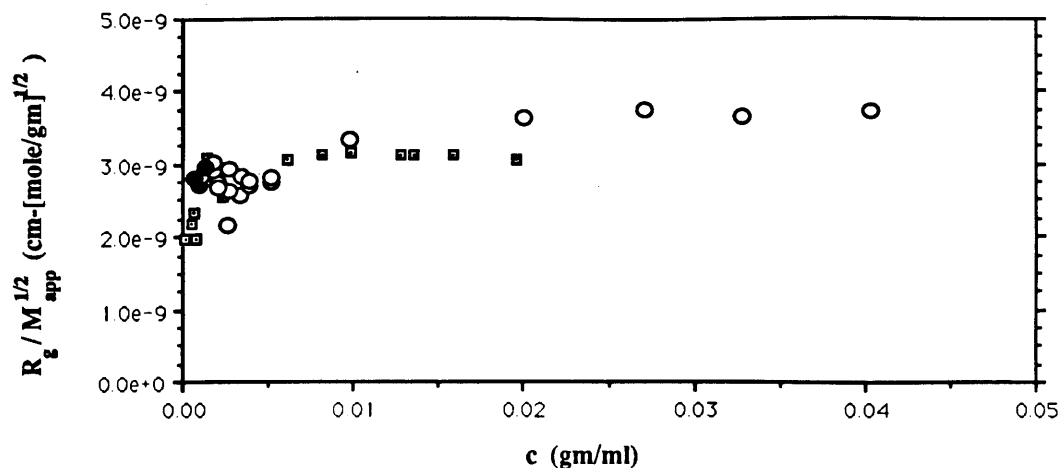


**Figure 5-24:** The concentration dependence of the ratio  $\frac{R_g}{M_{app}^{1/2}}$  for di- $C_8$  lecithin- $H_2O$  under a variety of temperature and solution conditions.

The open squares are from the previous study of Tausk *et al.* [7] who made their measurements using phosphate buffer solution at room temperature ( $10^{-2}$  M phosphate buffer, pH = 6.9,  $T = 25^\circ \text{C}$ ), and used lithium iodide salt in the solution (0.2 M LiI) to depress the coexistence curve for liquid-liquid phase separation. The open circles are from the  $55^\circ \text{C}$  isotherm data presented earlier in this section. The closed circles are from the  $35^\circ \text{C}$  isotherm data also presented earlier in this section. It is worthy to note that despite the variety of solution conditions and temperatures for the di- $C_8$  lecithin-water micellar data presented in this figure, the magnitude of the ratio  $\frac{R_g}{M_{app}^{1/2}}$  is similar in all cases.

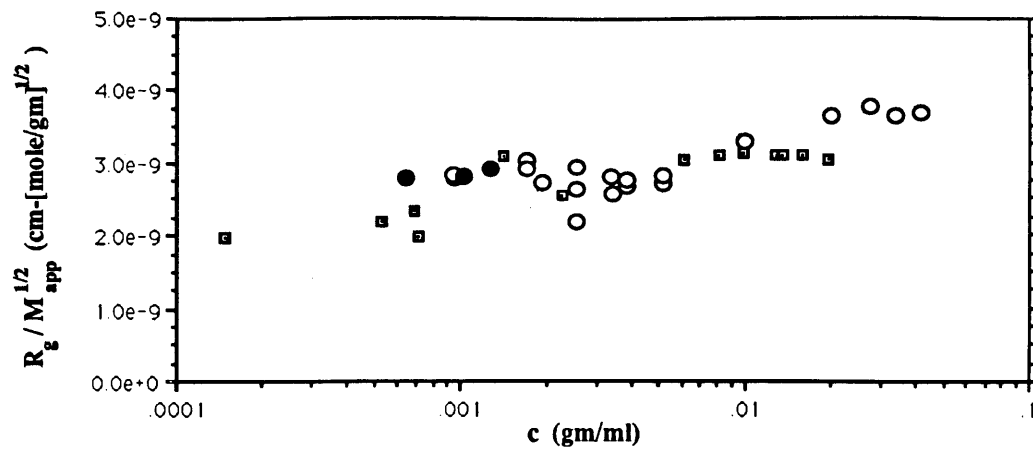


**Figure 5-25:** The same data as in Fig. 5-24 presented on a semi-log plot to elucidate the low concentration regime.

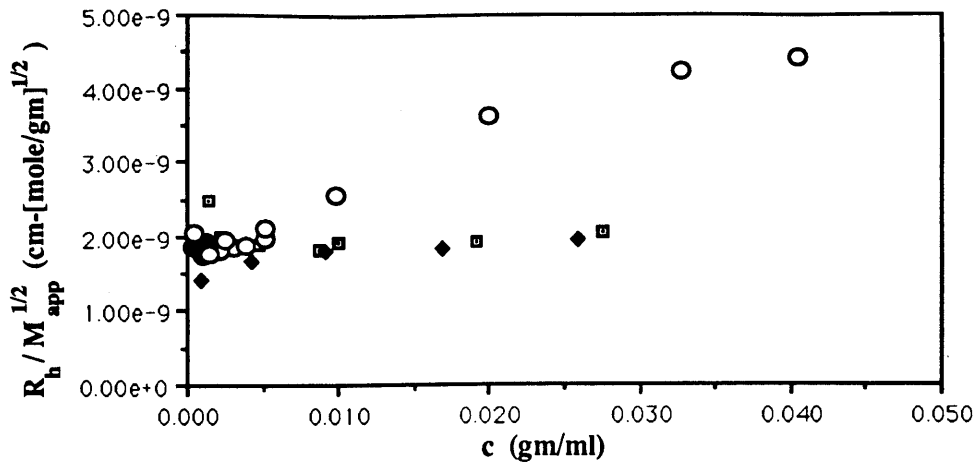


**Figure 5-26:** The ratio  $\frac{R_h}{M_{app}^{1/2}}$  versus concentration for di-C<sub>7</sub> lecithin-water, and di-C<sub>8</sub> lecithin-water solutions.

The open circles are derived from the data given earlier for the di-C<sub>8</sub> lecithin - H<sub>2</sub>O solutions on the 55° C. isotherm which is 10° C. above the upper consolute point. The critical isochore is near 0.020 gm/ml ( $X = 0.0007$ ) as indicated by the minimum in the osmotic susceptibility data of Fig. 5-21. The closed circles (bunched up at low concentration) are from di-C<sub>8</sub> lecithin solutions on the 35° C. isotherm. These data points are in the one phase region on the low concentration side of the coexistence curve, see Fig. 5-3. For comparison, data from the di-C<sub>7</sub> lecithin solutions of Sec. 5.2 are also shown: the open squares are from the di-C<sub>7</sub> - H<sub>2</sub>O solutions; and the closed diamonds are from the di-C<sub>7</sub> - D<sub>2</sub>O solutions.

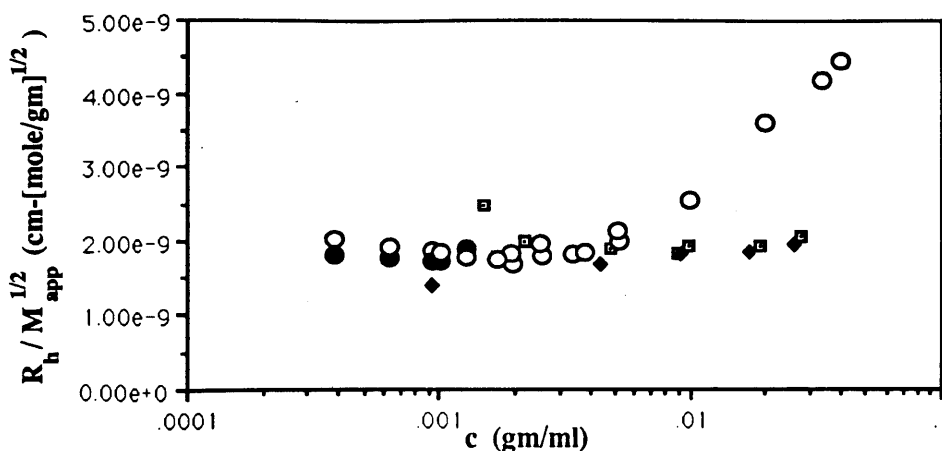


**Figure 5-27:** The data of Fig. 5-26 is replotted on a semi-log graph to elucidate experimental data points at low concentration.

See the figure caption for Fig. 5-26 for an explanation of the data.

like micelle. The disk-like micelle is usually conjectured to resemble a fragment of a lamellar bi-layer, with a thickness corresponding to the bi-layer thickness, and a concentration dependent radius. So, in the case of one dimensional growth, the molecular weight of the micelle is proportional to the contour length of the rod; in the case of two-dimensional growth, the micelle molecular weight is proportional to the square of the disk-micelle radius.

Recall that in Figs. 5-24, and 5-25 we showed that the ratio  $\frac{R_g}{M_{app}^{1/2}}$  had weak concentration dependence despite large changes in  $R_g$ , and  $M_{app}$ . Tausk *et al.* [7] initially observed this weak concentration dependence of  $\frac{R_g}{M_{app}^{1/2}}$  in the di-C<sub>8</sub> lecithin-aqueous buffer micellar system: the buffer composition in their experiments was 10<sup>-2</sup> M phosphate buffer, pH = 6.9, and 0.2 M LiI. By adding the LiI salt they were able to depress the upper consolute point of the liquid-liquid phase separation to well below the 25° C

isotherm on which they made their measurements. According to the later salt dependent coexistence curve position measurements of Haung *et al.* [12], the the upper consolute point would have be depressed to  $\sim 5^\circ$  C with the critical isochore at  $\sim 0.015$  gm/ml: therefore, the measurements of Tausk *et al.* were at least  $20^\circ$  C above the coexistence curve, well into the single phase region.

Tausk *et al.* attempted to interpret the concentration independence of  $\frac{R_g}{M_{app}^{1/2}}$  in terms of single particle properties in order to establish the probable shape of the micelles. They determined that the micelles were unlikely to be disk-like, since the magnitude of  $\frac{R_g}{M_{app}^{1/2}}$  would require that the disks be no thicker than 0.2 nm, whereas the disk model predicts that the thickness be approximately 4 nm, which corresponds to the thickness of a lamellar bi-layer. If the micelles grew as stiff rods, they reasoned that  $R_g$  would be proportional to  $M_{app}$ , rather than the  $M_{app}^{1/2}$  dependence they observed: therefore, they ruled out the stiff rod model. If the micelles grew as random coils, then the coil contour length would be directly proportional the molecular weight of the micelles. Random coil statistics would predict that the contour end to end distance would be proportional to the square root of the contour length. Since the random coil end to end distance is directly proportional to  $R_g$ , random coil statistics predict  $\frac{R_g}{M_{app}^{1/2}} = \text{constant}$ , which is just Tausk *et al.* observed. However, from their measurements of  $M_{app}$  Tausk *et al.* found that the contour lengths of the micelles were too short compared to the contour end to end distance in order to justify applying random coil statistics. They then suggested that the micelle might be worm-like: that is to say the that the micelles might be rod like but with a degree of flexibility They also suggested that the micelles might possibly be branched



worm-like rods: however, as we now shall show, it is not necessary to assume that the micelles are branched rods to explain the data of Tausk *et al.*.

Table 5-1 presents the various predictions for  $R_g$ ,  $R_h$ , and  $M$  for each of four models for micellar shape: sphere, oblate ellipsoid, stiff rod, and worm. The hydrodynamic model for the oblate ellipsoid is from the work of Perrin [13]; the hydrodynamic model for the stiff rod is from the work of Broersma [14]. For the worm like particle, we used the predictions of Yamakawa [15, 16].

The stiff rod model contains a parameter,  $r_{rod}$  which is the radius of the rod cross section. When we apply this model in this chapter, we will assume in all cases that  $r_{rod} = 2$  nm which corresponds to the approximate length of a di-C<sub>8</sub> lecithin molecule [1]. In both the stiff rod model, and in the "worm" model the parameter  $C_L$  is the contour length which is simply the length of the particle if it was stretched out in a straight line. On a short enough segment, the worm-like particle will be locally cylindrical. The parameter  $r_{worm}$  which appears in the "worm" model is analogous to  $r_{rod}$ : it is the radius of the cross section of a "worm" segment. The parameter  $\xi_p$  which also appears in the "worm" model is called the persistence length. The persistence length is a measure of how far one must follow along the length of the contour for the worm to "forget" the direction it was pointing. Formally the persistence length is defined from the relation

$$\exp(-1) = \langle \mathbf{e}(0) \cdot \mathbf{e}(\xi_p) \rangle_{ensemble} \quad (5-6)$$

where  $x$  is the distance along the contour from position 0, and  $\mathbf{e}(x)$  represents the unit normal vector parallel to the direction in space the contour is pointing at  $x$ , where  $x$  is the distance along the contour. The calculation of the molecular weight,  $M$ , requires knowledge of the micelle density  $\rho$ . We used  $\rho = 0.93$  gm/cc which is the value given by Tausk *et al.* for the di-C<sub>7</sub> lecithin micellar system [6].

Based on the predictions contained in Table 5-1, a plot was made of the various theoretical predictions of the dependence of the micelle molecular weight  $M$  on  $R_g$ . The resulting plot is presented in Fig. 5-28 along with the data of Tausk *et al.* which was recovered from Figs. 5 and 6 of reference [7]. Only the high concentration data points of reference [7] are shown because it was not possible to recover the low concentration points unambiguously. The oblate ellipsoid model assumed a fixed semi-minor axis dimension of  $a_2 = 2$  nm corresponding to the approximate long dimension of a di- $C_8$  lecithin molecule [1]. The worm model used to generate the curve labeled "worm" in Fig. 5-28 assumed a local segment radius,  $r_{worm} = 2$  nm, and  $\xi_p = 15$  nm. The stiff rod model also assumed a local segment radius  $r_{rod} = 2$  nm. So the data of Tausk *et al.* which falls in between the curve labeled "worm" and "stiff rod" evidentially could be described by the worm model with a persistence length intermediate between  $\xi_p = 15$  nm, and  $x_p = \infty$ . If a model for one dimensional growth applies such as the worm model, or the stiff rod model, and the segment diameter is 2 nm, then the right hand axis of Fig. 5-28, labeled  $C_L$  gives the contour length of the worm or stiff rod that corresponds to the micelle molecular weight  $M$ . To apply the models of Table 5-1 to the data of Tausk *et al.* we must assume that the dependence of  $M$  on  $R_g$  is dominated by single particle effects rather than collective interactions, and we do not really have a sufficient evidence to justify that assumption. Therefore, we have not attempted to find the exact value of the worm model parameter  $\xi_p$  which fits the data of Tausk *et al.*, because to do so might be misleading about the extent we really understand this system.

Whereas Tausk *et al.* made their measurements on a system with relatively high salt

Table 5-1: Various predictions for  $R_g$ ,  $R_h$ , and  $M$  based on micellar shapes.

...shape...	... $R_g$ ...	... $R_h$ ...	... $M$ (gm/mole)...	...source...
sphere	$\sqrt{3/5} r_{sphere}$	$r_{sphere}$	$\frac{4\pi}{3} r_{sphere}^3 \rho N_a$	$R_g$ : Eq. (4-17)
oblate ellipsoid	$(\frac{2a_1^2}{5} + \frac{a_2^2}{5})^{1/2}$	$\frac{a_2(x^2 - 1)^{1/2}}{\text{atan}((x^2 - 1)^{1/2})}$ $x \equiv a_1/a_2$	$\frac{4\pi}{3} a_1^2 a_2 \rho N_a$	$R_h$ : Perrin 1936; Tanford 1961, p. 327 $R_g$ : Eq. (4-16) $a_1$ = semi-major axis $a_2$ = semi-minor axis
rod	$(\frac{C_L^2}{12} + \frac{r_{rod}^2}{2})^{1/2}$	$\frac{C_L}{2s - 0.19 - 8.24/s + 12/s^2}$ $s \equiv \ln(C_L/r_{rod})$	$\pi r_{rod}^2 C_L \rho N_a$	$R_h$ : Broersma 1960 $R_g$ : Eq. (4-16)
worm	$[C_L \xi_p / 3 - \xi_p^2 + 2\xi_p^3 / C_L - (2\xi_p^4 / C_L^2)(1 - \exp(-\frac{C_L}{\xi_p}))]^{1/2}$		$\pi r_{worm}^2 C_L \rho N_a$	$R_g$ : Yamakawa 1971 $R_h$ : Yamakawa 1973
		$L < \sigma$ $L \xi_p / (A_1 L^{1/2} + A_2 + A_3 / L^{1/2} + A_4 / L + A_5 / L^{3/2})$		
		$L > \sigma$ $L \xi_p / (C_1 \ln(L/D) + C_2 + C_3 L + C_4 L^2 + C_5 L^3 + C_6 (D/L) \ln(L/D) + C_7 (D/L) + C_8 (D/L)^2 + C_9 (D/L)^3 + C_{10} (D/L)^4)$		
		$D \equiv R/\xi_p$ $L \equiv \frac{C_L}{2\xi_p}$ $\sigma \equiv 2.278$		

(continued on next page)

$$\begin{aligned}
A_1 &\equiv 1.843 \\
A_2 &\equiv -(1 - 0.01412D^2 + 0.00592D^4)\ln(D) - 1.0561 - 0.1667D \\
&\quad - 0.190D^2 - 0.0224D^3 + 0.019D^4 \\
A_3 &\equiv 0.1382 + 0.6910D^2 \\
A_4 &\equiv -(0.04167D^2 + 0.00567D^4)\ln(D) - 0.3301 + 0.5D \\
&\quad - 0.5854D^2 - 0.0094D^3 - 0.0421D^4 \\
A_5 &\equiv -0.0300 + 0.1209D^2 + 0.0259D^4 \\
C_1 &\equiv 1 - 0.01412D^2 + 0.00592D^4 \\
C_2 &\equiv 0.3863 - 0.1667D + 0.0016D^2 - 0.0224D^3 - 0.0007D^4 \\
C_3 &\equiv 0.1667 + 0.0222D^2 + 0.0017D^4 \\
C_4 &\equiv 0.01883 - 0.00789D^2 - 0.00038D^4 \\
C_5 &\equiv -0.002039 + 0.000805D^2 + 0.000017D^4 \\
C_6 &\equiv 0.04167D + 0.00567D^3 \\
C_7 &\equiv 0.5 + 0.0786D - 0.0094D^2 + 0.0107D^3 + 0.0039D^4 \\
C_8 &\equiv -0.06250 + 0.00132D^2 - 0.00055D^4 \\
C_9 &\equiv 0.001302D + 0.000181D^3 \\
C_{10} &\equiv 0.001953 - 0.000064D^2 + 0.00027D^4
\end{aligned}$$

Table 5-1 continued

concentration to suppress the coexistence curve, in this study we made measurements on di-C<sub>8</sub> lecithin in pure water. The data  $M$  versus  $R_g$  dependence of this data from the 55 ° C isotherm is presented in Figs. 5-29 and 5-30 as open circles. The closed circles in Fig. 5-30 are data from the 35° C isotherm. This data is from the entire concentration range over which we were able to measure  $R_g$ :  $0.001 \text{ gm/ml} < c < 0.040 \text{ gm/ml}$ , see fig. 5-19. The low concentration part of this data coincides with the theoretical prediction for stiff rods of Table 5-1, with  $r_{rod} = 2 \text{ nm}$ . The low concentration points are from  $c < 0.006 \text{ gm/ml}$ , and  $R_g < 25 \text{ nm}$ .

Figs. 5-31, and 5-32 show the dependence of  $M$  upon  $R_h$ . The theoretical curves shown in the figures were generated from the equations in Table 5-1 with  $r_{rod} = 2 \text{ nm}$ , as before.

## 5.5 The effects of polydispersity on the deduction of micelle shapes

In this section, we will explore the effects of the expected broad size distributions on the deduction of the previous section that the micelles are stiff rods. To make such an exploration, we need to formulate some kind of plausible size distribution in terms of the molecular weight,  $M$ . The exact characteristics of the distribution are not really that important, since what we are trying to do in this section is just to get a feel for what a very broad distribution of micelle molecular weights might do to our ensemble averages,  $M_w$ ,  $\langle R_g^2 \rangle_z^{1/2}$ , and  $\langle 1/R_h \rangle_{z-1}$ . To make a sample formulation of a broad distribution that may be applicable to micellar systems, we can appeal to the "ladder" model [3, Eq. (23)] which produces an exponentially decaying distribution of micelle molecular weights at a given concentration:

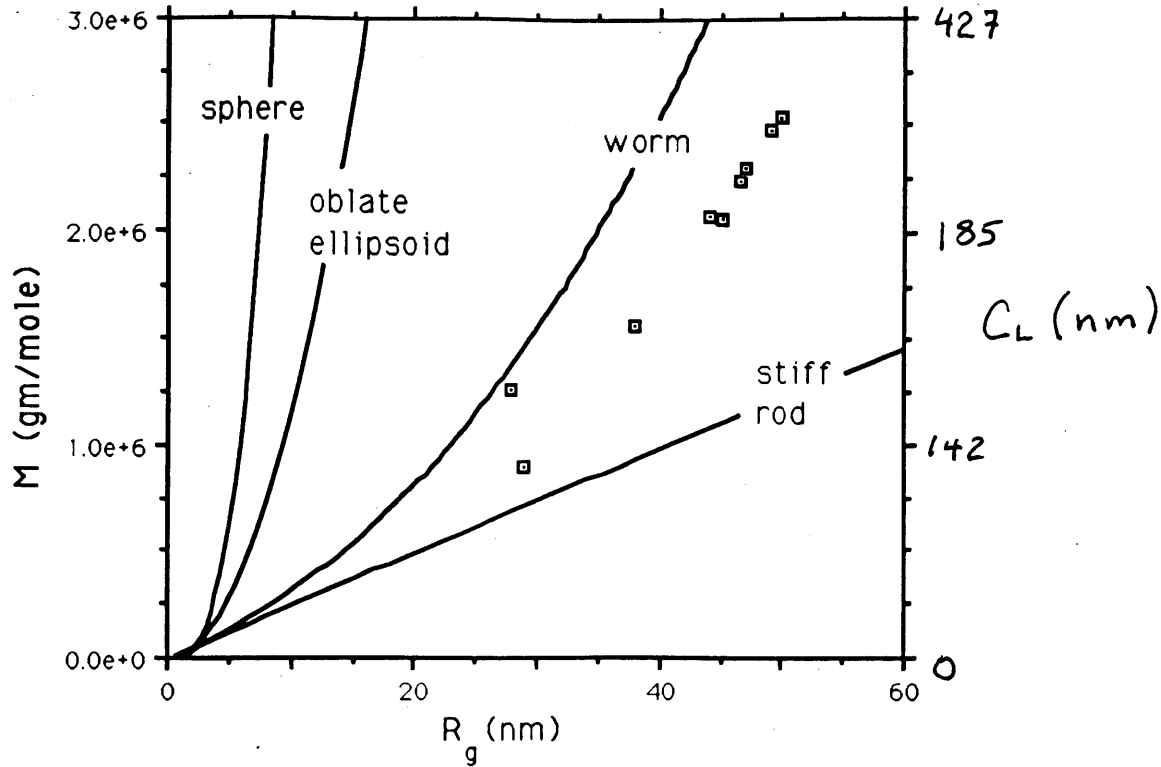


**Figure 5-28:** The molecular weight of di-C<sub>8</sub> lecithin micelles versus  $R_g$  and comparison to various shape dependent predictions.

The data points, presented as open squares, are from the previous work of Tausk *et al.* [7]. They used an aqueous buffer composed of  $10^{-2}$  M phosphate, pH = 6.9, and 0.2 M LiI. The theoretical curve labeled "oblate ellipsoid" was generated from the appropriate equations of Table 5-1, with the assumption that the semi-minor axis was fixed at 2 nm. The theoretical curve labeled "worm" was also generated from the appropriate equations of 5-1 with the assumptions that the local worm cross section was fixed at 2 nm, and the persistence length was  $\xi_p = 15$  nm. The curve labeled "stiff rod" also assumed a cross section radius of 2 nm. If this data can be interpreted in terms of single particle properties, then it may indicate that di-C<sub>8</sub> lecithin micelles, under these solution conditions, have a flexible worm like structure, with a local segment cross section radius of 2 nm, and  $15 < \xi_p < \infty$ . The axis labeled  $C_L$  on the right hand side of the figure is the contour length of the micelles if either the stiff rod or the worm model applies.

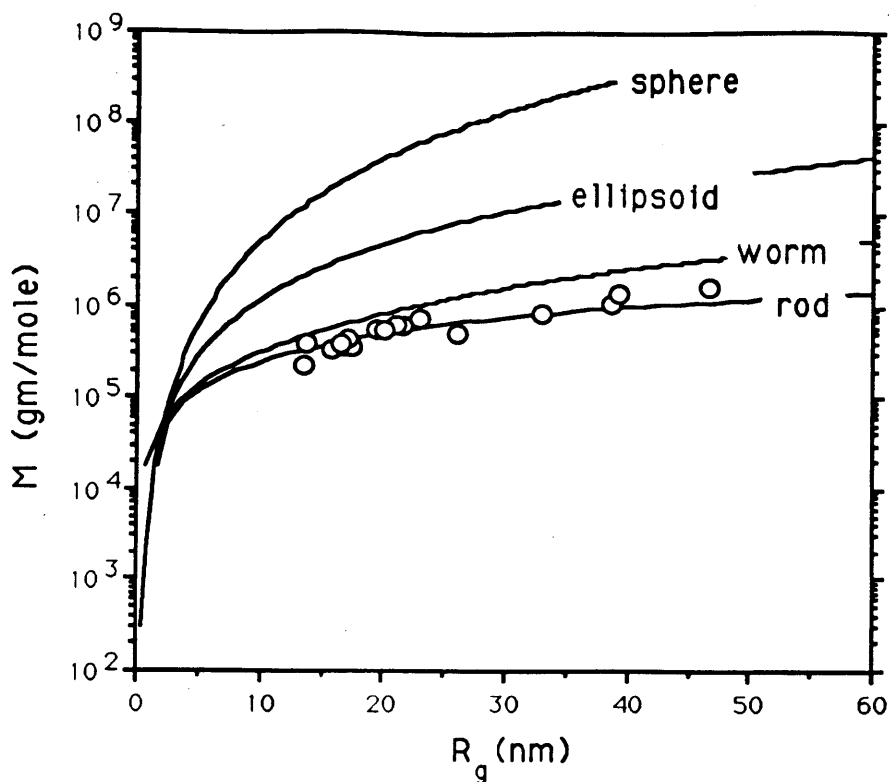


**Figure 5-29:** The molecular weight of di-C<sub>8</sub> lecithin micelles versus  $R_g$  and comparison to various shape dependent predictions.

The data shown as open circles, is from the 55° isotherm of this study. See Fig. 5-3 for the position of this isotherm with respect the coexistence curve for liquid-liquid phase separation. The data shown is derived from Figs. 5-16 and 5-19. Data from all concentrations are shown. The theoretically predicted curve for the stiff rod micelle molecular weight dependence on  $R_g$  is labeled "rod" in the figure, and it assumes a rod diameter of 2.0 nm. The theoretically predicted curve for the worm-like flexible micelle molecular weight dependence is labeled "worm" in the figure, and it assumes a local segment diameter of 2.0 nm and a persistence length of 15 nm. The theoretically predicted curve for the oblate ellipsoid micelle molecular weight dependence is labeled "ellipsoid" in the figure, and it assumes an ellipsoid semi-minor axis of 2.0 nm. The theoretically predicted curve for the spherical micelle molecular weight dependence is labeled "sphere" in the figure.

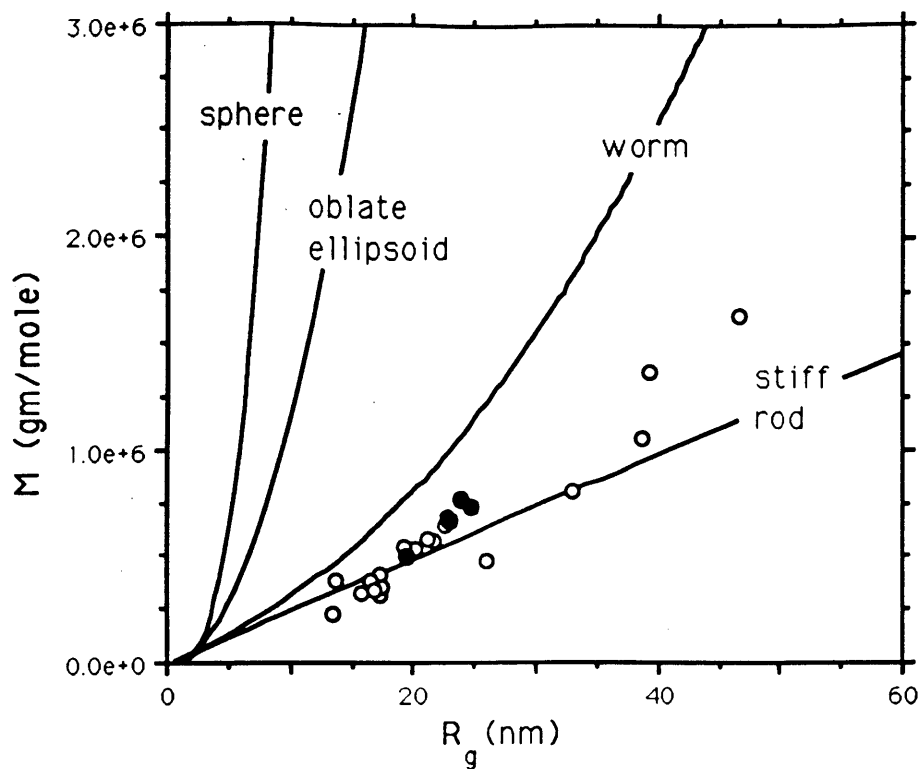


**Figure 5-30:** The molecular weight of di-C<sub>8</sub> lecithin micelles versus  $R_g$  and comparison to various shape dependent predictions.

The open circles are data from the 55° C isotherm. The closed circles are data from the 35° C isotherm. Pure H<sub>2</sub>O was used as the solvent. Data points with  $R_g < 25$  nm are from the low concentration regime:  $c < 0.006$  gm/ml.



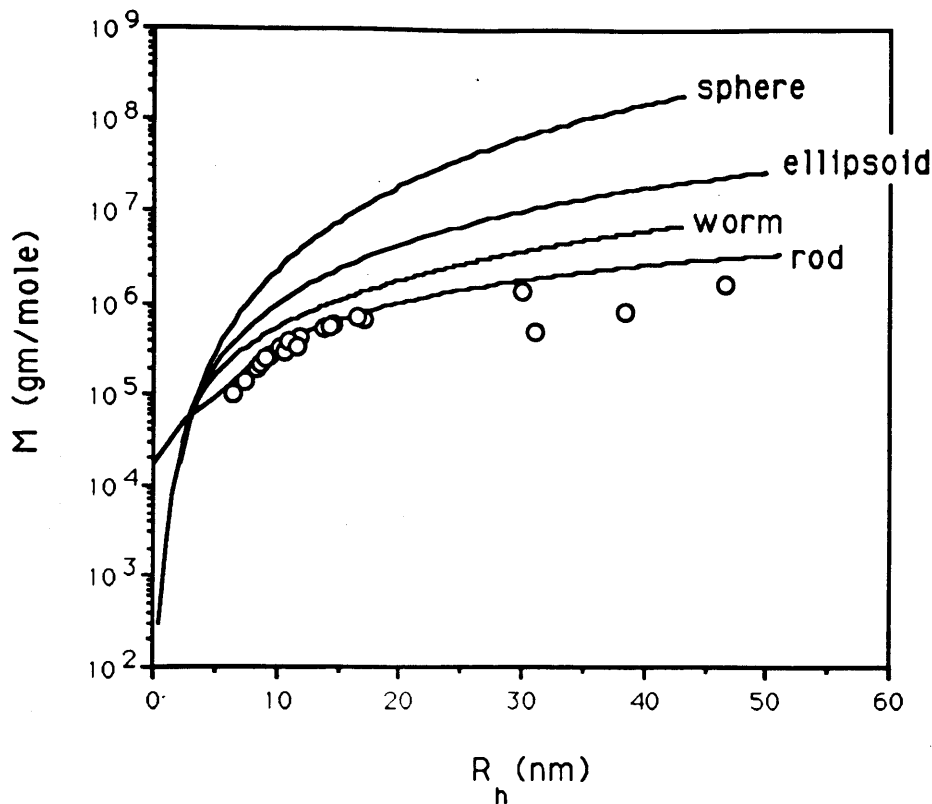


**Figure 5-31:** The molecular weight of di- $C_8$  lecithin micelles versus  $R_h$  and comparison to various shape dependent predictions.

The data shown as open circles, is from the  $55^\circ$  isotherm of this study. See Fig. 5-3 for the position of this isotherm with respect the coexistence curve for liquid-liquid phase separation. The data shown is derived from Figs. 5-16 and 5-19, and data from all concentrations are shown. The theoretically predicted curve for the stiff rod micelle molecular weight dependence on  $R_h$  is labeled "rod" in the figure, and it assumes a rod diameter of 2.0 nm. The theoretically predicted curve for the worm-like flexible micelle molecular weight dependence is labeled "worm" in the figure, and it assumes a local segment diameter of 2.0 nm and a persistence length of 15 nm. The theoretically predicted curve for the oblate ellipsoid micelle molecular weight dependence is labeled "ellipsoid" in the figure, and it assumes an ellipsoid semi-minor axis of 2.0 nm. The theoretically predicted curve for the spherical micelle molecular weight dependence is labeled "sphere" in the figure.

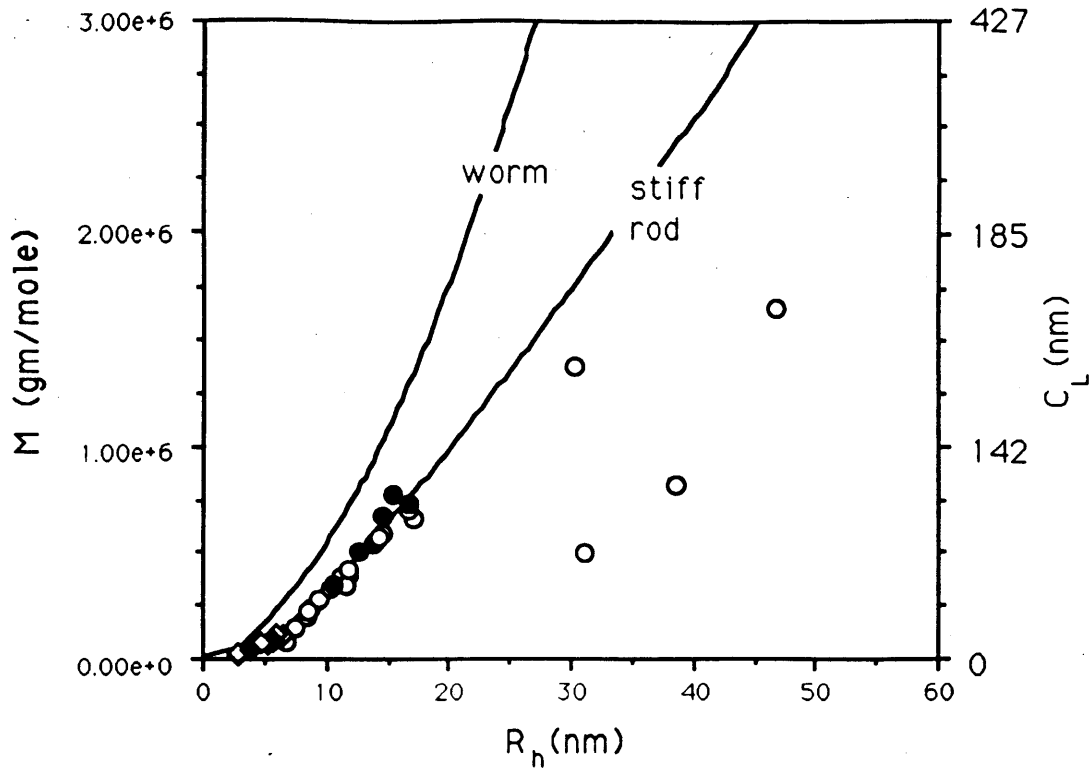


**Figure 5-32:** The molecular weight of di-C<sub>8</sub> lecithin, and di-C<sub>7</sub> lecithin micelles versus  $R_h$  with comparison to various shape dependent predictions

The data from the di-C<sub>8</sub> lecithin micellar system on the 55° C isotherm are shown as open circles. The di-C<sub>8</sub> lecithin data from the 35° C isotherm are shown as closed circles. For the di-C<sub>8</sub> lecithin isotherm data, points with  $R_h < 20$  nm are from the low concentration regime:  $c < 0.006$  gm/ml. The closed diamonds near the origin are data from the di-C<sub>7</sub> lecithin system in H<sub>2</sub>O solvent. The open diamonds are from the di-C<sub>7</sub> lecithin system in D<sub>2</sub>O solvent. The right hand axis is labeled  $C_L$  designates the contour length of a worm-like, or rod-like micelle with a molecular weight corresponding to the left hand axis, and assuming that  $r_{rod} = r_{worm} = 2$  nm.

$$f(M) = A \exp\left(\frac{-M}{B}\right) \quad (5-7)$$

with

$$M \geq M_0$$

where  $f(M)$  is a distribution function proportional to the number of micelles with molecular weight  $M$ ,  $A$  is a normalization constant, and  $B$  is a parameter that defines the width of the distribution, and will be shown to be related to the average micelle molecular weight.  $M_0$  is the molecular weight of a "minimum" micelle.

We can use Eq. (5-7) to determine the number average molecular weight,  $M_N$ :

$$M_N = \frac{\int_{M_0}^{\infty} dM M \exp\left(\frac{-M}{B}\right)}{\int_{M_0}^{\infty} dM \exp\left(\frac{-M}{B}\right)} \quad (5-8)$$

If we want to get fancy, we can also determine  $M_N$  in terms of a moment generating function,  $G(t)$ , which we define as

$$G(x) = \int_{M_0}^{\infty} dM \exp(Mx) \exp\left(\frac{-M}{B}\right). \quad (5-9)$$

Therefore, we can write,

$$M_N = \frac{G^1(0)}{G(0)} \quad (5-10)$$

where  $G^1(0) = \left. \frac{dG(x)}{dx} \right|_{x=0}$ . We can also write  $M_w$ ,  $M_z$ ,  $M_{z+1}$ , and etc..., in terms of the

moment generating function, giving

$$M_w = \frac{G^2(0)}{G^1(0)} \quad (5-11)$$

$$M_z = \frac{G^3(0)}{G^2(0)}$$

$$M_{z+1} = \frac{G^4(0)}{G^3(0)}$$

where  $G^l(0) = \left. \frac{d^l G(x)}{dx^l} \right|_{x=0}$ .

Suppose there exists a function of  $M$ ,  $h(M)$ , and we wish to find its number weighted average,  $\langle h \rangle_N$ , its weight weighted average,  $\langle h \rangle_w$ , and its so-called z weighted average,  $\langle h \rangle_z$ . Using the distribution of Eq. (5-7), these averages are defined as

$$\langle h \rangle_N = \frac{\int_{M_0}^{\infty} dM h \exp\left(\frac{-M}{B}\right)}{\int_{M_0}^{\infty} dM \exp\left(\frac{-M}{B}\right)} \quad (5-12)$$

$$\langle h \rangle_w = \frac{\int_{M_0}^{\infty} dM h M \exp\left(\frac{-M}{B}\right)}{\int_{M_0}^{\infty} dM M \exp\left(\frac{-M}{B}\right)} \quad (5-13)$$

$$\langle h \rangle_z = \frac{\int_{M_0}^{\infty} dM h M^2 \exp\left(\frac{-M}{B}\right)}{\int_{M_0}^{\infty} dM M^2 \exp\left(\frac{-M}{B}\right)} \quad (5-14)$$

If the distribution is not too broad, then it follows that  $M_0$  is similar to  $M_N$ . The converse is, if the distribution is very broad, then  $M_0$  must be very small compared to  $M_N$ , that is  $M_0 \ll M_N$ . So, without making too much error in Eq. (5-8), we can take  $M_0 = 0$  in which case the integrals in the numerator and the denominator of Eq. (5-8) can be identified as gamma functions. Recall that the definition of a gamma function is

$$\Gamma(a) \equiv K^a \int_0^{\infty} t^{a-1} \exp(-Kt) dt \quad (5-15)$$

from which we can write Eq. (5-8) as

$$M_N = \frac{B^2 \Gamma(2)}{B \Gamma(1)} = B \frac{1!}{0!} = B \quad (5-16)$$

Referring back to Fig. 5-32, we will regard the experimental points,  $M_{app}$ , as approximately equal to the weight averaged molecular weight,  $M_w$ . Although there is probably no good way to check this validity assumption, it is more likely to be true at the

lowest concentrations. On the the other hand, we may regard the theoretically generated curves as functions of  $R_h$ . That is, for each value of  $R_h$ , we can generate a point on the theoretical curve,  $M_{theoretical}$ . Now,  $R_h$  is really the average  $\langle \frac{1}{r_h} \rangle_z^{-1}$  which makes the type of average implied in  $M_{theoretical}$  a little bit complicated.<sup>2</sup>

Before getting into the complications of  $M_{theoretical}$  we will first examine the ratios  $\frac{M_w}{M_n}$ ,  $\frac{M_z}{M_w}$ ,  $\frac{M_{z+1}}{M_z}$ , given the distribution in Eq. (5-7), and  $M_0 = 0$ . Using the above equations we have

$$\frac{M_w}{M_n} = \frac{\int_0^\infty dM M^2 \exp\left(\frac{-M}{B}\right) \int_0^\infty dM \exp\left(\frac{-M}{B}\right)}{\int_0^\infty dM M \exp\left(\frac{-M}{B}\right) \int_0^\infty dM M \exp\left(\frac{-M}{B}\right)} = \frac{2! 0!}{1! 1!} = 2 \quad (5-17)$$

$$\frac{M_z}{M_w} = \frac{\int_0^\infty dM M^3 \exp\left(\frac{-M}{B}\right) \int_0^\infty dM M \exp\left(\frac{-M}{B}\right)}{\int_0^\infty dM M^2 \exp\left(\frac{-M}{B}\right) \int_0^\infty dM M^2 \exp\left(\frac{-M}{B}\right)} = \frac{3! 1!}{2! 2!} = \frac{3}{2} \quad (5-18)$$

$$\frac{M_{z+1}}{M_z} = \frac{\int_0^\infty dM M^4 \exp\left(\frac{-M}{B}\right) \int_0^\infty dM M^2 \exp\left(\frac{-M}{B}\right)}{\int_0^\infty dM M^3 \exp\left(\frac{-M}{B}\right) \int_0^\infty dM M^3 \exp\left(\frac{-M}{B}\right)} = \frac{4! 2!}{3! 3!} = \frac{4}{3} \quad (5-19)$$

It is interesting to note from the above comparisons that the higher order averages have better agreement with one another.

$M_{theoretical}$  depends on the particle volume which was inferred from  $R_h$  by inter-

<sup>2</sup>In this section, when we refer to the hydrodynamic radius in lower case, i.e.  $r_h$ , then we will be referring to the size of a single particle in the ensemble;  $R_h$  will refer to the ensemble average measured with the light scattering experiment, i.e.  $R_h = \langle \frac{1}{r_h} \rangle_z$ . (See Sec. 4.5)

preting  $R_h$  in the context of a particular particle shape, see Table 5-1. For example, if we consider the equation for the stiff rod  $R_h$  in the limit that  $C_L \gg r_{rod}$  (i.e., a long skinny rod), then

$$r_h = \frac{C_L}{2 \ln(C_L/r_{rod})} \equiv L X(L) \quad (5-20)$$

where  $X(L)$  is a very slowly changing function of  $L$ . Since  $X(L)$  changes very slowly as  $L$  is increased, Eq. (5-20) is approximately linear in  $L$  (for  $L \gg r_{rod}$  over a restricted range of less than one decade in  $L$ ). Inspection of the curve labeled "stiff rod" in Fig. 5-32 confirms the above argument about the linearity of  $r_h$ . Therefore, substituting Eq. (5-20) into the equation for the rod molecular weight from Table 5-1 gives

$$M_{theoretical} = \pi r_{rod}^2 \rho N_a \frac{r_h}{X(L)} \quad (5-21)$$

which is to say,

$$\frac{1}{M_{rod}} \sim \frac{1}{r_h} \quad (5-22)$$

where we are using the symbol  $\sim$  to mean that the quantity on the left varies approximately like the quantity on the right. So it follows from Eq. (5-22) that for long, skinny rods,

$$\left\langle \frac{1}{r_h} \right\rangle_z^{-1} \sim \left\langle \frac{1}{M} \right\rangle_z^{-1} \quad (5-23)$$

which means that

$$M_{theoretical} \approx \left\langle \frac{1}{M} \right\rangle_z^{-1}. \quad (5-24)$$

So for long skinny rods,

$$\frac{M_{app}}{M_{theoretical}} = M_w \left\langle \frac{1}{M} \right\rangle_z \quad (5-25)$$

$$= \frac{\int_0^{\infty} dM M^2 \exp\left(\frac{-M}{B}\right) \int_0^{\infty} dM \left(\frac{1}{M}\right) M^2 \exp\left(\frac{-M}{B}\right)}{\int_0^{\infty} dM M \exp\left(\frac{-M}{B}\right) \int_0^{\infty} dM M^2 \exp\left(\frac{-M}{B}\right)} = \frac{2! 1!}{1! 2!} = 1.$$

Our simplified analysis does indicate that polydispersity would have no effect on our deduction from Fig. 5-32 that the particles are stiff rods.

Now we will consider the effects of polydispersity on deduction of Fig. 5-30 that the micelles form stiff rods. Inspection of Table 5-1 shows that when  $C_L \gg R_g$ , then  $C_L \sim \langle R_g^2 \rangle_z^{1/2}$ . Also, we have from Table 5-1, that  $C_L \sim M_{theoretical}$ ; therefore, we have in the limit  $C_L \gg R_g$ ,  $M_{theoretical} \sim \langle R_g^2 \rangle_z^{1/2}$ . This gives

$$M_{theoretical} = \langle M^2 \rangle_z^{1/2} \quad (5-26)$$

We are now in a position to compare  $M_{app}$  with  $M_{theoretical}$ :

$$\frac{M_{app}}{M_{theoretical}} = \frac{M_w}{\langle M^2 \rangle_z^{1/2}} \quad (5-27)$$

$$= \frac{\int_0^{\infty} dM M^2 \exp\left(\frac{-M}{B}\right) \left[ \int_0^{\infty} dM M^2 \exp\left(\frac{-M}{B}\right) \right]^{1/2}}{\int_0^{\infty} dM M \exp\left(\frac{-M}{B}\right) \left[ \int_0^{\infty} dM M^2 M^2 \exp\left(\frac{-M}{B}\right) \right]^{1/2}}$$

$$= \frac{2! [2!]^{1/2}}{1! [4!]^{1/2}} = 0.56$$

From the above comparison between the ensemble averages implied in  $M_w$  and  $M_{theoretical}$ , it is possible that the data presented in Fig. 5-30 may fall in a range which fit the worm model better than the stiff rod model. That is to say, the data and models of Fig. 5-30 indicate that the micelles may be stiff rods or worms.

## 5.6 Conclusion

In this chapter we used static light scattering to deduce the magnitude of the ladder model micelle growth potential  $\ln(K)$  in solutions of di-C<sub>7</sub> lecithin mixed with pure D<sub>2</sub>O and found agreement with the earlier results of Chen *et al.* who used small angle neutron scattering. We also measured  $\ln(K)$  in a solution of di-C<sub>7</sub> lecithin mixed with pure H<sub>2</sub>O and found a slightly smaller value indicating less of a tendency for micelles to grow in H<sub>2</sub>O as compared to D<sub>2</sub>O.

We measured  $\ln(K)$  for di-C<sub>8</sub> lecithin in pure water using static light scattering and found that our result was consistent with the earlier result of Thurston who estimated a possible range of values for  $\ln(K)$ . Thurston estimated  $\ln(K)$  by using dynamic light scattering, and then interpreting his results in the context of an assumed model for the micelle shape.

We also compared our experimental results for the osmotic susceptibility in the di-C<sub>8</sub> lecithin system along the 55° C isotherm with the explicit predictions of the theory of Thurston, Blankschtein, Fisch, and Benedek [10]. According to our comparison, the prediction underestimates the osmotic susceptibility by almost an order of magnitude along this isotherm. This discrepancy may mean that the theory of Thurston *et al.* may need modification before it can be extended to include the di-C<sub>8</sub> lecithin micellar system.

Finally we used both static light scattering, and dynamic light scattering to deduce that both di-C<sub>7</sub> lecithin micelles, and di-C<sub>8</sub> lecithin micelles, in pure water, form stiff rods (or possibly worms, in the case of di-C<sub>8</sub> lecithin) of diameter 4 nm.



## References for Chapter 5

- [1] G. M. Thurston.  
*Studies of Phase Separation in Micellar Solutions.*  
PhD thesis, Massachusetts Institute of Technology, 1986.
- [2] R. J.M. Tausk, J. Th. G. Overbeek.  
Physical Chemical Studies Of Short-Chain Lecithin Homologues. IV. A Simple Model For The Influence Of Salt And The Alkyl Chain Length On The Micellar Size.  
*Biophysical Chem.* 2:64, 1974.
- [3] P.J. Missel, N.A. Mazer, G.B. Benedek, C.Y. Young.  
Thermodynamic Analysis of the Growth of Sodium Dodecyl Sulfate Micelles.  
*J. Phys. Chem.* 84():1044 - 1057, 1980.
- [4] N.A. Mazer, G.B. Benedek, M.C. Carey.  
Quasielastic Light-Scattering Studies of Aqueous Biliary Lipid Systems. Mixed Micelle Formation in Bile Salt-Lecithin Solutions.  
*Biochemistry* 19:601-615, 1980.
- [5] R. J.M. Tausk, J. Karmiggelt, C. Oudshoorn, J. Th. G. Overbeek.  
Physical Chemical Studies Of Short-Chain Lecithin Homologues. I. Influence Of The Chain Length Of The Fatty Acid Ester And Of Electrolytes On The Critical Micelle Concentration.  
*Biophysical Chem.* 1:175-183, 1974.
- [6] R. J.M. Tausk, J. van Esch, J. Karmiggelt, G. Voordouw, J. Th. G. Overbeek.  
Physical Chemical Studies Of Short-Chain Lecithin Homologues. II. Micellar Weights of Dihexanoyl- and Diheptanoyllecithin.  
*Biophysical Chem.* 1:184-203, 1974.
- [7] R. J.M. Tausk, C. Oudshoorn, J. Th. G. Overbeek.  
Physical Chemical Studies Of Short-Chain Lecithin Homologues. III. Phase Separation and Light Scattering Studies on Aqueous Dioctanolylllecithin Solutions.  
*Biophysical Chem.* 2:53-63, 1974.
- [8] S. H. Chen, T. L. Lin, C. F. Wu.  
SANS Study of Structure, Growth, and Polydispersity of Short-Chain Lecithin Micellar Systems. A Ladder Model Analysis.  
*Physics of Amphiphilic Layers.*  
Springer-Verlag, New York, 1987, pages 241-252.
- [9] G. M. Thurston, D. B. Blankschtein, M. R. Fisch, and G. B. Benedek.  
Theory of thermodynamic properties and phase separation of micellar solutions with lower consolute points.  
*J. Chem. Phys.* 84(9):4558-4562, 1986.
- [10] D. Blankschtein, G. M. Thurston, G. B. Benedek.  
Theory of Phase Separation in Micellar Solutions.  
*Phys. Rev. Lett.* 54(9):955-958, 1985.

- [11] D. Blankschtein, G. M. Thurston, G. B. Benedek.  
Phenomenological theory of equilibrium thermodynamic properties and phase separation of micellar solutions.  
*J. Chem. Phys.* **85**(12):7268-7288, 1986.
- [12] Y. X. Huang, G. M. Thurston, D. Blankschtein, and G. B. Benedek.  
The effect of salt identity and concentration on liquid-liquid phase separation in aqueous micellar solutions of C<sub>8</sub>-lecithin.  
*J. Chem. Phys.* **92**(3):1956-1962, 1990.
- [13] F. Perrin.  
*J. Phys. Radium* **7**:1, 1936.
- [14] S. Broersma.  
*J. Chem. Phys.* **32**():1626, 1960.
- [15] H. Yamakawa.  
*Modern Theory of Polymer Solutions*.  
Harper & Row, 1971, pages 56.
- [16] H. Yamakawa, & M. Fuji.  
*Macromolecules* **6**:407, 1973.

## 6. Light Scattering Studies Of Mixed Biological Lecithin and Detergent Micellar Systems

*Certainly scientists will fight hard for a favorite idea, and they are pleased when theories stand up to the test of experience, but they don't sit around wringing their hands when a theory is found wanting. A mismatch between theory and experiment means exciting new problems to be solved, and, eventually, a better theory.*

*From Chet Raymo's column in the Boston Globe, 25-Feb-1991.*

*If everyone always agreed with one another, then the world would be a boring place.*

*Virgil Martinonis, on why he likes discussions about politics.*

### 6.1 Introduction

Physical studies of the shape, and the concentration dependence of the size of mixed detergent-lecithin micelles are vital to development of the basic understanding of how such systems function in biological and pharmaceutical processes such as cholesterol transport [1, 2] and vesicle reconstitution [3].

The lecithin molecule has a zwitterionic phosphoryl-choline head group and a double hydrocarbon tail [4, p. 475]. In the previous chapter, micellar systems composed of pure water, and the short hydrocarbon tail lecithin homologues, di-C<sub>7</sub>, and di-C<sub>8</sub> lecithin were studied. Di-C<sub>7</sub>, and Di-C<sub>8</sub> lecithins are very soluble in pure water and have critical micelle concentrations (CMC) of approximately 1 mg/ml and .1 mg/ml respectively [5].

The lecithins studied in this chapter are the long hydrocarbon tail egg-yolk lecithins (PC) which are nearly insoluble in pure water [4, p. 483]. Egg-yolk lecithins have a heterogeneous mixture of hydrocarbon tail lengths ranging from 16 to 22 carbons long. (Need reference) When mixed with pure water, these lecithin-water mixtures form one phase liquid crystal systems at high lecithin concentrations, or a two phase liquid crystal

plus aqueous system at more dilute lecithin concentrations [4, p. 511]. The liquid crystals formed in the more dilute phase can be converted into lamellar vesicles by several means: sonication, addition of alcohol, dialysis, or aqueous dilution of detergent solubilized lecithin in the form of mixed micelles [4, p. 483, 6].

In this chapter, we will use light scattering to examine the effects of three detergents on the shapes of aqueous lecithin-detergent mixed micelles: octylglucoside (OG) a non-ionic detergent often used for vesicle reconstitution [7, 8]; and two ionic bile-salts sodium taurochenodeoxycholate (NaTCDC), and sodium cholate (NaC) [9]. Detergent-egg yolk lecithin micellar solutions such as the ones we studied can be diluted from a one-phase mixed micellar state into a two-phase lamellar plus aqueous state. In these systems, the dilution toward the multiple phase state is accompanied by strong growth of the molecular aggregates as evidenced by light scattering [10, 11].

Earlier light scattering work by Mazer *et al.* [10] on lecithin-detergent mixed micellar systems focused on the effects of bile salts on the shape sizes of the mixed micelles. They used dynamic light scattering and relative intensity light scattering at one scattering angle to deduce the mixed micellar shape. This deduction was accomplished using the following procedure. The weight averaged molecular weight was assumed to be proportional to the scattered light intensity divided by the molecular weight, an assumption consistent with the Eq. (4-23) which neglects intermicellar interactions. The molecular weight so obtained was on an arbitrary scale and for comparative purposes only since the absolute scattered light intensity, and the refractive index increment was not measured. They compared the dependence of this deduced relative molecular weight on the micelle

hydrodynamic radius obtained from dynamic light scattering, and found that of the three models they considered, stiff rod, sphere, and disk-like, that their data fit the disk-like model best.

The light scattering work presented here expands on the previous work in the following ways: (i) scattered light was detected at twelve scattering angles. Detection at multiple angles allowed extrapolation of the diffusion coefficient to zero scattering angle, extrapolation of the intensity to zero scattering angle, and determination of the radius of gyration  $R_g$  when  $R_g > 10$  nm (limited by stray light from the 1 cm diameter sample cells). (ii) We determined the *absolute* intensity of the scattered light and the refractive index increment  $dn/dc$  of the solutions from which we deduced the micelle apparent molecular weight  $M_{app}$ .

We compared the mixed octylglucoside-lecithin micellar system, the mixed bile salt-lecithin micellar systems, and the simple di-C<sub>8</sub> PC and di-C<sub>7</sub> PC micellar systems, systems using our techniques. We found that our data in the mixed detergent-lecithin systems may be consistent with a model in which the micelles in the lecithin rich regime of the phase diagram grew to form rods and inconsistent with the previously proposed disk-like model. Further, we determined that the earlier, less complete data of Mazer *et al.* is consistent with a worm-like flexible rod model. Our comparison of the ratios  $\frac{R_g}{R_h}$ , and  $\frac{R_h}{M_{app}^{1/2}}$ , from the mixed detergent-lecithin systems and from the pure short chain lecithin micellar systems of the previous chapter, showed remarkable similarity further supporting the conclusion that in all of these systems mixed micellar aggregates form (possibly flexible) rods in the lecithin rich regime of the micellar phase.

### 6.1.1 A critical examination of the previous findings of Mazer *et al.*

In their seminal paper of 1980 on bile salt-lecithin micellar solutions, Mazer, Benedek, and Carey [10] presented light scattering evidence which they felt strongly supported a disk-like morphology for mixed bile salt-lecithin micelles. The proposed disk-like micelles were conjectured to resemble fragments of a lecithin lamellar bilayer, with corresponding thicknesses of 5 nm. In this model, the disk-like micelles would have concentration dependent radii, but a fixed thickness. The experimental foundation for the conclusion of Mazer *et al.* that mixed bile salt-lecithin micelles formed disks is presented in Fig. 6-1 which was photocopied into this thesis from reference [10]. Fig. 6-1 presents the dependence of experimentally measured ratio  $\frac{I}{c}$  versus  $R_h$  for the ternary micellar system composed of taurocholate, egg yolk lecithin, and saline water (0.15 M NaCl). The experimental points presented in this figure are from a range of temperature and concentration conditions:  $0.006 \text{ gm/ml} \leq c \leq 0.025 \text{ gm/ml}$ ; and  $20^\circ \text{ C} \leq T \leq 60^\circ \text{ C}$ . The vertical axis,  $\frac{I}{c}$  is the intensity of light scattered from the solution at one scattering angle divided by the solution concentration. Although it is not directly stated in reference [10], we can infer from a previous publication of Mazer *et al.* (reference [12]), that  $I$  was measured at a  $90^\circ$  scattering angle with a laser light source at  $\lambda_0 = 514 \text{ nm}$ . If micelle interactions can be neglected, then the ratio  $\frac{I}{c}$  is proportional to the micelle weight averaged molecular weight times the micelle angular dependent form factor; that is,  $\frac{I}{c} \sim M_w P(\theta)$  (for example, see Sec. 4.4). The intensities measured were not absolute, they were relative. That is, the experimentally measured light scattering intensities presented in Fig. 6-1 were compared to a single, but unspecified, standard. Since the absolute scat-

tered light intensity was unknown, for the convenience of comparison with theoretical models, Mazer *et al.* normalized the ratio  $\frac{I}{c}$  to be identically one when  $R_h = 5$  nm. The theoretical curves shown in Fig. 6-1 were produced by equations similar to those presented in Table 5-1 of this thesis, and by the appropriate equations for the particle form factor.

Fig. 6-2 is a different representation of the same information as in Fig. 6-1. The  $\frac{I}{c}$  axis is shown in linear form to show more detail. Although curve II', the expected dependence of  $\frac{I}{c}$  on  $R_h$  for polydisperse disks, is closest to the experimental data, it cannot really be characterized as being a very good fit.

A model for the micelle shape that Mazer *et al.* did not consider, is that in which the micelles are flexible, worm-like rods. Such a model has been found appropriate for other micellar systems such as cetylpyridinium bromide (CPB) in aqueous solution where it was found that  $\xi_p = 20$  nm with  $r_{worm} = 3$  nm [13]. In Fig. 6-3, the curve labeled "worm" was generated from the worm equations of Table 5-1 with  $r_{worm} = 2.5$  nm, and  $\xi_p = 15$  nm. The "worm" curve was created by incrementing the contour length,  $C_L$ , in each of the three separate equations for  $R_h$ ,  $R_g$ , and  $M$  in the worm model. The ratio  $\frac{I}{c}$  was then calculated from

$$\frac{I}{c} = A M P(90^\circ) \quad (6-1)$$

where  $A$  is a normalization constant chosen so that  $\frac{I}{c} = 1$  when  $R_h = 5$  nm (to match the way the Mazer data was normalized);  $M$  is the molecular weight from Table 5-1; and  $P(90^\circ)$  is the micelle form factor at the  $90^\circ$  scattering angle. Eq. (4-27) was used to generate an approximate value for  $P(90^\circ)$  based upon the value of  $R_g$ .

There may be faults with the way the curve labeled "worm" in Fig. 6-3 was generated, such as neglecting polydispersity, and the use of an approximate form factor: however, its display does make it clear that the light scattering data of Mazer *et al.* can be explained by a model quite different from the one they originally proposed. In the following sections, we will show that the disk model cannot explain the light scattering data we observed in similar aqueous bile salt-lecithin micellar solutions.

### **6.1.2 Recent small angle neutron scattering work, and electron microscopy work in detergent-lecithin systems.**

In the previous section we saw that the light scattering data of Mazer *et al.* on the taurocholate, egg yolk lecithin micellar could be fairly well fit by the worm model with  $r_{worm} = 2.5$  nm, and  $\xi_p = 15$  nm. Recent small angle neutron scattering work by Hjelm *et al.* [14] on the glycocholate, lecithin micellar system found evidence for rod like particles with  $r_{rod} = 2.7$  nm. No evidence for a disk morphology was found in this system.

Vinson, Talmon, and Walter [15] recently used a cryo-transmission electron microscopy technique to examine micelles formed from octylglucoside and lecithin. Their images revealed that worm like structures were formed. No evidence for disk like micelles was observed in this system.

Vinson, Talmon, and Walter [16] also used their electron microscopy technique to study sodium cholate, lecithin micelles at pH 7.2 and the their images revealed that this material formed rods. No evidence for disk like micelles was observed in this system either.

In light of the above findings, and in light of our alternative explanation of the



original Mazer light scattering data, it does seem that detergent - lecithin micelles form rods or worms, and not disks as was originally proposed.

### **6.1.3 Phase diagrams and dilution paths of the micellar system studied in this work**

As mentioned previously, biological lecithin is nearly insoluble in water by itself. However, its solubility, in the form of micellar aggregates, can be made quite high when certain biological detergents are present. In this chapter, the effects of three different types of biological detergents on lecithin micellar systems will be studied. The detergents are octylglucoside (OG), and the two the bile salts, sodium taurochenodeoxycholate (NaTCDC), and sodium cholate (NaC). Octylglucoside is not a bile salt and has a very different structure compared to the bile salts. The bile salt monomer is a bug shaped molecule with an ionic group at the head, several hydrophylic OH groups on its bottom side, and a hydrophobic, hydro-carbon backbone. In contrast, octylglucoside has a non-ionic head group, and a single 8 carbon, hydro-carbon tail.

Fig. 6-4 shows the approximate ternary phase diagram at 20° for the NaTCDC, lecithin (PC), saline (0.15M NaCl) system at the dilute corner of the phase diagram. For this study, a stock solution at 0.100 gm/ml total lipid concentration was prepared with a NaTCDC to PC molar ratio of 1.7. Light scattering studies were made as the stock solution was diluted with saline solution through the micellar phase along the indicated dilution path. The liquid crystal plus aqueous solution phase boundary was encountered on dilution to 0.001 gm/ml, which is very near the H<sub>2</sub>O vertex in Fig. 6-4. According to dynamic light scattering results presented elsewhere for similar systems [10], and by

static and dynamic light scattering results presented here, the micellar aggregates grow in size as the solution is diluted with the saline buffer.

Figs. 6-5, and 6-6 are phase diagrams for the ternary octylglucoside, PC, and water system; and the ternary NaCholate, PC, and water system.

## 6.2 Experimental Procedures

### 6.2.1 Apparatus

The experiments presented here were performed using the light scattering spectrophotometer described in Chapter 2. This instrument was described in great detail in Chapter 2; however, a short description of it is given here. A vertically polarized argon-ion laser operating at  $\lambda_0 = 488\text{nm}$  was used as the light source. Scattered light was detected at 12 fixed angles spaced equally in  $\log(q(\theta))$  where  $q(\theta) = 4\pi n/\lambda_0 \sin(\theta/2)$ , and  $n$  is the solvent index of refraction,  $\lambda_0$  is the wavelength of incident light *in vacuo*, and the  $\theta$  is the scattering angle which ranged from  $11.5^\circ$  to  $162.6^\circ$ . The instrument employed a circulating, dust free, purified water bath for sample cell index matching, temperature control, and light scattering intensity calibration. All light scattering measurements presented in this chapter were performed at  $20^\circ\text{C}$ .

### 6.2.2 Static Light Scattering.

The key features of the measurement protocol were: (i) rapid and repeated sequential sampling of the transmitted beam intensity,  $I_t$ , and the scattered intensity at each angle,  $I(\theta)$ , (ii) division of  $I(\theta)$  by  $I_t$ , and (iii) averaging of  $I(\theta)/I_t$  (denoted by  $\langle I(\theta)/I_t \rangle$ ). This protocol reduced inaccuracies due to drifts in laser power and photomultiplier response, and it automatically corrected  $I(\theta)$  for sample turbidity, provided that cylindrical scattering cells were used [17].

To determine the samples' Rayleigh ratio,  $R(\theta)$ , we measured  $\langle I_{\text{ref}}(\theta)/I_t \rangle$  from the reference solvents, benzene and toluene (spectrophotometric grade, Aldrich, Milwaukee, Wisconsin), which have known Rayleigh ratios  $R_{\text{ref}}$ .  $R(\theta)$  of the samples were calculated from calculated from [18]

## 606 BIOCHEMISTRY

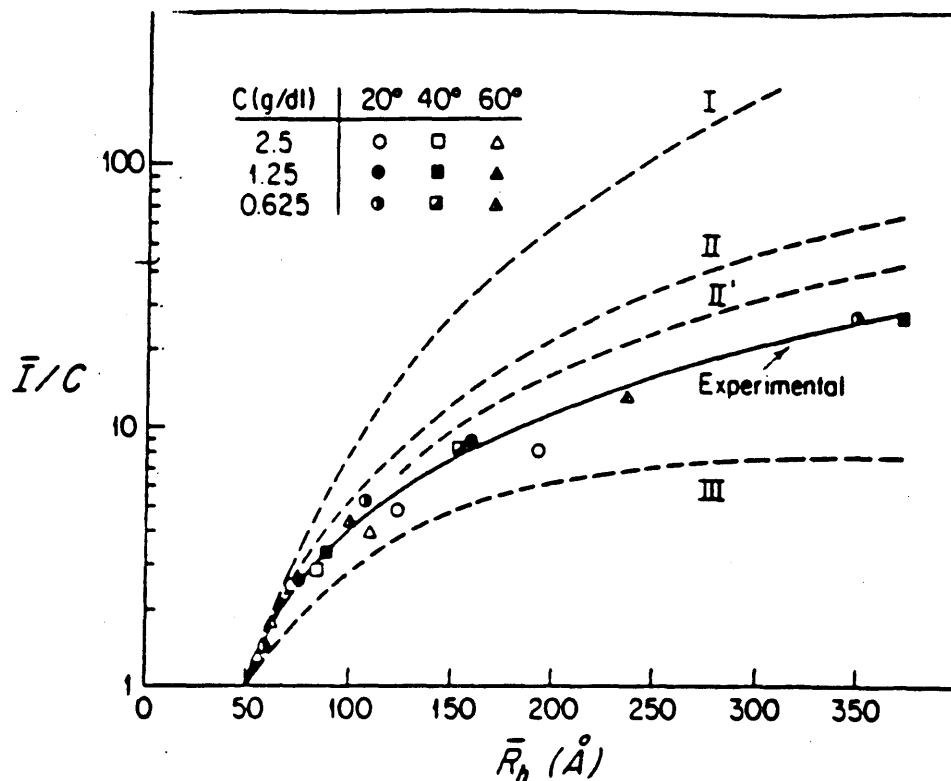


**Figure 6-1:** The light scattering data of Mazer *et al.* from the Taurocholate, lecithin, and water mixed micelle system.

This figure is copied from reference [10], Fig 7. The curves labeled with roman numerals are theoretical predictions based on equations similar to those presented in Table 5-1 of the previous chapter. Curve I is the expected dependence of  $I/c$  on  $R_h$  for spherical micelles; Curve II is the expected dependence of  $I/c$  on  $R_h$  for monodisperse disks; Curve II' is the expected dependence of  $I/c$  on  $R_h$  for polydisperse disks; Curve III is the expected dependence of  $I/c$  on  $R_h$  for stiff rods.  $I/c$  is intensity scattered at  $90^\circ$  scattering angle,  $c$  is the concentration. If interactions are neglected, then the quantity  $I/c$  is proportional to  $M_w P(90^\circ)$  where  $M_w$  is the weight averaged molecular weight of the micelles and  $P(90^\circ)$  is the micelle form factor at  $90^\circ$  scattering angle.

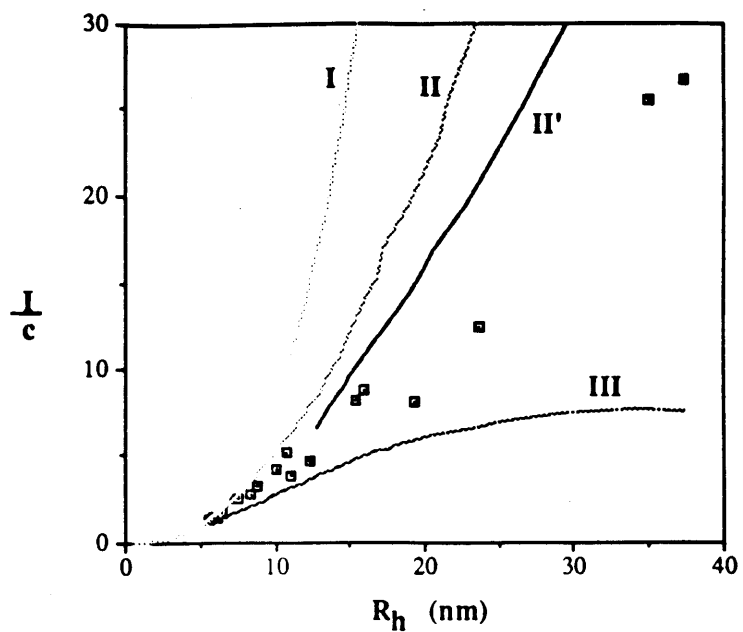


**Figure 6-2:** This is the same information as in Fig. 6-1, except displayed on a linear - linear plot.

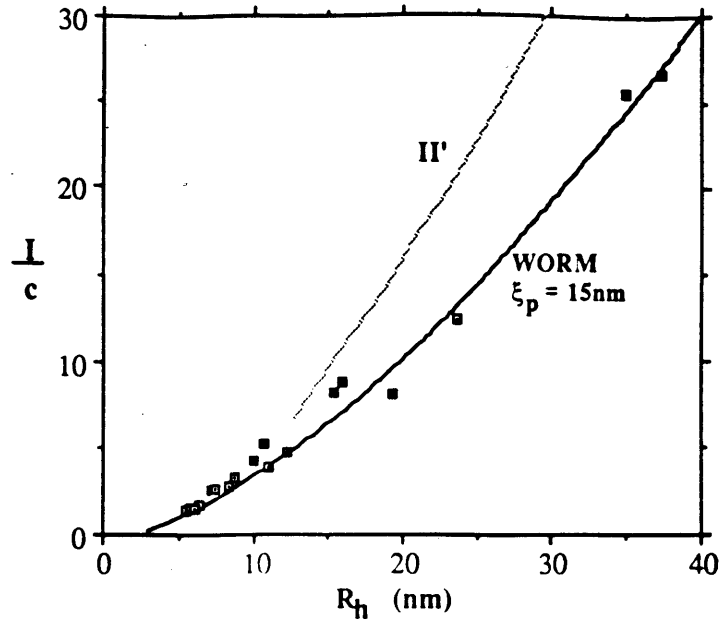


**Figure 6-3:** This the experimental data of Fig. 6-1 displayed along with the new worm model interpretation.

Curve  $II'$  is the theoretical dependence of  $I/c$  versus  $R_h$  for polydisperse disks as presented in Fig. 6-1. The curve labeled "WORM" was produced from the Yamakawa worm model of Table 5-1 as described in the text.

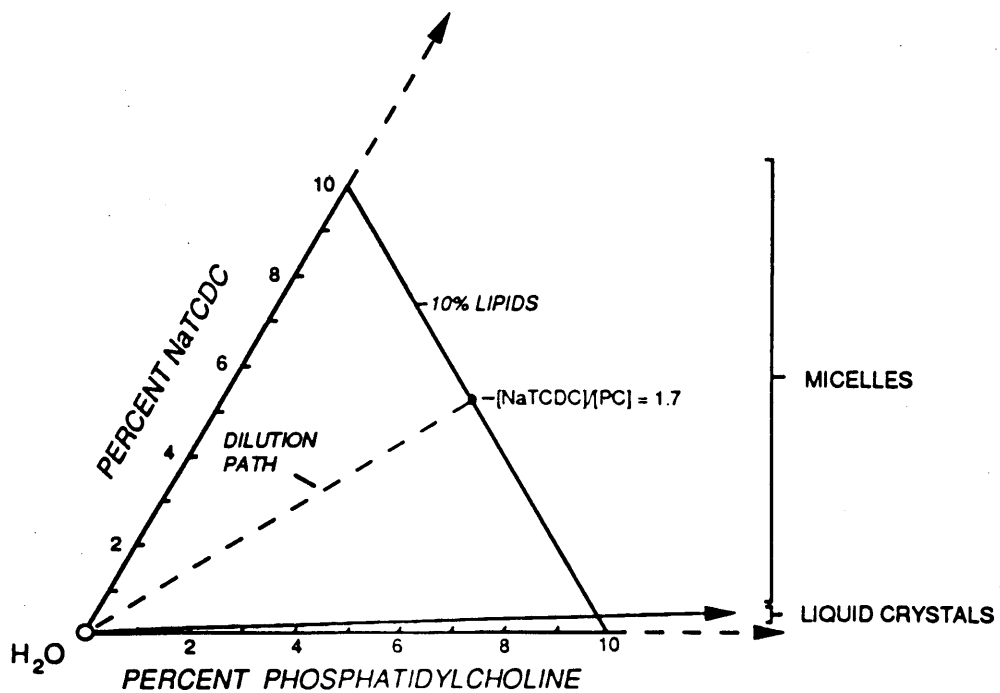


**Figure 6-4:** The phase diagram for the ternary TCDC, lecithin, and saline system.

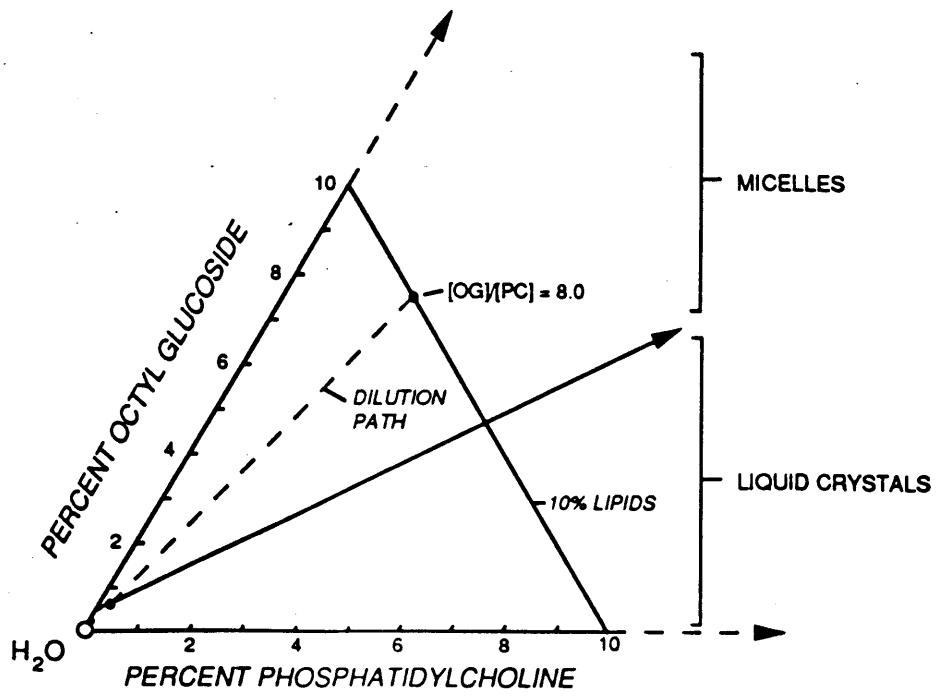


**Figure 6-5:** The phase diagram for the ternary OG, lecithin, and saline system.



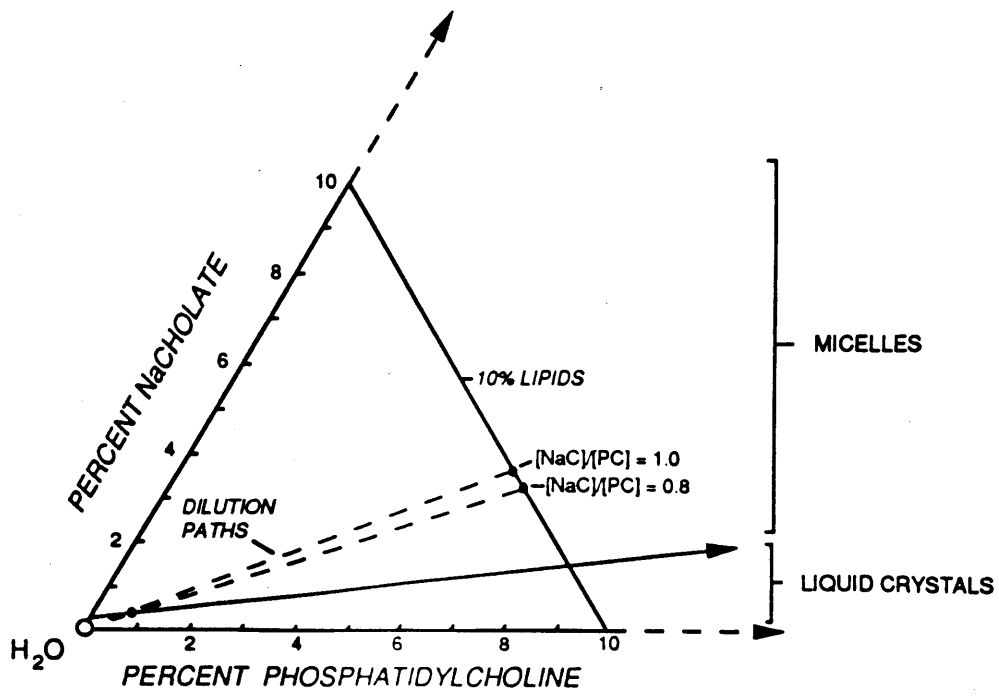


**Figure 6-6:** The phase diagram for the ternary NaC, lecithin, and saline system.

$$R(\theta) = [\langle I(\theta)/I_r \rangle / \langle I_{ref}(\theta)/I_r \rangle] (n/n_{ref})^2 R_{ref} \quad (6-2)$$

where  $R_{ref}$  is the Rayleigh ratio of the reference solvent, and  $n$  and  $n_{ref}$  are the refractive indices of the solution and the reference solvent, respectively. At 23°C and  $\lambda_0 = 488$  nm, we used  $R_{ref} = 39.6 \times 10^{-6} \text{ cm}^{-1}$  for toluene, and  $R_{ref} = 35.4 \times 10^{-6} \text{ cm}^{-1}$  for benzene [19].  $R_{ref}$  and  $n_{ref}$  were compensated for temperature dependence using reported values. [20, 21] The instrument calibration was monitored using the circulating water bath whose Rayleigh ratio was determined to be  $(2.51 \pm .02) \times 10^{-6} \text{ cm}^{-1}$  at  $\lambda_0 = 488\text{nm}$ , by comparison with benzene and toluene.

$R_g$  was determined from fitting  $R(\theta)$  to the form

$$R(\theta)^{-1} = R(0)^{-1} (1 + (1/3)R_g^2 q(\theta)^2). \quad (6-3)$$

The micelle *apparent* molecular weight,  $M_{app}$ , was found using the Debye formula

$$K[c - IMC]/R(0) = 1/M_{app} \quad (6-4)$$

where  $R(0) \equiv \lim_{\theta \rightarrow 0} R(\theta)$ ;  $K = 4\pi^2 n^2 (dn/dc)^2 / \lambda_0^4 N_a$ ;  $c$  is the total lipid concentration;  $IMC$

is the detergent critical micelle concentration; and  $N_a$  is Avogadro's number. If micelle interactions are not significant, then  $M_{app} = M_w$ , where  $M_w$  is the weight averaged molecular weight of all lipid aggregates.

All of the samples studied showed negligible depolarized light scattering (less than 1 part in  $10^3$ ) so no correction for anisotropic scattering was made. For the sodium cholate system, we used  $IMC = 0.003 \text{ gm/ml}$ ; for the sodium taurochenodeoxycholate system, we used  $IMC = 0$ ; and for the octylglucoside system, we used  $IMC = 0.005 \text{ gm/ml}$  [8]. All light scattering measurements were made at 20° C.

### 6.2.3 Dynamic Light Scattering.

Dynamic light scattering measurements were made with the same instrument using all scattering angles. The homodyne autocorrelation function,  $g^2(q, \tau)$ , was collected with a 128 channel Langley Ford model 1096 correlator.  $g^2(q, \tau)$  was reduced with the cumulants method [22] to find the first cumulant,  $\Gamma(q)$ . An effective diffusion coefficient  $D(q)$  was derived from  $D(q) = \Gamma(q)/q^2$ . The extrapolation of  $D(q)$  to zero  $q$ ,  $D(0) \equiv \lim_{q^2 \rightarrow 0} D(q)$  was used to derive a hydrodynamic radius,  $R_h$ , using the Stokes-Einstein equation,

$$R_h = k_B T / 6\pi\eta D(0) \quad (6-5)$$

where  $T$  was the temperature,  $k_B$  is Boltzmann's constant, and  $\eta$  was the solvent viscosity.

### 6.2.4 Materials Preparation.

(i) Grade I egg phosphatidylcholine (Lipid Products, South Nutfield, Surrey, U.K.) was >99% pure by high performance liquid chromatography and thin layer chromatography (2005g application). Sodium cholate (NaC), sodium taurochenodeoxycholate (NaTCDC) and octyl glucoside (OG) (Calbiochem, San Diego, CA) were of the highest available purities (>99% pure by thin layer chromatography).

(ii) Following coprecipitation from stock solutions (CHCl<sub>3</sub>/MeOH 1:1, v:v), dried detergent/phosphatidylcholine lipid films were resuspended in 0.15M NaCl aqueous buffer (containing 0.01M NaHCO<sub>3</sub> - Na<sub>2</sub>CO<sub>3</sub> at pH 9 in the case of NaC) that included 3.0mM NaN<sub>3</sub> as an antimicrobial agent. Prior to dilution for light scattering experiments, prepared solutions were equilibrated at 20°C for at least 24 hours with periodic vortex mixing under an atmosphere of argon.

### 6.2.5 Sample dilution prior to light scattering

Samples were placed in 1cm diameter culture tubes and diluted to the desired concentration with the appropriate solvent and stored under nitrogen. After dilution, samples were mixed with a vortex mixer until optical inspection showed that samples were completely mixed, as evidenced by the absence of an observable index of refraction gradient. After vortex mixing, samples were centrifuged ( $\sim 1300 \times g$ ) at  $20^\circ \text{C}$  for at least 30 minutes to force dust to settle. Samples thus prepared were visually observed to be dust free by inspection with a  $20\times$  microscope at a  $17.4^\circ$  scattering angle before commencing with light scattering experiments.

### 6.2.6 Measured values of $dn/dc$

Table 6-1 gives the refractive index increments,  $dn/dc$  of several of mixed micellar systems under different solvent conditions, and different detergent to lecithin molar ratios. All measurements were made by starting with a 0.10 gm/ml stock solution and measuring the concentration dependence of the index of refraction on an Abbe type refractometer (Bausch and Lomb, model Abbe-3L). In all cases, the index of refraction was observed to be a linear function of concentration.

## 6.3 Light scattering results

Fig. 6-7 shows  $M_{app}^{-1}$  versus concentration for the NaTCDC system along the dilution path indicated previously in Fig. 6-4. Fig. 6-8 show the same data as in Fig. 6-7, except that it is displayed on a log - log plot to elucidate low concentration points. In both figures, there is evident a very abrupt change in the way  $M_{app}^{-1}$  depends on concentration at  $\sim 0.003 \text{ gm/ml}$ . The apparent molecular weight data is displayed as  $M_{app}^{-1}$

**Table 6-1:** Index of refraction increments for several micellar systems at 20° C

Detergent type	Solvent conditions	Detergent/lecithin molar ratio	Remarks	dn/dc (ml/gm)
NaC	0.15 M NaCl	∞	no lecithin	0.174
NaC	0.4 M NaCl	∞	no lecithin	0.179
NaC	0.15 M NaCl	3.0		0.172
NaC	0.15 M NaCl	2		0.170
NaC	0.15 M NaCl	1.0		0.167
NaC	0.15 M NaCl	0.8	T = 20.5 C	0.153
NaC	0.4 M NaCl	1.0		0.157
NaTCDC	0.15 M NaCl	1.67		0.157
OG	0.15 M NaCl	8.0		0.147

to show its suggestively linear dependence on concentration when  $c > 0.003$  gm/ml. If the data at low concentration, for  $0.001$  gm/ml  $< c < 0.003$  gm/ml, can be interpreted in terms of single particle properties, then this data show that  $M_w$  grows dramatically as the lamellar plus aqueous phase boundary is approached by dilution along the path indicated in Fig. 6-4. At  $c = 0.003$  gm/ml,  $M_{app} = 56,000$  gm/mole; and at  $c = 0.001$  gm/ml,  $M_{app} = 2,900,000$  gm/mole.

Fig. 6-9 shows the concentration dependence of the hydrodynamic correlation range,  $\xi_h$ , and the static correlation range,  $\xi_s$ , in the same NaTCDC system. Here we follow the convention previously described in Chapter 5 with regards to using  $\xi_h$  and  $\xi_s$ . That is, when interparticle interactions are not present, then  $\xi_h \equiv R_h$ , and  $R_g \equiv \sqrt{3}\xi_s$ . Fig. 6-9 also shows an abrupt change in the way  $\xi_h$  changes with concentration at about  $0.002$  gm/ml, near the same concentration as the abrupt change in Fig. 6-7.

Light scattering results for  $R_g$ ,  $R_h$  and  $M_{app}$  from the OG system along the dilution path indicated in Fig. 6-5 also showed dramatic growth near the lamellar plus aqueous phase boundary. In this system, at about  $0.020$  gm/ml there was also observed a very abrupt change in the way  $M_{app}$ , and  $\xi_h$  behaved with respect to concentration.

Light scattering results from the NaC system along the two dilution paths indicated in Fig. 6-6, like the above systems, showed dramatic growth near the phase boundary. There was no abrupt change in the way  $M_{app}^{-1}$  behaved with concentration over the range of concentrations studied. However, perhaps by coincidence, or maybe for some deeper reason, the plots of  $M_{app}^{-1}$  versus concentration were also linear over the entire concentration range.

## 6.4 Discussion

Fig. 6-10 shows the all the data of  $M_{app}$  versus  $R_h$  for the NaTCDC system. Also shown for comparison, are the "oblate ellipsoid" model, and the "stiff rod" model which were generated from the equations of Table 5-1. The oblate ellipsoid curve was generated by using an ellipsoid semi-minor axis of  $a_2 = 2.5$  nm and a density of  $\rho = 1.0$  gm/cc. The stiff rod curve was generated by using  $r_{rod} = 2.5$  nm, and  $\rho = 1.0$  gm/cc. The values of  $a_2$ , and  $r_{rod}$  were chosen to correspond to the approximate length of a biological lecithin molecule. As can be seen, the data is not in good agreement with either curve, but it is much closer to the stiff rod curve.

Fig. 6-11 shows a similar plot as Fig. 6-10 for the OG system.

Fig. 6-12 shows the  $M_{app}$  versus  $R_h$  data for the NaC system on the  $[NaC/PC] = 0.8$  dilution path shown previously in Fig. 6-6.

Fig. 6-13 shows the value of the ratio  $\frac{R_h}{M_{app}^{1/2}}$  versus concentration for several of the lecithin micellar systems studied in this thesis. Displayed in this way, all of these systems appear to have the remarkably similar property that  $\frac{R_h}{M_{app}^{1/2}}$  is weakly concentration dependent despite large changes separately in  $R_h$ , and in  $M_{app}$ . Also, the ratio  $\frac{R_h}{M_{app}^{1/2}}$  is very similar in all of these different systems. Note that if these lecithin micellar systems were disk-like micelles of fixed thickness,  $t_{disk}$ , but concentration dependent radii, we could compute the value of  $t_{disk}$  from the magnitude of  $\frac{R_h}{M_{app}^{1/2}}$ . For  $R_h \gg t_{disk}$  it would be expected that the ratio  $\frac{R_h}{M_{app}^{1/2}}$  would be concentration independent, which is suggestive of what we actually observed.

We will now explicitly calculate the value of  $t_{disk}$  from the magnitude of  $\frac{R_h}{M_{app}^{1/2}}$ . For convenience of notation, let  $\frac{R_h}{M_{app}^{1/2}} \equiv A$ . Since we do not have a hydrodynamic model for a disk like object, we will use the formula of Perrin [23] for an oblate ellipsoid from Table 5-1:

$$R_h = (t_{disk}/2) \times ((2r_d)^2/t_{disk}^2 - 1)^{1/2} / \tan^{-1} \{ ((2r_d)^2/t_{disk}^2 - 1)^{1/2} \} \quad (6-6)$$

where  $r_d$  is the disk radius. In the limit that  $r_d \gg t_{disk}$  the Perrin model probably has reasonable correspondence to the case of a large flat disk. In this limit  $R_h = (2/\pi)r_d$ . The molecular weight of the disk,  $M_d$  would be given by

$$M_d = \pi r_d^2 t_{disk} \rho N_a \quad (6-7)$$

From the definition,  $A \equiv R_h/M_{app}^{1/2}$ , it follows that the disk thickness,  $t_{disk}$ , in the limit that  $r_d \gg t_{disk}$  is given by

$$t_{disk} = \{ (\pi^3/4) N_a \rho A^2 \}^{-1} \quad (6-8)$$

where  $\rho$  is the density of the disk material,  $A$  was defined above, and  $N_a$  is Avogadro's number. From Fig. 6-13 we see that  $A = (1.7 \pm 0.2) \times 10^{-2} \text{ nm}/(\text{gm/mole})^{1/2}$  over two decades of concentration. Using this value of  $A$  in Eq. (6-8) along with  $\rho = 10^{-21} \text{ gm/nm}^3$  (1 gm/cc), reveals that  $t_{disk} = 0.7 \pm 0.3 \text{ nm}$ . Since the lecithin bilayer disk micelle model explicitly assumes that  $t_{disk} \sim 5 \text{ nm}$ , our experimental finding of  $t_{disk} = 0.7 \text{ nm}$  shows that the disk model cannot explain the magnitude of the ratio  $\frac{R_h}{M_{app}^{1/2}}$  self consistently.

Mazer *et al.* used a slightly different hydrodynamic model to relate the disk radius to the hydrodynamic radius, see reference [10], Table A1. According to this alternative model, in the limit  $r_d \gg t_{disk}$ , then  $R_h = 3/4 r_{disk}$ , or  $r_{disk} = 4/3 R_h$ . Inserting this alternative relation between  $R_h$  and  $r_d$  into Eq. (6-7) gives



$$t_{disk} = \left[ \frac{16}{9} \pi \rho N_a A^2 \right]^{-1}. \quad (6-9)$$

If we use  $A = 1.7 \times 10^{-2} \text{ nm}/[\text{gm/mole}]^{1/2}$ , and  $\rho = 10^{-21}$ , as in the previous paragraph, then we get  $t_{disk} = 1 \text{ nm}$ . This alternative value of  $t_{disk}$  is much less than the disk the value of 5 nm needed to satisfy the bilayer disk model.

Also shown in Fig. 6-14 is the value of the ratio  $\frac{R_g}{R_h}$  versus concentration for several of the various lecithin micellar systems studied in thesis. For an oblate ellipsoid where  $a_1 \gg a_2$ , the equations of Table 5-1 indicate that the the ratio  $\frac{R_g}{R_h} \sim 1.0$ . (For example, this assertion can be seen graphically in Fig. 4 of reference [24].) If the micelles were elongated objects such as long rods, or random coils, such as worms where  $C_L \gg \xi_p$ , then it would be expected that  $\frac{R_g}{R_h} \geq 1.5$ , which is what is actually indicated in Fig. 6-14. This observation lends even further credence to the assertion that the disk model is inappropriate for describing these micellar systems.

## 6.5 Conclusion

In this chapter we showed that widely accepted disk model of Mazer *et al.* [10] is not very well supported by Mazer *et al.*'s own light scattering data from the taurocholate, lecithin micellar system. However, we did show that the worm model of Table 5-1 could fit Mazer's data, with  $r_{worm} = 2.5 \text{ nm}$ , and  $\xi_p = 15 \text{ nm}$ .

In the introduction to this chapter, we cited several previous findings of other workers who found results at variance with the disk micelle model that was previously expected to apply in the case of mixed detergent, biological lecithin micelles. Hjelm *et al.* [14] used small angle neutron scattering on the glycocholate lecithin micellar system

and found rods of radius 2.7 nm. Vinson *et al.* [15] used a cryo-transmission electron microscope technique on the octylglucoside, lecithin system and found image worm like aggregates, but no disks. Vinson *et al.* [16] also used their technique on the sodium cholate, lecithin micellar system and found images of rods, but no disks in that system either.

In the present work, we examined three mixed-detergent, lecithin micellar systems using the techniques of static and dynamic light scattering, with the purpose of deducing the likely micelle shape. From the light scattering data we measured the dependence of  $M_{app}$ , and  $R_h$  on concentration in the three systems. In Figs. 6-10, 6-11, and 6-12 we compared the experimental dependence of  $M_{app}$  on  $R_h$  with two models for the micelle shape: oblate ellipsoid with a minor-axis of 2.5 nm; and the stiff rod model with a rod radius of 2.5 nm. In the case of all three mixed detergent, lecithin micellar systems we found that our data was in very poor agreement with the oblate ellipsoid model, but that it had much better correspondence with the stiff rod model.

We also made the empirical observation that the experimentally measured ratio  $\frac{R_h}{M_{app}^{1/2}}$  was nearly concentration independent over two decades of concentration for all of the lecithin micellar systems studied in this thesis, see Fig. 6-13. The weak concentration dependence of the ratio  $\frac{R_h}{M_{app}^{1/2}}$  could suggest a disk morphology. However, we deduced from the magnitude of  $\frac{R_h}{M_{app}^{1/2}}$  that the conjectured disk thickness would be only one fifth of that expected from the bilayer disk model. Thus, the disk model is shown to be implausible by the magnitude of the ratio  $\frac{R_h}{M_{app}^{1/2}}$  presented in Fig. 6-13.

The above findings lead us to conclude that micellar aggregates in mixed detergent, lecithin solutions do not form disks as proposed by Mazer *et al.*, rather they form rod-like or worm-like aggregates.



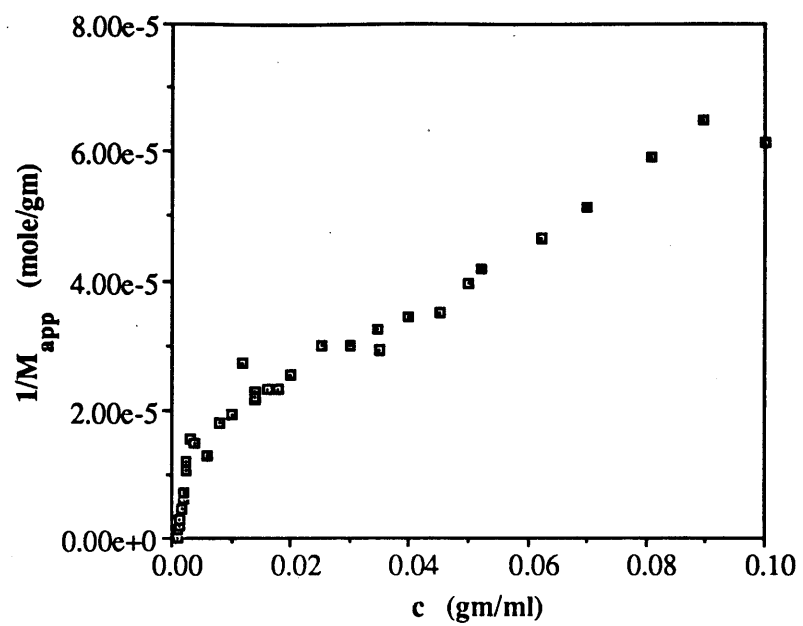


**Figure 6-7:** A plot of  $M_{app}^{-1}$  versus  $c$  for the NaTDCDC, lecithin, saline mixed micellar system.

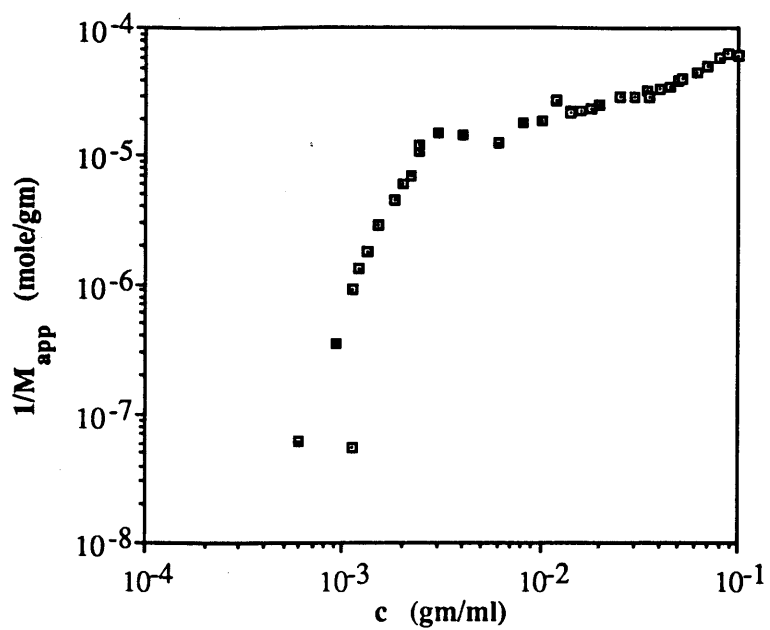


**Figure 6-8:** A log-log plot of  $M_{app}^{-1}$  versus  $c$  for the NaTCDC, lecithin, saline mixed micellar system.

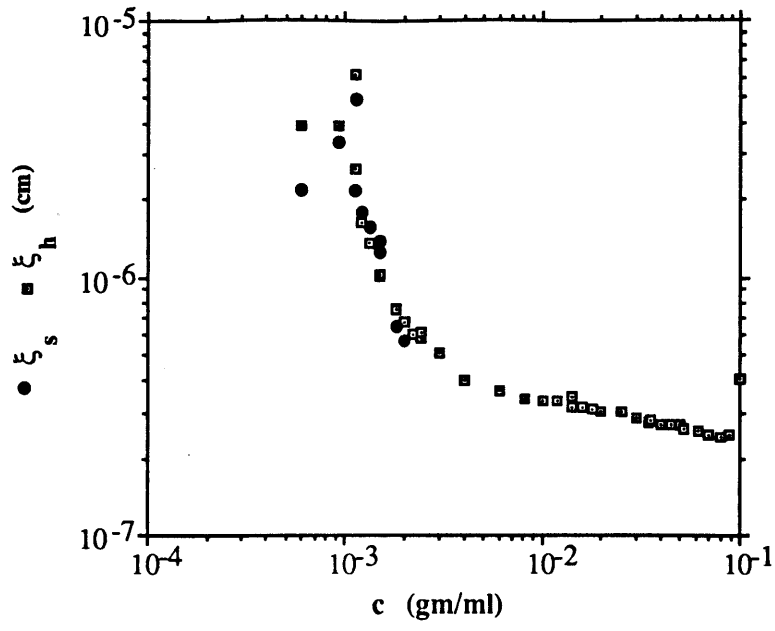


**Figure 6-9:** A log-log plot of  $\xi_h$ , and  $\xi_s$  versus  $c$  for the NaTCDC, lecithin, saline mixed micellar system.

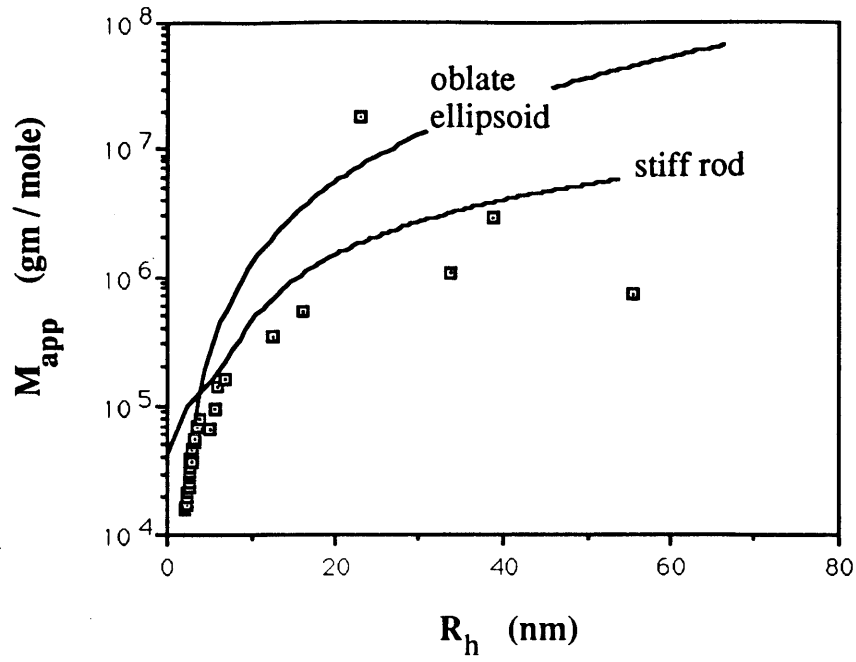
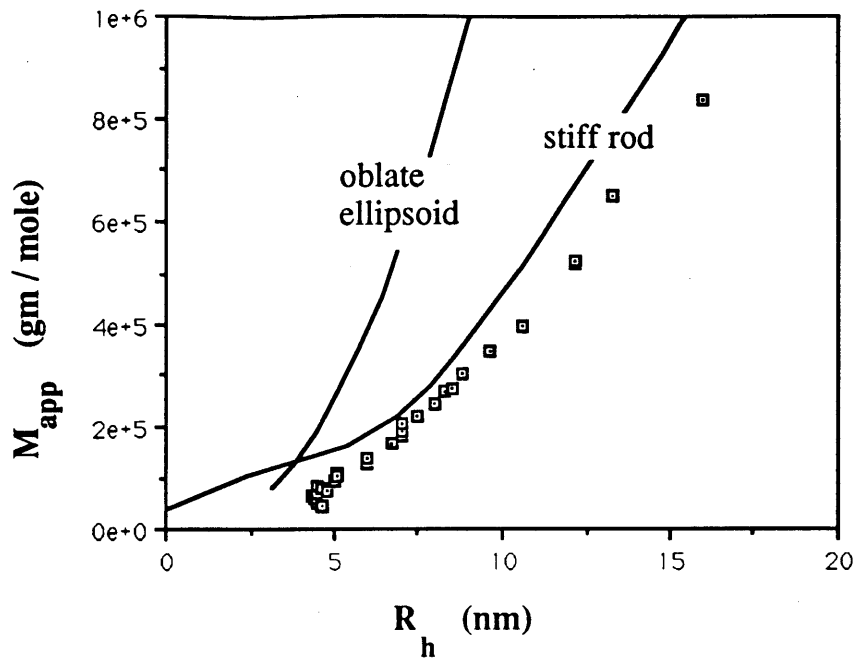


Figure 6-10: A plot of  $M_{app}$  versus  $R_h$  for the NaTDCD, lecithin, saline mixed micellar system.



**Figure 6-11:** A plot of  $M_{app}$  versus  $R_h$  for the OG, lecithin, saline mixed micellar system.



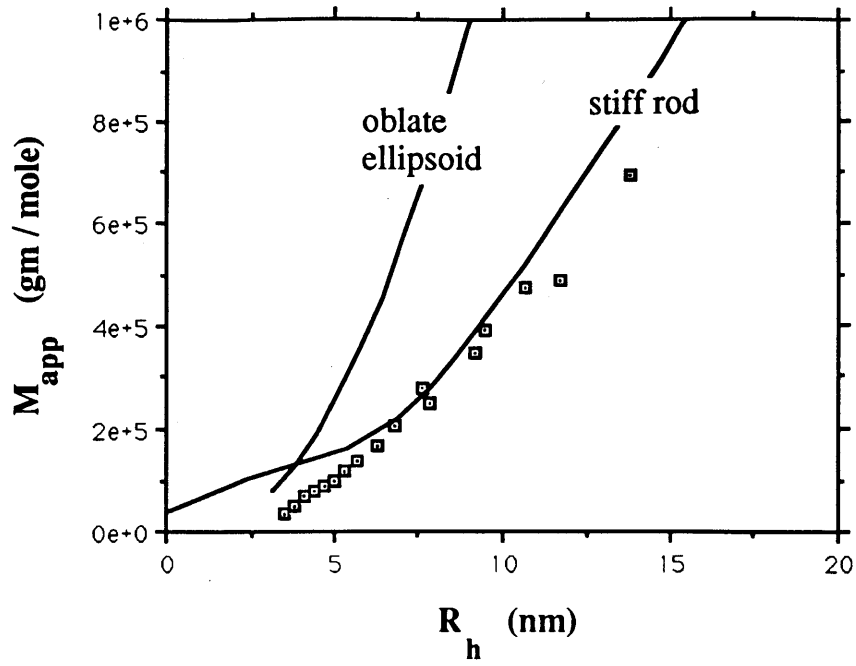
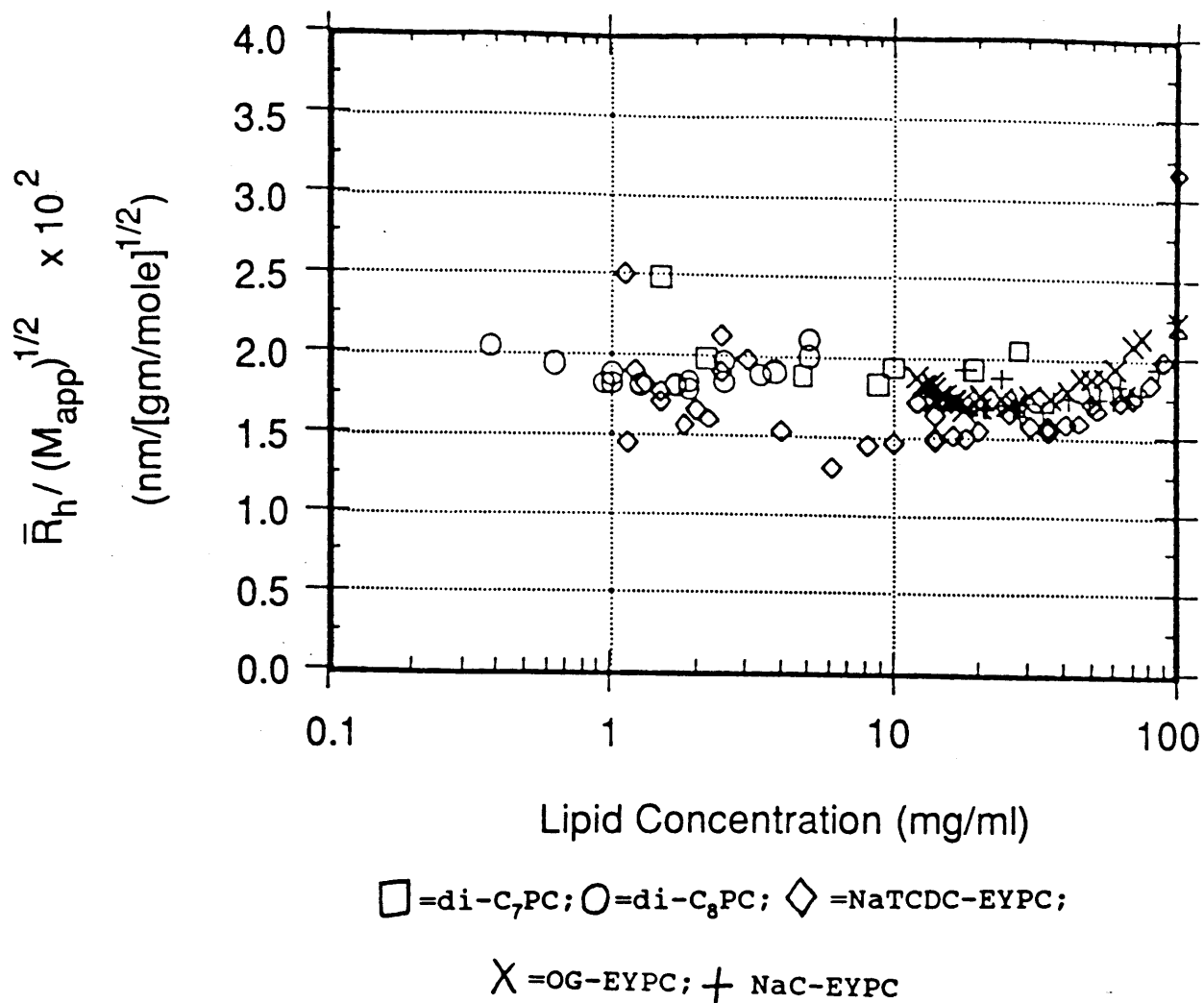
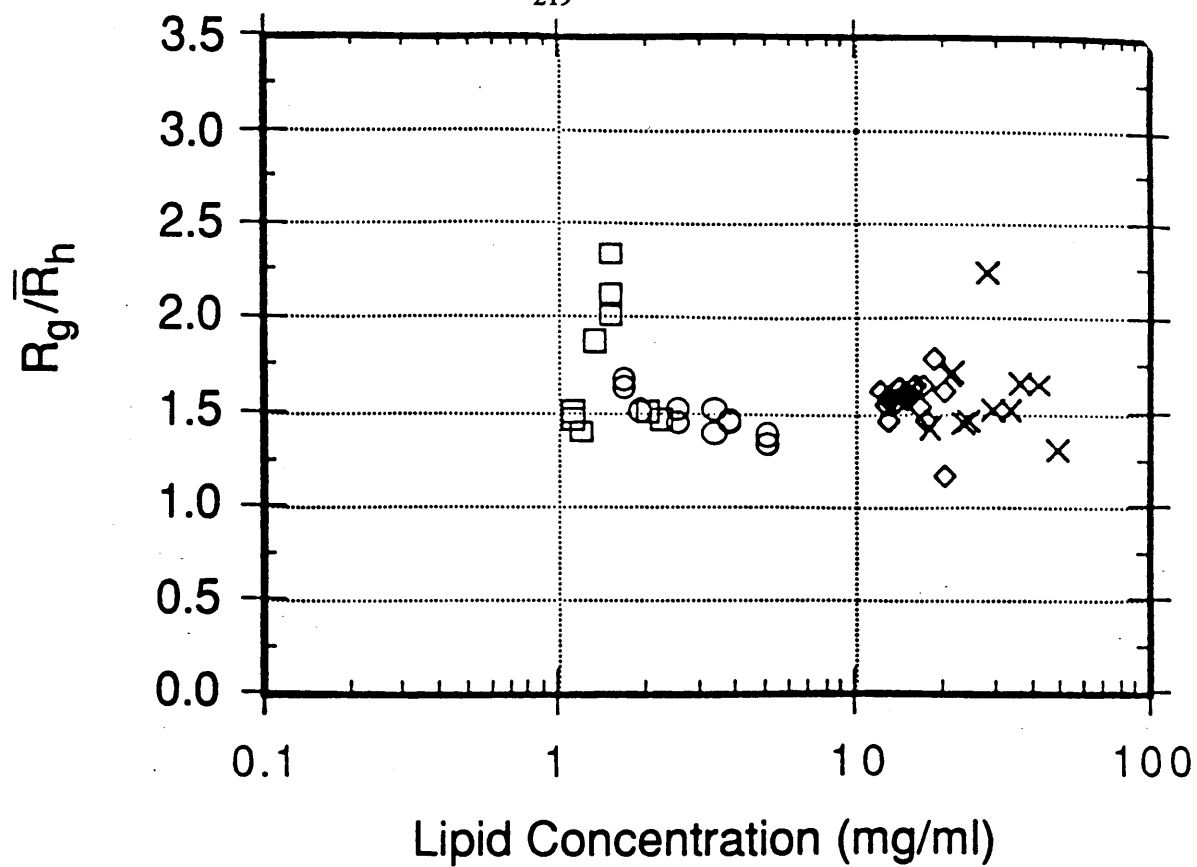


Figure 6-12: A plot of  $M_{app}$  versus  $R_h$  for the NaCl, lecithin, saline mixed micellar system.



**Figure 6-13:** A plot of the ratio  $\frac{R_h}{M_{app}^{1/2}}$  versus  $c$  for several of the various lecithin micellar systems studied in this thesis.

The di-C<sub>8</sub> lecithin data is from the 50° C isotherm. In the data from the di-C<sub>8</sub> lecithin system, high concentration data for  $c > 0.006$  gm/ml is not shown because of the proximity of the curve for liquid-liquid phase separation.



○ = di-C<sub>8</sub>PC; □ = NaTCDL-EYPC; ◇ = OG-EYPC; × = NaC-EYPC

Figure 6-14: A plot of the ratio  $\frac{R_g}{\bar{R}_h}$  versus  $c$  for several of the various lecithin micellar systems studied in this thesis.

## References for Chapter 6

- [1] N.A. Mazer, M.C. Carey.  
Quasielastic Light-Scattering Studies of Aqueous Biliary Systems. Cholesterol Solubilization and Precipitation In Model Bile Solutions.  
*Biochemistry* 22:426-442, 1983.
- [2] G.J. Somjen, T. Gilat.  
Contribution of vesicular and micellar carriers to cholesterol transport in human bile.  
*J. Lipid Res.* 26():699-704, 1985.
- [3] Tomlinson, E.  
Theory and practice of site-specific drug delivery.  
*Adv. Drug Delivery Rev.* 1():87-198, 1987.
- [4] D. Small.  
*Handbook of Lipid Research #4: The Physical Chemistry of Lipids From Alkanes to Phospholipids.*  
Plenum Press, 1986.
- [5] R. J.M. Tausk, J. van Esch, J. Karmiggelt, G. Voordouw, J. Th. G. Overbeek.  
Physical Chemical Studies Of Short-Chain Lecithin Homologues. II. Micellar Weights of Dihexanoyl- and Diheptanoyllecithin.  
*Biophysical Chem.* 1:184-203, 1974.
- [6] M. Carey, D. Small.  
*Am. J. Med.* 49():590, 1970.
- [7] M. L. Jackson, C. F. Schmidt, D. Lichtenberg, B. J. Litman, and A. D. Albert.  
*Biochemistry* 21():4576-4582, 1982.
- [8] M. Ollivon, O. Eidelman, R. Blumenthal, and A. Walter.  
Micelle-Vesicle Transition of Egg Phosphatidylcholine and Octyl Glucoside.  
*Biochemistry* 27(5):1695-1703, 1988.
- [9] P. P. Nair, and D. Kritchevsky.  
*The Bile Acids: Chemistry, Physiology, and Metabolism.*  
Plenum Press, 1971.
- [10] N.A. Mazer, G.B. Benedek, M.C. Carey.  
Quasielastic Light-Scattering Studies of Aqueous Biliary Lipid Systems. Mixed Micelle Formation in Bile Salt-Lecithin Solutions.  
*Biochemistry* 19:601-615, 1980.
- [11] P. Schurtenberger, N. Mazer, W. Kansig.  
Micelle to Vesicle Transition in Aqueous Solutions of Bile Salt and Lecithin.  
*J. Phys. Chem.* 89(6):1042-1049, 1985.

- [12] N.A. Mazer, M. C. Carey, R. F. Kwasnick, G.B. Benedek.  
Quasielastic Light-Scattering Studies of Aqueous Biliary Lipid Systems. Size,  
Shape, and Thermodynamics of Bile Salt Micelles.  
*Biochemistry* **18**:3064-3075, 1979.
- [13] J. Appell, G. Porte.  
Quantitative Estimate of the Orientational Persistence Length of Flexible Elongated  
Micelles of Cetylpridinium Bromide.  
*J. of Colloid and Interface Science* **87**(2):492-499, 1982.
- [14] R. P. Hjelm Jr., P. Thigarajan, H. Alkan.  
A Small-Angle Neutron Scattering Study of the Effects of Dilution on Particle  
Morphology in Mixtures of Glycocholate and Lecithin.  
*J. Appl. Cryst.* **21**:858-863, 1988.
- [15] P. K. Vinson, Y. Talmon, and A. Walter.  
Micelle-Vesicle Transition of Phosphatidylcholine and Octyl Glucoside  
Elucidated by Cryo-Transmission Electron Microscopy.  
*Biophys. J.* **56**:669-681, 1989.
- [16] P. K. Vinson, Y. Talmon, A. Walter.  
Cryo-TEM Reveals Structural Transitions of Egg PC and Sodium Cholate Mixtures.  
*Biophys. J.* , 1990.
- [17] H. R. Haller, C. Destor, and D. S. Cannell.  
Photometer for quasielastic and classical light scattering.  
*Rev. Sci. Instrum.* **54**:973-983, 1983.
- [18] D. J. Coumou.  
Apparatus For The Measurement Of Light Scattering In Liquids: Measurement  
Of The Rayleigh Factor Of Benzene And Some Other Pure Liquids.  
*J. Colloid Science* **15**:408-417, 1960.
- [19] Bender, T.M., Lewis, R.J. and Pecora, R.  
Absolute Rayleigh ratios of four solvents at 488 nm.  
*Macromolecules* **19**:244-245, 1986.
- [20] J. Ehl, C. Loucheux, C. Reiss, and H. Benoit.  
Mesure de l' increment d' indice de refraction de differentes solutions de hauts  
polymeres, et du rapport de Rayleigh de quelques liquides, en fonction de la  
temperature.  
*Makro. Chem.* **75**:35, 1964.
- [21] R. M. Waxler, C. E. Weir, H. W. Shamp Jr.  
Effect of Pressure and Temperature Upon the Optical Dispersion of Benzene,  
Carbon Tetrachloride and Water.  
*J. Res. Natl. Bur. Stand., Sect A* **68A**(5):489, 1964.
- [22] D. E. Koppel.  
Analysis of Macromolecular Polydispersity in Intensity Correlation Spectroscopy:  
The Method of Cumulants.  
*The Journal of Chemical Physics* **57**(11):4814 - 4820, 1972.

- [23] F. Perrin.  
*J. Phys. Radium* 7:1, 1936.
- [24] C. Y. Young, P. J. Missel, N. A. Mazer, G. B. Benedek, M. C. Carey.  
Deduction of Micellar Shape from Angular Dissymmetry Measurements of Light Scattered from Aqueous Sodium Dodecyl Sulfate Solutions at High Sodium Chloride Concentrations.  
*J. Phys. Chem.* 82:1375-1378, 1978.

## 7. CONCLUSION

This experimental thesis described the design, construction, calibration, and operation of a general purpose instrument for performing both static and dynamic light scattering experiments on macromolecular solutions over a broad temperature range. This instrument was used to perform a variety of experiments: the Rayleigh ratio of water, and the turbidity of several scintillator fluids were measured; several simple lecithin micellar systems were studied; and several mixed detergent, lecithin micellar systems were studied.

In Chapter 5 of this thesis, we described our measurements on two simple lecithin micellar systems, di-C<sub>7</sub> lecithin in D<sub>2</sub>O and H<sub>2</sub>O, and di-C<sub>8</sub> lecithin in H<sub>2</sub>O. From the concentration dependence of the scattered light intensity extrapolated to zero scattering angle, we measured the micelle aggregation number as a function of concentration in these systems. At low concentrations in each of these systems, we found that the amphiphile aggregation number scaled like the square root of the amphiphile mole fraction. This observation is consistent with the prediction of the ladder model [1] for micellar concentration dependent growth, and with the earlier observations of Tausk *et al.* [2, 3, 4]. From our comparison to the ladder model, we deduced the ladder model growth parameter  $\ln(K)$  in each of the micellar systems. In di-C<sub>7</sub> lecithin in D<sub>2</sub>O we found a value of  $\ln(K)$  which is compatible with earlier small angle neutron scattering measurements of Chen *et al.* [5]. We also found that di-C<sub>7</sub> lecithin micelles grow larger in D<sub>2</sub>O than in H<sub>2</sub>O. We also measured the concentration dependence of the aggregation number, and the osmotic susceptibility of Di-C<sub>8</sub> lecithin in H<sub>2</sub>O on two isotherms at 55°

C, and 35° C. From our data on the concentration dependence of the micelle aggregation number at low concentration, we deduced that on the 55° C isotherm  $T\ln(K) = 7100^\circ \text{K}$ , and on the 35° C  $T\ln(K) = 7200^\circ \text{K}$ , where  $K$  is the ladder model growth parameter, and  $T$  is the temperature. These values of  $T\ln(K)$  are consistent with the range of possible values Thurston [6] found by using only dynamic light scattering to deduce the concentration dependence of the micelle  $R_h$ , and then interpreting  $R_h$  in the context of a worm hydrodynamic model: for a range of hypothetical worm stiffnesses from stiff rod to very flexible, Thurston found that  $6900^\circ \text{K} < T\ln(K) < 7300^\circ \text{K}$ .

Thurston *et al.* [7] also developed a mean field theory to explain the phenomena of liquid-liquid phase separation in micellar solutions. For the di-C<sub>8</sub> lecithin micellar solution, which undergoes such a phase separation, Thurston *et al.* used the position and shape of the observed coexistence curve to measure the parameter  $T\ln(K)$  in the context of their theory. According to this method,  $T\ln(K) = 8100^\circ \text{K}$ , which is different than the values given above using static light scattering in this work, and dynamic light scattering in the earlier work. In the current work, we also used the light scattering intensity extrapolated to zero scattering angle, to measure concentration dependence of the osmotic susceptibility along the 55° C isotherm. Based on parameters derived from the position of the coexistence curve, the theory of Thurston *et al.* can also predict the concentration dependence of the osmotic susceptibility at 55° C. However, this predicted osmotic susceptibility is an order of magnitude less than what we actually observed. In light of our new findings, the theory of Thurston *et al.* may require modifications for application to the di-C<sub>8</sub> lecithin micellar system.



In this thesis, we also examined three types of mixed detergent, biological lecithin micellar systems. We studied the effects of the detergents octylglucoside, sodium cholate, and sodium taurochenodeoxycholate on mixed detergent, lecithin micellar aggregates. In these three micellar systems, we examined the molecular weight dependence on  $R_h$  in order to deduce the likely micelle shape. We compared the  $M_{app}$  dependence on  $R_h$  with two micelle models, the oblate ellipsoid with a semi-minor axis of 2.5 nm, and the stiff rod model of radius 2.5 nm. In this comparison, we found that in all three systems, our data had very poor agreement with the oblate ellipsoid model, but that it had some correspondence with the stiff rod model.

By examination of the concentration dependence and magnitude of the ratio  $\frac{R_h}{M_{app}^{1/2}}$  we also found other evidence against the disk model. We observed that the ratio  $\frac{R_h}{M_{app}^{1/2}}$  was nearly concentration independent over two decades of concentration in all of the micellar systems studied in this thesis. This relative concentration independence of  $\frac{R_h}{M_{app}^{1/2}}$  could suggest the presence of disk like micelles, except that the observed magnitude of  $\frac{R_h}{M_{app}^{1/2}}$  requires that the disks be only 0.7 nm thick. On the other hand, the micelle disk model assumes that the disk resembles a fragment of a lecithin bilayer: therefore, the disk model requires that the disk be at least 5 nm thick, twice the length of a biological lecithin molecule. Therefore, we find that the disk model cannot explain the magnitude of the ratio  $\frac{R_h}{M_{app}^{1/2}}$  self consistently. In a previous presentation of this work, we had stated that [8] the weak concentration dependence of  $\frac{R_h}{M_{app}^{1/2}}$  was consistent with worm like rods with a radius 2.5 nm, and a persistence length of 26 nm. However, this interpretation of

the ratio  $\frac{R_h}{M_{app}^{1/2}}$  assumes that the contour length of the worm is long compared to the persistence length. Since this assumption may not be valid for smaller micelles, we cannot justify using the ratio  $\frac{R_h}{M_{app}^{1/2}}$  to measure the persistence length of the micelles. However, the magnitude of  $\frac{R_h}{M_{app}^{1/2}}$  did allow us to discriminate against the bilayer disk model, as noted above.

## References for Chapter 7

- [1] P.J. Missel, N.A. Mazer, G.B. Benedek, C.Y. Young.  
Thermodynamic Analysis of the Growth of Sodium Dodecyl Sulfate Micelles.  
*J. Phys. Chem.* 84():1044 - 1057, 1980.
- [2] R. J.M. Tausk, J. van Esch, J. Karmiggelt, G. Voordouw, J. Th. G. Overbeek.  
Physical Chemical Studies Of Short-Chain Lecithin Homologues. II. Micellar  
Weights of Dihexanoyl-and Diheptanoyllecithin.  
*Biophysical Chem.* 1:184-203, 1974.
- [3] R. J.M. Tausk, C. Oudshoorn, J. Th. G. Overbeek.  
Physical Chemical Studies Of Short-Chain Lecithin Homologues. III. Phase  
Separation and Light Scattering Studies on Aqueous Dioctanlollylecithin  
Solutions.  
*Biophysical Chem.* 2:53-63, 1974.
- [4] R. J.M. Tausk, J. Th. G. Overbeek.  
Physical Chemical Studies Of Short-Chain Lecithin Homologues. IV. A Simple  
Model For The Influence Of Salt And The Alkyl Chain Length On The Micel-  
lar Size.  
*Biophysical Chem.* 2:64, 1974.
- [5] Tsang-Lang Lin, Sow-Hsin Chen ,and Mary F. Roberts.  
Thermodynamic Analysis of the Structure and Growth of Asymmetric Linear  
Short-Chain Lecithin Micelles Based on Small-Angle Neutron Scattering  
Data.  
*Jornal of the American Chemical Soc.* 109():2321, 1987.
- [6] G. M. Thurston.  
*Studies of Phase Separation in Micellar Solutions.*  
PhD thesis, Massachusetts Institute of Technology, 1986.
- [7] D. Blankschtein, G. M. Thurston, G. B. Benedek.  
Theory of Phase Separation in Micellar Solutions.  
*Phys. Rev. Lett.* 54(9):955-958, 1985.
- [8] R. A. Chamberlin, D. Cohen, G. M. Thurston, G. B. Benedek, M. C. Carey.  
Light Scattering Evidence for Worm-like Mixed Detergent Lecithin Micelles.  
Materials Research Society, in Boston, 27 Nov 1989.

## ...Autobiographical Note...

I was born on 19 Feb 1958 in Palo Alto, California to Richard Addison Chamberlin, and Jane Levin Chamberlin. In 1975, I was graduated from University High School, Los Angeles, California. I served on active duty in the United States Air Force from 2 Oct 1975 to 31 April 1979. In the Air Force, I was trained to be a weather observer, and the highest grade I attained was E-4 (three stripes). I was graduated from the University of California, Santa Barbara (UCSB) in 1984 with a Bachelor of Science degree with a major in Physics "With High Honors".

Military Honors: USAF Commendation Medal, April 1979

Academic Honors: UCSB Chancellor's Scholarship, 1983  
UCSB Physics Dept. Arnold Nordsieck Memorial Prize, 1984

Publications:

"New Evidence Concerning the Griffiths First Sum Rule for Tricritical Light Scattering", A. Kumar, R. Chamberlin, D.S. Cannell, I.L. Pegg, C.M. Knobler, & R. L. Scott, Phys. Rev. Lett. **54**, 20 (1985)

"Size and Structure in Antibody - Antigen Complexes", R. Murphy, H. Slayter, P. Schurtenberger, R. Chamberlin, C. Colton, & M. Yarmush, Biophys. J. **54**, 45 (1988)

"Observation of Critical Phenomena in a Protein - Water Solution", P. Schurtenberger, R. Chamberlin, G. Thurston, J. Thomson, G. Benedek. Phys. Rev. Lett. **63**, 19 (1989)

## ...Acknowledgements...

The work presented here was supported in part by the following grants to Prof. George Benedek: National Science Foundation Grant numbers 84-08630-DMB, and 84-18718-DMR; and by the Jessie B. Cox Charitable Trust. I thank Prof. Benedek for making these, and other resources available to me during the period over which this work was performed. I also thank the Physics Department for providing me with a Teaching Assistantship position during my last year so I could finish this thesis.

If finishing this thesis can be deemed a "success" in my life, then I must give credit to the people who prepared me for this effort, and who urged me on. My late grandmother, Lydia Levin, helped me more than anyone. Mrs. Ellen Gottesman Beckwitt taught me how to be a good citizen and imparted to me a love of scholarship. Kenneth Ronney showed me what science and technology are about. My sojourn in the United States Air Force provided me with the material resources I needed to work on my undergraduate degree at the University of California at Santa Barbara. I am grateful to the United States government for making my undergraduate education possible through the GI Bill, and the Pell grant program.

The one person who had the greatest influence on my development as an experimental physicist is Prof. David Cannell. I am very lucky to have had the privilege of working with him for several years while I was an undergraduate. Prof. Cannell suggested that I attend MIT for graduate school, and Prof. Benedek urged me to stay once I came. Their faith in me has a lot to do with why I remained in the graduate program.

Hansruedi Haller showed me the "right" way to do things in the lab. George

Thurston, and Peter Schurtenberger made many helpful suggestions about what systems to study and how to understand my data. I enjoyed my short association Mike Fisch with whom I had some discussions during the design stages of my light scattering instrument. Michael Broide helped me survive my final years in the graduate program.

I had short and informal collaborations with Bruce Carvalho on the di-C<sub>7</sub> lecithin measurements, and with Peter Rothschild on the BOREX scintillator turbidity measurements. I had a longer, and quite enjoyable collaboration with David Cohen, and Prof. Martin Carey on our studies of the three component biological lecithin, detergent, and water micelle systems. I think our collaboration will continue, since we still need to write a paper. David Cohen produced several of the figures used in Chapter 6.

My friends were very supportive of my efforts. First among them is David Longval. Virgil and Regina Martinonis made me feel like a very welcome guest in the Northeast. My sailing friends helped me keep amused during my "re-charge" periods. Some of these sailing "buds"<sup>3</sup> are John Scannel, Justin Scott, Jack Carney, Ben Block, Sam Latrenta, and Sue Walsh. And finally, my brother Chris provided me with some of those little gems of wisdom that helped keep everything in perspective.

---

<sup>3</sup>As in "buddy".